Flowable One-Part Alkali Activated Materials: Challenges and Techniques

Nourhan Ali

A Thesis

In the Department of

Building, Civil and Environmental Engineering

Presented in Partial Fulfillment of the Requirements

For the Degree of

Doctor of Philosophy (Building, Civil and Environmental Engineering) at

Concordia University

Montreal, Quebec, Canada

April 2025

CONCORDIA UNIVERSITY

School of Graduate Studies

This is to certify that the thesis prepared
By: **Nourhan Ali**

Entitled: **Flowable One-Part Alkali Activated Materials: Challenges and Techniques**

and submitted in partial fulfillment of the requirements for the degree of

Doctor of Philosophy (Civil Engineering)

complies with the regulations of the University and meets the accepted standards with respect to originality and quality.

Signed by the final Examining Committee:

_____ Chair
Dr. Nematollaah Shiri

_____ External Examiner
Dr.Khandaker Hossein

_____ Arm's Length Examiner
Dr. Mehdi Hojjati

_____ Examiner
Dr. Samuel Li

_____ Examiner
Dr. Chunjiang An

_____ Thesis Supervisor
Dr. Ahmed Soliman

Approved by _____
Dr. Po-Han Chen, Graduate Program Director

2025-04-24

_____
Dr. Mourad Debbabi, Dean of Gina Cody School of Engineering and Computer Science

Abstract

Flowable One-Part Alkali Activated Materials: Challenges and Techniques

Nourhan Ali, Ph.D.

Concordia University, 2025

Canada has committed to achieving net zero greenhouse gas emissions by 2050, and the construction sector plays a critical role in meeting this target. Cement production alone contributes nearly 8% of global CO_2 emissions, making it essential to explore alternatives to Ordinary Portland Cement (OPC). One promising solution is the use of alkali-activated materials (AAMs), which are produced from industrial by-products and can substantially reduce both carbon emissions and energy consumption in concrete production. Among these, one-part alkali-activated slag (AAS), often referred to as "just add water AAM," is particularly attractive because of its ease of application and ability to achieve high early strength without heat curing. Despite these advantages, one-part AAS still faces significant challenges, including low workability, rapid slump loss, and short setting times, which limit its practical use in ready-mix and on-site applications. While some studies have examined chemical admixtures to enhance AAM performance, there remains limited research on the specific behavior of one-part AAS systems. In particular, little attention has been given to the effects of mixing protocols, retarders, and viscosity-modifying admixtures on both fresh and hardened properties. To address these gaps, this research is divided into four phases. The first phase evaluates the effect of changing ingredient addition sequences on reaction kinetics. Based on these findings, the optimized sequence is carried into the following phases. The second phase investigates the influence of mixing times, speeds, and styles (continuous versus discrete) on the fresh and rheological behavior of one-part AAS. The third phase examines the use of chemical retarders to improve workability and extend slump life without compromising strength. Finally, the fourth phase explores the role of viscosity-modifying admixtures (VMAs) in stabilizing the mix and enhancing flowability and setting behavior. By systematically studying these variables, this research advances understanding of one-part AAS and highlights pathways to improve its fresh properties. The outcomes are expected to support broader adoption of sustainable binders in construction and contribute to Canada's net-zero emission goals.

Acknowledgments

First and foremost, I would like to thank Allah for His countless blessings throughout my life and for guiding me through all the challenges. I would also like to express my heartfelt gratitude to my supervisor, Dr. Ahmed Soliman, for his unwavering support, patient guidance, and invaluable feedback throughout my research journey. His mentorship has been invaluable in shaping this thesis and fostering my growth as a researcher.

Additionally, I extend my sincere gratitude to my examiners for their valuable time and constructive feedback, which have greatly enhanced the quality of this work.

I am deeply grateful to my beloved parents, whose unconditional love, unwavering support, and constant encouragement have been my pillars of strength throughout this academic journey.

Special thanks to my dear husband, Mohamed. I could not have wished for a more supportive and loving partner. His unwavering love, steadfast support thoughtful insights, intellectual discussions, and selfless sacrifices have been a source of immense strength and inspiration to me. I am also deeply grateful to my baby girl, Lina, whose presence inspired and encouraged me to finalize my work. Finally, I extend my sincere gratitude to my dear friend, Dr. Aya Doma, whose support, positivity, and guidance made this journey easier, more enjoyable, and truly unforgettable.

I extend my sincere gratitude to the School of Graduate Studies, Concordia University (Canada), for providing the Ph.D. scholarship and financial support.

I am deeply thankful to Dr. Alexandre Arnold for recording the NMR spectra and to Mr. Gwenaël Chamoulaud at Université du Québec à Montréal for recording the X-ray diffraction (XRD) and Thermal Gravimetric Analysis (TGA), as well as for his valuable discussions. Special thanks also go to Mr. Dileep Palakkeel for recording the Inductively Coupled Plasma (ICP) and Dr. Dmytro Kevorkov for recording the Scanning Electron Microscope (SEM) at Concordia University.

To the beloved soul of my late father, who passed away during this journey.
I hope I have made you proud with all that I have achieved.
Your memory continues to inspire me every day.

Contributions of Authors

This thesis is compiled per Concordia University's Faculty of Graduate Studies regulations. It includes sections that have been published or are under consideration for publication in peer-reviewed journals and conference proceedings.

This thesis adheres to Concordia University's Faculty of Graduate Studies regulations. The candidate solely carried out experimental and theoretical work, developed the models, wrote initial drafts, and authored all publications listed below. Advice and guidance were provided for the whole thesis by the academic supervisor Dr. Ahmed Soliman.

1- **Nourhan EL-sayed** and Ahmed Soliman (2022). "Alkali Activated Concrete Workability and Effect of various Admixtures: A review" The CSCE Annual Conference of The Canadian Society. (**Chapter 2**)

2- **Nourhan Ali** and Ahmed Soliman (2024). " Review: Investigation Effect of Different Factors on Fresh and Hardened Properties of One-Part Alkali Activated Materials" The CSCE Annual Conference of The Canadian Society. (**Chapter 2**)

3- **Nourhan Ali** and Ahmed Soliman (2024). "Effect of Ingredients Adding Sequences on Rheological Properties of Alkali-Activated Slag Paste" Innovative Infrastructure Solutions 9 (2024) 145. https://doi.org/10.1007/s41062-024-01462-0. (**Chapter 3**)

4- **Nourhan Ali** and Ahmed Soliman (2024). " Understanding the Effect of Mixing Time on the Rheological Behavior of Alkali Activated Slag Paste" The CSCE Annual Conference of The Canadian Society. (**Chapter 4**)

5- **Nourhan Ali** and Ahmed Soliman (2024)." Influence of mixing protocols on flow retention of one-part alkali activated slag systems" Construction and Building Materials Journal, https://doi.org/10.1016/j.conbuildmat.2024.138467. (**Chapter 4**)

6- **Nourhan Ali** and Ahmed Soliman (2025). " Evaluating the Impact of Mixing Techniques on Shrinkage Behavior of One-part Alkali-Activated Slag Systems " The CSCE Annual Conference of The Canadian Society. Submitted (**Chapter 4**)

7- **Nourhan Ali** and Ahmed Soliman (2025)."Single and Multi-response Optimization of Retarded Admixture on Alkali Activated Slag Rheological Behavior by the Taguchi Method" Construction and Building Materials Journal, https://doi.org/10.1016/j.conbuildmat.2024.139812. (**Chapter 5**)

8- **Nourhan Ali** and Ahmed Soliman (2025)."Influence of Viscosity Modifier Addition Methods on the Rheological Behavior of Alkali-Activated Slag Systems" Construction and Building Materials Journal, https://doi.org/10.1016/j.conbuildmat.2025.141714. (**Chapter 6**).

Table of Contents

List of Figures

List of Tables

List of Acronyms

AAMs	Alkali activated materials
AAS	Alkali activated slag
OPC	Ordinary Portland cement
RMC	Ready Mix Concrete
LCA	Life Cycle Assessment
ERS	End Result Specifications
IT	Initial Setting Time
FT	Final Setting Time
C-S-H	Calcium-silicate-hydrate
C-(A)-S-H	Calcium-(alumino) silicate-hydrate
N-A-S-H	Alkali- alumino-silicate- hydrate
RH	Relative humidity
GHGs	Green House Gas emissions
CaO	Calcium Oxide
RHA	Rice Husk Ash
HT	Hydrotalcite
FA	Fly ash
T	Temperature
Waterglass	Sodium silicate
MS	Micro Silica
CSS	Calcinated Salt Sludge
SR	Soda Residue
SPs	Superplasticizers
PC	Polycarboxylate
N	Naphthalene
M	Melamine
LS	Lignosulfonate
PFS-SP	Polycarboxylate-based superplasticizer
GGBFS	Ground granulated blast furnace slag
Nb-SP	Modified naphthalene-based superplasticizer
PNS	Poly naphthalene sulfonate
PFS-SP	Invented laboratory-prepared SP
PNS	Poly naphthalene sulfonate
TCT-P	Thermo-chemical-treated powders
SG	Sodium Gluconate
STP	Sodium Triphosphate

CL	Calcium Lignosulphonate
w/s	Water to Solid Ratio
w/b	Water to Binder Ratio
ASTM	American Society for Testing and Materials
XRD	X-ray Diffraction
TGA	Thermogravimetric Analysis
FTIR	Fourier-Transform Infrared Spectroscopy
SEM	Scanning Electron Microscopy
EDS	Energy-Dispersive X-ray Analysis
AD	Activator Dosage
RT	Retarder Type
RD	Retarder Dosage
GRA	Grey Relational Analysis
TOPOSIS	Technique for Order of Preference by Similarity to Ideal Solution
ICP-MS	Inductively Coupled Plasma Mass Spectrometry
AP	Acidification
CH	Climate Change
FT	Freshwater Ecotoxicity
MT	Marine Ecotoxicity
TT	Terrestrial Ecotoxicity
NRE	Non-renewable Energy Resources
EP	Eutrophication
HT	Human Toxicity
RD	Resource Depletion
ODP	Ozone Depletion
POF	Photochemical Oxidant Formation
B	Borax
M	Maleic Acid
N	Nano Zinc Oxide
C	Calcium Carbonate
XRF	X-ray Fluorescence
S/N	Signal-to-Noise Ratio
FD	Flow Diameter
YS	Yield Stress
PV	Plastic Viscosity
CS	Compressive Strength
TSP	Time of Second Peak
ANOVA	Analysis of Variance

VMA	Viscosity Modifier Admixture
AASC	Alkali-Activated Slag Concrete
SAPs	Super Absorbent Polymers
HPMC	Hydroxypropyl Methylcellulose
LC_3	Limestone Calcined Clay Cement

Chapter 1: Introduction

1.1. General background

Cement production contributes about 8% of total carbon emissions [1–3] and consumes about 40% of global energy [4]. Hence, several researchers focused on finding an environmentally friendly alternative to cement (e.g. sulphate-aluminate cement [5], high-calcium fly ash–Portland cement [6], and lime calcined clay cement [7]). Alkali Activated Materials (AAMs) are promising alternatives [8,9] as they are prepared by activating industrial by-products (i.e. precursor) using high-alkaline activators [10–14]. Solid precursors for alkali activation are typically amorphous aluminosilicate materials such as ground-granulated blast-furnace slag (GGBFS) [15–17], metakaolin [18,19], silica fume, rice husk ash [20–22], and fly ash (FA) [23–26]. Alkali activators include compounds with hydroxide (i.e. KOH and NaOH) and silicate components (i.e. K_2SIO_3 and Na_2SiO_3) [27]. Studies have employed various activators such as sodium hydroxide (NaOH) [28], sodium silicate (Na_2SiO_3) [29–31], sodium carbonate (Na_2CO_3) [32–34], sodium aluminate ($NaAlO_2$), sodium sulfate (Na_2SO_4), and potassium hydroxide (KOH) to raise the pH of mixtures or agricultural waste materials such as rice straw ash [35] and rice husk ash [36]. This increase in pH facilitates the inclusion of alkali cations, thereby accelerating the dissolution of precursors and enhancing the alkali activation process [23]. Generally, the efficiency of the binder activation process depends on the type of precursor and activator and its pH value, which controls the degree of hydration and product formation [37].

AAMs can be categorized as "two-part" or "one-part" based on the nature of the activator. In two-part AAMs, a high alkalinity liquid–based activator is used to activate the precursor, while powder activator is used in one-part AAMs [38–40]. The easier and safer handling of powder activators promoted one-part AAMs usage in various construction applications than two-part AAMs [41–44]. However, the rapid slump-loss of AAMs (either two-part or one-part) is a major acceptance barrier in the construction sector [45]. Additionally, drying shrinkage is a significant concern, particularly for alkali-activated slag-based materials [46]. Many studies reported rapid setting time and loss of workability of AAMs, especially for AAS systems activated by silicate [47–49]. This was ascribed to the high dissolution rate of the silicate activator, which accelerates the formation of primary C-(A)-S-H gel, developing the microstructure [50,51]. In addition, high heat is liberated

during slag particle dissolution because this dissolution increases the rate of hydration product formation.

Over the past three decades, the RMC industry has grown significantly, prompting shifts in customer expectations. Traditionally, suppliers focused on concrete's transfer and arrival at construction sites as the primary performance metrics. However, this perspective needs expansion. Bickley et al. introduced the concept of End Result Specifications (ERS), emphasizing the importance of evaluating concrete's in-situ performance through testing [52]. In practice, the performance of RMC has largely been assessed using direct methods, particularly strength, which aligns with the conventional understanding within the industry. Unfortunately, testing for rheology and fresh properties has often been overlooked. To ensure a comprehensive evaluation of performance and widen the use of one-part AAS on site, it is crucial to prioritize in-situ testing of rheology and fresh properties and align these evaluations with specific criteria to meet ERS requirements. This focus will be emphasized in the objectives of the thesis, as it addresses the critical aspects of mixing time and methods, which are essential too in RMC production.

1.2. problem statement

Most of the studies in the literature focused on utilizing various types and dosages of admixtures, particularly superplasticizers, to retard the hydration reaction and consequently extend the slump life, especially for two-part AAMs [45,53–56]. However, the stability and solubility of admixtures in such a highly alkaline environment [57], along with their adsorption on precursor grains, resulted in poor performance [58,59]. Hence, other studies investigated the impact of varying admixtures' addition time on AAMs' fresh properties [59,60]. It was reported that the delayed addition of polycarboxylate ether (PCE) to AAMs reduced the static yield stress, leading to better flowability [59]. Another approach focused on studying the effect of extending the mixing time on two-part AAS properties [61]. The findings confirmed the benefits of prolonging mixing time on hardened properties; however, no attention was given to variations in fresh properties. This highlighted a knowledge gap in the literature that, to the best of the authors' knowledge, no previous work had tackled. Therefore, investigating the effect of prolonging mixing time on one-part AAS will increase its potential for RMC applications. RMC mixtures are usually exposed to long continuous mixing during delivery [62,63]. The maximum allowed mixing time is 90 minutes for RMC according to the ASTM C94 "Standard Specification for Ready-Mixed Concrete" [48]. Hence, to design an AAS system activated by meta-silicate to produce high-strength material, it is

essential to understand the significance of extending mixing time and changing the ingredients' adding sequence.

On the other hand, research on incorporating retarders into one-part AAS systems remains limited. Most studies have focused on extending the setting times of one-part AAMs by incorporating various materials such as metakaolin, bentonite, natural pozzolan, red mud, and other mineral additives. These materials reduce high-calcium precursors by partially or fully replacing slag with low-calcium alternatives [64]. Another approach involves using inhibitors of calcium carbonate precipitation, such as anti-scaling agents, including the phosphonate molecule HEDP (tetrasodium 1-hydroxyethylidene) [65]. This gap in research highlights the need to assess the efficiency of different retarder types and their interactions with various ingredient proportions, such as water content, activator dosage, and retarder dosage, in one-part AAS systems. Additionally, identifying the most effective factors that significantly influence the rheological properties of AAS is crucial. Finally, the interaction between OPC and viscosity-modifying admixtures (VMAs) is well understood [66–68], but the behavior of VMAs in AAS systems remains largely unexplored. Existing studies have demonstrated how increasing VMA dosages influence the hydration kinetics of OPC; however, the effects of different mixing strategies and VMA addition timings on the hydration kinetics of AAS mixtures have not been investigated. This gap highlights the need to examine the influence of the VMA addition method (adding the VMA separately (undissolved in water) and dissolving the VMA in water before incorporation). Additionally, assessing the timings of VMA addition (early addition (1 minute after dry mixing the powder ingredients) and delayed addition (25 minutes after dry mixing)).

1.3. Research objectives

Numerous tonnes of blast-furnace slag, a by-product of raw iron manufacturing, and various other industrial by-products are annually generated, creating a significant environmental challenge if left to be landfilled. Hence, utilizing these industrial by-products is an urgent need. According to the LCA study, AAS concrete is considered a promising alternative with the potential to reduce the environmental impact of concrete products substantially. It achieves a remarkable 73% reduction in GHGs and a 43% decrease in energy demand compared to OPC concrete [69]. Beyond environmental advantages, AAS concrete showed exceptional mechanical properties (i.e. a notably high compressive strength of up to 130 MPa). Furthermore, AAS exhibits superior durability present acid, sulfate, and fire attack resistance. However, challenges in applying AAS concrete

have been identified, such as poor workability, rapid slump loss, and short setting time. These challenges present difficulties in casting concrete elements and limiting AAS's broad applicability on construction sites. These challenges highlight the need for further research and development to enhance AAS systems' workability and handling characteristics. This makes it a more versatile and widely adopted alternative to ready-mix OPC concrete. Accordingly, the objectives of this study and the scope of work are as follows :

1- Clarifying the effect of changing the sequence of ingredient addition in AAS paste (slag, water, and meta-silicate activator) on initiating the reaction for synthesizing AAS paste. This is a preliminary step to confirm the suitability of the sequence of the main ingredients used without adding any external additives.

2- Investigating the effect of applying various mixing regimes in terms of mixing time and mixing type (discrete or continuous) on fresh and hardened properties of AAS paste activated by various dosages of meta-silicate. This is the first step in gaining a preliminary understanding of the impact of extending mixing time and changing mixing type on fresh properties, including rheological properties and hardened properties of AAS paste. Variance analysis (ANOVA) will also be applied to evaluate the significance of each parameter.

3- Evaluating the efficiency of various retarders (types—dosages) in enhancing AAS paste's workability, slump life, and rheological behavior. Besides, applying LCA on optimized mixtures.

4- Exploring the rheological behavior of AAS pastes with VMA added at different times and using various methods, either pre-dissolved in water or added separately.

Additionally, the experimental plan for four phases designed to achieve the main research objectives is outlined in **Fig. 1.1**, and the detailed framework of the thesis is depicted in **Fig. 1.2**.

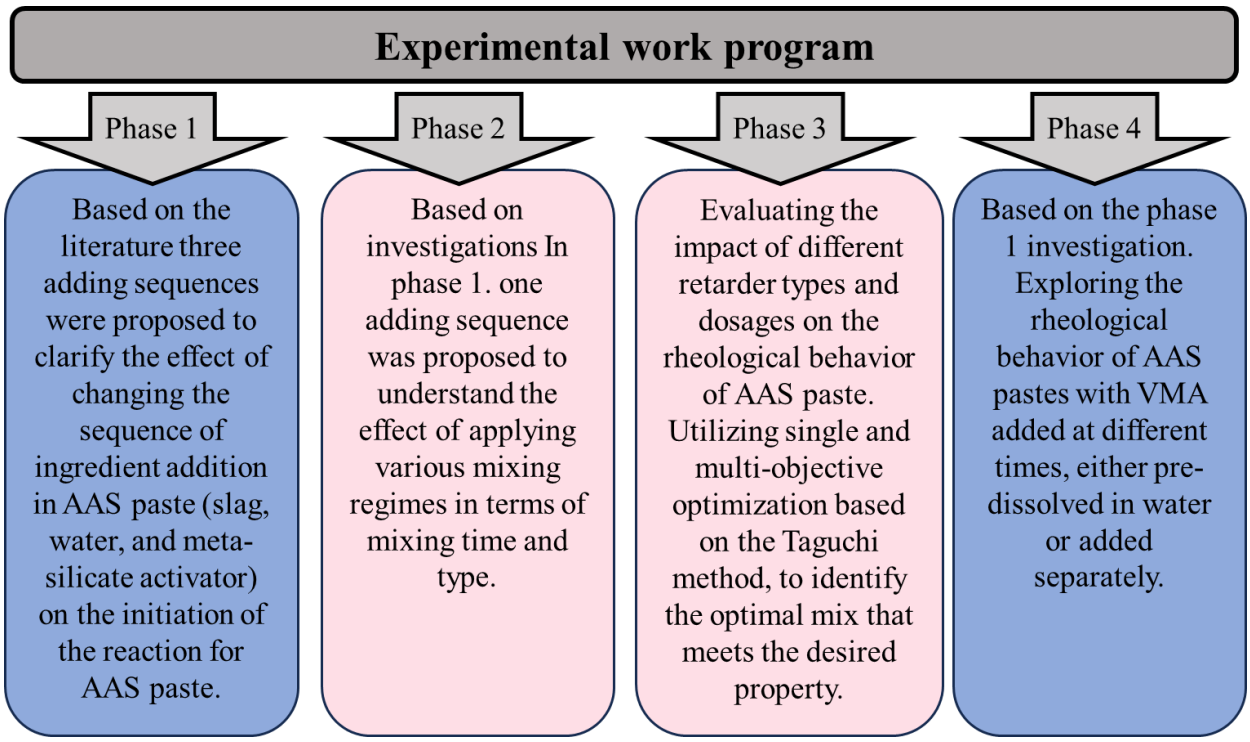

Fig. 1.1: Experimental work program phases.

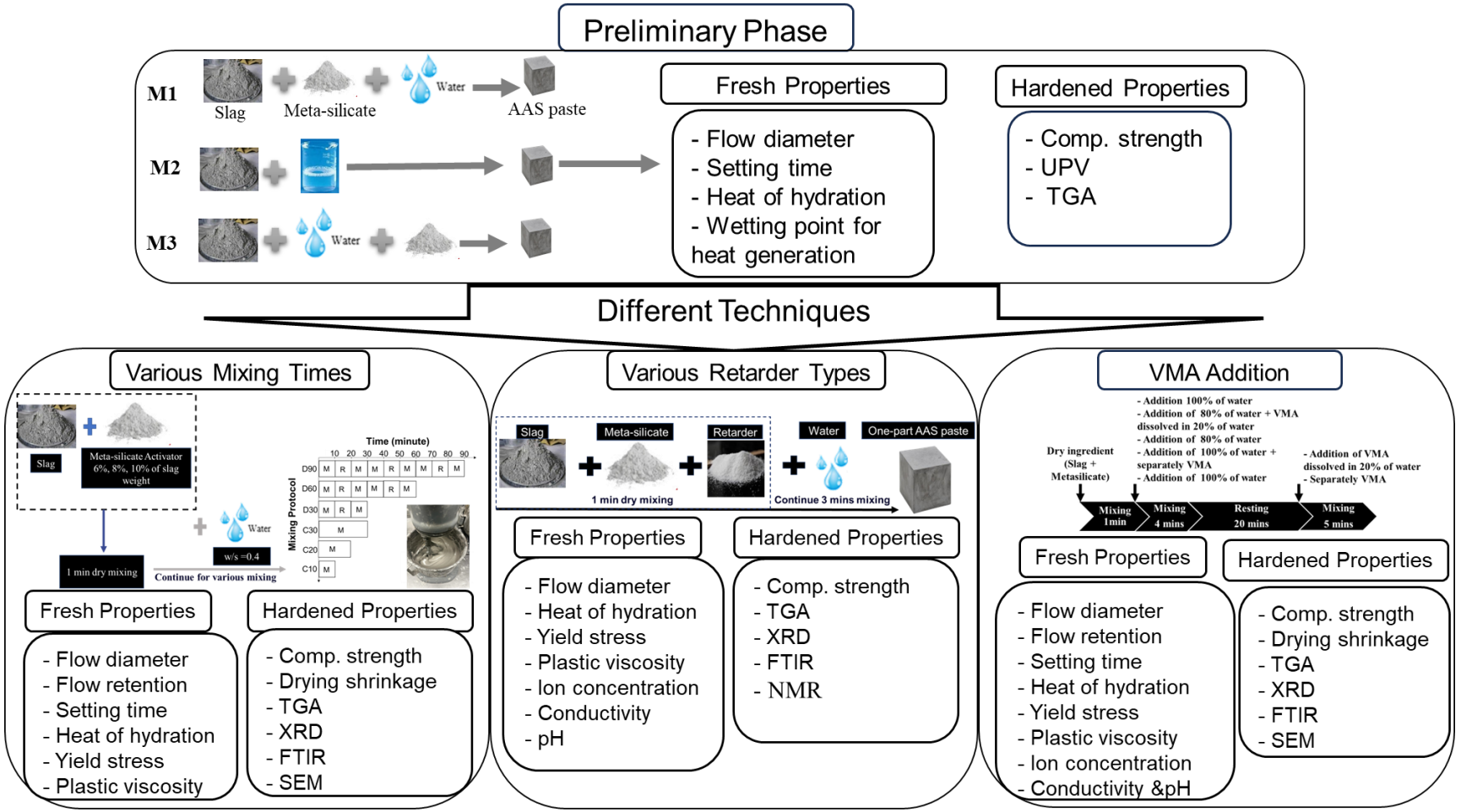

Fig. 1.2: Framework of the thesis.

1.4. Thesis Structure

This thesis is structured to provide a comprehensive investigation of the proposed techniques influencing the flowability of one-part AAS. It includes a series of experimental studies to evaluate the fresh, rheological, and hardened properties of one-part AAS. Additionally, statistical models were developed to determine the optimal dosage of various ingredients for enhancing flowability. The following chapters present the research methodology, key findings, and their implications for the field:

Chapter 2 provides a comprehensive review of the literature on previous and recent studies concerning producing two-part and one-part AAMs using various precursor types, activators, and dosages. It examines the factors influencing the rheological behavior of AAMs and the strategies employed to improve their flowability. Additionally, the chapter highlights the challenges and limitations of existing studies, offering a critical analysis of the research gaps in the field.

Chapter 3 examines the effect of varying the sequence of ingredient addition (slag, water, and meta-silicate activator) on initiating the reaction for synthesizing AAS paste. This investigation serves as a preliminary step to validate the appropriateness of the sequence used for the main ingredients without incorporating external additives. This phase is crucial for identifying the optimal addition sequence based on the fresh properties of the paste. The mixtures for subsequent phases will be selected based on the determined optimal sequence.

Chapter 4 offers a fundamental understanding of the effects of prolonged mixing time and mixing type (continuous or discrete) on the development of AAS microstructure and its associated fresh and hardened properties. The findings aim to assist in-situ engineers and RMC manufacturers in planning tasks and scheduling AAS concrete delivery to ensure higher productivity and optimal performance for cast elements. Additionally, variance analysis (ANOVA) was employed to assess the significance of each parameter, while the Pearson correlation coefficient was calculated to illustrate the correlation matrix.

Chapter 5 investigates the effect of various retarders, including borax, calcium carbonate, maleic acid, and nano-ZnO, on delaying the reaction of one-part sodium silicate-activated slag. The study explores key factors such as the water-to-solid ratio (w/s), activator dosage, and retarder dosage.

The Taguchi method is employed for single and multi-optimization to determine the optimal proportions based on specific criteria, minimize the number of required mixtures, and assess the efficiency trends of the retarders. Furthermore, an equation is developed to quantify the significance of each factor on rheological behavior. This investigation also seeks to deepen understanding of how these retarders influence the rheological properties of one-part AAS systems. Additionally, it provides a comparative LCA study, offering valuable insights into the environmental impact of these optimized mixtures.

Chapter 6 investigates the influence of both the timing (early or delayed addition) and the method (separate addition, either dissolved in water or added directly without dissolution) of VMA incorporation on the rheological properties of AAS. The study aims to provide valuable insights into how VMA addition can optimize the mineral hydration process in one-part AAS systems, addressing critical workability challenges and advancing the understanding of their rheological performance.

Chapter 7 summarizes the main conclusions and key achievements of the thesis, highlighting the impact of the proposed techniques on the flowability behavior of AAS. It also outlines recommendations for future research based on the findings, providing a foundation for further advancements in the field.

Chapter 2: Literature review

2.1. Introduction

The extreme emissions of greenhouse gases (i.e.CO_2) lead to significant environmental challenges on a global scale. The construction industry plays a substantial role in this carbon footprint, contributing around 8% of total emissions from cement production [1–3]. Worldwide cement production produced CO_2 emissions of 981 kg CO_2 eq per 1 kg of cement in 2018 [70]. To address this environmental concern, AAMs that are prepared from industrial or agricultural byproducts (aluminosilicate materials) and alkaline activators, have great attention for their low energy consumption and environmentally friendly attributes [8,9]. Moreover, their promoting characteristics such as high strength, high chemical resistance, and temperature resistance compared to OPC [71]. However, challenges such as rapid setting time, drying shrinkage, workability, and issues with the use of high aqueous corrosive solutions in the preparation process prevent the widespread adoption of traditional AAMs (two-part AAMs by using solution activator) [23]. To tackle these challenges, starting in 2004 a new production method known as one-part AAMs was developed by the "just add water" approach [72]. The production process of one-part AAMs is simpler due to using a powder activator and adding water on-site, such as the OPC preparation process [57]. Hence, this method enhances commercial value and feasibility for construction applications such as self-sensing materials, which enable the rapid identification of damage and corrosion in situ [73,74]. Despite the advantages of one-part AAMs, technical challenges exist, including rapid setting time, poor workability, and rapid slump loss, especially for slag-based one-part AAMs activated by meta-silicate. While recent studies emphasize the positive aspects of one-part AAMs and address the workability of binary (fly ash/slag) one-part AAMs [59,75], there is a growing interest in exploring alternative alkali activators. This shift is driven by the high environmental footprint and costs associated with conventional chemical-based activators, such as sodium hydroxide and sodium silicate [76–79]. However, there is a lack of scientometric analysis and performance evaluation, particularly regarding the mixing methods used in producing one-part AAMs. Additionally, inconsistencies in conclusions across different studies hinder the widespread promotion and application of one-part AAMs.

This chapter presents a scientometric analysis of AAMs, focusing on one-part and two-part AAMs, with particular emphasis on the rheological behavior of one-part AAMs, as this is the central focus

of the thesis. The analysis was conducted using VOSviewer software to map and visualize research trends and patterns. Following the scientometric analysis, a systematic literature review was performed, specifically targeting the behavior of one-part AAMs. A key gap identified in the literature is the lack of understanding regarding the impact of different mixing times and procedures on the performance of one-part AAMs. Notably, existing studies vary significantly in their approaches, employing different mixing times and speeds, which complicates the comparison of results. Furthermore, there is limited research on the effect of different retarder types and the compatibility of VMAs when incorporated into AAS systems activated by meta-silicate. This chapter highlights these gaps and underscores the need for further investigation to optimize the performance of one-part AAS.

2.2. Background

The production of traditional AAMs (inorganic polymeric materials) commenced in 1940 [64]. However, the practical development and advancement of AAMs were pioneered by Joseph Davidovits in the 1970s. Davidovits proposed that alkaline activating solutions could react with silicon (Si) and aluminum (Al) in aluminosilicate-rich materials (precursor) of natural origin such as metakaolin [80] and mineral wools [81], or industrial by-products, such as fly ash and calcium silicate slag, to produce AAMs [82], or solid waste such as red mud [83] and waste glass [84,85]. This process, known as polymerization, results in the formation of durable and sustainable binders. AAMs are synthesized under highly alkaline conditions through a chemical reaction between solid aluminosilicate oxides and alkali metal silicate solutions. This reaction forms amorphous to semi-crystalline, three-dimensional polymeric structures comprising Si-O-Al-O bonds as shown in **Fig. 2.1** [86].

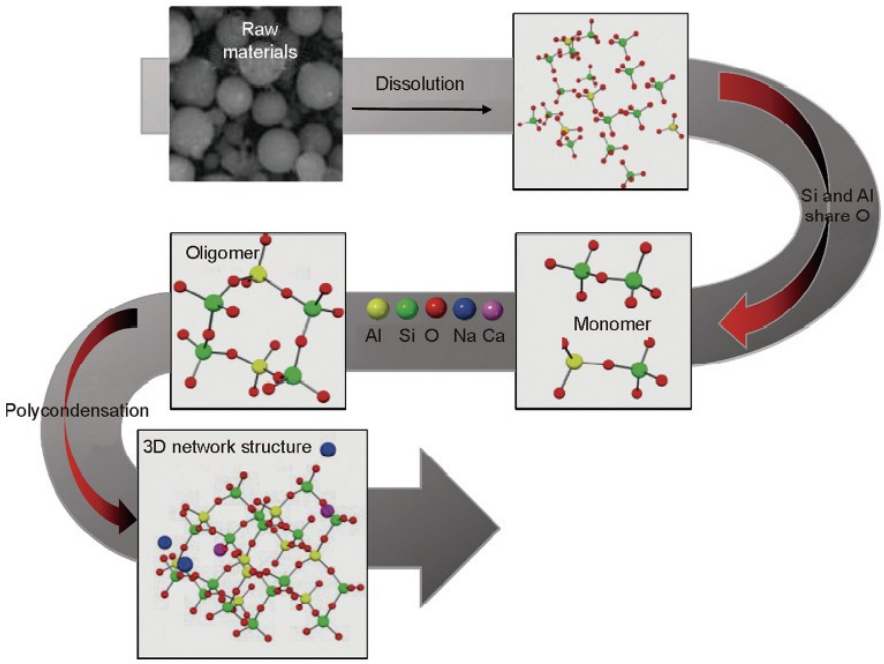

Fig. 2.1: Geopolymerization process [86].

The polymerization mechanism enables the utilization of a wide range of aluminosilicate materials, making it possible to produce AAMs from various sources that contain Si and Al. This versatility is further demonstrated by the schematic reaction pathways depicted in Eqs. 2.1 and 2.2 [82], highlighting the transformative potential of these materials in sustainable construction practices.

$$n(Si_2O_5,Al_2O_2) + 2nSiO_2 + 4nH_2O \xrightarrow{NaOH,KOH} n(OH)_3\text{-}Si\text{-}O\text{-}\overset{(-)}{Al}(OH)_2\text{-}O\text{-}Si\text{-}(OH)_3 \qquad \text{Eq. 2.1}$$

$$n(OH)_3\text{-}Si\text{-}O\text{-}\overset{(-)}{Al}(OH)_2\text{-}O\text{-}Si\text{-}(OH)_3 \xrightarrow{NaOH,KOH} (Na,K)\text{-}(\text{-}Si\text{-}O\text{-}\overset{(-)}{Al}(O)_2\text{-}O\text{-}Si\text{-}O\text{-}) + 4nH_2O \qquad \text{Eq. 2.2}$$

Recent research indicates that AAMs are frequently confused with geopolymers. However, as illustrated in **Fig. 2.2**, geopolymers can be considered a subset of AAMs [87], as the primary gel formation in geopolymers predominantly results from aluminosilicate sources. This broader representation clarifies the relationship between the two categories, emphasizing that geopolymers are a specific type of AAM [88]. The hydration process of both two-part and one-part geopolymers is presented in **Fig. 2.3**.

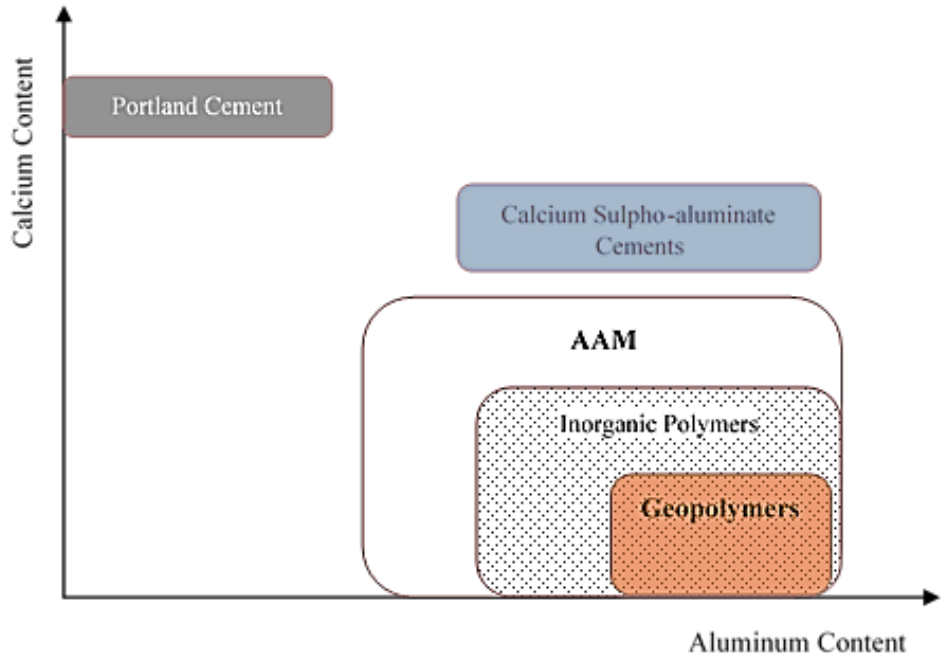

Fig. 2.2: Classification of binders by calcium and aluminum contents [88].

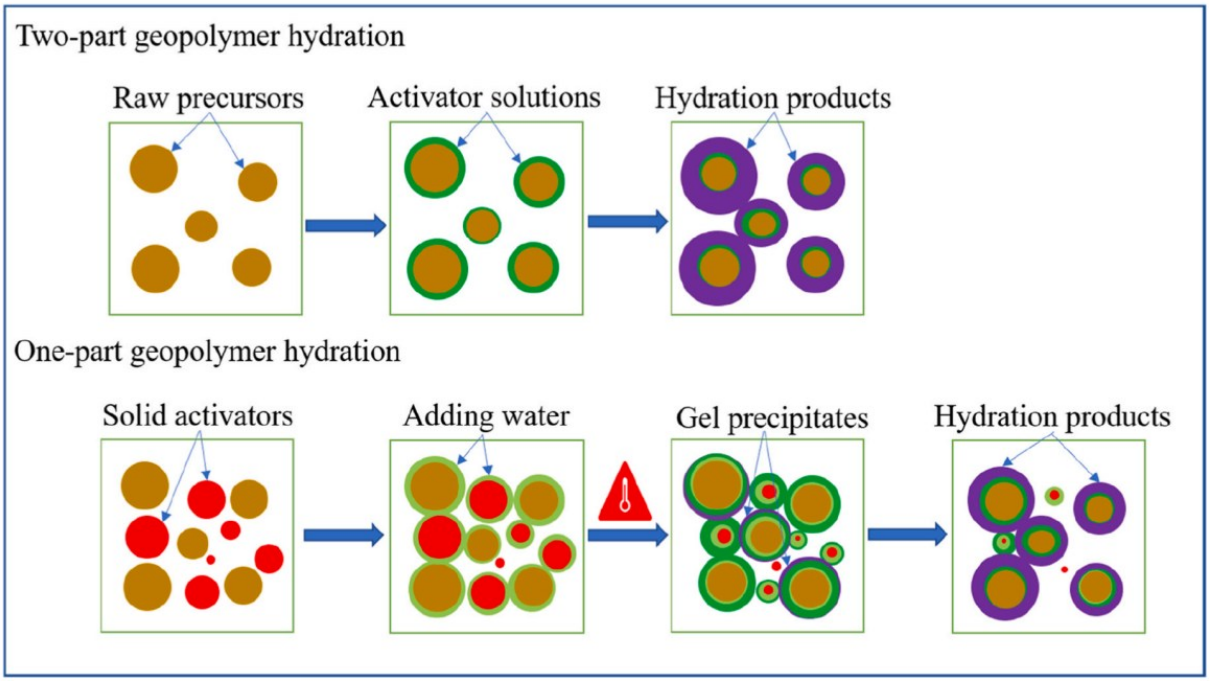

Fig. 2.3: Hydration process of the two-part and one-part geopolymer [89].

AAMs can be classified based on the state of the activator used: one-part AAMs (also known as "just add water" AAMs), which are produced using a solid powder activator, and two-part AAMs, which are produced using an alkaline solution (**Fig. 2.4**). The adoption of one-part AAMs

technology, characterized by the "just add water" approach, began in 2004. This method was developed to mitigate the potential hazards associated with handling highly alkaline aqueous solutions, which are commonly used in two-part AAMs. The production process of one-part AAMs is simpler compared to two-part AAMs. In two-part AAMs, activation requires the preparation of concentrated aqueous alkali solutions, which are highly viscous and corrosive due to their high alkalinity [90]. These properties make handling, transportation, and in-situ casting more challenging and pose safety risks [91]. In contrast, one-part AAMs eliminate these issues by using solid activators, making them more practical for large-scale applications.

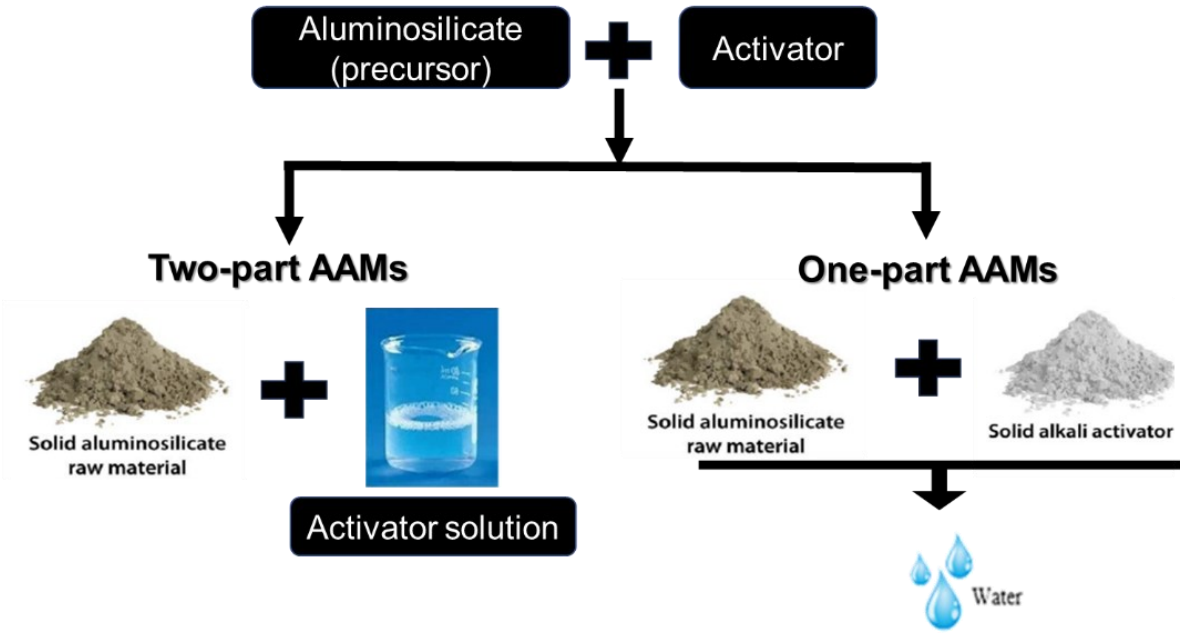

Fig. 2.4: Types of AAMs.

The framework of this chapter consists of 2 stages:

(1) Collect data by using a Scopus database of four keywords: AAMs, two-part AAMs, one-part AAMs, and the workability of one-part AAMs as shown in **Fig. 2.5**. Data were utilized to determine the number of publications associated with each keyword and to generate clusters for each term. The analysis was conducted in January 2025, with a detailed scientometric evaluation performed to assess the volume of documents and research trends related to each keyword.

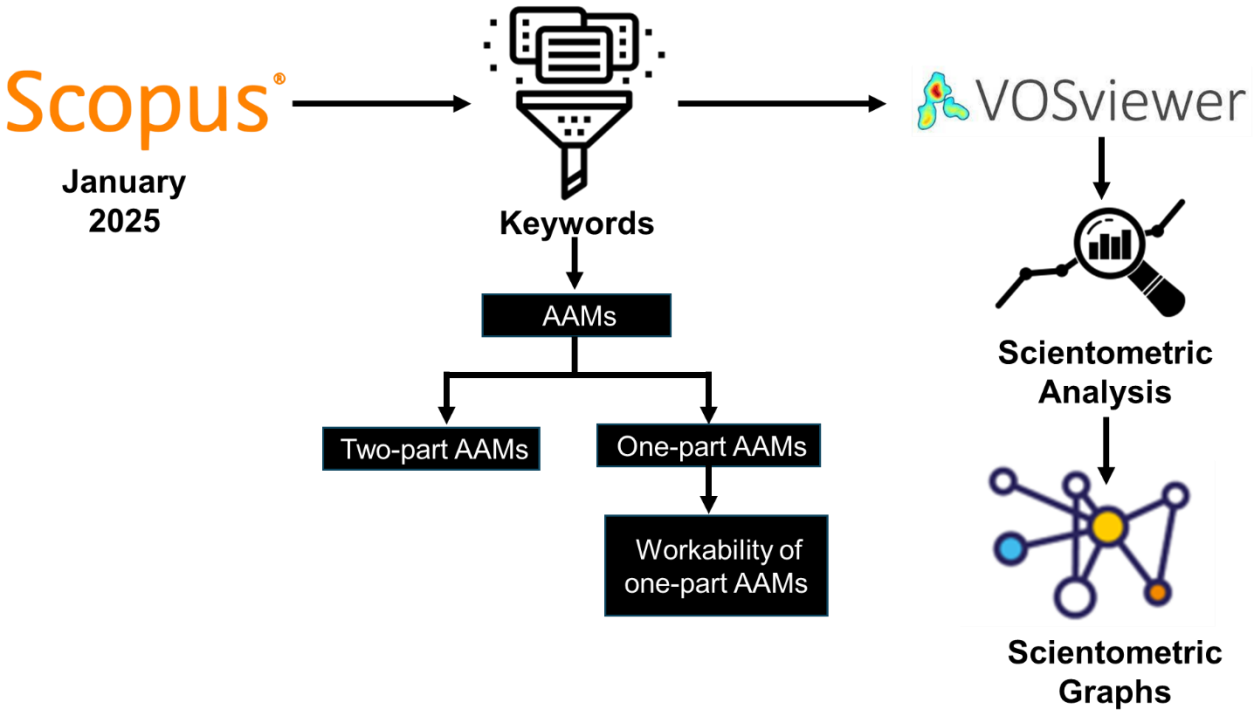

Fig. 2.5: Flowchart of the steps for conducting a scientometric analysis.

(2) Systematic review by analyzing data content and specifying research focus, gaps, trends, and future research directions related to one-part AAMs' rheology, fresh and hardened properties.

2.3. Scientometric review keyword co-occurrence network

Authors' keywords reflect the primary focus of the published studies and illustrate the scope of research within a specific domain [92]. A keyword co-occurrence network is a distance-based map where the distance between keywords indicates the strength of their relationship.

The distance is determined by calculating a strength link value, which represents the number of publications in which two keywords appear together. A larger distance between keywords signifies a weaker relationship, while the size of each circle corresponds to the frequency of the keyword's use in publications.

To enhance the clarity of clustering, a threshold (minimum number of keyword occurrences) was set for each keyword after several trials. Normalization was applied using the Lin Log/modularity method [92]. A scientometric analysis was conducted for each keyword as follows:

2.3.1. Keyword AAMs

The inquiry revealed significant advancements over the past 13 years, with approximately 4,402 studies published. The Scopus search was limited to specific criteria: subject areas (Materials

Science, Engineering, and Chemical Engineering), document types (articles and reviews), source type (journals), and language (English). To enhance the clarity of clustering, a threshold of 10 minimum occurrences was set for each keyword after multiple trials.

The visualization of the keyword network map is presented in **Fig. 2.6**. A total of 1,199 keywords were selected for the analysis. The keyword co-occurrence network was divided into 5 clusters, each represented by a distinct color and focusing on specific research themes. Cluster 1 (Red), with 326 keywords, highlights research on the durability and mechanical properties of AAMs, along with studies on life cycle assessment, sustainability, and environmental impacts, as indicated by the large circle sizes. Cluster 2 (Green), with 268 keywords, focuses on the chemical activation of geopolymers and the characterization of hydration products using tests such as XRD, TGA, SEM, and FTIR, with large circles reflecting a high volume of publications. Cluster 3 (Blue), with 265 keywords, focuses on workability, though smaller circle sizes suggest fewer publications in this area. Cluster 4 (Yellow), with 218 keywords, is dedicated to the microstructure analysis of slag as a precursor in AAMs, with large circles indicating extensive research. Finally, Cluster 5 (Purple), with 122 keywords, represents emerging areas such as machine learning models, rheology, forecasting, and 3D printing of AAMs, with tiny circles highlighting limited studies and pointing to potential future research directions.

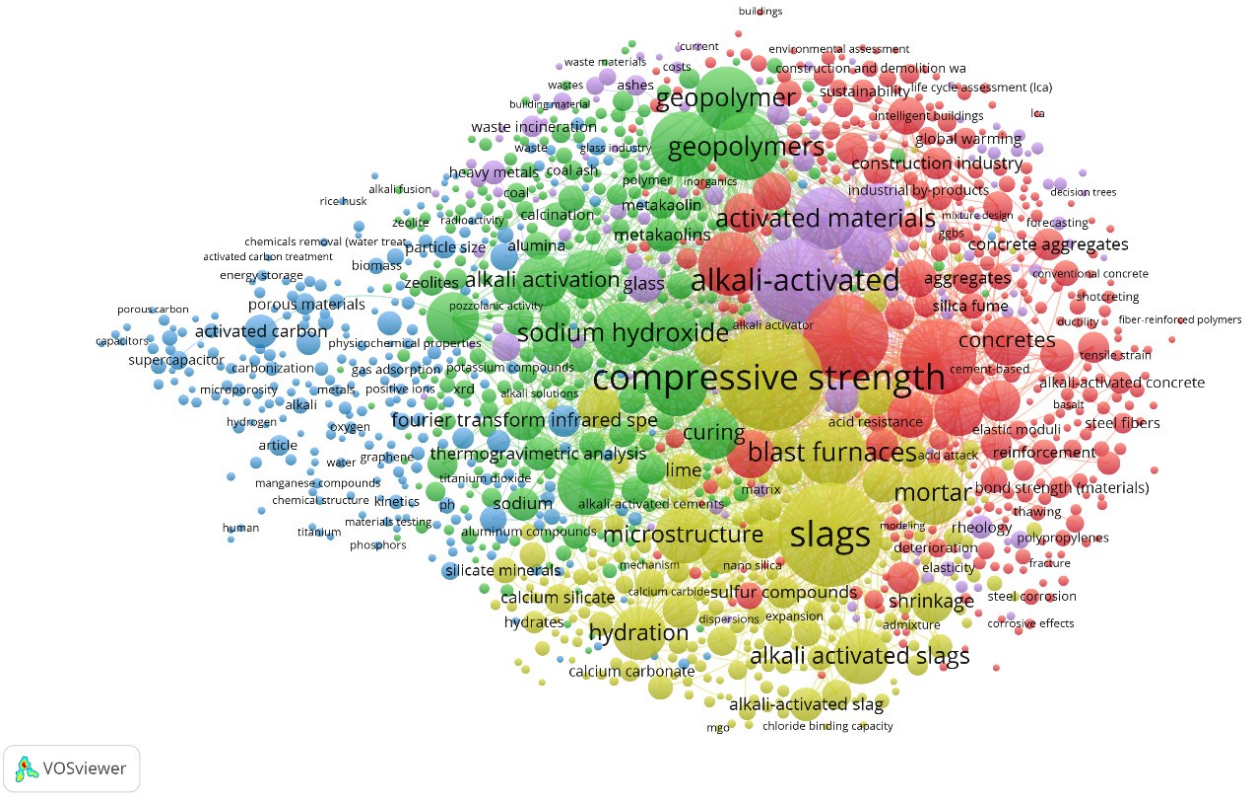

Fig. 2.6: Visualization of the AAMs network map.

Additionally, a time zone map was generated to illustrate the evolution of research trends related to AAMs over time, as shown in **Fig. 2.7**. In this map, each node represents the average year in which a keyword appeared in published studies. For example, around 2021, research focused on slag-based AAMs activated by sodium hydroxide. More recently, the emphasis has shifted toward producing high-performance alkali-activated concrete, special types of concrete such as self-consolidated concrete, and studying the durability and LCA of alkali-activated concrete.

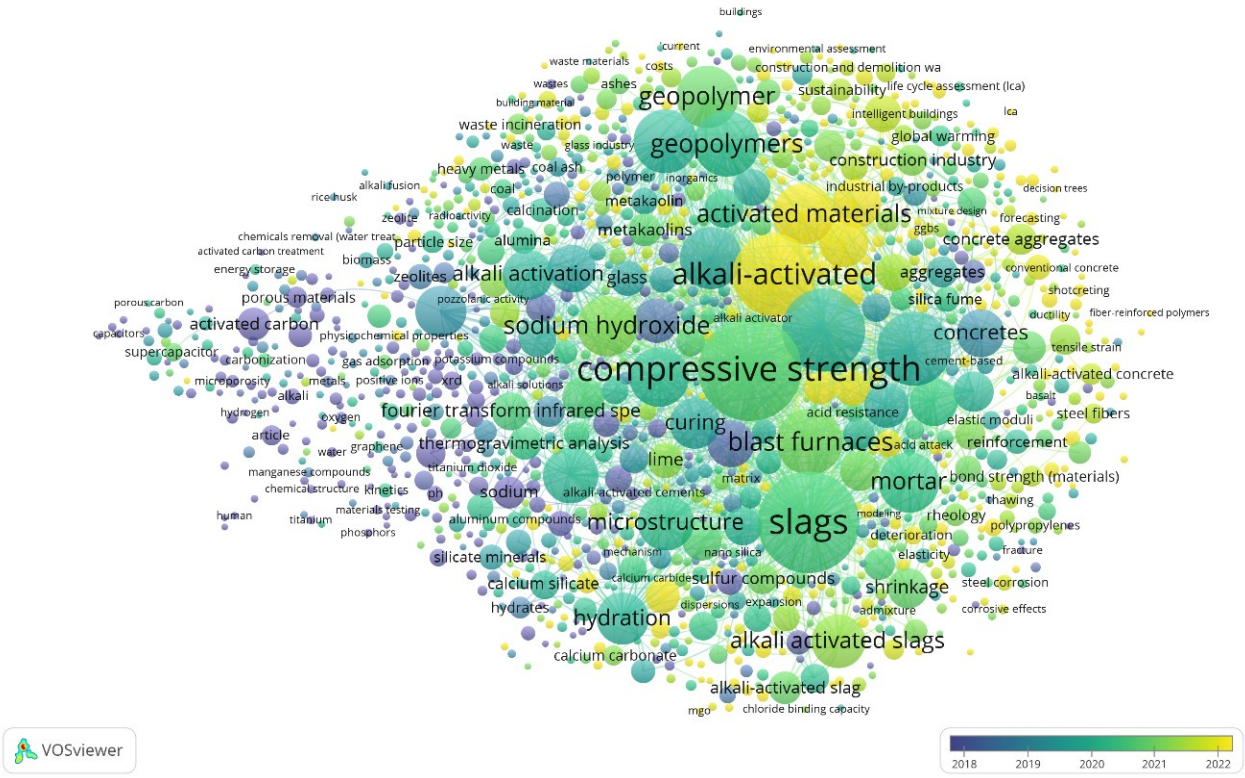

Fig. 2.7: Time zone map of the keywords.

2.3.2. Keyword two-part AAMs

The inquiry demonstrated that research in this field began in 1995 and has seen significant advancements over the past 6 years, with approximately 129 studies published. The Scopus search was conducted without filters, focusing on searching by the article title, abstract, and keywords. To improve the clarity of clustering, a threshold of two (minimum number of keyword occurrences) was set after multiple trials. This threshold ensures that only meaningful keywords are included in the analysis.

The visualization of the resulting keyword network map is presented in **Fig. 2.8**. A total of 77 keywords were selected for the analysis, divided into 7 clusters, each represented by a distinct color and focusing on a specific research focus. Cluster 1 (Red), with 16 keywords, highlights a large volume of research on the hydration of precursors (slag, fly ash, metakaolin) and sustainability, indicated by large circle sizes. Cluster 2 (Green), with 13 keywords, focuses on the fresh and mechanical properties of one-part AAMs, middle circle sizes reflecting a limited number of publications. Cluster 3 (Blue), with 12 keywords, highlights no-cement two-part AAMs using

slag and fly ash. Cluster 4 (Yellow), with 10 keywords, explores thermal conductivity and chloride diffusion in slag-based AAMs. Cluster 5 (Purple), with 10 keywords, addresses drying shrinkage and strength of slag alkali-activated concrete. Cluster 6 (Baby Blue), with 9 keywords, covers fiber-reinforced binders, water glass activation, and setting time, with smaller circles indicating a need for further research. Finally, Cluster 7 (Orange), with 7 keywords, focuses on recycled and waste thermal treatment for producing activators and precursors, with tiny circles highlighting significant research gaps.

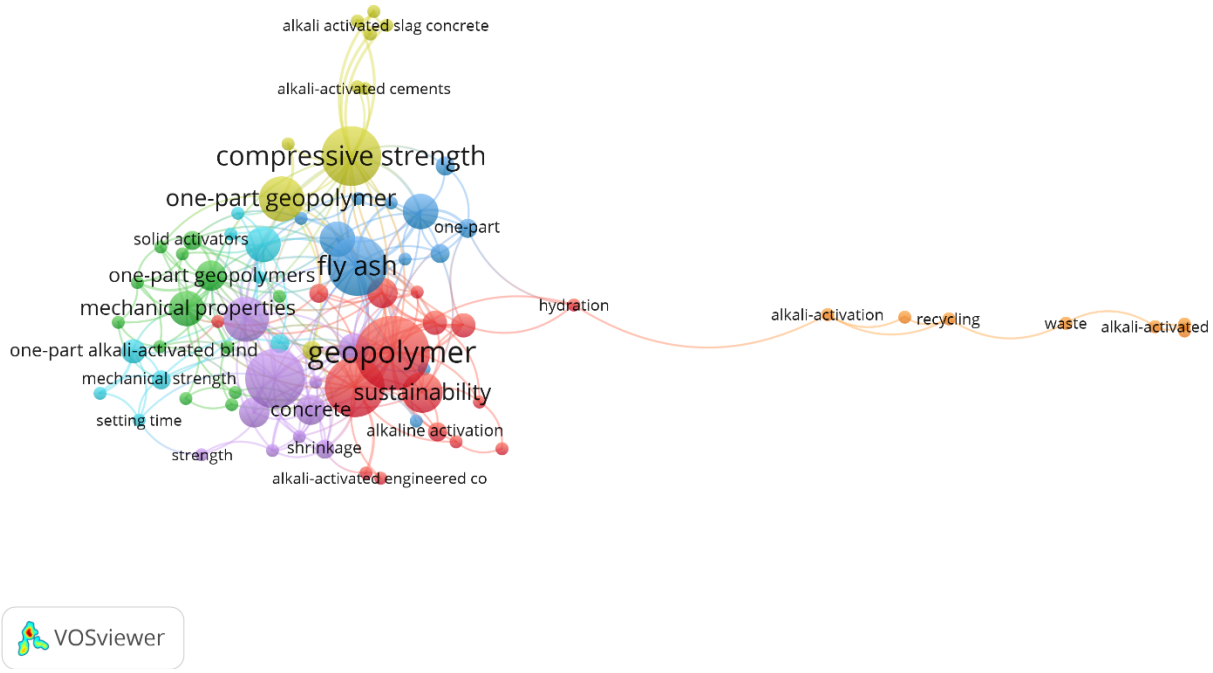

Fig. 2.8: Visualization of the two-part AAMs network map.

Additionally, a time zone map was generated to illustrate the evolution of research trends related to two-part AAMs over time, as shown in **Fig. 2.9**. In this map, each node represents the average year in which a keyword appeared in published studies. For instance, around 2022, research primarily focused on setting time, shrinkage, and strength of two-part AAMs. More recently, the emphasis has shifted toward producing one-part AAMs, understanding the hydration process, and exploring the use of different aluminum precursors and activators. This shift reflects the growing interest in simplifying AAM production by dry mixing and enhancing material performance.

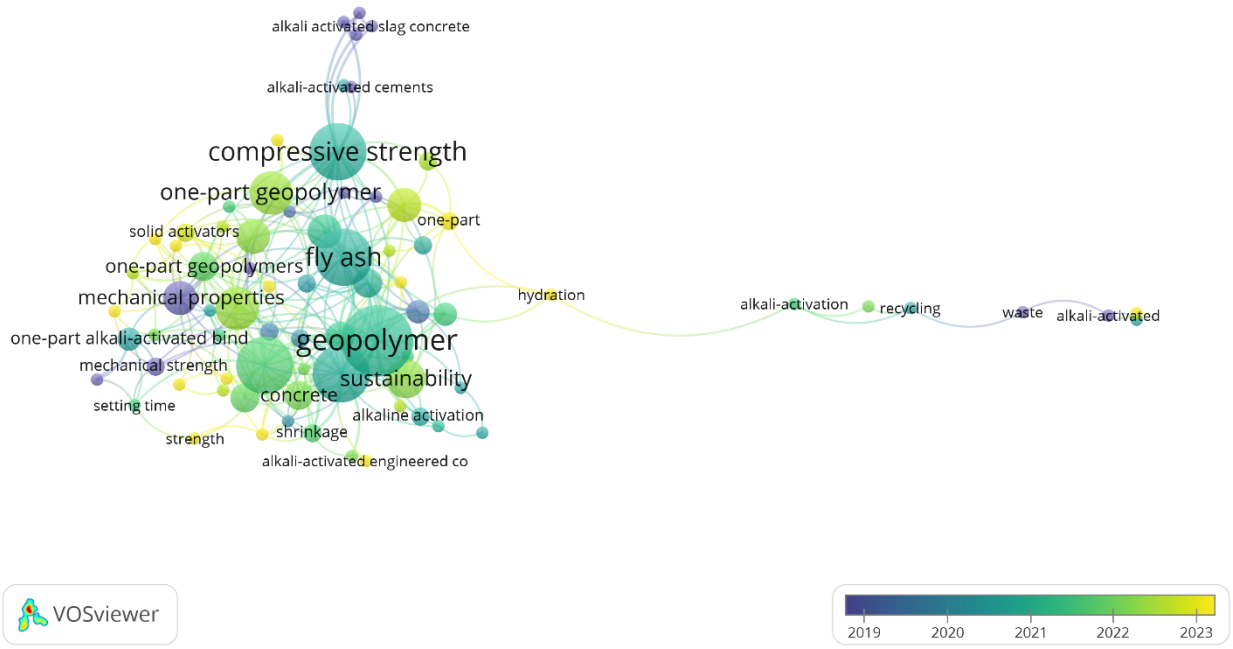

Fig. 2.9: Time zone map of the two-part AAMs keyword.

2.3.3. Keyword one-part AAMs

The inquiry emphasized that research in this field began in 2016 and has seen significant progress over the past 5 years, with approximately 291 studies published. The Scopus search was conducted without any filters, encompassing all available data. To enhance the clarity of clustering, a threshold of two (minimum number of keyword occurrences) was established after several trials. The resulting keyword network map, which visualizes the relationships and trends, is presented in **Fig. 2.10**.

A total of 179 keywords were selected for the analysis, divided into 9 clusters, each represented by a distinct color and focusing on a specific research focus. The small circle sizes in most clusters indicate a limited number of publications, highlighting the need for further research in these areas. Cluster 1 (Red), with 32 keywords, emphasizes studies on the durability, workability, and mechanical properties of one-part AAMs, particularly the use of different superplasticizers and rheology. Cluster 2 (Green), with 26 keywords, focuses on inorganic polymers, various precursors, and no-cement one-part AAMs. Cluster 3 (Blue), with 25 keywords, explores different activators and repair materials. Cluster 4 (Yellow), with 24 keywords, is dedicated to fluidity and setting time, particularly with the incorporation of admixtures such as retarders. Cluster 5 (Purple), with 23 keywords, centers on sustainability, circular economy, and LCA. Cluster 6 (Baby Blue), with

14 keywords, focuses on the strength and drying shrinkage of alkali-activated concrete. Cluster 7 (Orange), with 14 keywords, highlights special types of alkali-activated concrete, such as 3D printing. Cluster 8 (Brown), with 14 keywords, examines recycled waste, hydration, and the global warming potential of one-part AAMs. Finally, Cluster 9 (Pink), with 7 keywords, focuses on hydration analysis tests of one-part AAMs, including FTIR, XRD, SEM-EDS, and isothermal calorimetry.

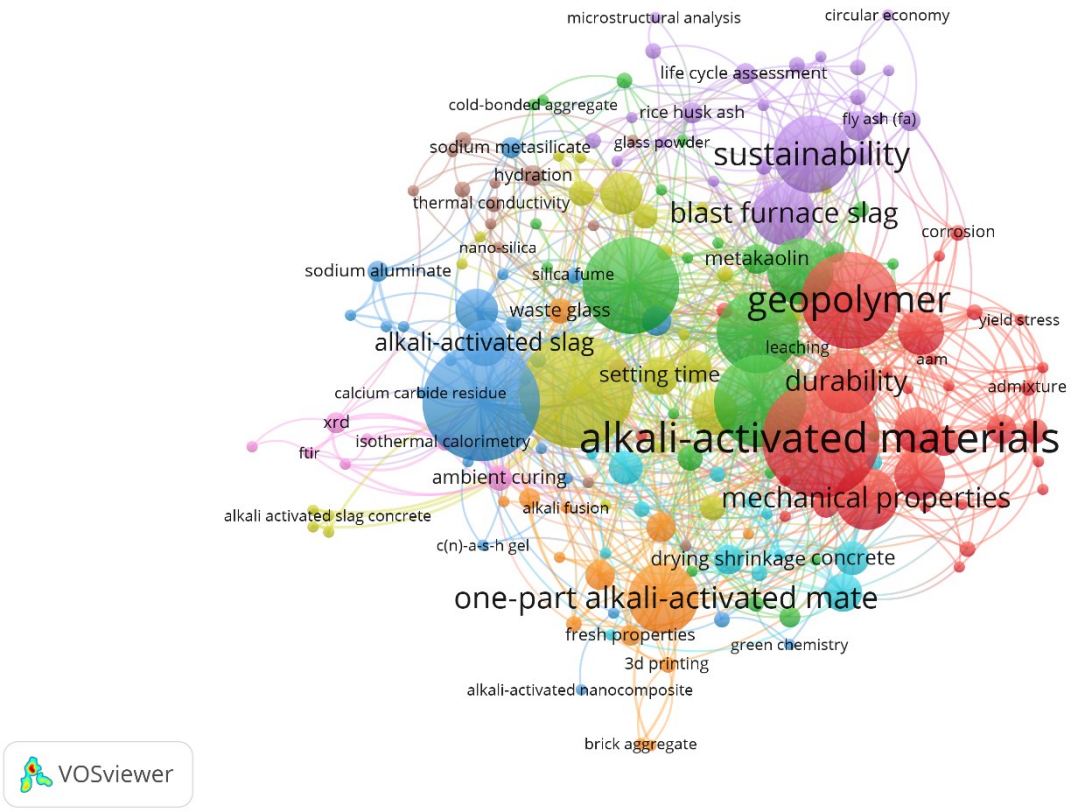

Fig. 2.10: Visualization of the one-part AAMs network map.

Furthermore, a time zone map was created to track the evolution of research trends in one-part AAMs over time, as depicted in **Fig. 2.11**. In this map, each node represents the average year in which a keyword appeared in published studies. For example, around 2024, research primarily focused on workability and drying shrinkage of one-part AAMs. More recently, the focus has shifted toward rheology, circular economy, LCA, and the incorporation of borax and nano-silica in one-part AAMs. This shift highlights the growing interest in enhancing the performance of AAMs.

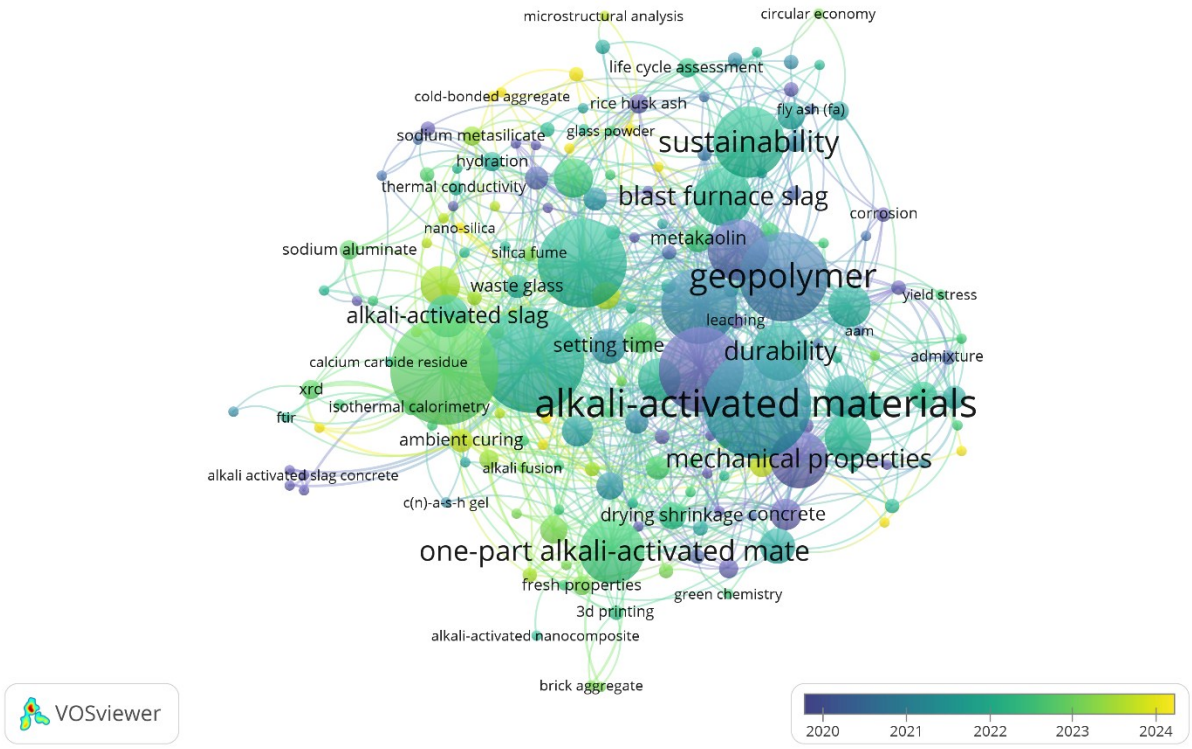

Fig. 2.11: Time zone map of the one-part AAMs keyword.

2.3.4. Keyword workability of one-part AAMs

The inquiry depicted that research on the workability issue of one-part AAMs began in 2017 and has made significant progress over the past 4 years, with approximately 39 studies published. The Scopus search was conducted without filters, encompassing all available data. A threshold of two (minimum number of author keyword occurrences) was established after several trials, resulting in 30 keywords. The resulting keyword network map, which visualizes relationships and trends, is presented in **Fig. 2.12**.

The analysis of the keywords provides an overview of the research focus on addressing the workability of one-part AAMs, while also highlighting several research limitations: Workability Studies: Most research has focused on improving workability by applying different admixtures and measuring initial workability. However, the small size of the flowability node indicates a limited number of studies on slump retention, and there is no mention of the effect of mixing procedures on workability. Rheology and Retarders: The small label sizes for keywords such as rheology, retarder, and borax suggest a lack of studies exploring the potential of borax as an additive or investigating the rheology of one-part AAMs. The small label sizes across all 4 clusters

underscore the potential for further research in these areas, which will be a key focus of this thesis. The study aims to implement different techniques to address these gaps and advance the understanding of one-part AAMs.

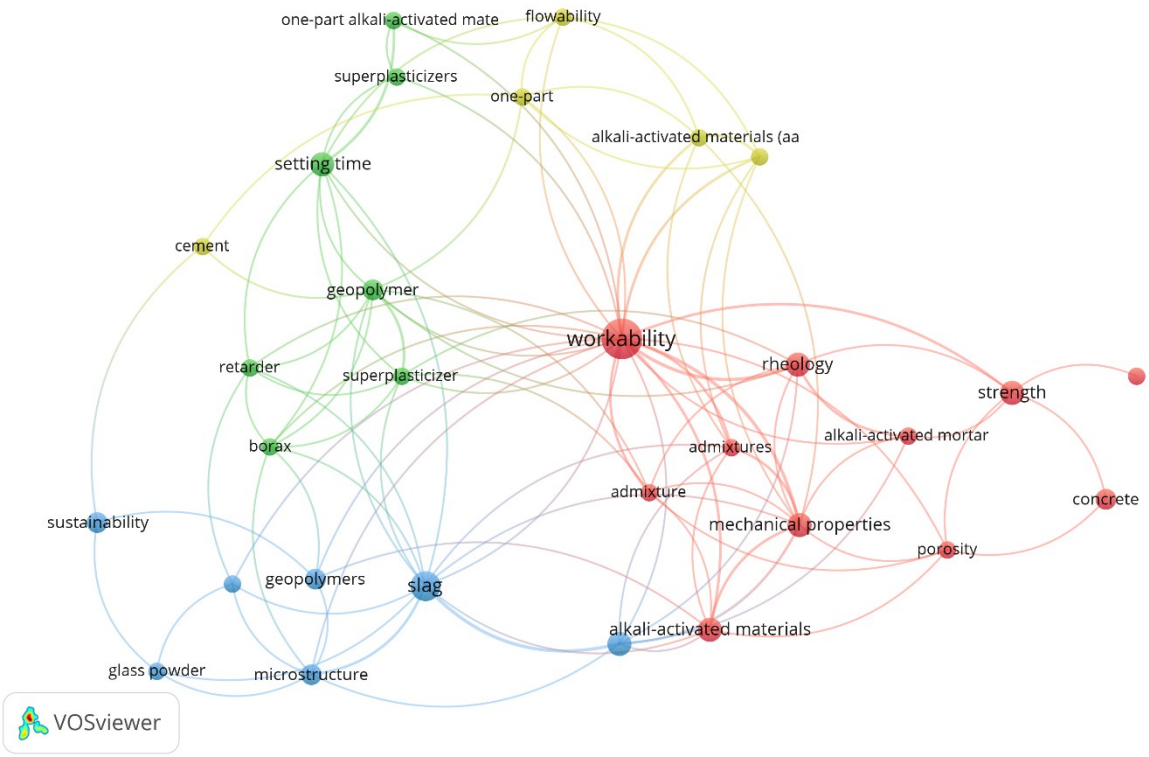

Fig. 2.12: Visualization of the workability of one-part AAMs network map.

A time zone map was generated to track the evolution of research trends in the workability of one-part AAMs over time, as illustrated in **Fig. 2.13**. The map confirms the growing need for research on the microstructure and rheology of one-part AAMs, as the most recent publications have predominantly focused on these topics. This trend highlights the importance of advancing understanding in these areas to address current gaps and improve material performance.

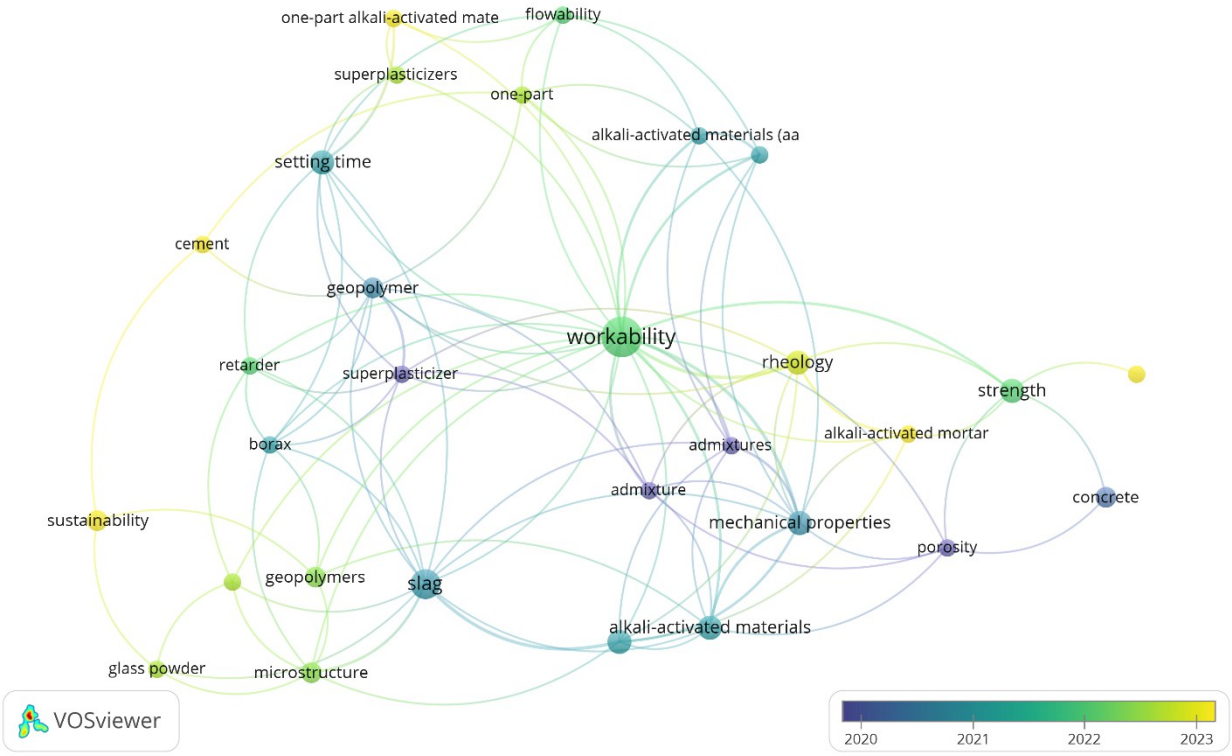

Fig. 2.13: Time zone map of the workability of one-part AAMs keyword.

2.4. Systematic review

The chemical composition of both the precursor and the alkali activator plays a crucial role in determining the material properties of AAMs [93]. Besides, an excessively high or low concentration of the alkali activator negatively impacts the workability and mechanical properties of AAMs [94]. The influence of various factors on the behavior of AAMs, including the type and dosage of activators, mixing water temperature, added admixtures, and mixing procedures, will be thoroughly discussed in the following sections.

2.4.1. Effects of activator types and dosages on one-part AAMs performance

The type and dosage of the used activators have vital effects on AAMs' fresh and hardened properties [95]. Hence, many studies investigated the impact of activators. For instance, Almakhadmeh et al. [96] reported a 68% decrease in AAS paste slump life when increasing the Na_2SiO_3 activator dosage from 6% to 10% of the binder (slag) weight. It was reported that the spread diameter decreased from 190 mm to 100 mm in 70 min and 25 min at activator dosages of

6% and 10% at 0 °C water temperature, respectively. This could be attributed to the high alkalinity of Na_2SiO_3 (pH=13.4 at saturation), which resulted in the rapid dissolution of the precursor and fast setting [97]. Shi and Day demonstrated two primary causes for the rapid setting of AAS for different activators. The first was due to slag dissolution, and the second was the formation of a primary C-S-H gel due to the presence of $[SiO_4]^{4-}$ ions in the solution [98].

Cong Ma et al. [99] found that the replacement of Na_2SiO_3 by Na_2CO_3 slightly affected the fluidity of all mixtures but extended the FT. This was attributed to the low amounts of Ca^{+} and SiO_4^{4-} leading to a lower pH solution and consequently delaying the geopolymerization process. Hence, the early strength of one-part AAMs mixtures will decrease, and the late strength will not change. On the other hand, one-part AAMs activated by Na_2SiO_3-anhydrous and Na_2CO_3 showed low potential environmental impact while maintaining the performance.

In another study held by Luukkonen et al. [91], one-part blast furnace slag mortars activated by three different solid silica and alkali sources: anhydrous sodium meta-silicate, MS with NaOH, RHA with NaOH, and NaOH were studied. A slight difference in solubility was observed between MS and RHA. For the setting time test, the trend observed for setting times was MS + NaOH > RHA + NaOH > sodium silicate. The compressive strength of Na_2SiO_3-activated mortar was high (around 98 MPa) compared to MS or RHA with NaOH, resulting in significantly lower compressive strength regardless of the mixture composition.

Several studies have identified limitations associated with AAMs, which include the following:

1- Instability in the supply of raw materials, such as industrial byproducts and calcined clay, 2- Co_2 emissions generated during the production of alkaline activators, 3- Challenges in handling due to the corrosive and hazardous nature of alkali activators, 4- Issues related to the standardization and large-scale industrialization of the material, and 5- Negative user acceptance of AAMs [100]. Hence, many studies have focused on developing alternative activators derived from waste materials to address these limitations. For instance, Beomjoo et al. investigated the use of calcined oyster shells (i.e. waste product from the fisheries industry composed of over 90% calcium carbonate) as an activator for AAS paste [101]. The activator was used at percentages of 5%, 10%, 15%, and 20% of the slag weight. Results revealed that at 3 days, specimens containing 5%, 10%, 15%, and 20% calcined oyster shell powder exhibited similar compressive strengths (12.9–13.9 MPa). By 28 days, the mix with 5% calcined oyster shell powder achieved the highest compressive strength (35 MPa), while higher dosages (10%, 15%, and 20%) resulted in

progressively lower strengths of 33.4 MPa, 27.2 MPa, and 21.7 MPa, respectively. These results indicate that increasing the calcined oyster shell content beyond 5% leads to a decline in compressive strength. This reduction is attributed to unreacted calcined oyster shell powder and excess CaO, which hinder portlandite consumption and limit C-S-H formation, essential for later-age strength. Additionally, a high concentration of hydroxide ions can induce gel precipitation, hindering alkali activation and further reducing strength [102].

During hydration, the dissolution of CaO significantly increased the heat of hydration at early ages, particularly in mixes with 15% and 20% calcined oyster shell powder. However, a low dosage (5%) contributed to pore-size refinement, leading to improved compressive strength. These findings highlight the potential of using calcined oyster shell powder as an activator for AAS, particularly at low dosages (5%).

In another study, Adriano et al. [103] investigated the effect of calcined materials, specifically ceramic waste and commercial kaolin, on fly ash-based AAMs paste activated with a combination of NaOH and Na_2SiO_3. The paste produced using a mixture of fly ash and calcined ceramic residue (FACCW) had a w/s ratio of 0.6, while the paste made with fly ash and calcined commercial kaolin (FACCK) had a higher w/s ratio of 0.9. Results revealed that the compressive strength of AAMs increased with the addition of calcined ceramic waste. Early strength development was also notable, with 20 wt% CCW yielding 15.3 MPa at 7 days—54% higher than those with calcined commercial kaolin (CCK). Increasing CCW to 30 wt% further enhanced strength, reaching 28 MPa at 7 days, a 59% improvement over CCK-based samples. The superior performance of CCW was attributed to its contribution of Na_2O and SiO_2, which enhanced N-A-S-H gel formation and densified the microstructure. In contrast, CCK required more water, reducing gel formation efficiency and leaving unreacted particles embedded in the matrix, potentially causing defects and lower strength. SEM analysis confirmed the presence of alkali carbonation reaction products, indicating stable structures. Overall, the study demonstrated the potential of ceramic industry residues and fly ash as sustainable precursors for AAM production, as they enhance alkalinity and improve mechanical and physical properties.

Lilan et al. [104], Investigated the behavior of one-part Na_2CO_3-activated slag pastes modified with $Ca(OH)_2$ and $Mg(OH)_2$ as co-activators. The Na_2CO_3 dosage was set at 10% of the slag weight, while $Ca(OH)_2$ and $Mg(OH)_2$ were added at a combined dosage of 5%, with varying mass ratios (1:4, 2:3, 3:2, and 4:1) of slag. Results showed that both the IT and FT shortened linearly as

the $Ca(OH)_2/Mg(OH)_2$ ratio increased, indicating that $Ca(OH)_2$ was more effective in accelerating reaction kinetics than $Mg(OH)_2$. This was attributed to the higher solubility of $Ca(OH)_2$, which released more OH^- ions, thereby enhancing slag dissolution [105]. Specifically, as the $Ca(OH)_2$ content increased from a ratio of 1 to 4, the IT was shortened from 70 to 45 minutes, while the FT was shortened from 125 to 75 minutes. The pastes hardened within two hours, highlighting the role of Ca-rich activators in promoting the formation of C-A-S-H. In contrast, the Na_2CO_3-only activated binder (C0) exhibited the setting after more than 24 hours and delayed strength development, with negligible compressive strength at 1 day and only 4.5 MPa at 3 days. However, binders modified with $Ca(OH)_2/Mg(OH)_2$ activators achieved 1-day compressive strengths ranging from 6.5 MPa to 12.8 MPa, confirming their effectiveness in accelerating reaction kinetics. By 7 days, compressive strengths ranged from 30.6 MPa to 37.5 MPa, approaching the 28-day strengths of 39.5 MPa to 45.5 MPa. This rapid early-age strength gain confirmed the effectiveness of $Ca(OH)_2$ in enhancing mechanical performance. Hence, increasing the $Ca(OH)_2$ content improved compressive strength but significantly reduced setting time, making it a more effective accelerator than $Mg(OH)_2$ in Na_2CO_3-activated slag.

Chen et al. [106], investigated the activation of AAS using solid waste salt sludge (CSS) from sodium hydroxide production and soda residue (SR) from sodium carbonate production. The activator dosage varied, with SR: slag initially set at 30:70, then SR was progressively replaced by 5–30% CSS. The w/b ratio was 0.5. Results revealed that the optimal mix ratio (CSS: SR: slag = 15:15:70) resulted in an IT of 3.0 hours and FT of 7.75 hours. Mortar fluidity was 141 mm with manufactured sand and 158 mm with river sand. Compressive strength initially increased with CSS addition, peaking at 15% CSS (S15R15) with 14.3/33.3/53.7/59.1 MPa at 3, 7, 28, and 56 days, before declining at higher CSS levels. SR-only activation (S0R30) had the lowest strength (1.3/2.6/7.5/16.8 MPa), confirming its weak activation effect. The strongest activation was at CSS: SR=1, achieving 11.0/12.8/7.2/3.5 times higher strengths than SR-only activation and 1.7/2.5/2.6/2.5 times higher than CSS-only activation, demonstrating the superior synergistic effect of CSS and SR on AAS.

Thus, among all solid alkali activators studied, sodium silicate has the highest potential to enhance properties due to its high reactivity. However, its major drawback is the short setting time.

2.4.2. Effects of mixing water temperature on one-part AAMs performance

The effect of mixing water temperature on the behavior of AAS has been explored in only one prior study, as no research has yet addressed the influence of various ingredient temperatures on the properties and performance of AAMs. Almakhadmeh et al. [96] reported that the higher the mixing water temperature, the faster the slump loss rate of AAS paste mixtures such as traditional concrete [107]. High water temperature leads to fast precursor dissolution due to the activator's rapid increase in pH. The elapsed time between the IT and FT remained almost constant for the same activator dosage, irrespective of the mixing water temperature. This finding indicates that the hydration progress of the mixture after the initial setting is more dependent on the reaction of the mixture components rather than the mixing water temperature. Furthermore, the temperature in the alkaline activation was reflected in the activation energy obtained [108]. Mixtures prepared by 0°C and 30 °C water, the initial temperatures were 12.4 °C and 20.2 °C for 6% activator and 33.2 °C and 43.3 °C for 10% activator, respectively. Moreover, the lower the mixing water temperature, the longer the dormant period indicates cold water's retarder effect. The mixing water temperature had a higher effect on early-age strength as the increase in 1-day strength for mixtures prepared by 0 °C water was higher than that prepared by 30 °C water at activator 10%. Similar results were observed for all activator dosages (6% and 8%), where increasing the dosage from 8% to 10% resulted in a strength change of 112% in mixtures prepared with 30°C water, compared to 200% (double increase) in those mixed with 0°C water. Furthermore, mixtures prepared with colder mixing water exhibited lower shrinkage than those prepared with warmer water. Thus, reducing mixing water temperature is an effective mechanism that is used in retarding the alkali reactions, enhancing the workability, improving early compressive strength, and reducing the shrinkage of AAS paste while maintaining almost the same late-age compressive strength.

To the best of the authors' knowledge, there is a lack of studies on the effects of water temperature on admixtures' efficiency in AAMs, as the rapid increase in pH results in the quick dissolution of precursors, which may affect the steric and electric repulsion of admixture and adsorption of admixtures on the precursor surface. Moreover, retempering by withholding mixing water, changing the adding sequence of ingredients, and using a long mixing time will affect the fresh and hardened properties of one-part AAMs.

2.4.3. Effects of chemical admixtures on one-part AAMs performance

Different types and dosages of SPs and retarder admixtures were used to enhance the workability of AAMs based on precursor and activator types, as shown in **Table 2.1.** Alrefaei et al. reported that using a PC as SP was the most efficient among other types. It resulted in the highest increase in setting time, relative slump, and compressive strength values for fly ash/slag-based pastes activated by $Ca(OH)_2$ and Na_2SO_4 [75]. This can be attributed to the long lateral chain of PC causing steric repulsion [109–111]. The retardation of setting time might be ascribed to the adsorption characteristics of SPs on the aluminosilicate raw material particles (fly ash or slag). This adsorption in high-alkaline environments causes a delay in the alkali activation of the precursor materials [112]. In a different study by Alrefaei et al. [39], It was observed that adding all SPs improved the relative slump of one-part AAMs. The increase in the relative slump was 225%, 249%, and 262% for N, M, and PC admixtures compared to the control mixture without admixtures, respectively. Various SPs' effects on the relative slump could be attributed to the different stability behaviors of various SPs in the high alkali media [113]. For the compressive strength, the reductions in the strengths were 12%, 5%, and 7% for N, M, and PC admixtures compared to the control mixture, respectively. In mixtures containing PC SPs, the compressive strength reductions were 7%, 3%, 3.5%, and 4.5% for w/b ratios of 0.4, 0.38, 0.36, and 0.34, respectively, compared to the control mixture. Conversely, using M admixture resulted in compressive strength drops of 5%, 8.5%, and 12% for w/b ratios of 0.4, 0.38, and 0.36, respectively.

Luukkonen et al. [56] reported that LS, M, and N-based SPs are more effective than polycarboxylate SPs for AAS mortar. However, the LS-based superplasticizer was the most efficient as it improved the workability by increasing the spread by 41%, reducing the yield stress by 51%, and decreasing the viscosity by 27%. It also increased the setting time by 70% and the compressive strength by 19% compared to the control mixture when used at a dosage of 0.5% of binder weight. Oderji et al. reported that borax SPs increased the flowability and prolonged flow loss in all binders (fly ash/ slag), regardless of slag content. It was observed that the mixtures incorporating borax exhibited higher initial flow diameters and better retention of flowability over time. Including borax decreased the compressive strength of the alkali-activated binders at early ages but improved strength at later ages. Furthermore, adding borax reduced crack width or greater resistance to cracking compared to the control mixtures that did not contain borax. This agrees

with Oderji et al. [38], who reported that borax superplasticizer is the most effective superplasticizer for fly ash/slag alkali-activated pastes due to its retarder effect compared to Sodium Triphosphate, Polycarboxylate, Sodium Gluconate, Sodium Lignosulphonate, and Calcium Lignosulphonate.

Another critical factor is the time of PC addition. According to the previous study by Alrefaei et al. [59], early adding reduced the compressive strength of the one-part AAMs. This agreed with several previous studies [59,114]. The delayed addition of a PC is more likely to achieve a better compressive strength than the early addition. Besides, delayed addition caused a higher drop in rheological properties (static yield stress, dynamic yield stress, and plastic viscosity). The static yield stress for delayed addition of PC was significantly reduced when increasing PC content from 0.5 % to 3% of binder weight. Thus, the effectiveness of SPs depends on the alkali activator's type and concentration and the precursor's type. There is no best performance and optimum admixture dosage for all activators and precursors [111,115]. Moreover, most studies avoid using slag-based AAMs activated by meta-silicate despite superior properties due to the rapid workability loss challenge.

2.4.4. Effects of mixing procedure on one-part AAMs performance

Regarding the mixing time, most studies utilize mixing times ranging from 3 to 6 minutes at both slow and high speeds. Longer mixing times (including resting time) and delayed addition of SPs have demonstrated their efficiency in enhancing the behavior of one-part AAMs, as will be discussed in **Table 2.1**. To the best of the authors' knowledge, no study has investigated the effect of varying mixing times on the properties and performance of one-part AAMs, particularly in the RMC applications. This represents a significant gap in the literature, as understanding the influence of mixing duration could provide critical insights into optimizing the processing, workability, and performance of these materials for RMC applications.

Table 2.1: One-part AAMs studies in the literature that used various chemical admixtures.

Ref.	precursor	Alkaline activator (binder wt%)		Mixing method	w/b	Admixtures		Effect of admixtures on the properties of AAMs		Best Admixture
		Type	Dosage (%)			Type	Dosages (binder wt%)	Flow diameter (mm)	Compressive strength	
[116]	GGBFS	NaOH	10%	Each TCT-P was mixed with water and admixture.	0.31 0.34 0.35	(Nb-SP) (PFS-SP) (PFS-SP)	0.75% 0.25%	-Increased -Increased -Increased	-Decreased -Decreased -Slight decreased	PFS-SP
[71]	0.85 :0.7 FA / 0.15:0.3 GGBS	Na_2SiO_3	5% : 11%	Dry mixing for all solids. Then, water was added, and the mixing continued for 3 minutes.	0.3 0.45	borax	3%: 9%	-Increased	-Increased	7% borax
[56]	GGBFS	Microsilica + NaOH	2.0% 2.4%	Mortar was prepared by mixing dry solids for 3 minutes; tap water was added, and mixing was continued for 3 minutes.	0.35 0.3	PC M PNS LS	0.5%	-Increased -Increased -Increased -Increased	-Increased -Increased -Increased -Increased	LS
[39]	0.5 FA/0.5 GGBS	Na_2SiO_3	12%	Dry mixed for 2 min on slow speed. Then, 60–80% of water was added to the mix. The SP was diluted in the remaining water and then added to the mix. The mixing required 5–6 min.	0.4 0.38 0.36 0.34	PC N M	1%	-Increased -Increased -Increased	-Slight decreased -Decreased -Slight decreased	PC
[75]	0.5 FA/0.5 GGBS	$Ca(OH)_2$ /Na_2SO_4	12%	Dry mixed for 2 min on slow speed. 60–80% of the water was added while the remaining water diluted the SP. The whole mixing procedure required 5–6 min	0.4 0.27	PC N M	1%	-Increased -Increased -Increased	-Increased -Increased -Increased	PC

[38]	0.85 FA/0.15 GGBS	Na_2SiO_3	8%	Dry mixed for 2 min. Then, water was added to the mixture, and mixing was continued for 3 more minutes.	0.28 0.3 0.32	SG SL CL SPT PC Borax	2% 2%,4%,6%,8%	-Increase -Increase -Decrease -Increase -Increase -Decrease	-Decreased -Decreased -Decreased -Increase -Increase	Borax
[117]	0.5 :0.7 FA / 0.3:0.5 GGBS	Na_2SiO_3	8% 9% 10%	All solid constituents (fly ash, slag, sodium meta-silicate, borax, and sand) were mixed for 2 minutes. Water was then gradually added while continuously mixing for an additional 3 minutes.	0.3	Borax	3, 4 and 5%	-Decreased	-Decreased	4% borax
[118]	Waste red brick powder 0.55:0.70/ silica fume 0.15:0.236/ calcium carbide residue 0.15:0.20	calcium carbide residue		First, the superplasticizer was completely dissolved in tap water. Next, the three precursor materials were thoroughly mixed. Finally, the liquid component was gradually added to the powder mixture and stirred until fully blended.	0.26 0.35 0.44	PC M N	1, 1.5 and 2% 2, 2.5 and 3% 2, 2.5 and 3%	-Increase -Increase -Decrease	-Decreased -Decreased -Increased	1.5% PC
[59]	0. 5 FA/0. 5 GGBS	Na_2SiO_3	8%	Dry mixed. Two mixing methods were used (overall mixing time 30 min). The early PCE addition samples were prepared following method 1: the total amount of water was added at the beginning of the mixing procedure, and 90% of the mixing water was added to the dry ingredients, followed by the remaining 10% of the water used to dilute the PCE, then mixed	0.42	PCE Delay addition Early add	0.25% 0.5% 1% 2% 3% 4%	-Increase -Slight increase	-Slight decrease -Decrease	Delay addition of PCE (1%)

				at a 720 rpm speed for 1 minute. After 19 minutes of resting, the slurry was remixed at high speed for another 3 minutes, rest for six minutes, and mixed for one minute. Method 2 was achieved by delaying adding PCE and the remaining 10 % water till the end of the 19-minute resting period, and the remaining method 2 was similar to method 1.						

In conclusion, most existing studies have focused on incorporating various admixtures, such as superplasticizers or retarders, into binary AAMs composed of fly ash and slag. However, limited research has explored slag as a sole binder activated solely by sodium meta-silicate, and only a few studies have investigated slag activated by NaOH or a combination of NaOH and sodium meta-silicate. The effectiveness of admixtures in AAMs is highly dependent on the reactivity and chemical nature of the precursor and activator, as the polymerization process in AAMs fundamentally differs from the hydration reaction in OPC.

To address these gaps, this study focuses on a constant precursor (slag) and activator (sodium meta-silicate) system, employing various techniques to evaluate the behavior of slag-based AAMs activated by sodium meta-silicate in the presence of various retarders and viscosity-modifying admixture. Additionally, the study investigates the influence of extended mixing times and different mixing methods (resting versus continuous mixing) on the rheological properties of these materials. This work aims to provide deeper insights into optimizing the performance of slag-based AAMs for practical applications.

Chapter 3: Effect of ingredients adding sequences on rheological properties of alkali-activated slag paste

3.1. Introduction

The world approach is to decrease the dependence on OPC which is considered harmful to the environment with other sustainable green binders that have a less harmful impact on the environment [1,119–121]. Hence, AAMs are considered a sustainable alternative to OPC due to their low energy consumption and low greenhouse emissions [3,122–124]. Moreover, the promoting characteristics of AAMs such as high strength, high chemical resistance, and temperature resistance [8]. AAMs can be classified based on the activator state (powder or solution): one-part AAMs or "just add water" AAMs that are produced by powder activator and two-part AAMs that are produced by solution [125]. The production process of one-part AAMs is simpler compared to two-part AAMs because two-part AAMs are activated by prepared concentrated aqueous alkali solutions [126]. These solutions are viscous and corrosive due to high alkalinity resulting in difficulty in handling and casting in-situ applications [91].

The key barrier preventing AAMs' wider utilization is the gap in knowledge regarding their interaction behavior [65,127,128]. Moreover, problems of flowability affect the placing of concrete [129,130]. The main cause of rapid setting is the high hydration heat produced from the interaction of ingredients that accelerates the formation of hydration products [131]. So, many studies were conducted to investigate the rheological behavior of AAMs and demonstrate addressing ways of the poor workability of AAMs [124,132].

Other studies focused on the preprocessing (pretreatment) of precursors or activators to make them ready to react and improve polymer reaction efficiency [57,133–138]. However, there is a gap in determining the most convenient adding sequence for different ingredients to prolong setting time and decrease the competitive adsorption phenomenon between precursor and activator on water without declining compressive strength and other mechanical properties. Hence, This study aims to change the adding sequence of the main ingredients (precursor, activator, and water) on flowability, setting time, heat of hydration, and compressive strength. The sequences evaluated include: (1) mixing slag and meta-silicate, followed by adding water; (2) mixing slag, followed by

adding meta-silicate dissolved in water; and (3) mixing slag and water, followed by adding meta-silicate.

3.2. Experimental work

3.2.1. Materials

For all mixtures, granulated blast furnace slag (GGBS) with a specific gravity of 2920 kg/m^3, Blaine fineness of 515 m^2/kg, and an average diameter of around 14.5 μm was used as the precursor. GGBS is one of the commonly used precursors due to its high reactivity, ambient curing, and rapid strength development [13,14]. Anhydrous sodium meta-silicate (Na_2SiO_3) was used as a powder activator [139–141]. A constant activator dosage of 6% by weight of slag and a fixed water-to-solid ratio (w/s) of 0.40 were used for all mixtures [96]. Three mixtures with different sequences of adding mixing ingredients, namely M1 (mixing slag, meta-silicate then add water), M2 (mixing slag then add meta-silicate dissolved in water), and M3 (mixing slag, water then add meta-silicate) were mixed, placed, and tested. Most studies used the dry mixing of precursors and activators before adding water for one-part AAMs [59,96,142].

3.2.2. Mixtures preparation and testing procedures

All mixtures were prepared, cured, and tested under the laboratory ambient condition (i.e. temperature (T) = 23 ± 2 °C and relative humidity (RH) = 45 ± 5%). All mixtures' ingredient-adding sequences are illustrated in **Fig. 3.1**. The total mixing time was 4 min for all mixtures. For M1, initially, slag and powder anhydrous sodium meta-silicate activator were dry mixed for 1 min then gradually added water while mixing continued for about 3 min [96]. This sequence of dry mixing for approximately 5 minutes is the most commonly used method in the majority of studies of one-part AAMs [143]. For M2, initially, slag was mixed for 1 min then gradually added meta-silicate dissolved in water while mixing continued for about 3 min. For M3, initially, slag and water were mixed for 1 min then added meta-silicate while mixing continued for about 3 min.

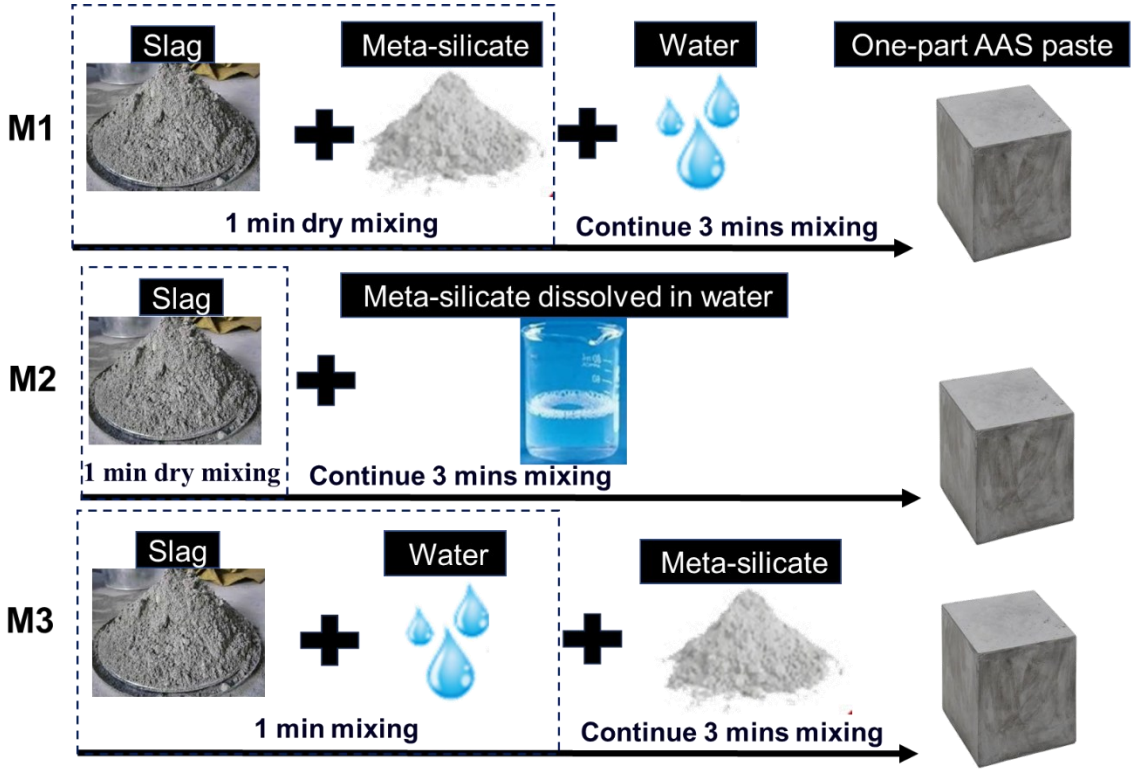

Fig. 3.1: Mixing adding sequences.

Flowability was evaluated using the mini-slump cone test. After removing the filled mini-cone, the final spread diameter (D_f) of the sample was an average of two measurements in perpendicular directions as shown in **Fig. 3.2**.

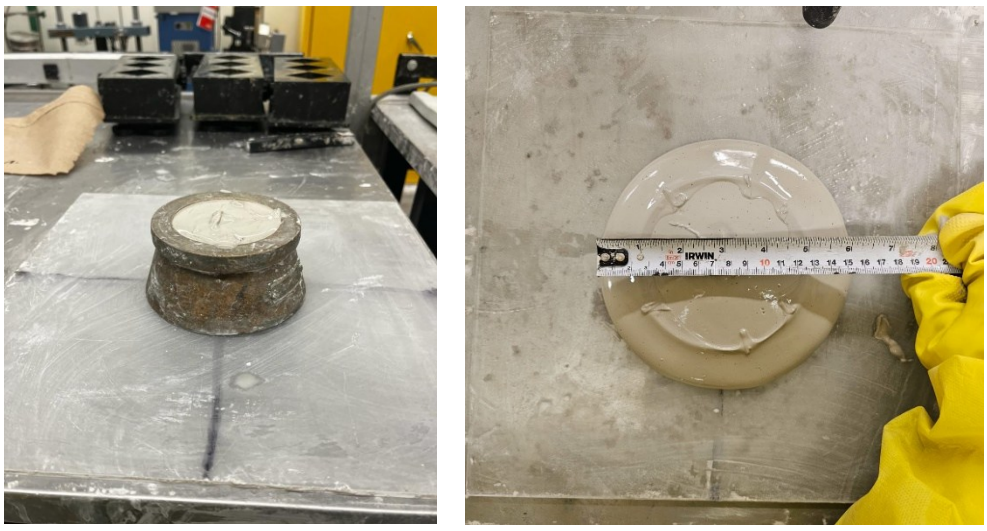

Fig. 3.2: Flow diameter test method.

For the setting time, samples were prepared and tested using a Vicat needle according to ASTM C191-99 ‘‘Standard test method for time of setting of hydraulic cement by Vicat needle”. The test setup is shown in **Fig. 3.3**.

Fig. 3.3: Vicat apparatus.

The heat flow at the wetting point (i.e. once the reaction started) was conducted following the method using a custom setup [96]. The sample preparation and isolation process, before connecting with the thermocouple for temperature measurement, is illustrated in **Fig. 3.4**. Moreover, the isothermal calorimetry test was conducted on specimens during the first 65 hrs. of hydration to obtain the heat profile. The calorimeter chamber used for testing is depicted in **Fig. 3.5**.

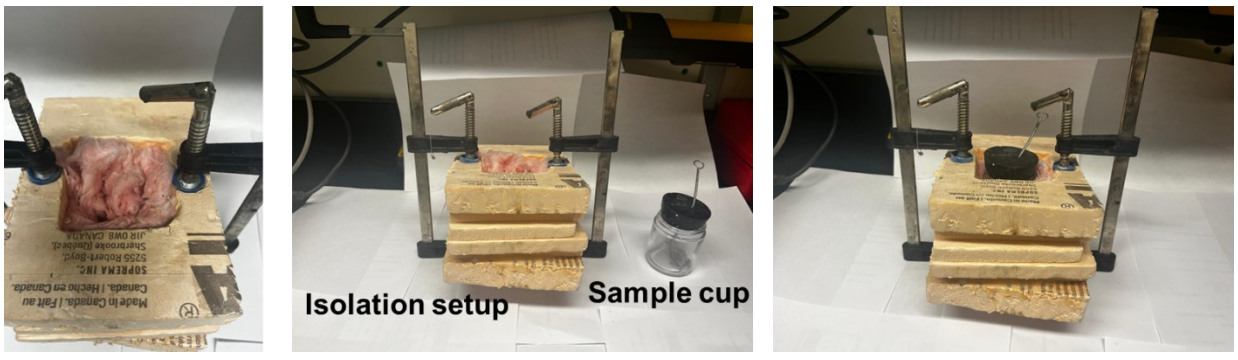

Fig. 3.4: Isolation of sample for wetting point test.

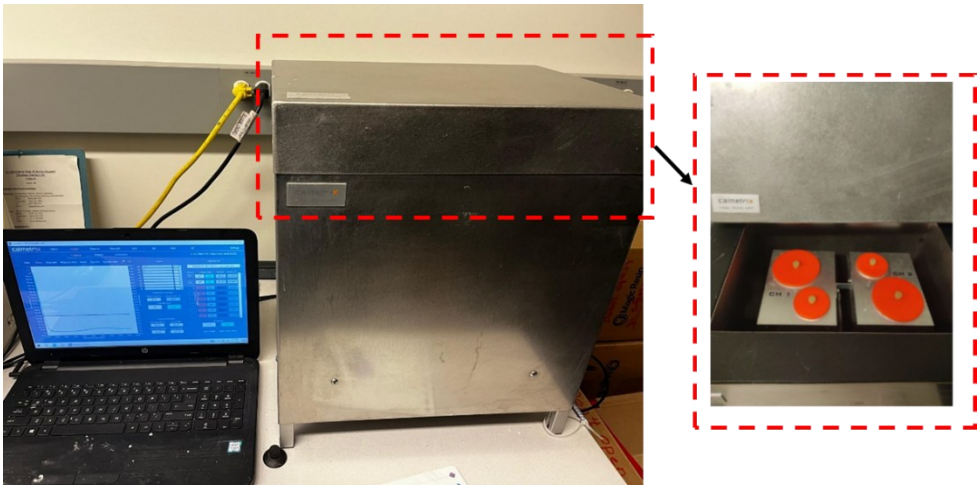

Fig. 3.5: Isothermal calorimetry test setup.

According to hardened properties, Cubic specimens 50 mm were used to measure the compressive strengths at ages 1, 3, and 7 days according to the ASTM C 109–20 ‘‘Standard Test Method for Compressive Strength of Hydraulic Cement Mortars” [144]. After 24 hours, the specimens were de-molded and stored in sealed plastic bags to prevent cracking caused by water evaporation. They were kept at laboratory ambient temperature to avoid leaching of the activator into water [64]. The test setup is shown in **Fig. 3.6**.

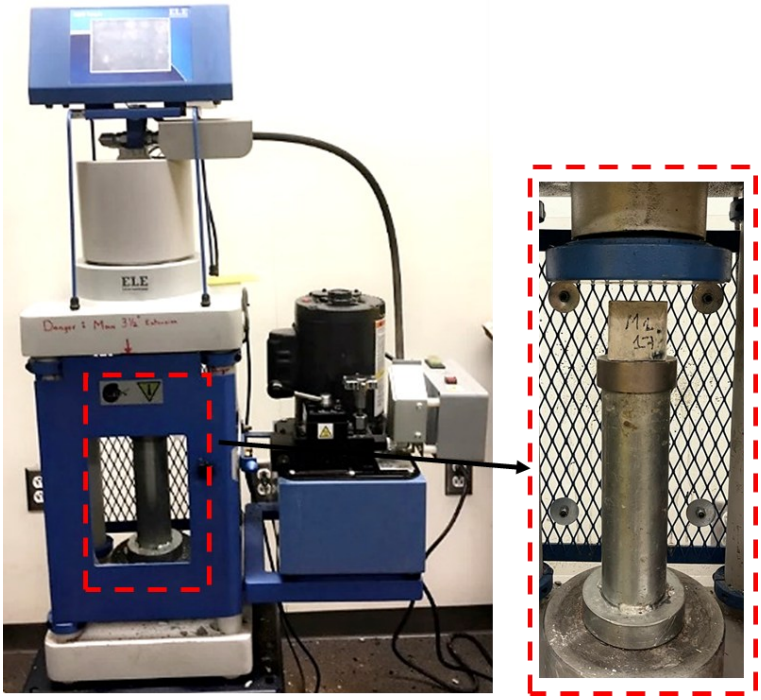

Fig. 3.6: Compressive strength test setup.

Ultra Pulse velocity (UPV) was also conducted to manifest the density variation and reveal any internal defects at ages 1, 3, and 7 days. The test was conducted according to ASTM C597 (Standard Test Method for Pulse Velocity Through Concrete) [145]. The test setup used was as shown in **Fig. 3.7**.

Fig. 3.7: Ultra pulse velocity test setup.

The formation of different hydration products was evaluated by conducting Differential Scanning Calorimetry (DSC) using a TA instrument. The hydration product formation was evaluated at age 3 days to determine the early hydration products as after 1 day the hydration process still occurs. Samples weighing approximately 16 mg were heated from 23 °C to 650°C at a heating rate of 10 °C/min.

3.3. Results and discussions

3.3.1. Effect of ingredient adding sequence on fresh properties

3.3.1.1. Mini-slump

The effect of different adding sequences of the ingredient on the spread diameter was insignificant as the spread diameters were 15, 15.5, and 15 cm for M1, M2, and M3, respectively. These findings indicate that a gradual increase in pH when adding water to slag and meta-silicate causes almost the same dissolution rate of slag under the effect of OH^- and the hydrolysis of silicate anions when adding meta-silicate to water [146]. This may be attributed to the release of hydroxide (OH^-) after

the contact between slag and water in the existence of the activator which causes an increase in pH regardless of the time of adding water [147].

3.3.1.2. Setting time

Fig. 3.8 illustrates the initial and final setting time for three mixtures with different adding sequences of ingredients. Generally, regardless of the time of adding water or activator, the elapsed time between the initial and final setting times did not change significantly as it was around 350 min. On the other hand, when adding a dissolved activator for the M2 **t**he initial and final setting times slightly decrease to 260 and 620 min, respectively compared to M1 and M3. It can be attributed to the relatively rapid dissolution of the precursor as the activator dissolved in water and silicate species are ready for reaction [23]. The dissolution of the solid activator and slag are exothermic reaction processes [96]. Hence, adding meta-silicate dissolved with water increases the amount of released temperature due to the relatively high rate of slag dissolution. However, the decrease in setting time is not significant here because 6% of the activator is used. Hence, it may be more noticeable when using high dosages of activators.

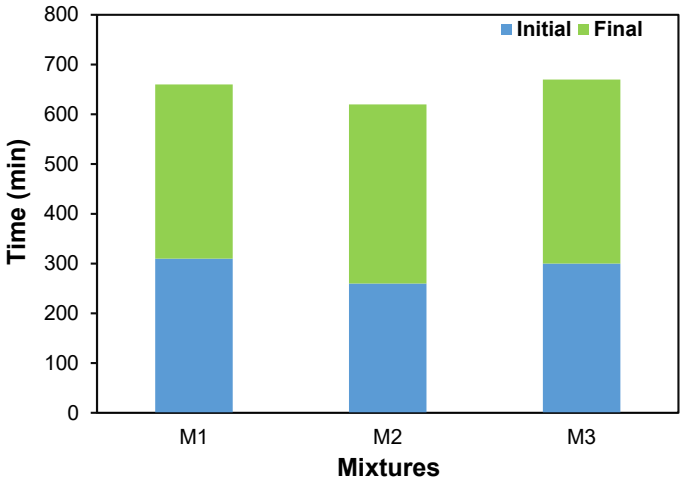

Fig. 3.8: Setting time results for AAS mixtures.

The final setting time for M1 and M3 was almost the same 660 and 670 min, respectively. Because when slag is mixed with water (M3), it doesn't react due to the low pH of the medium. High pH is essential to initiate the reaction. Similarly, when powder meta-silicate is mixed with slag (M1), the meta-silicate activator requires water to dissolve and create a high pH. This is in agreement with the result reported in the literature, the final setting time for AAS paste activated by 6% of Na_2SiO_3 is around 650 min when adding water to the meta-silicate activator and slag [96].

3.3.1.3. Heat flow profile

3.3.1.3.a) Pre-wetting for solids ingredients and dissolution heat

Fig. 3.9 depicts the wetting point at which the reaction was initiated. M2 is the highest mixture that generates temperature because of adding dissolved activator in water on slag, leading to the rapid dissolution of slag and the initiation of polymerization due to the high pH of adding solution [148]. Then, the temperature decreased. For M1 after adding water to slag and meta-silicate powder, the gradual increase in pH delayed the dissolution rate of slag. Hence, the increase in temperature when adding water was lower than M2, indicating a higher hydration rate. Similarly, adding a powder activator to slag and water (M3), took some time to increase the pH to dissolve the slag particles due to the absorption of water by slag particles [124].

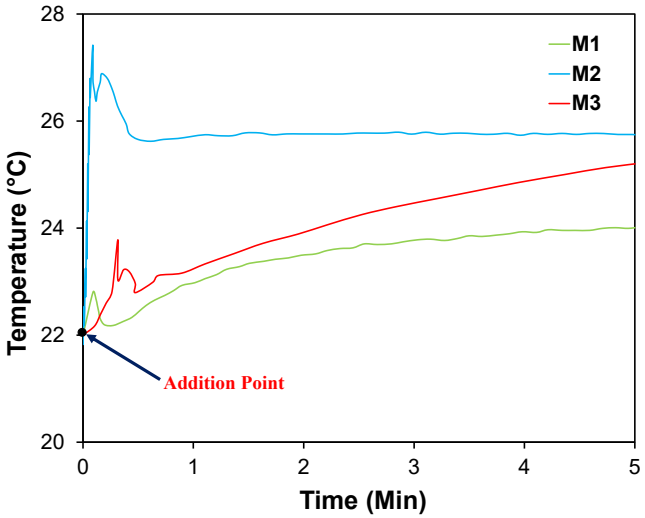

Fig. 3.9: Wetting point for heat generation.

3.3.1.3.b) Heat liberation under ambient conditions by the isothermal calorimeter

Fig. 3.10 shows the heat profile for the tested mixtures over 65 hours. The first peak for all mixtures was almost the same and occurred immediately after mixing because of the dissolving of slag under the influence of OH^- and the hydrolysis of silicate anions [149]. Then, the long-dormant period of all mixtures occurred before the second peak. The second peak existence differed as it took place after around 40, 25, and 55 hours for M1, M2, and M3 respectively. The appearance of this peak is dependent on the type of precursor used and has been observed specifically when slag is utilized as the precursor [150]. This complies with previous results of setting time since the initial setting time for M2 was the shortest time (260 mins).

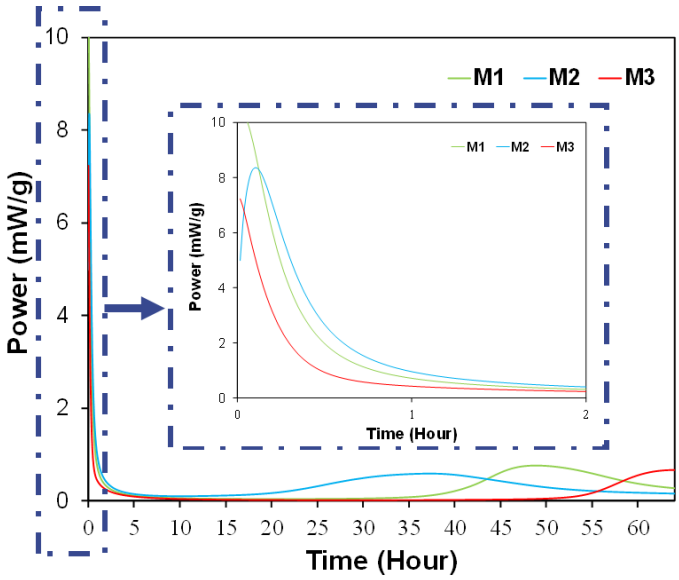

Fig. 3.10: Heat evolution curves at 65-h early hydration age of ground AAS mixtures.

3.3.2. Effect of ingredient adding sequence on hardened properties

3.3.2.1. Compressive strength

All mixtures did not exhibit strength at age 1 day. For 3 and 7 days, M2 showed a slight increase in strength values around 22.4 and 25.3 MPa, respectively as shown in **Fig. 3.11**. This confirms the results of the heat of hydration test as the second peak occurred after around 25 hours for M2, while it occurs after 40 hours and 55 hours for M1 and M3 respectively. The strength development of all mixtures was almost the same which indicates the slight effect of adding a sequence of ingredients on strength development. On the other hand, there was a marginal increase in the compressive strength of M2.

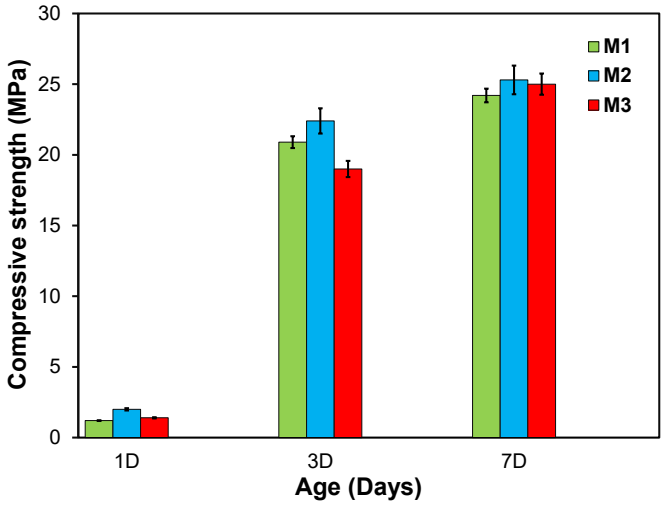

Fig. 3.11: Compressive strength results for AAS mixtures.

3.3.2.2. Ultra pulse velocity

Fig. 3.12 presents the UPV results for three mixtures at different ages. In general, microstructure development increased over time for all mixtures. At 1 day, only a slight change was observed among the three mixtures. M2 exhibited a higher velocity compared to M1 and M3, aligning with the wetting point and compressive strength results. From 3 to 7 days, the microstructure development was nearly identical across the mixtures, indicating that most of the reaction occurred within the first 3 days.

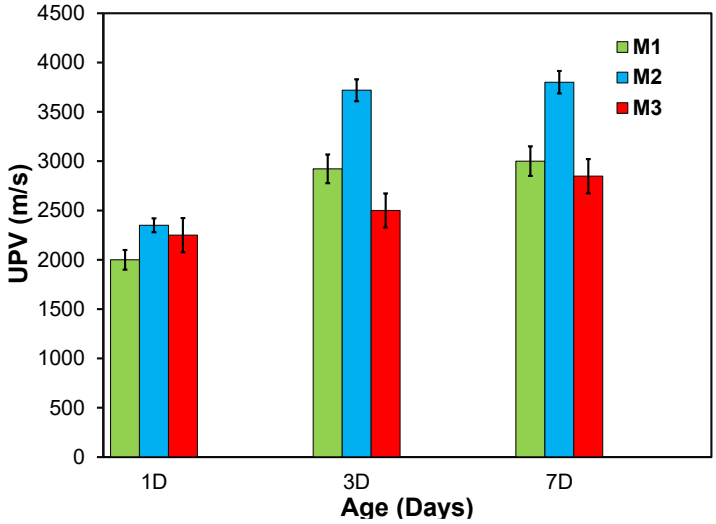

Fig. 3.12: UPV results for AAS mixtures.

3.3.2.3. Differential scanning calorimetry

Fig. 3.13 illustrates the findings of the DSC test conducted on specimens at age 3 days since 1 day exhibited low strength, which indicated that the hydration process still occurred, and the objective was to measure the early hydration products as much as possible. Near 200 °C, the weight loss is due to the dehydration of calcium aluminate silicate hydrated C-(A)-S-H gel [14]. The highest peak was obtained at M2, confirming the previously discussed setting time results and heat profiles. The second endothermic peak between 300 and 400 °C is because of the decomposition of hydrotalcite [14].

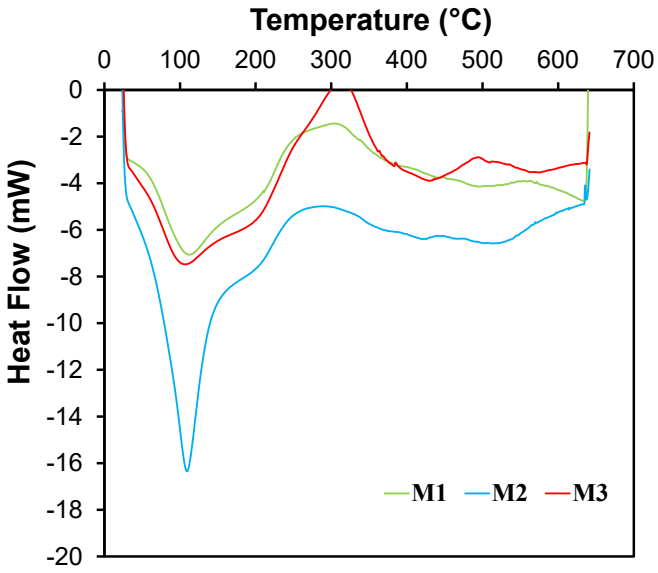

Fig. 3.13: DSC results for AAS mixtures.

3.4. Conclusion

This study demonstrates that the order of adding water or activator on slag to produce AAS mixtures is an important factor that changes various properties at small dosages of activator. These conclusions can be extracted from this study:

- The shortest initial setting time was achieved by adding meta-silicate dissolved with water to slag (M2) due to the relatively rapid dissolution rate of slag.
- The highest elaborated temperature of reaction occurs when adding dissolved meta-silicate to slag (M2).
- There is a slight change in flowability and compressive strength when changing the adding sequence of water or slag.
- The optimal mixture, M1 (prepared using the dry ingredients mixing), demonstrated an acceptable setting time and heat profile. It successfully avoided the short setting time and a short dormant period, making it suitable for use in the following chapters. Implementing this adding sequence, along with different techniques, influenced its rheological behavior.

Chapter 4: Influence of mixing protocols on flow retention of one-part alkali activated slag systems

Based on the investigation conducted in Chapter 3, which compared the adding sequences of the main ingredients, the optimal sequence was identified as the dry mixing of the activator and precursor before adding water. This sequence achieved reasonable flowability and setting time. Building on these findings, the current chapter employs this optimal mixing sequence to explore the effects of varying mixing times and techniques (continuous and discrete). These variations are comprehensively assessed for their impact on the fresh, rheological, and hardened properties of AAS, providing a deeper understanding of their behavior.

4.1. Introduction

Cement production is responsible for about 8% of the total carbon emissions [1–3] and consumes about 40% of global energy [4]. This motivated researchers to explore more environmentally friendly alternatives (such as sulfate-aluminate cement [5], high-calcium fly ash–Portland cement [6], and lime-calcined clay cement [7]). Among these alternatives, AAMs are promising alternatives [8,9]. AAMs are prepared by activating aluminosilicate precursors (i.e. slag and fly ash) using high alkalinity activators [10–14]. Generally, AAMs can be categorized as "two-part" or "one-part" based on the nature of the activator used. A high alkalinity liquid-based activator is used to activate the precursor in two-part AAMs, while a powder activator is used in the one-part AAMs [23,40]. One-part AAMs offer significant economic advantages over two-part AAMs, including simplified handling, reduced labor, and minimized safety concerns, as they combine all components into a single dry mix that only requires the addition of water. This ease of use lowers transportation, storage, and equipment costs, making them more accessible and practical for various construction projects [41,42]. Additionally, by mimicking traditional cement handling, one-part AAMs promote broader adoption due to using powder activator [40]. These benefits, combined with their potential for reduced carbon footprints and enhanced durability, make one-part AAMs a strong alternative for sustainable construction practices [8].

The rapid flowability loss of AAMs is the main challenge hindering the wider acceptance (i.e. short slump-life) in the construction sector [47,48]. This is usually attributed to their fast

microstructure development and hydration products' formation (i.e. Calcium-Alumina-Silica-Hydrates (C-(A)-S-H) gel [51]. Hence, several studies have focused on utilizing various types and dosages of admixtures to retard the hydration reaction and consequently extend the slump-life [38,53–55]. However, these admixtures' stability and solubility issues in such a highly alkaline environment [28,29] and their adsorption on precursor particles reduced their efficiencies [58,59]. Other studies investigated the impact of varying admixtures' addition time on AAMs' fresh properties [59,60]. The delayed addition of polycarboxylate ether reduced the static yield stress of AAMs, leading to better workability [59]. Another approach focused on studying the effect of extending the mixing duration (up to 30 min) on two-part AAS properties [129]. A marginal improvement in fresh and hardened properties was reported. However, due to the difference in the activator natural between two-part and one-part systems, the applicability of these approaches is still questionable. Addressing such a knowledge gap will present a potential for wider acceptance of AAS and applications such as RMC, which often experiences long mixing during delivery [62,63]. According to the ASTM C94 "Standard Specification for Ready-Mixed Concrete", the mixing duration was limited to 90 minutes [129]. Continuous mixing for 90 minutes is an extensive energy process and sometimes is impossible. Hence, it is essential to understand the potential and effects of mixing pause on developing fresh properties.

Therefore, this study will investigate the applicability of extending the mixing time technique on flow retention and highlight the impact of mixing interruption or pause. It will also emphasize the correlation between the dissolution of the slag and powder activator, the microstructure development rate from one side, and the effect of breakage induced during remixing.

4.2. Research Significance

Extensive research has explored ways to overcome AAMs' poor flowability, such as changing precursors, activators, mixture design, adding admixtures, and extending the mixing time. However, the effects of extending the mixing time and changing the protocol were not investigated for one-part AAS. This study investigates, for the first time, the effect of extending mixing time with and without interruptions on the rheological properties of AAS. The outcomes are anticipated to facilitate the development of ready-mix one-part AAS, assisting ready-mixture concrete manufacturers in planning and scheduling delivery to ensure higher productivity with optimum performance for cast elements.

4.3. Experimental Work

4.3.1. Materials

For all mixtures, GGBS with a specific gravity of 2920 kg/m^3, Blaine fineness of 515 m^2/kg, an average diameter of around 14.5 μm, and a basicity coefficient of 1.06 was used as precursor. The chemical composition of the GGBS is summarized in **Table 4.1**. Mixture proportions were based on previous studies for one-part AAS: Anhydrous sodium meta-silicate (Na_2SiO_3) was used as a powder activator and added at different dosages of 6%, 8%, and 10% by slag weight [42,151]. For all mixtures, a constant w/s = 0.40 was used [133].

Table 4.1: The chemical composition of GGBS (wt.%).

SiO_2	Al_2O_3	CaO	FeO_3	SO_3	Na_2O	MgO	TiO_2	MnO	Sum
36.20	10.20	37.10	0.50	2.70	0.30	11.60	0.92	0.25	99.77

4.3.2. Mixing techniques

Initially, GGBS and Na_2SiO_3 were dry mixed for 1 minute, followed by gradually adding water over 1 minute while mixing. Then, mixing continued for different durations according to the applied mixing protocols [152]. A trial mixture following the 3-mins mixing time procedure suggested by previous studies was initially evaluated [42]. After that, the 10-minute mixing time was found to be an optimum duration to achieve the same flowability as the 3 minutes while maintaining the flowability life [42]. On the other hand, the maximum allowed mixing time of 90 minutes was selected as the longest mixing time according to the ASTM C94 recommendation [153]. Six mixing protocols were applied: 1) Continuous mixing for 10 mins (**C10**); 2) Continuous mixing for 20 mins (**C20**); 3) Continuous mixing for 30 mins (**C30**); 4) Discrete mixing for 30 mins (10 mins mixing, then 10 mins relaxation time (i.e. resting) and mixing again for 10 mins) (**D30**); 5) Discrete mixing for 60 mins (same mixing sequence for D30, repeated once) (**D60**); and 6) Discrete mixing for 90 mins (same mixing sequence for D30, repeated twice) (**D90**). Different mixing protocols are illustrated in **Fig. 4.1**. All mixing was conducted at a constant mixing speed of 139 rpm [39].

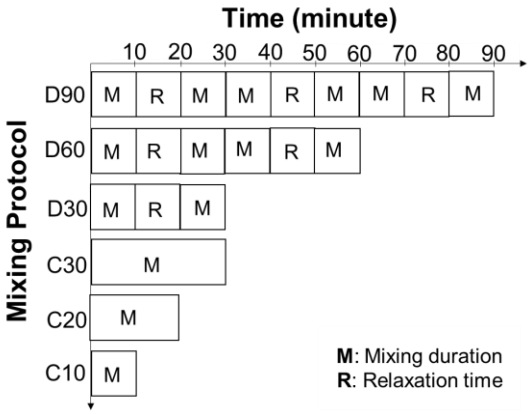

Fig. 4.1: Applied mixing protocols.

4.3.3. Mixtures preparation and testing procedure

All mixtures were prepared, cured, and tested under the laboratory ambient condition (i.e. T= 23 ± 2 °C and RH = 55 ± 5%). Flowability was evaluated using the mini-slump cone test immediately after each mixing protocol [96]. After removing the filled mini cone, the final spread diameter (D_f) was taken as an average of two measurements in two perpendicular directions. This was also considered as the initial flow diameter for each applied mixing protocol. The mini-slump was repeated every 2.5 mins for the first 10 mins, then at 5-minute intervals until there was no spread (i.e. D_f = 100 mm), which is considered as the end of flowability life [96].

The initial and final setting times were determined according to ASTM C191-99 (Standard test method for the time of setting of hydraulic cement by Vicat needle) [154]. The initial and final setting times were measured from water addition to powder ingredients (i.e. wetting point) for all mixing protocols [155]. The paste sample was placed in a cone covered by a plastic sheet and stored in ambient condition.

Isothermal calorimetry was applied to evaluate the rate of early hydration for all tested mixtures according to ASTM C 1679 (Standard Practice for Measuring Hydration Kinetics of Hydraulic Cementitious Mixtures Using Isothermal Calorimetry) [156]. Approximately 70g of paste was externally prepared for each mixture and then loaded into the isothermal calorimeter. The estimated time between finishing mixing and loading the sample into the calorimeter was about 1 minute after applying different mixing protocols. The heat evolution and cumulative heat released were then recorded and normalized by the dry binder mass. The operating temperature of the chamber was adjusted to 25°C, and the measurements were carried out for 48 hours.

The thermogravimetric analyses were carried out to monitor the development of different hydration products using a TA instrument. Small pieces were cut from selected specimens at age 3 days, ground to powder, and sieved on a No. 200 sieve (**Fig. 4.2**). A sample weighing approximately 16 mg was heated at 10 °C/min up to 850°C. Collected data and curves were analyzed using TA Instruments thermal analysis software [96].

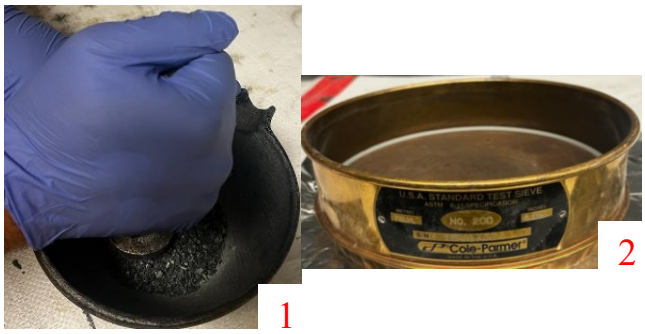

Fig. 4.2: The preparation steps for TGA, XRD, and FTIR samples.

Cubic specimens 50 mm were used to evaluate the compressive strengths at ages 3, 7, and 28 days following the ASTM C 109-20 (Standard Test Method for Compressive Strength of Hydraulic Cement Mortars) [144]. All specimens were de-molded after one day and stored inside sealed plastic bags in ambient laboratory conditions until testing age [157].

Moreover, prismatic specimens 25 × 25 × 285 mm were used to measure drying shrinkage following ASTM C 157/C127-17 (Standard Test Method for Length Change of Hardened Hydraulic-Cement Mortar and Concrete) [158]. All specimens were de-molded after three days (**Fig. 4.3**) and the initial readings were recorded before storing them under ambient laboratory conditions.

Fig. 4.3: Demoulded shrinkage specimens.

The unrestrained one-dimensional drying shrinkage was measured using a comparator provided with a dial gauge with an accuracy of 10 μm/m for up to 1 month. The used shrinkage test setup was shown in **Fig. 4.4**. Change in length was determined by using the following equation (**Eq. 4.1).**

Fig. 4.4: Shrinkage gauge used.

$$\textbf{Length Change (\%)} = \frac{L_f - L_i}{G} \times 100 \qquad \textbf{Eq. 4.1}$$

Where: L_f is the Final length of the specimen; L_i is the Initial length of the specimen; G is the nominal length of the comparator gauge used to measure the length.

A Brookfield R.S.T (**Fig. 4.5**). rheometer, with a four-blade vane (length of 60 mm and diameter of 30 mm), was used to determine rheology evolution with time for paste mixtures. Flow curve tests were captured every 15 minutes during the first hour after mixing to evaluate changes in dynamic yield stress and plastic viscosity with time, as shown in **Fig. 4.6**. It should be mentioned that loading the samples into the rheometer measuring cup took around 5 minutes, which was not included in the 1-hour measuring duration [159]. The pastes in the rheometer measuring cups were

covered with a plastic sheet to prevent evaporation during measurement. For the shear protocol applied, paste samples were initially subjected to a high-speed pre-shear to break down the structure build-up. Then, the paste remained at relaxation for 30 seconds to dissipate the residual stress due to pre-shear [160], followed by the ascending and descending shear rate steps as shown in **Fig. 4.7**. Dynamic yield stress and plastic viscosity were determined by applying Bingham fitting (**Eq. 4.2**) in the downward part of each flow curve [160].

Fig. 4.5: Rheometer setup.

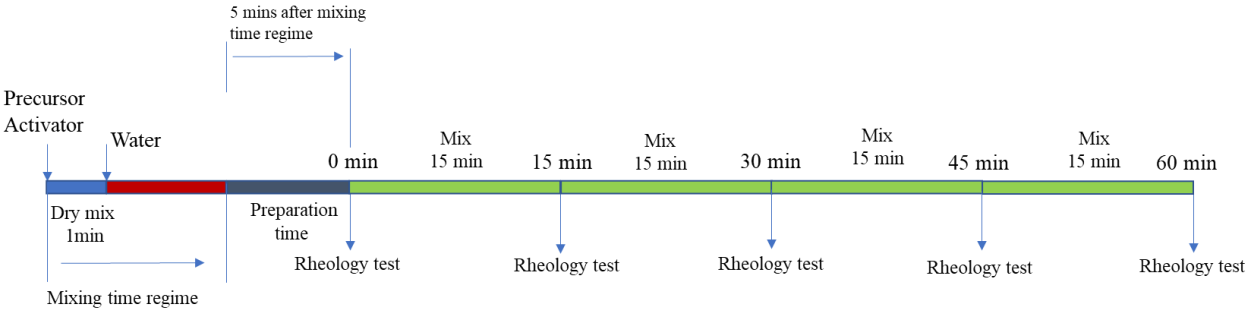

Fig. 4.6: Testing protocol for rheology test.

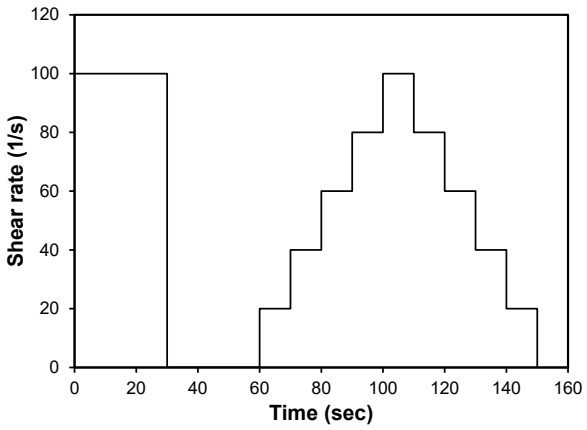

Fig. 4.7: Shear protocol used in flow curve test.

$$\tau = \tau_0 + \mu \cdot \gamma \qquad \textbf{Eq. 4.1}$$

Where: τ is the shear stress; τ_0 is the dynamic yield stress in Pa; μ is the plastic viscosity in Pa ·s.; γ is the shear rate in 1/s.

X-ray diffraction (XRD) and Fourier-transform infrared spectroscopy (FTIR) were used to examine the microstructure development and hydration products' formation. XRD was conducted according to ASTM C1365-18 (Standard Test Method for Determination of the Proportion of Phases in Portland Cement and Portland-Cement Clinker Using X-Ray Powder Diffraction Analysis) using a Bruker D8 Advance diffractometer (Cu K α radiation, 1.5406 Å) with an imaging plate detector to collect data from $10^o < 2\theta \leq 90^o$ (**Fig. 4.8**). Fourier-transform infrared spectroscopy (FTIR) spectra was obtained using a Nicolet 6700 spectrometer (Thermo Scientific). Frequencies were scanned in the range of 3150–650 cm^{-1}(**Fig. 4.9**).

Moreover, scanning electron microscopy (SEM) analysis was conducted on small chunks from selected specimens using a Hitachi S-3400N SEM at 15.0 kV accelerating voltage. This was coupled with energy-dispersive X-ray analysis (EDS) using a JEOL 35-cf spectrophotometer for elemental mapping and spot analysis [161].

Fig. 4.8: The equipment used for XRD analysis.

Fig. 4.9: The equipment used for FTIR analysis.

4.4. Results and Discussion

4.4.1. Fresh properties

4.4.1.1. Mini- slump

Fig. 4.10 illustrates the impact of different mixing protocols on the initial flow diameter for various AAS mixtures. Results indicated that extending the continuous mixing time had a higher effect on AAS mixtures with a lower activator dosage. For example, increasing the mixing time from 10 to 30 minutes resulted in a 27% increase in the initial flow for mixtures with a 6% activator and no change for those with a 10% activator. This effect can be attributed to the high free water content in a low activator mixture due to its lower consumption in hydration [160]. Moreover, GGBS particles dissolved slower at low activator dosages, decreasing the amount of Ca^{2+} and

Mg^{2+} cations released. These cations react with available silicate species, forming double-charged cations around precursor particles and facilitating agglomeration. Hence, the low cation concentrations in low activator mixtures slow agglomeration, leading to better flowability [42,162]. This also explains the longer flow life for low activator mixtures illustrated in **Fig. 4.11**. The lower the activator dosage, the lower the formed hydration products, extending the flow life due to the lower degree of microstructure development. This can explain the lower flowability loss rate for low activator mixtures (e.g. 0.5 mm/min for 6% activator) compared to high activator mixtures (e.g. 0.72 mm/min for 8% activator). Additionally, a high activator dosage did not show flowability life as the initial flow diameter was 100 mm, except for mixing protocols D30 and D60.

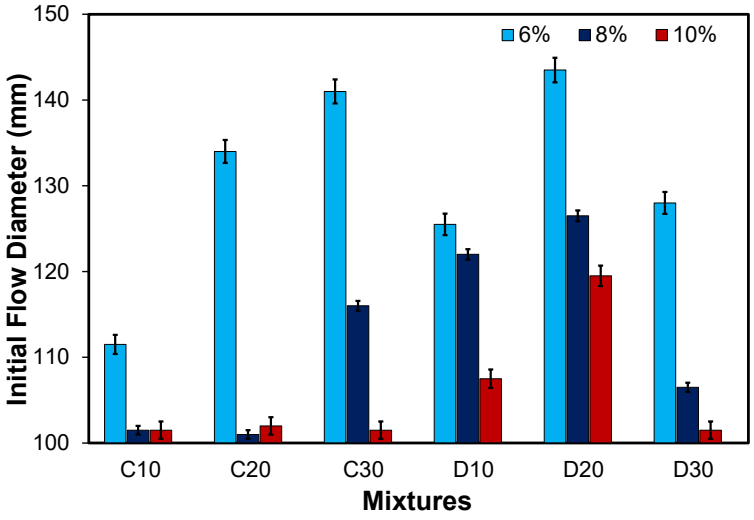

Fig. 4.10: Initial flow diameter results for AAS mixtures prepared by different mixing protocols and activator dosages.

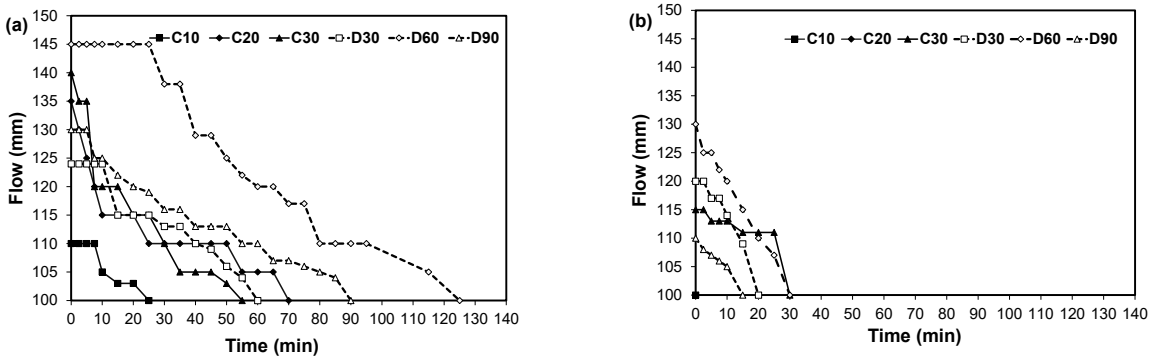

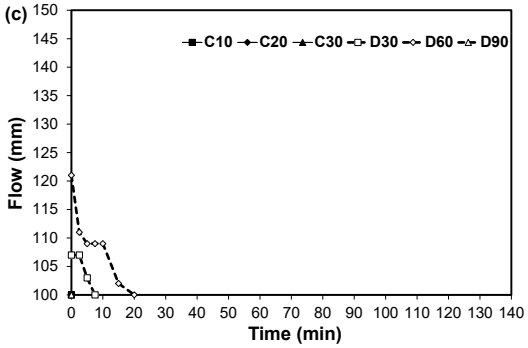

Fig. 4.11: Flow results for AAS mixtures prepared by different mixing protocols and activator dosages: a) 6%, b) 8%, and c) 10%.

For discrete mixing protocols, the initial flow diameter increased as the mixing duration increased to 1 hour (D60) and decreased after that (D90), regardless of the activator dosage. For example, for mixtures with activator dosages of 6% and 10%, the initial flow diameters under the D60 protocol increased by 16.9% and 13% compared to the D30 protocol. This phenomenon can be attributed to the compensatory effects of mixing and relaxation processes on the mixture's microstructure development. Mixing enhances the dissolution rate of different species, accelerating the hydration, while remixing after a relaxation period will have the same effect as mixing but also break down formed hydration products. Conversely, the relaxation period provides more time for hydration products to form, helping in the microstructure and interparticle links' developments [42]. The formed hydration products and developed links during the relaxation time will be broken down by remixing as illustrated schematically in **Fig. 4.12**. Initially, GGBS dissolution releases the ions and early-formed hydration products are controlled by the activator dosage. Besides, extending the mixing time enhances dissolution and increases hydration products' formation rate (which will depend on the activator dosage). During relaxation time, both systems (low and high dosages) experience increased formation for hydration products. Once remixed, the formed links are broken, facilitating flow. However, after a long mixing duration, most of the free water is already consumed, and even the breakage of the formed hydration products will have a minor effect on the mixture's ability to flow as the interparticle spacing becomes narrower [163]. This explains the variation in the behavior between various protocols. For protocols D30 and D60, the remixing effect will have a dominant impact on the flow behavior, while for protocol D90, it had a minor impact.

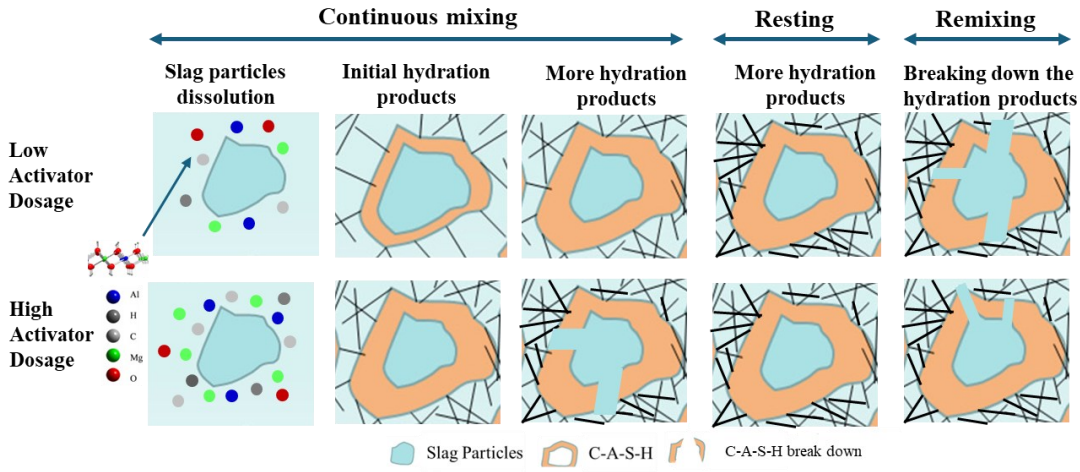

Fig. 4.12: Schematic diagram of the hydration of AAS mixtures with continuous and discrete mixing.

Another interesting finding is the varying impact of continuous and discrete mixing on the initial flow for mixtures exposed to mixing protocols with similar lengths (i.e. C30 and D30) and/or mixing duration (i.e. C20 and D30). For protocols with the same length (i.e. 30 min), C30 exhibited a higher initial flow than D30 at a low activator dosage. Conversely, at a high activator dosage, the trend was reversed. This can be attributed to low free water, increased cation ions, and agglomeration of the precursor particles boosted during relaxation time for high activator mixtures, as explained earlier. On the other hand, for the same mixing duration (i.e. same given shearing), the relaxation had the dominant effect over remixing at low activator dosages. The presence of relaxation (D30 with a 10-minute relaxation period) enhances the development of hydration bonds for a low activator dosage. Conversely, in C20, continuous breakage of the formed hydration products facilitates movement, resulting in a higher initial flow (**Fig. 4.12**). At high activator dosage, the remixing effect dominated as most hydration products and linkages were developed at the initiation of the relaxation period, minimizing its effect. Conversely, remixing breaks down the high-formed hydration links and interlocks, allowing the mixture to move again.

4.4.1.2. Setting time

Initial setting time is generally correlated to forming primary C-(A)-S-H gel [163]. At a high activator dosage, the high dissolution rate of slag accelerates the hydration product formation, leading to a shorter setting time [96]. **Fig. 4.13** illustrates the effects of different mixing protocols on the setting times of AAS mixtures. Increasing the mixing from 10 mins to 20 mins shortened the initial setting time by 20.2% and 16.2% and the final setting time by 4.4% and 8.4% for

mixtures with 6% and 10%, respectively. However, increasing the mixing time from 20 to 30 minutes had a slight to negligible effect on the setting time (i.e. < 5% shortening). This can be ascribed to the minimal difference in precursor and activator dissolution rates between 20 and 30 minutes of mixing time.

Changing the mixing protocol from continuous to discrete mixing while maintaining the same mixing duration (i.e. same shearing), insignificantly affected the setting time. For instance, for D30, the extension in the initial setting time was 13 mins and 227 mins, and the final setting time was 10 mins and 95 mins compared to C20 for mixtures activated by 6% and 10%, respectively. As explained earlier, this can be attributed to the compensation effects between relaxation and remixing (**Fig. 4.12)**.

After the same mixing age (from water addition, including relaxation time), discrete mixing extended the initial and final setting time compared to continuous mixing. For instance, at activator dosages of 6% and 10%, the initial setting time was extended by 50 mins and 227 mins, and the final setting time was increased by 10 mins and 34 mins for (D30) compared to (C30), respectively. Moreover, doubling the mixing time from 30 mins (D30) to 1 hour (D60), for mixtures with activator dosages 6% and 10%, the initial setting time was extended by 330 mins and 10 mins, and the final setting time was extended by 300 mins and 34 mins, respectively. However, at a longer mixing time (i.e. 1.5 hours for D90), there was a reduction in the initial and final setting time. Mixtures with activator dosages 6% and 10% experienced D90 mixing protocol, exhibited 6.5% and 32.5% shorter initial setting time and 5.48 % and 21.15% shorter final setting time compared to D60, respectively. This can be ascribed to the mixing protocol (i.e. mixing and relaxation period) effects on the precursor dissolution rate. During the mixing time, the movement of mixing tools increases the dissolution rate; conversely, during the relaxation time, the dissolution rate will drop. Switching between mixing and relaxation will vary the dissolution rate and, consequently, the ion concentrations in the pore solutions, affecting setting and hardening behavior. To some extent, such continuous deformation of the mixture during mixing will break the initially formed hydration products and disturb the adhesion bonding between them [42]. This will weaken the load-supporting ability for formed hydration clusters, delaying hardening and setting (**Fig. 4.12)**. On the other hand, more hydration products are formed during relaxation, leading to a higher internal adhesion bonding and stable microstructure [164]. This was confirmed by the heat flow results, which will be explained in the following section.

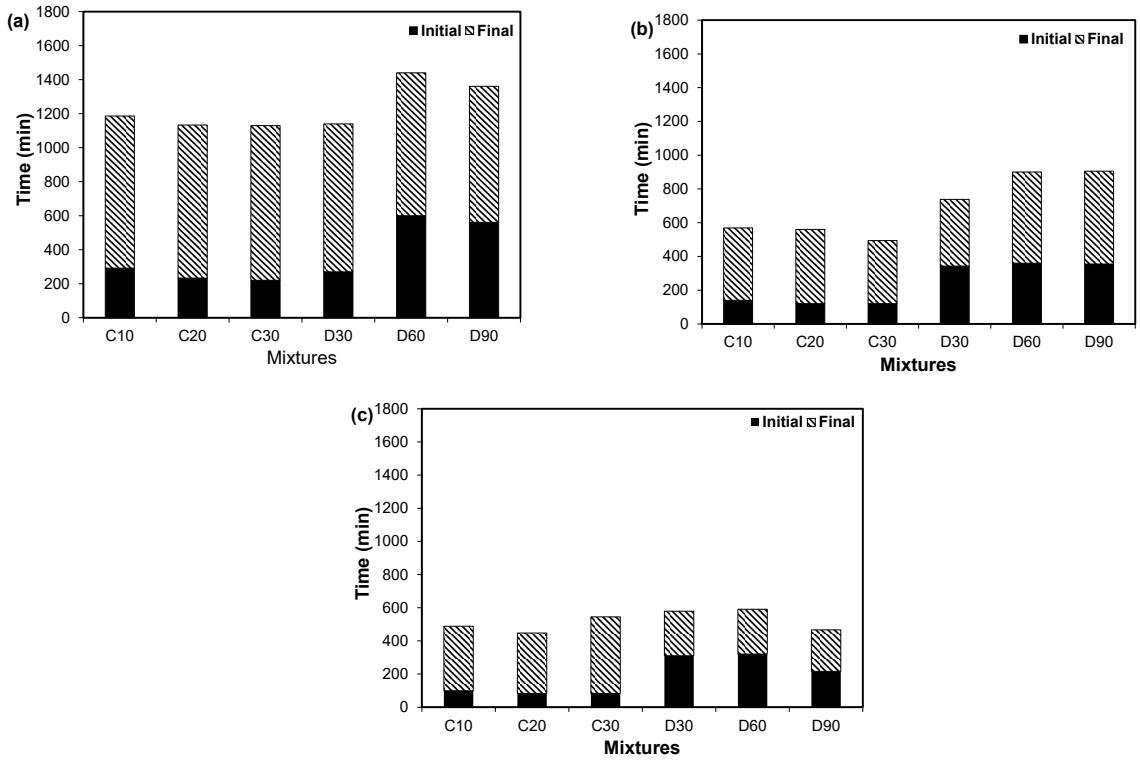

Fig. 4.13: Setting time results for AAS mixtures prepared by different mixing protocols and activator dosages a) 6%, b) 8%, and c) 10%.

4.4.1.3. Heat flow profile (Isothermal calorimetry)

All mixtures exhibited similar heat flow profiles with five distinguished stages: dissolution, induction, acceleration, deceleration, and the steady period [165]. Dissolution occurs when solid aluminosilicate precursors undergo dissolution in the alkaline activator solution. Then, induction involves initiating the chemical reactions between the dissolved precursors and the activator. Subsequently, the acceleration stage occurs, showing a rapid increase in the rate of chemical reactions, leading to significant strength development [166]. The acceleration phase will be followed by deceleration, at which the rate of reactions slows down. Finally, the reaction reached a relatively stable state (i.e. the steady period) [159]. **Fig. 4.14** shows the heat evolution for AAS mixtures exposed to different mixing protocols.

After 20 mins of mixing, the dissolution stage was not detected for all activator dosages (**Fig. 4.14**). This indicates that extending the mixing time beyond 10 minutes conceals the dissolution stage. This may be related to a change in the balance between the slag dissolution and the precipitation of the hydration products [167]. Moreover, lower hydration peaks were captured as the mixing time extended regardless of the activator dosage and the applied mixing protocol. For instance, the

hydration peak values decreased by 26.9% and 16.1% as continuous mixing increased by 20 mins (i.e. C30 vs C10) and decreased by 10.0% and 15.6% by comparing D90 and D30, for mixtures with activator dosages 6% and 8%, respectively (**Fig. 4.15)**. This emphasizes the dominant effect of mixing time. Extending the mixing time increases the dissolution rate for low activator mixtures, leading to denser microstructure as shown in **Fig. 4.16**, triggering more ions to react and form hydration products [164]. EDS results also supported this finding since the amount of reacted slag particles can be correlated to the detected Mg%. The higher the unreacted slag particles, the higher the detected Mg%. Hence, the reduction in Mg% for 30 minutes of continuous mixing proved the higher dissolution of slag particles and formation of C-A-S-H [168]. Mixtures with higher activator dosages will reach the triggered ion threshold earlier than mixtures with lower dosages, which will need more time, resulting in earlier hydration peaks. However, extending the mixing time beyond the threshold time for low and high activator mixtures will offset the effect of increasing the activator dosage and applying a longer mixing protocol.

On the other hand, altering the mixing protocols did not significantly affect the dormant period. However, the primary factor influencing the dormant period was the activator dosage. It was found that increasing the activator dosages shortened the dormant period and increased the achieved peak, which can be attributed to the fast initial nucleation process and formation of hydration products [169]. The same trend was observed for both continuous and discrete mixing protocols. For example, the dormant period decreased by 74.2% and 70.5% for AAS mixtures activated by 10%, compared to those activated by 6% for continuous and discrete mixing protocols.

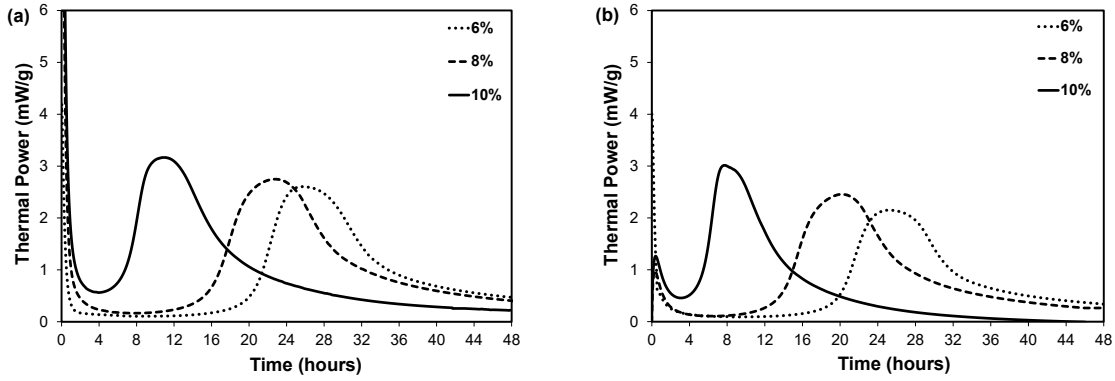

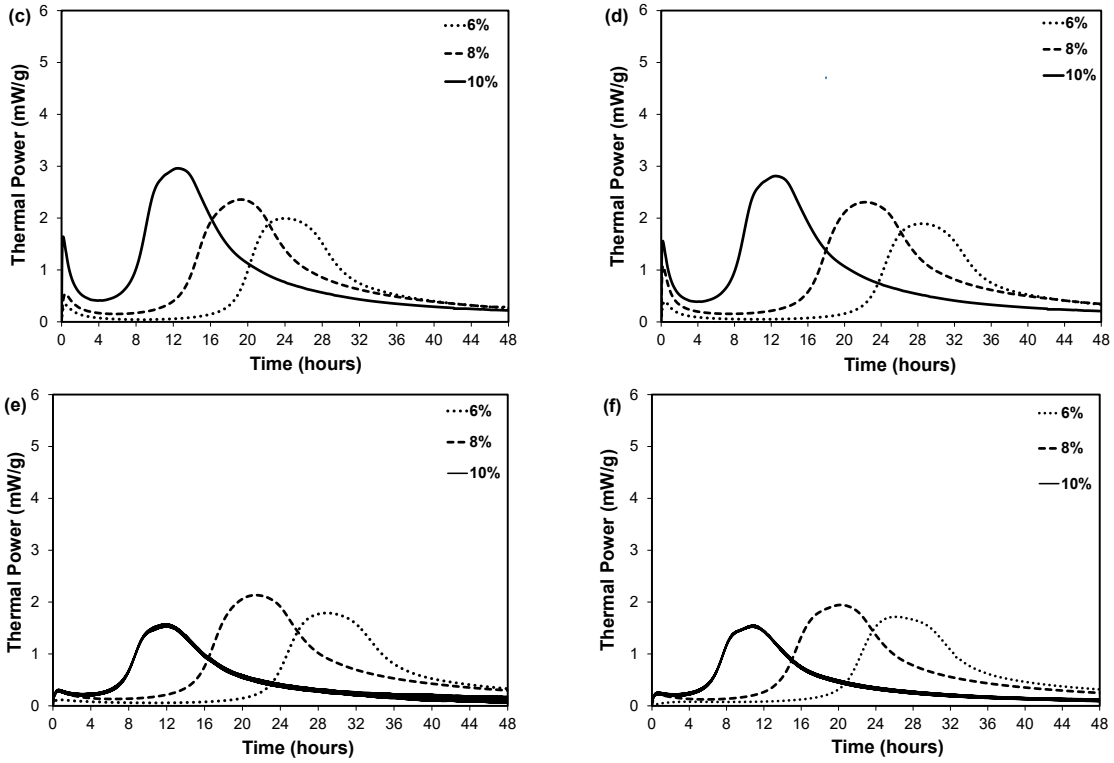

Fig. 4.14: Heat of hydration of AAS mixtures for different activator dosages a) C10, b) C20, c) C30, d) D30, e) D60, and f) D90.

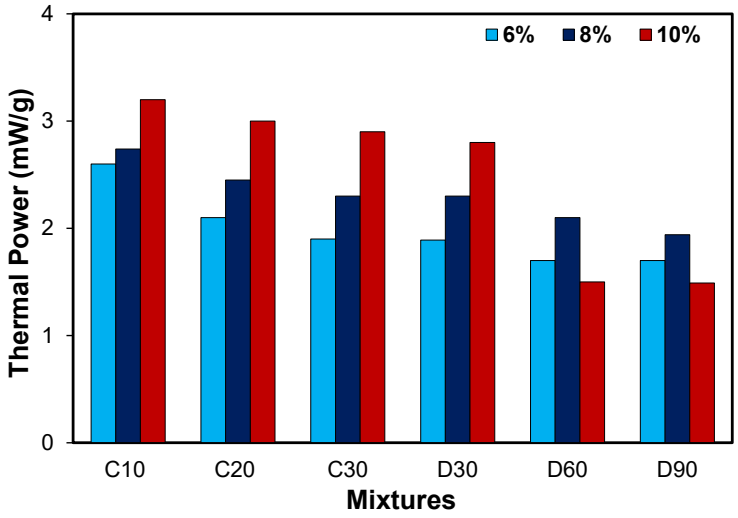

Fig. 4.15: Thermal power for the second peak of AAS mixtures prepared by different mixing protocols and activator dosages.

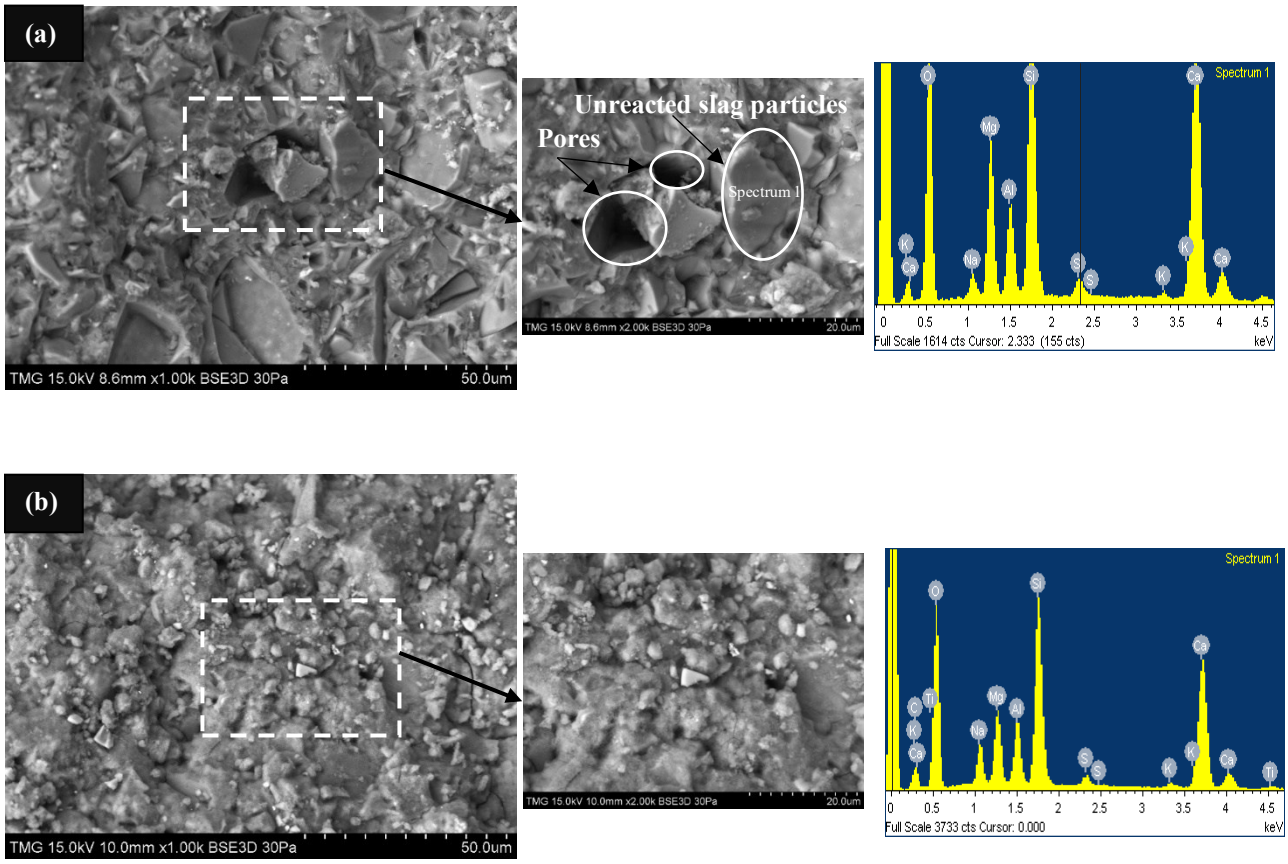

Fig. 4.16: SEM micrograph and EDS spectrum at 3 days age for mixtures activated by 6% under different mixing protocols a) C10 and b) C30.

4.4.1.4. Flow curve tests

Fig. 4.18 illustrated flow curves based on the shear protocol down part during the first hour after applying various mixing protocols. Results revealed an increase in the required external shear stress value to break down the developed hydration product bonds at various measuring points for all AAS mixtures. This was the same for all mixing protocols and used activator dosages. For instance, the shear stress for mixtures activated by 6% at 0 min measurement point (as illustrated in **Fig. 4.6**) increased by 15.37 % and 13.18% as the mixing time increased from C10 to C30 and D30 to D90, respectively. This can be attributed to the fast build-up of the AAS microstructure. **Fig. 4.17** shows TGA results for mixtures activated by a 6% activator before applying the flow test. It is clear that the longer the mixing protocol, the higher the hydration products and developed microstructure at the moment of conducting the flow tests.

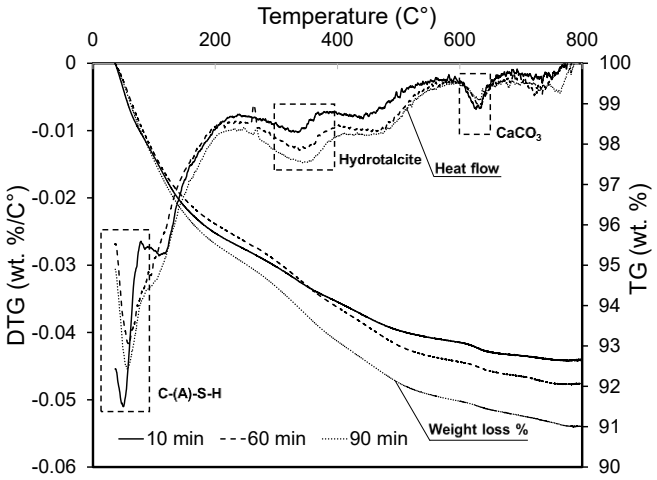

Fig. 4.17: TGA/DTG data of AAS mixtures activated by 6% under different mixing protocols.

On the other hand, the increase in the required shear stress had a descending trend as the activator dosage increased. For instance, the increase in shear stress over the shear strain testing range was 372 MPa and 381 MPa for mixtures with 6% activator and 218.62 MPa and 117.38 MPa for mixtures with 10% activator at 45 mins measurement point for mixing protocols C10 and D90, respectively. This agrees with the known shear-thinning behavior of AAMs (i.e. higher shear stress implies a reduction in the material's resistance to flow) [170].

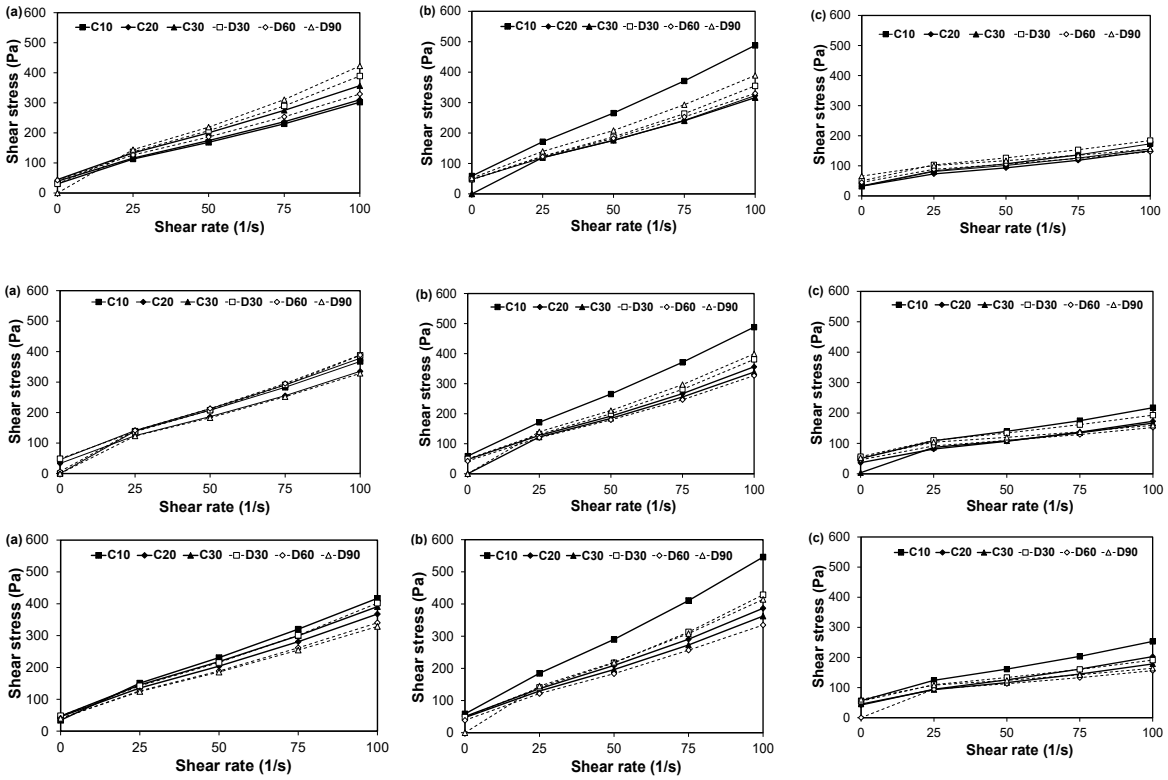

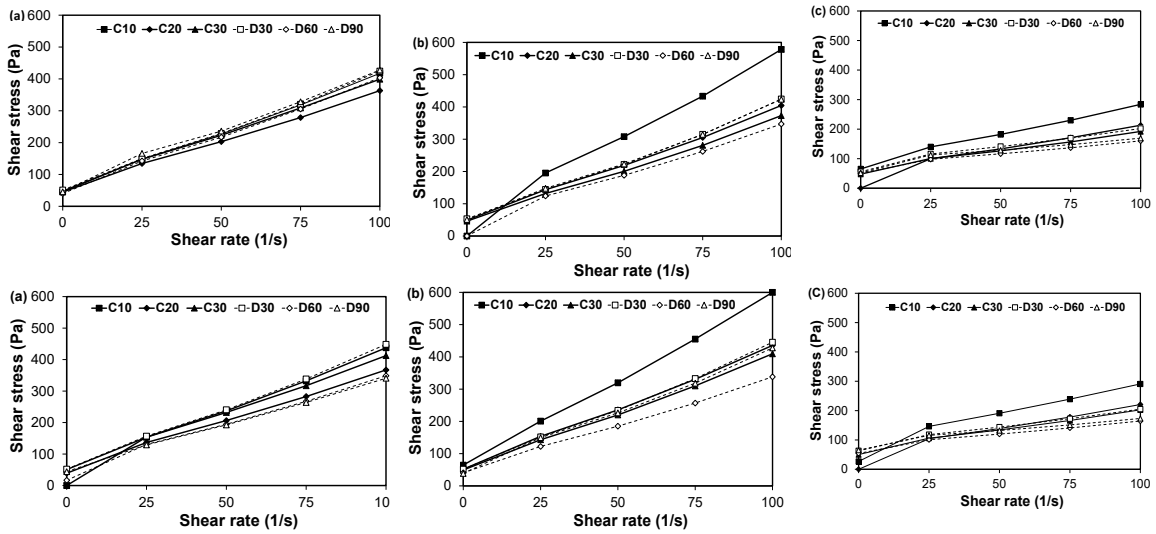

Fig. 4.18: Flow curves of AAS mixtures under different mixing protocols and activator dosages a) 6%, b) 8%, and c) 10% for the five measured points.

Fig. 4.19 shows the dynamic yield stresses of mixtures under different mixing protocols. Increasing the activator dosage increased the yield stress and decreased the plastic viscosity (as illustrated in **Fig. 4.20**), regardless of the applied mixing protocol. For instance, the dynamic yield stress increased by 10%, and plastic viscosity decreased by 51% as the activator dosage increased from 6% to 10%. Activator dissolution releases silica species, partially consumed in the reaction with the precursor. The remaining silica species form a liquid gel. The higher the activator dosage, the higher the formed liquid gel, leading to a high solid concentration, consequently increased yield stress and reduced plastic viscosity [167].

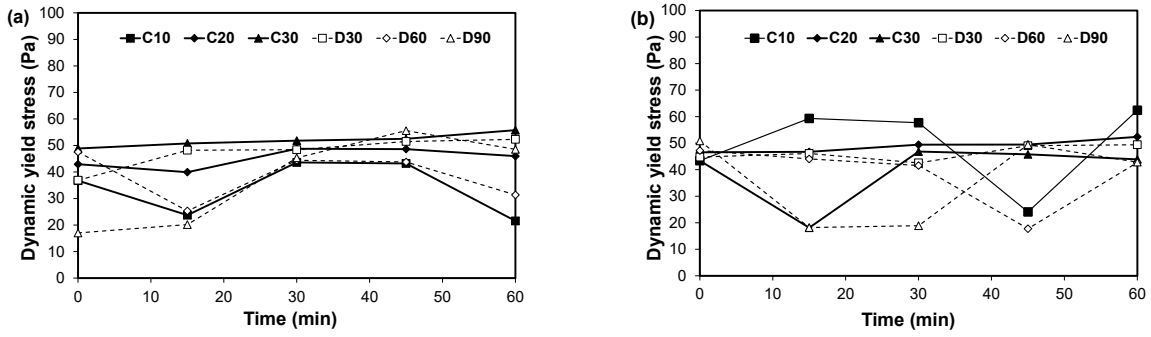

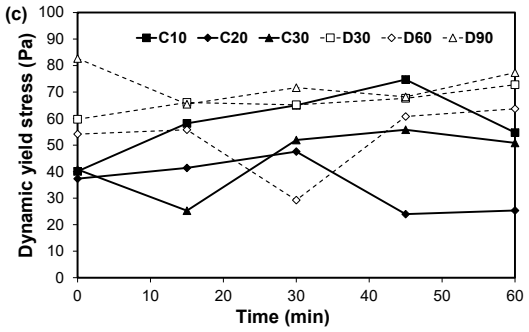

Fig. 4.19: Dynamic yield stress against time of AAS mixtures under different mixing protocols and activator dosages a) 6%, b) 8%, and c) 10%.

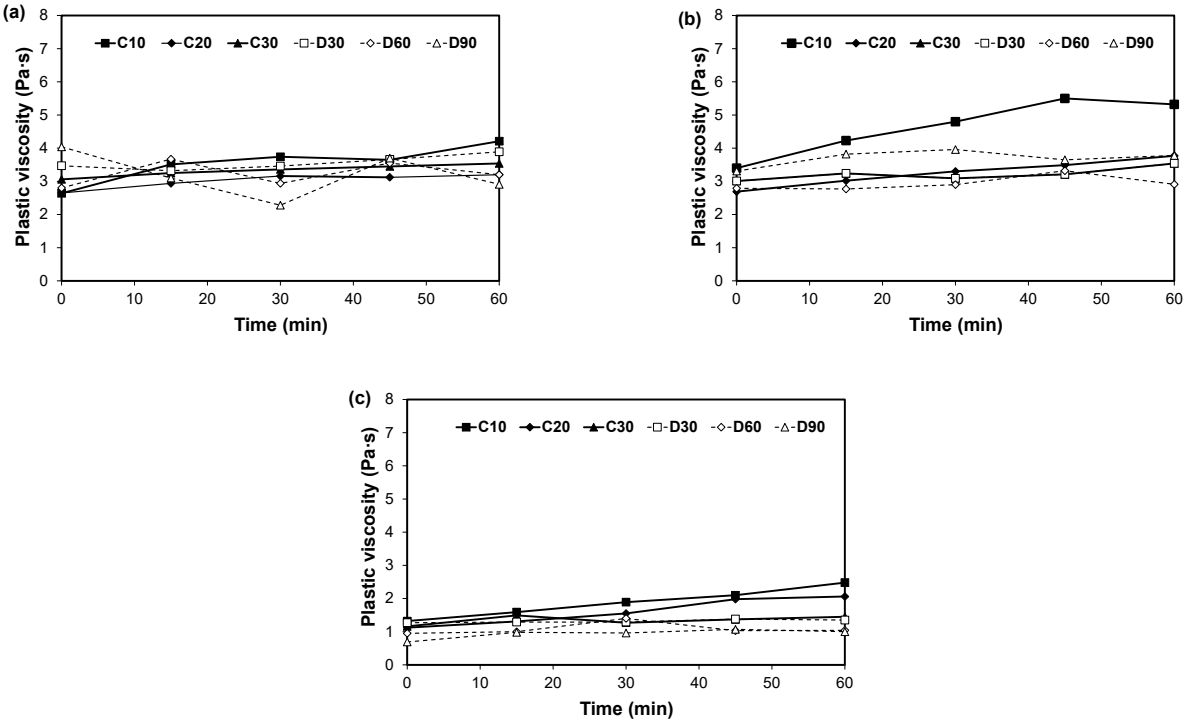

Fig. 4.20: Plastic viscosity against time of AAS mixtures under different mixing protocols and activator dosages a) 6%, b) 8%, and c) 10%.

Extending the mixing time increased the dynamic yield stress and plastic viscosity of low activator mixtures while having a minor effect at higher activator dosages. For instance, increasing the continuous mixing time from 10 to 30 minutes increased the dynamic yield stress and plastic viscosity by 24.86% and 13.73% for the 6% activator, respectively. Conversely, for the 10% activator, the changes were 0.74% and 0.14% for dynamic yield stress and plastic viscosity, respectively. Such minor changes at high activator can be attributed to the rapid structural build-up during the initial 10 min mixing. In mixtures activated with a 10% activator dosage under

mixing protocols C10 and D60, the microstructure was nearly identical. Conversely, for mixtures activated with a 6% activator dosage, the microstructure was denser with the D60 mixing protocol compared to C10 as shown in **Fig. 4.21**. Hence, extending the mixing time did not induce a significant development in the structure. This agrees with previous findings [51,167]. Besides, the undissolved silicate species at high activator dosages increased the solid fraction, resulting in more flocculation as the reaction proceeded [96,170]. Hence, a higher external shear (i.e. yield stress) is required to break down the interparticle linkages and initiate the flow. It should be mentioned that there was a fluctuation in the measured yield stress over the investigated period for all mixtures (**Fig. 4.19**). Generally, the drop in the yield stress can be attributed to the breakage of the interparticle flocs by the applied shear forces, while the increase is ascribed to the progress in the hydration reaction [159].

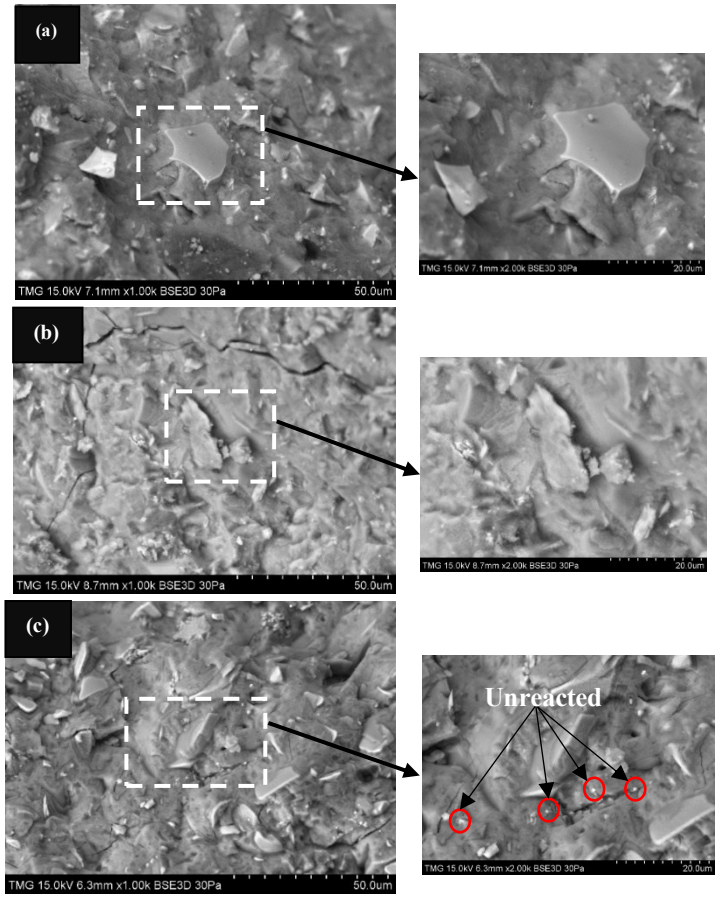

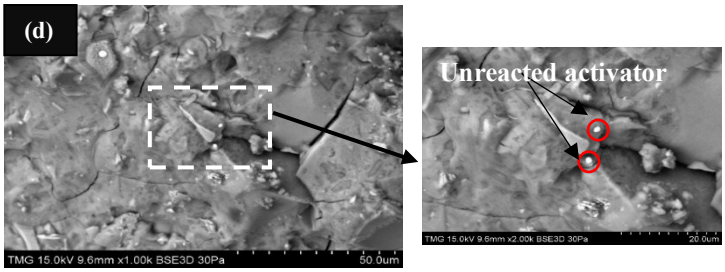

Fig. 4.21: SEM micrograph results of AAS mixtures activated by different dosages and mixed for various durations at 28 days age a) C10, b) D90 of mixtures activated by 6%, c) C10, and d) D90 of mixtures activated by 10%.

Continuous and discrete mixing had varying effects on the dynamic yield and plastic viscosity for mixtures exposed to protocols with similar length (i.e. C30 and D30) and/or mixing duration (i.e. C20 and D30). For protocols with the same length (i.e. 30 minutes), C30 exhibited higher yield stress and plastic viscosity at a low activator dosage than D30. Conversely, at a high activator dosage, the trend was reversed. This agrees with the initial flow results, as reported earlier. For instance, the dynamic yield stress and the plastic viscosity decreased by 28.83% and 21.56% for the 6% activator. Conversely, an increase in dynamic yield stress and the plastic viscosity of 14.45% and 46.42% were reported for mixtures with 10% activator, respectively.

For protocols with the same mixing duration (i.e. C20 and D30), the effects of changing the mixing from continuous to discrete on the dynamic yield stress and plastic viscosity varied based on the activator dosage. At a low activator dosage, reductions in dynamic yield stress and plastic viscosity values were observed, while the opposite trend was reported at higher dosages. For instance, for D30, the reduction in the dynamic stress and plastic viscosity values were 19 % and 9.43% compared to C20 for mixtures activated by 6%. Conversely, mixtures activated by 10% increased the dynamic yield stress and plastic viscosity by 60% and 13.39%, respectively. This can be attributed to the compensation effects between relaxation and remixing, as explained earlier (**Fig. 4.12)**. At high dosage, the relaxation boosts hydration product formation, increasing the formed links and, consequently, the yield stress increased. At a low activator, the remixing dominates as it increases link breakage and frees the movement of the material, leading to a lower yield stress.

Extending the discrete mixing time had varying effects on dynamic yield stress and plastic viscosity. At low activator dosages, comparing D30 and D90 mixing protocols, dynamic yield stress and plastic viscosity exhibited opposite trends: dynamic yield stress decreased while plastic viscosity increased. In high activator mixtures, dynamic yield stress and plastic viscosity decreased over the investigated period. For example, dynamic yield stress decreased by 51.05%, and plastic

viscosity increased by 40.6% for an activator dosage of 6% as the mixing protocol changed from D30 to D90. For 10% activator mixtures, dynamic yield stress decreased by 27.74%, and plastic viscosity decreased by 45.60%. This may be attributed to the many links formed between hydration products during cumulative relaxation time (i.e., 30 mins in D90), which were partially broken by remixing in the case of high activator mixtures. This agrees with a previous study on yield stress [42], reporting an increase in the solid volume fraction in the system as activator dosage increased and fixed water was used. This was attributed to the negative silicate charges that repel each other at low activator dosage, allowing better flow. On the contrary, at higher activator dosages, the high alkalinity accelerated the dissolution of slag particles, releasing double-charged ions, which will bridge particles, creating attractive forces responsible for agglomeration and thickening the material [160]. For plastic viscosity, mixtures with high activator showed low values, ascribed to the undissolved activator, inducing a ball-bearing effect that dispersed slag particles [159].

It can be concluded that AAS mixtures with various activators and under different mixing protocols had different dynamic yield stress and plastic viscosity. The increase in plastic viscosity will be generally related to the interparticle bridges formed by the early reaction products growing onto the slag particles. However, extending the mixing time reduces the plastic viscosity increase rate over the investigated period, as the formation rate of a similar number of flocs will be lower [167].

4.4.2. Harden properties

4.4.2.1. Compressive strength

Fig. 4.22 shows compressive strength results for AAS mixtures activated by various activator dosages under different mixing protocols. Generally, the strength increased with time regardless of activator dosages and applied mixing protocols. The higher the activator dosage, the higher the early strength gain (i.e. up to 7 days) due to the high dissolution rate of slag, which accelerates the hydration product formation [96]. For instance, in mixtures with activators 6% and 10%, the increase in strength from 7 to 28 days was 33.18% and 17.96% for C10 and 25.92% and 15.315% for D30, respectively.

Extending the continuous mixing time did not show a significant change in strength at early (i.e. 3 and 7 days) and later ages (i.e. 28 days). For instance, the change in strength when mixing time extended from 10 mins to 30 mins was around 0.8 MPa and 0.6 MPa with activators 6% and 10% for 3 and 7 days and 0.65 MPa and 0.3 MPa for 28 days. Discrete mixing showed a similar trend

in strength. The change in strength when mixing time extended from 30 mins (D30) to 90 mins (D90) was 0.25 MPa and 0.7 MPa with activators 6% and 10% for 3 and 7 days and 0.45 MPa and 0.5 MPa for 28 days.

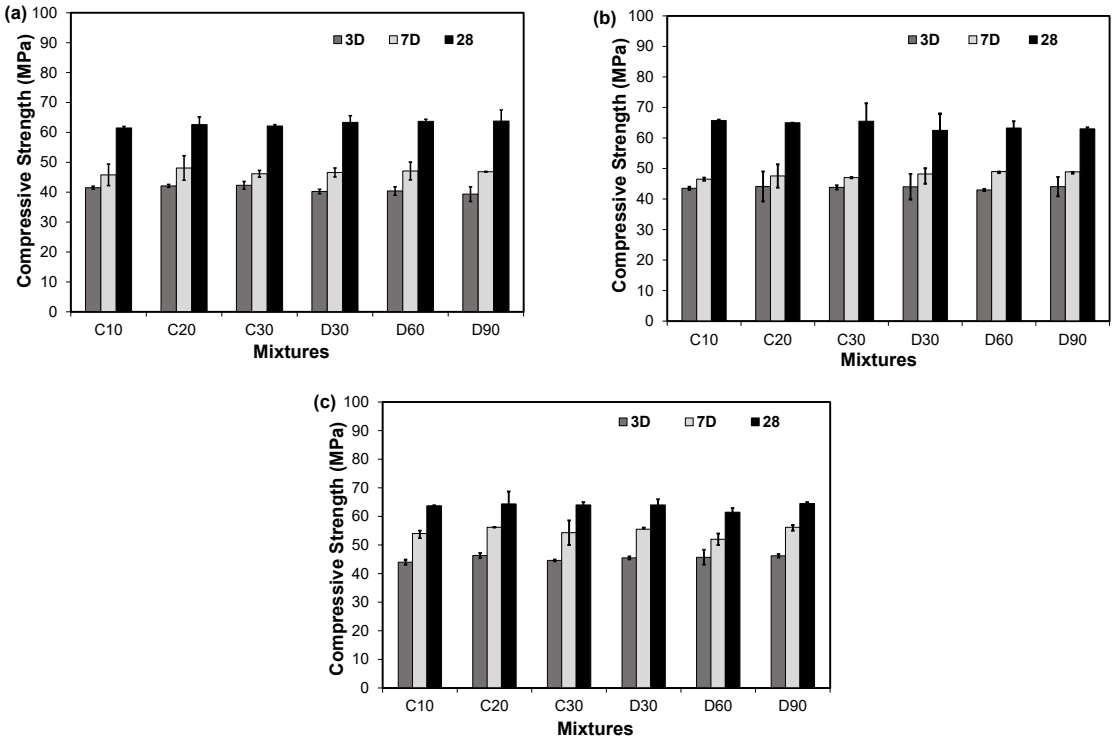

Fig. 4.22: Compressive strength results for AAS mixtures prepared by different mixing protocols and activator dosages at ages 3, 7, and 28 days a) 6%, b) 8%, and c) 10%.

Compressive strength results highlighted the minimal impact of various mixing protocols on early and late strength due to the similarity in the formed hydration products. XRD results showed the same crystalline phases (nature of the reaction products and amounts) for AAS activated by low and high dosages of activators under various mixing protocols (**Fig. 4.23**). For instance, the predominant crystalline phase presented is a crystalline C-A-S-H associated with a peak near 2θ = 29.5°. Additionally, other phases of C-A-S-H were detected around 32.1°and 50.1°. The second product is hydrotalcite detected at 2θ around 11.6°, 23.4° and 34.8°. The third product, quartz (SiO_2), was detected at 2θ around 29.4°. Akermanite was detected at around 2θ around 33.38° [96]. Additionally, these results agreed with the TGA/DTG profiles, which exhibited the same three main peaks at 60, 350, and 750 ℃ regardless of the mixing protocol (**Fig. 4.24**). The initial weight loss (spot 1), up to 60 °C, was due to the C-(A)-S-H gel formed in the AAS samples which is higher at an activator dosage of 10% compared to activator dosage of 6% [171]. A noticeable peak

was observed at a temperature of 350 °C (spot 2), signifying the dehydration of hydrotalcite [14,172]. Moreover, the third peak at about 750 °C (spot 3) was due to calcium carbonate ($CaCO_3$) decomposition. Mixtures activated by 6% presented the fourth peak at temperature 500 (spot 4), signifying the decomposition of either CaO or $Ca(OH)_2$ [173]. The slight increase in the intensity of the hydrotalcite endothermic peak for low activator mixtures with increasing mixing time indicates a higher formation of such phase due to the advance of the hydration reactions [174].

Similar to the outcomes from XRD analysis, the FTIR results indicate that variations in mixing protocols do not seem to influence the mineralogical composition of AAS pastes (**Fig. 4.25**). The spectra for all the pastes studied had absorption bands corresponding to the various phases of $CaCO_3$ signifying the presence of Ca in the samples. A small peak at 990 cm^{-1} occurred due to the symmetric stretching of the bonds Si-O-Si and Al-O-Si, representing the formation of the amorphous to semi-crystalline aluminosilicate materials [173,175]. Another peak occurred at 3082 cm^{-1}, representing the C–H stretching. Generally, increasing mixing time not only lengthens setting times and improves rheological properties but also slightly enhances compressive strength without affecting the nature of the reaction products.

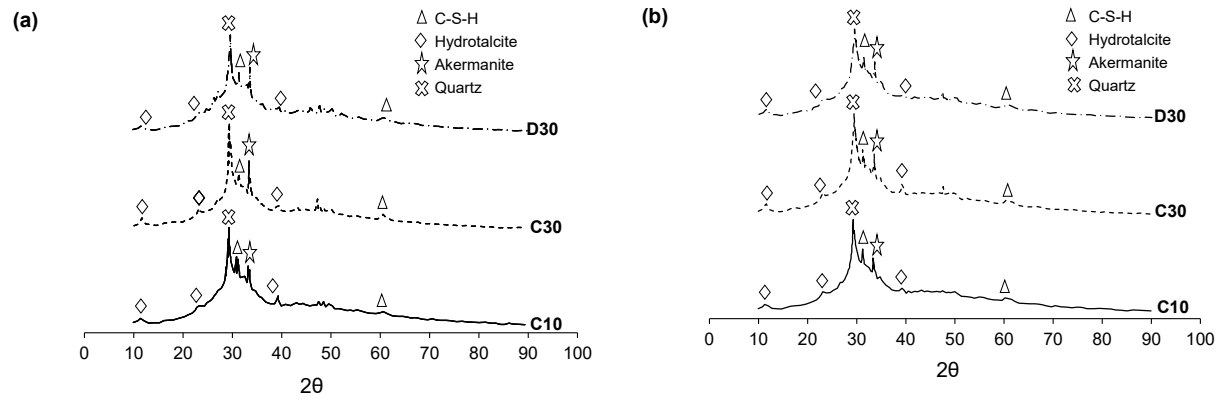

Fig. 4.23: XRD patterns of AAS mixtures under different mixing protocols and activators a) 6%, and b) 10%.

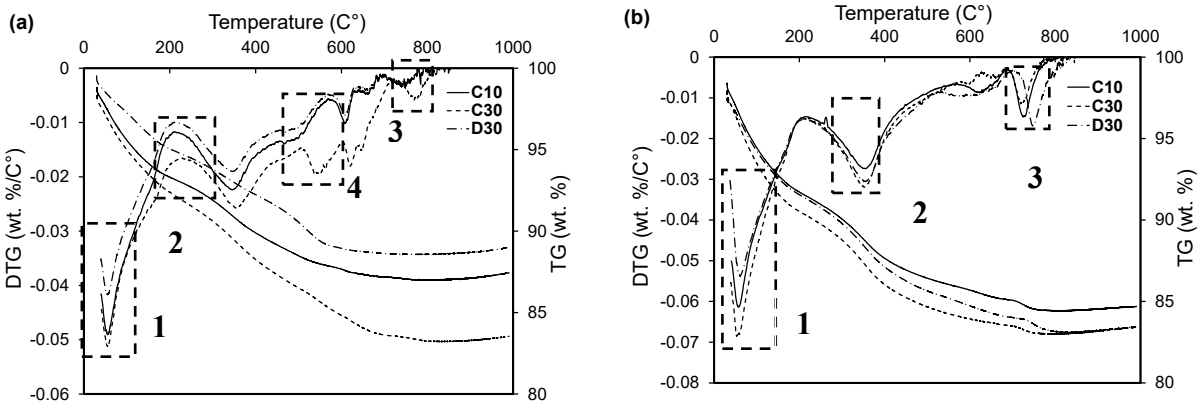

Fig. 4.24: TGA/DTG data of AAS mixtures at 3 days age under different mixing protocols and activators a) 6%, and b) 10%.

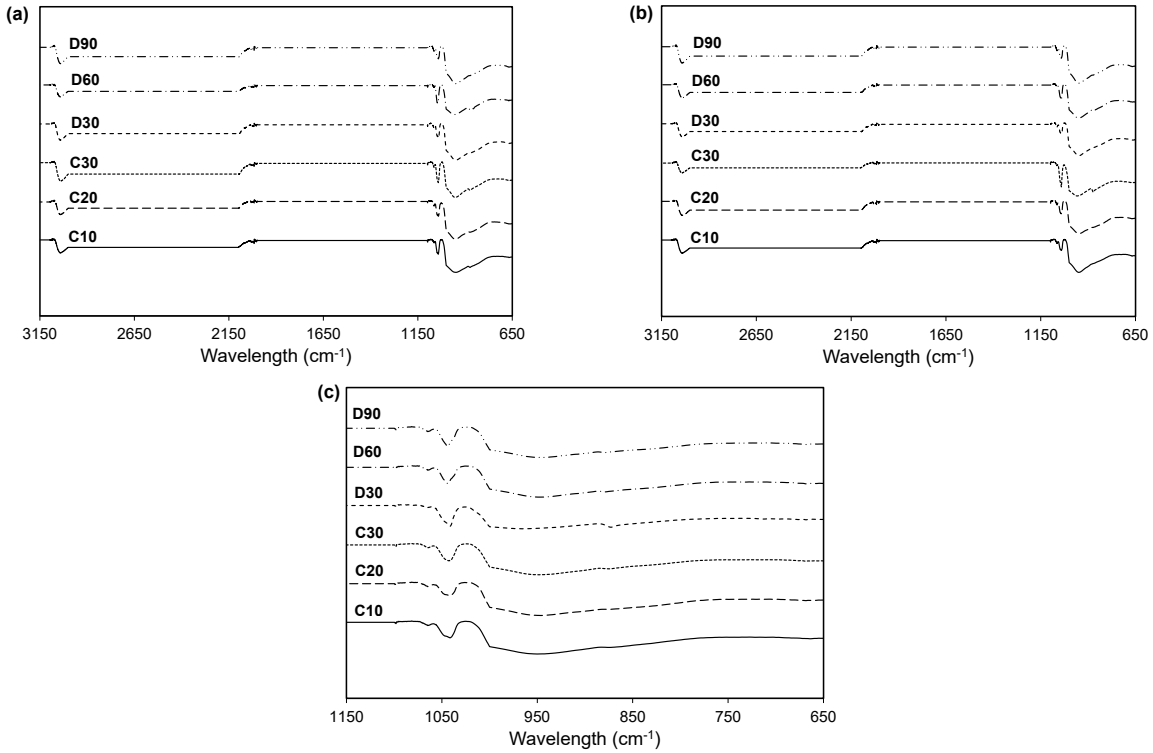

Fig. 4.25: FTIR spectra of AAS pastes under different mixing protocols and activators a) 6%, b) 8%, and c) 10%.

4.4.2.2. Drying shrinkage

Shrinkage is a crucial factor influencing the long-term durability and performance of concrete structures [176]. Drying shrinkage occurs due to the loss of internal water to the external environment through evaporation [177].

Fig. 4.26 shows the drying shrinkage behavior of AAS pastes. Generally, the drying shrinkage increased rapidly within the first 20 days after demolding. For AAS pastes, around 60% of the 30-day drying shrinkage was reached within 8 days. The increasing rate of drying shrinkage has considerably slowed by increasing activator dosage from 6% to 10%. This is attributed to the high activation degree for slag particles (differences in microstructure) resulting in a denser paste with lower porosity.

Lower drying shrinkage occurred because of the higher quantities of formed calcium silicate hydrate [178]. Since calcium silicate hydrate gel characteristics have a critical influence on the magnitude of drying shrinkage for OPC. Conversely, incorporating alkali cations like sodium into the C-A-S-H gel disrupts its molecular stacking, weakening interlayer interactions. This instability leads to greater collapse and redistribution during drying, causing higher shrinkage compared to the C-S-H gel in OPC systems [179]. Additionally, drying shrinkage under various mixing regimes depends on the loss of water from the mesopores and the size of the macropores which determines the easiness of evaporation of water from the mesopores [180,181].

For continuous mixing regimes, extending the mixing time from 10 mins to 30 mins decreased the drying shrinkage regardless of the activator dosage. This indicates that less water was available for evaporation due to higher water consumption in the reaction and breaking of formed C-A-S-H by continuous mixing. For example, the drying shrinkage decreased by 25.10%, 10.00%, and 5.32% from mixtures activated by 6%, 8%, and 10%, respectively. Because extending mixing time boosts water consumption and the amount of formed hydration products. Hence, the free water will be lower at a high activator level, and the hydration product formed will be lower than at a low activator level, resulting in a lower drying shrinkage [160].

Applying the same mixing duration while varying the mixing type from continuous to discrete affected the drying shrinkage. For instance, for 6% and 8% activated AAS, the drying shrinkage for 30 mins of continuous mixing was 10.98% and 32.92% lower than that for 20 mins of discrete mixing (i.e. total of 20 mins of mixing with a rest period of 10 mins), respectively. In contrast with low activator mixtures, at activator dosages of 10%, the drying shrinkage increased by 5.70 % for 30 mins of continuous mixing than for 20 mins of discrete mixing. This may be attributed to the breakup of formed hydration products through continuous mixing.

On the other hand, for discrete mixing regimes, results showed that activator dosage will be the dominating factor for drying shrinkage. For instance, comparing tripling the mixing time from 30

min (D30) to 90 min (D90) mixing regimes, for mixtures with activator dosages of 6% and 10%, the drying shrinkage increased by 39.13% and 17.71%, respectively. Conversely, the drying shrinkage decreased by 41.22% for mixtures with activator dosages of 8%.

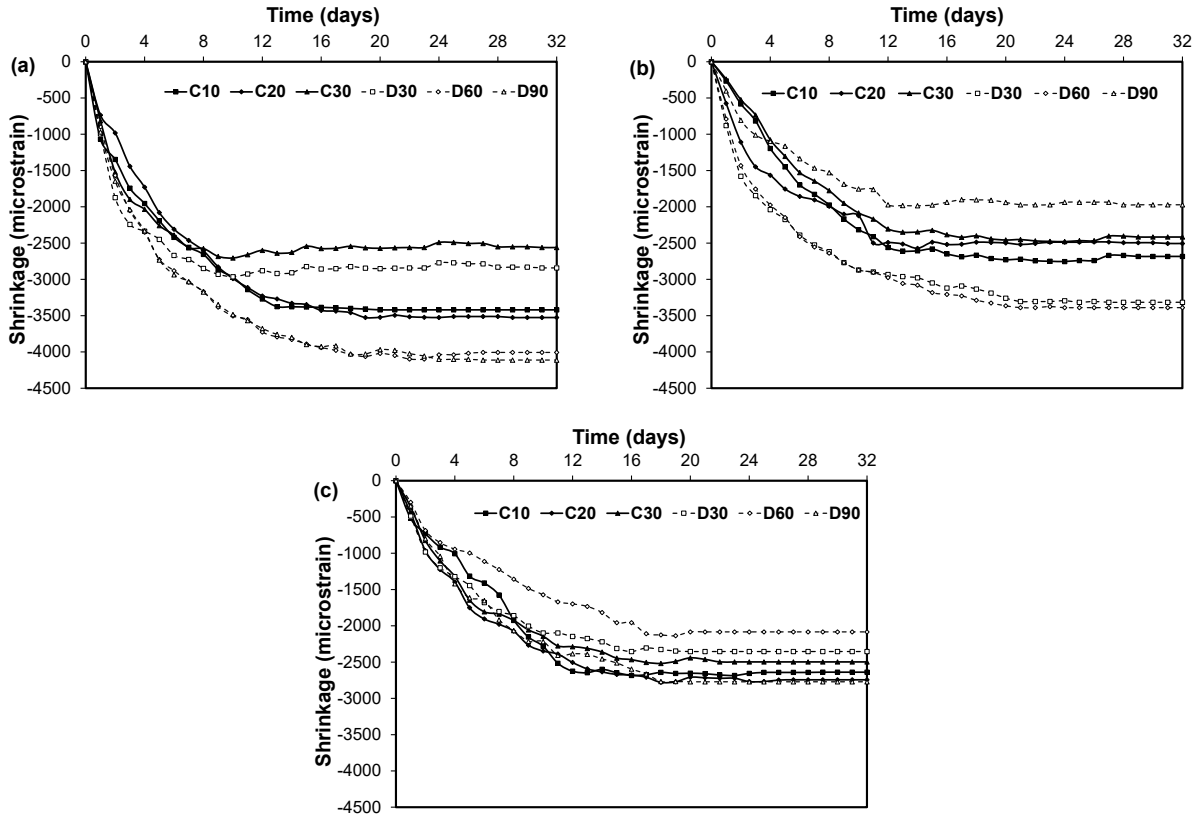

Fig. 4.26: Drying shrinkage of AAS pastes under different mixing regimes and activator dosages a) 6%, b) 8%, and c) 10%.

4.4.3. Statistical analysis

Fig. 4.27 illustrates the correlation matrix for various numerical factors (i.e., the relationship between applied variables and results of experimental tests). The correlation matrix was calculated using Python code to determine the Pearson correlation coefficient. Additionally, an analysis of variance (ANOVA) is applied to assess the P-value and F-value for the categorical factor (i.e. mixing type). The Pearson correlation coefficient, ranging from -1 to 1, indicates the strength and direction of linear relationships between numerical factors. A value of 1 signifies a perfect positive linear relationship, -1 indicates a perfect negative linear relationship, and 0 suggests no linear relationship. It's important to note that Pearson correlation assumes normal distribution and a linear relationship between variables [182].

In the correlation analysis, assuming correlation strength based on the value of Pearson correlation is categorized as follows: 0 to 0.4 indicates no or weak correlation, 0.4 to 0.6 indicates some correlation, 0.6 to 0.8 represents strong correlation, and 0.8 to 1 signifies a very strong correlation. The number at the intersection box between the horizontal and vertical factors represents the strength of the correlation. For example, the intersection box between activator dosage (at the horizontal axis) with the 3-day compressive strength (at the vertical axis) has a value of 0.67, which is within the strong correlation category range (i.e. 0.6 to 0.8). On the other hand, following the same procedure, mixing time demonstrates a weak correlation with all properties except the initial setting time.

ANOVA, conducted at a chosen significance level (commonly 0.05), involves assessing the P and F-values. The P-value represents the probability of obtaining a test statistic as extreme or more extreme than observed, assuming the null hypothesis is true. If the P-value is below the chosen significance level, the null hypothesis is rejected, indicating a statistically significant difference between group means at the 5% level. The F-value in ANOVA is the variance ratio between groups to variance within groups. A large F-value suggests a significant difference among group means. The P-value and F-value work together in hypothesis testing, where the P-value helps determine the significance of the F-value and assesses overall variability in the data [71]. The ANOVA analyses reveal that the behavior of AAS mixtures is not significantly influenced by the applied mixing type (i.e. continuous and discrete mixing) except for the initial setting time as depicted in **Table 4.2**.

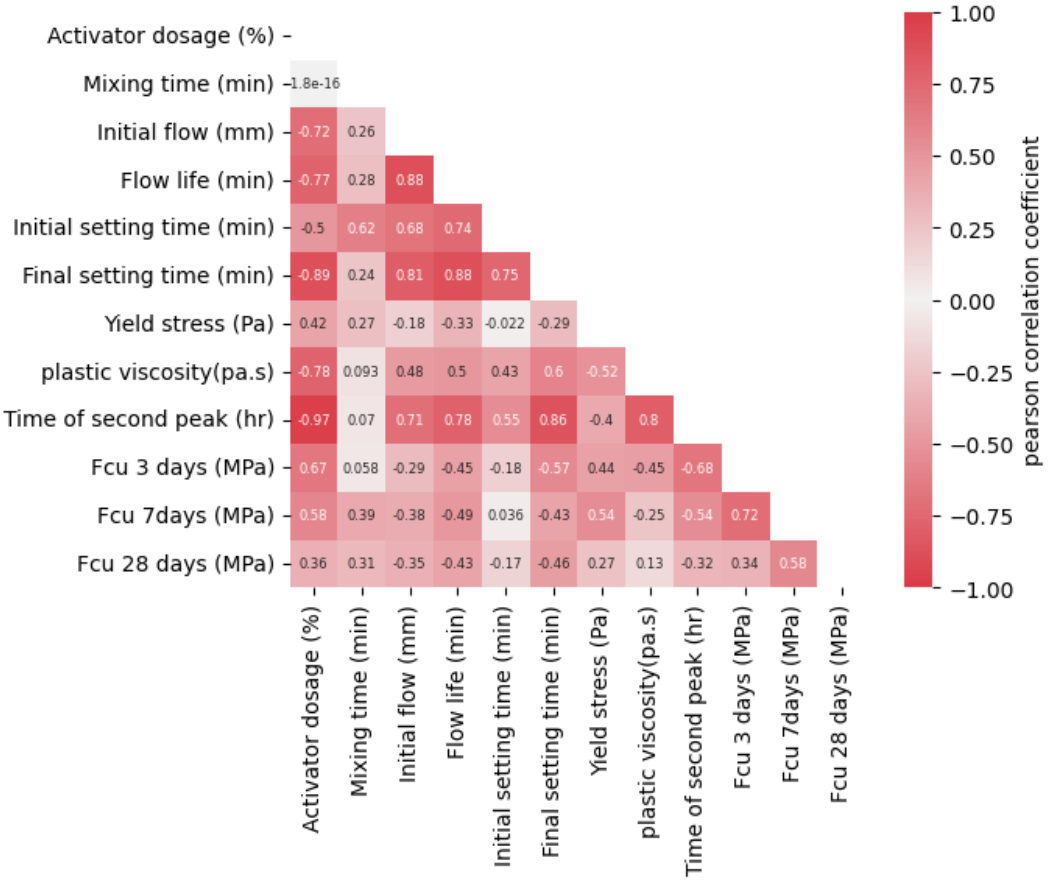

Fig. 4.27: Correlation matrix for various factors.

Table 4.2: P and F values of ANOVA for mixing type.

	Mixing Type	
Variables	F-value	P- value
Initial flow (mm)	1.8981	0.1418
Flow life (min)	1.4186	0.2349
Initial setting time (min)	19.1600	0.0001
Final setting time (min)	1.2220	0.1503
Yield stress (Pa)	2.1980	0.0545
Plastic viscosity (pa.s)	0.0023	1.000
Time of second peak (hr)	0.2033	0.5221
Fcu 3 days (MPa)	0.1627	0.9663
Fcu 7days (MPa)	3.6848	0.1035
Fcu 28 days (MPa)	0.1107	0.8328

4.5. Conclusions

This study provides a more fundamental understanding of the effect of mixing protocol (i.e. mixing time and relaxation duration) on AAS flow retention. The activator dosage controls the rates of slag particle dissolution and various hydration product formations, directly impacting the rheological properties of AAS mixtures. Besides, mixing facilitates a higher dissolution rate, while remixing impedes the build-up of the AAS mixture structure. Hence, the following conclusions can be drawn from the results as follows:

- The main effect of extending mixing time (either continuous or discrete) is the breakage of C-A-S-H gel links, reducing the mixtures' dynamic yield stress and plastic viscosity.
- Results highlight the minimal impact of various mixing protocols on early and late strength due to the similarity in the formed hydration products.
- The correlation matrix and ANOVA analysis emphasized the dominant effect of activator dosage on all evaluated properties.
- The potential maximum mixing time for ready-mix AAS (i.e. 60 min) should be shorter than that for OPC (i.e. 90 min according to ASTM C94).
- In general, various mixing protocols significantly influenced the properties of mixtures with low activator dosages, particularly in terms of flow retention and setting time (a marginal enhancement was observed). However, these protocols had little to no effect on the properties of mixtures with high activator dosages. This highlights that the dominant factor governing the properties of the mixes is the activator dosage, rather than the mixing protocol.

Chapter 5: Single and multi-response optimization of retarded admixture on alkali activated slag rheological behavior by the Taguchi method

Based on the investigation conducted in Chapter 3, which examined the adding sequences of the main ingredients, the optimal sequence was identified as the dry mixing of the activator and precursor (dry sequence) before adding water. This sequence achieved reasonable flowability and setting time. In Chapter 4, the effect of various mixing protocols on the properties of AAS systems with different activator dosages was explored. The findings revealed that extending the mixing time and altering the mixing type had a marginal effect on AAS activated with high dosages. However, at low dosages, slight enhancements were observed, particularly in flow retention and setting time. These results suggest that mixing protocols can be a viable option for improving the rheological properties of AAS with low activator dosages. Nonetheless, activator dosage remained the dominant factor influencing the properties. Building on these findings, the current chapter adopts the optimal mixing sequence from Chapter 3 to investigate the effects of varying retarder types and dosages, along with changes in activator proportions and w/s ratios. This study is particularly significant as it marks the first investigation of AAS systems activated by meta-silicate, where no standard recommendations for activator dosage, retarder dosage, or w/s ratios exist. Given that mixing time and type were not governing factors, a mixing time of 4 minutes was adopted for this chapter. A single and multi-optimization model was developed to determine the required rheological properties, providing a comprehensive assessment of the efficiency of various retarders. The study identifies the most effective retarder for achieving optimal properties, contributing valuable insights to the development of AAS systems.

5.1. Introduction

Cement production accounts for approximately 8% of global carbon emissions [1,2,86] and consumes about 40% of global energy [4]. Alternative cementitious materials are being explored to mitigate these impacts [183]. AAMs have emerged as promising alternatives to traditional OPC-

based systems [184]. AAMs are created by activating high or low-calcium aluminosilicate precursors (such as slag, fly ash, and red mud) with an alkaline activator [185].

AAMs are categorized as "two-part" or "one-part" based on the activator type. Two-part AAMs utilize a high-alkalinity liquid activator, while one-part AAMs use a powder activator [23,40]. The safety and ease of handling powder activators have made one-part AAMs more prevalent in construction applications [41,42,97]. AAS offers excellent mechanical strength and chemical resistance among various AAMs [186–188]. However, AAS faces challenges such as rapid hardening and short setting times (around 1 hour or less for the initial setting and 3 hours or less for the final setting). The setting durations vary depending on the type and dosage of activators and admixtures used, which poses limitations to its broader application [47,48].

Concrete admixtures (i.e., superplasticizers, retarders, and air-entraining agents) have improved OPC's workability, rheology, and mechanical properties. However, their effects differ in such extreme alkaline conditions of AAMs compared to OPC [59]. Extensive research has been conducted on the impact of various superplasticizers on one-part AAMs. Contradictory data reported in the literature can be attributed to changes in the interactions between admixtures, different types of precursors, varying activator types and dosages, and the water-to-binder ratio in the tested mixtures. For instance, Luukkonen et al. [56] found that lignosulphonate, melamine, and naphthalene superplasticizers are more effective than polyacrylate and polycarboxylate in one-part AAS with sodium hydroxide activators. Conversely, Oderji et al. [38] found that lignosulphonate admixtures adversely affected the workability and mechanical properties of one-part fly ash/slag-based AAMs activated by meta-silicate.

On the other hand, research on retarders is more limited. Studies have focused on incorporating various materials (i.e. metakaolin, bentonite, natural pozzolan, red mud, and other mineral materials) to extend setting times of one-part AAMs by reducing high calcium precursors (partial or full replacement of slag by other low calcium materials) [64]. Another approach involves using inhibitors of calcium carbonate precipitation, such as anti-scaling agents (i.e. phosphonate molecule HEDP (tetrasodium 1-hydroxy ethylidene) [65].

For example, Wang et al. [189] used anhydrous citric acid to prolong the setting time in slag-based AAM by evaluating the heat of hydration of different mixtures. Furthermore, Oderji et al. [38] improved paste workability by adding 4–8 wt% borax (by binder weight) to FA/slag-based AAM,

which demonstrated a retarding effect on the initial setting time. The addition of 8% borax delayed the initial setting time by approximately 215% compared to the control mixture.

While Zheng et al. [190] utilized partially carbonized CaO alkali activators with a $CaCO_3$ product layer to enhance CO_2 diffusion resistance and reduce polymerization rates. Additionally, Wang et al. [191] demonstrated that calcium hydrogen phosphate, used as a retarder at a 7% replacement rate, improved the performance of FA/slag-based AAMs by extending the initial and final setting times to 150 minutes and 230 minutes, respectively.

Based on the abovementioned review, Identifying the most effective admixtures for specific conditions remains a key research focus [64], with recommendations for studying the impact of retarders such as maleic acid and nano zinc oxide on the flowability of one-part sodium silicate-activated AAS cement [167].

The influence of primary parameters, such as the w/s ratio, activator dosage (AD), retarder type (RT), and dosage (RD), and their interactions on the properties of one-part AAS is still not well understood. Utilizing the statistical Taguchi method could significantly streamline the process of identifying optimal retarder types and dosages to enhance rheological properties [192]. This method has proven effective in various sectors, including engineering, services, and manufacturing industries [193], and can reduce the number of combinations required for optimization [194].

Hence, this research aims to determine the optimal mixture parameters for one-part AAS mixtures. Through conducting two phases: first, single-objective optimization using the Taguchi method, followed by multi-objective optimization using Taguchi in combination with Grey Relational Analysis (GRA) and the Technique for Order of Preference by Similarity to Ideal Solution (TOPSIS). In the validation phase, additional experiments were performed on the optimized mixtures to assess their flowability, rheological properties (yield stress and plastic viscosity), and compressive strength. Furthermore, microstructure analyses using XRD, TGA, and FTIR spectroscopy techniques were conducted to examine the reaction products formed. The rheological properties of AAS play a significant role in influencing life cycle assessment (LCA) analysis. Hence, the optimized mixtures' LCA was performed using the CML method (CML, 2016). Various environmental impact indicators were evaluated, including Acidification (AP), Climate Change (CH), Freshwater Ecotoxicity (FT), Marine Ecotoxicity (MT), Terrestrial Ecotoxicity (TT), Non-renewable Energy Resources (NRE), Eutrophication (EP), Human Toxicity (HT), Resource Depletion (RD), Ozone Depletion (ODP), and Photochemical Oxidant Formation (POF). These

environmental impacts were assessed using the openLCA program, based on the Ecoinvent v3.10 database. The methodology involved the following steps: environmental impact indicator values for each ingredient in the mixture (slag, silicate activator, and retarder) were extracted from the Ecoinvent database. Then, for each ingredient in a single mixture, its proportion in the mixture was multiplied by the corresponding environmental impact value extracted from the database. Finally, the individual contributions of all ingredients were summed to determine the total environmental impact of the mixture.

5.2. Research significant

Extensive research has evaluated the effects of superplasticizers and retarders on two-part AAMs using slag or slag combined with fly ash. However, limited research exists on the impact of retarders on one-part binary AAMs (slag-fly ash). Critical parameters such as the w/s ratio, AD, RT, and RD, and their interactions on AAS, are still unknown. This study is significant as it provides the first-time data on optimizing the mixing proportions of one-part AAS mixtures to achieve superior rheological properties while ensuring sufficient compressive strength when activated by anhydrous meta-silicate with various retarders. Additionally, it provides a comparative LCA study, offering valuable insights into the environmental impact of these optimized mixtures.

5.3. Experimental Work

5.3.1. Materials

GGBS conformed to ASTM C989 and was used as the aluminosilicate precursor for synthesizing alkali-activated binders. The GGBS has a specific gravity of 2920 kg/m³, Blaine fineness of 515 m²/kg, an average particle diameter of around 14.5 μm, and a basicity coefficient of 1.06. Anhydrous sodium meta-silicate (Na_2SiO_3) was used as the powdered activator. Various retarders, including nano zinc oxide (ZnO) (N), maleic acid (M), borax (sodium tetraborate decahydrate) (B), and calcium carbonate ($CaCO_3$) (C), were also utilized. The chemical composition of all materials, determined using X-ray fluorescence (XRF), is presented in **Table 5.1**. The XRD spectra of the activator and retarders (**Fig. 5.1**) indicated the presence of amorphous phases alongside minerals such as quartz, mullite, calcite, zincite, and hematite, representing the crystalline phases for the used activator and various retarders [185,195]. In contrast, the XRD spectra for GGBS revealed that most minerals were in an amorphous phase, except for two small peaks attributed to

calcite and akermanite [195]. **Fig. 5.2** shows optical microscope images of the materials, illustrating the differences in particle size and shape.

Table 5.1: Chemical Composition of precursor, activator, and various retarders used.

Chemical oxides (% by mass)	Al_2O_3	SiO_2	SO_3	K_2O	CaO	TiO_2	MnO	Fe_2O_3
Slag	10.20	36.20	1.76	0.38	37.10	1.02	0.33	0.36
Meta-silicate	0.52	13.61	0.24	0.06	0.97	0.02	-	0.02
Maleic acid	0.80	3.45	0.28	0.02	1.43	0.05	0.01	0.01
Borax	0.58	2.41	0.20	0.02	0.96	0.03	-	0.01
Calcium carbonate	-	1.34	0.167	-	55.41	0.05	0.01	0.06
Nano zinc oxide	-	1.11	0.07	-	1.04	-	-	0.01

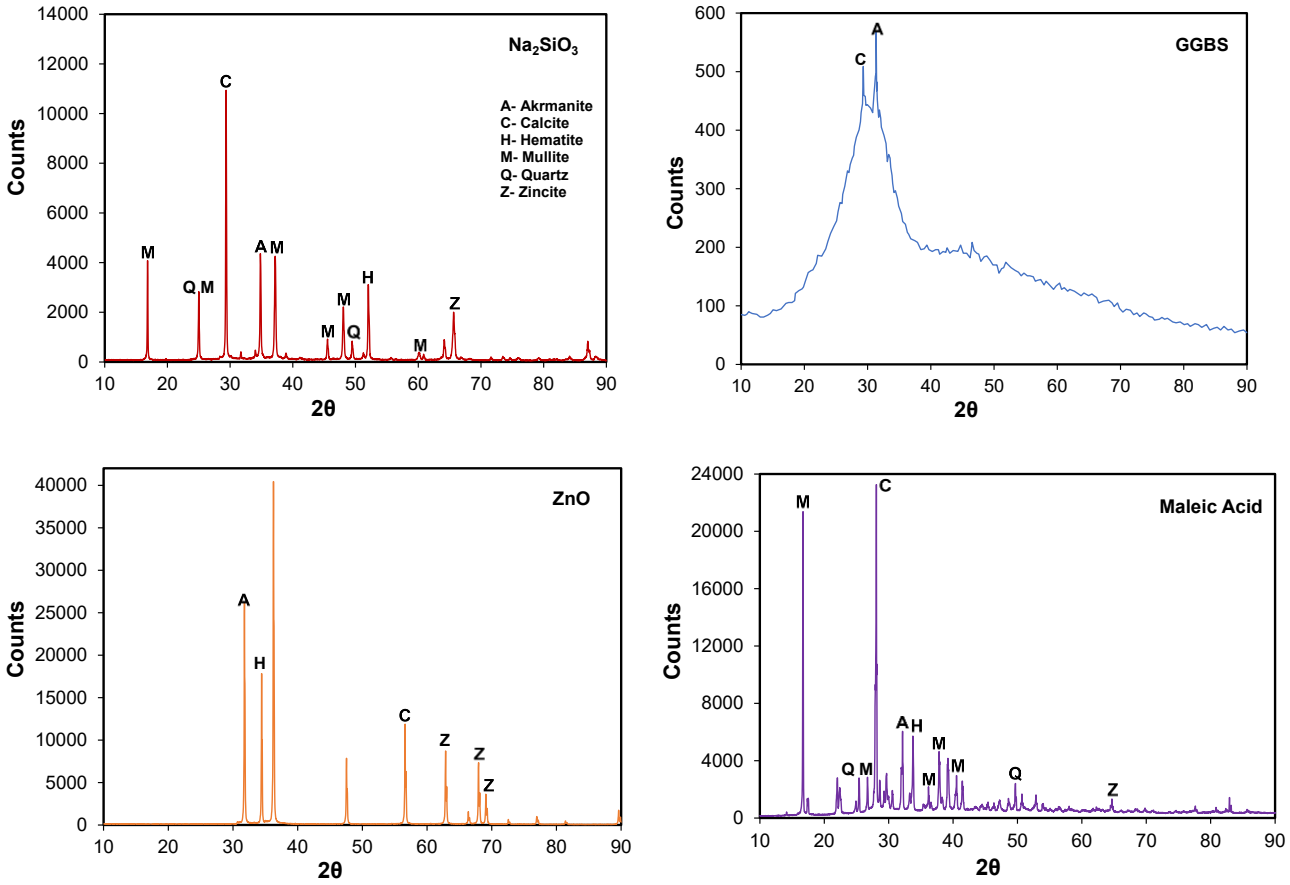

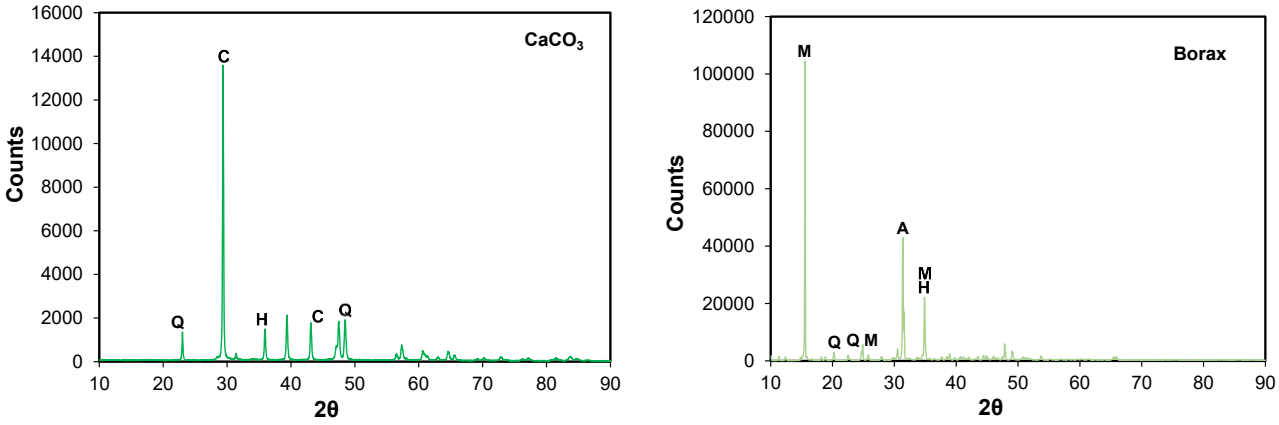

Fig. 5.1: XRD images of activator, precursor, and various retarders used.

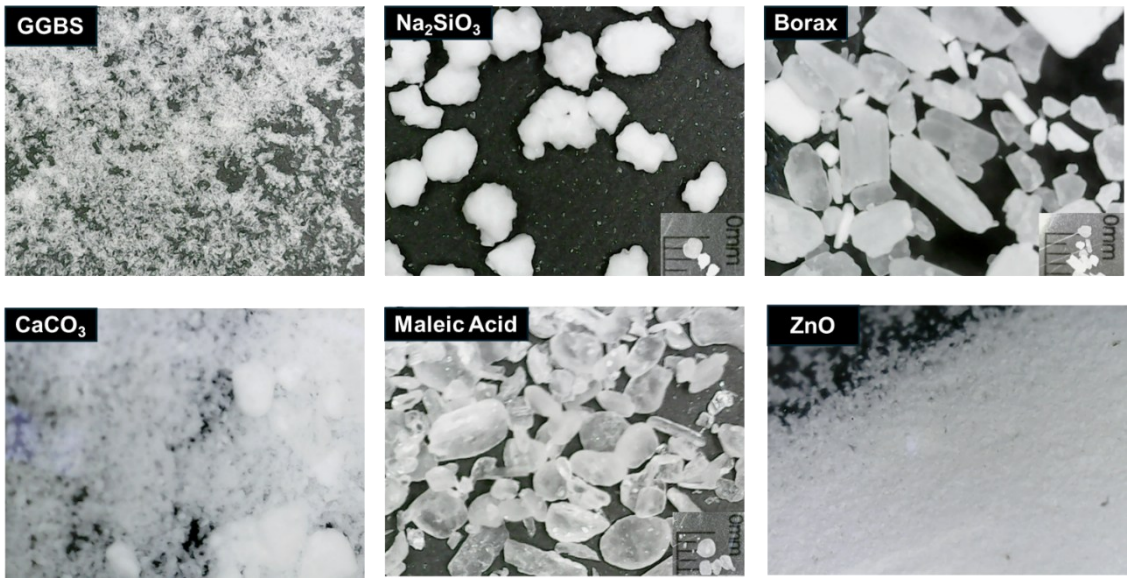

Fig. 5.2: Image of the precursor, activator, and various retarders used in the experiments by an optical microscope.

5.3.2. Framework for the Optimization Process

The developed framework will incorporate two optimization approaches: single-criteria and multi-criteria (**Fig. 5.3**). The single-criteria approach will identify the optimum mixture design for each criterion individually while highlighting the effects of the design factors on each criterion. This will be followed by implementing a multi-criteria approach considering multiple performance criteria. For instance, Taguchi's GRA was applied to all measured properties, and the TOPSIS method was employed on the selected four properties: flow diameter, yield stress, time of second peak (the end of dormant period), and compressive strength at 28 days.

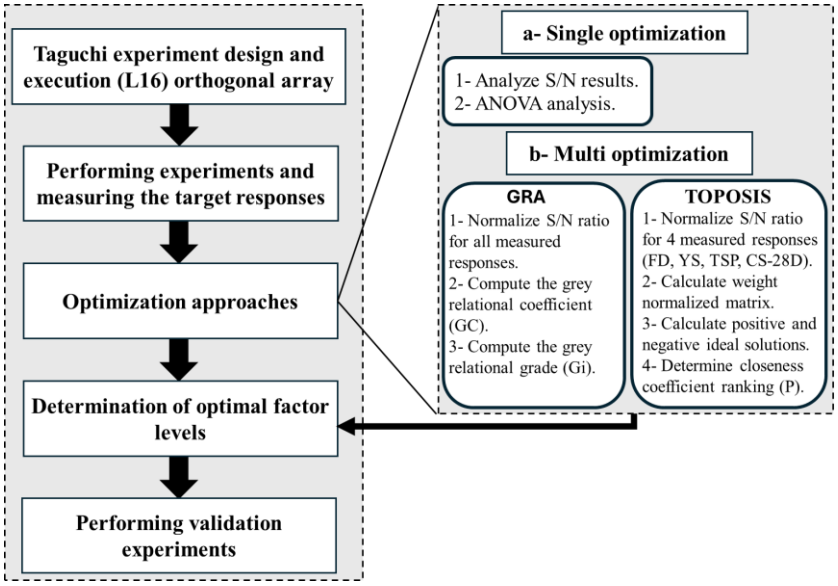

Fig. 5.3: Framework of the study.

5.3.3. Taguchi design of experiments

The Taguchi design of experiments, developed in the 1950s by Dr. Taguchi, is a fractional factorial approach that minimizes experimental runs by using the smallest necessary orthogonal array to optimize input parameters efficiently [168]. In this method, uncontrolled factors that introduce variability are called noise factors. Optimization occurs when the desired response exceeds the noise reduction factor, effectively minimizing the impact of noise on the target outcome. This is evaluated by using the signal-to-noise ratio (S/N) [168]. The primary aim of experimental design is to control and eliminate sources of error, thus increasing the S/N ratio to reduce variance from the target. There are three types of S/N ratio determination: “Larger is better”, “Smaller is better”, and “Nominal is better” as illustrated in **Eqs. 5.1 to 5.3** [196]: "larger-is-better" for maximizing responses, "smaller-is-better" for minimizing them, and "nominal-is-better," which focuses on achieving a specific target value with minimal deviation. A key advantage of Taguchi’s experiment design is its capacity to optimize target values based on calculated S/N ratios from the experimental result. Additionally, it minimizes the number of experimental runs by employing the smallest necessary orthogonal array, enabling efficient optimization of input parameters [168].

$$S/N_L = -10log_{10}\left(\frac{1}{n}\sum_{i=1}^{n}\frac{1}{Y_i^{\,2}}\right) \qquad (Larger\ is\ better) \qquad \text{Eq. 5.1}$$

$$S/N_S = -10log_{10}\left(\frac{1}{n}\sum_{i=1}^{n}Y_i^{\,2}\right) \qquad (Smaller\ is\ better) \qquad \text{Eq. 5.2}$$

$$S/N_N = -0log_{10}\left(\frac{1}{n}\sum_{i=1}^{n}(Y_i - Y_o)^2\right) \qquad (Nominal\ is\ better) \qquad \text{Eq. 5.3}$$

S/N is the signal-to-noise ratio, n is the number of experiments, Y_i is the response to be optimized, and Y_0 is the mean of responses.

5.3.4. Mix proportioning

AAS paste mixtures were designed using the Taguchi method for the experiment. Four key factors were identified to assess their influence on the performance of AAS mixtures: w/s ratio, AD, RT, and RD. The w/s ratio varied between 0.4 and 0.55 [174], while the AD ranged from 4% to 10%. Four types of retarders were used, with the RD varying from 0% to 1.5%. The four retarders used were N, M, B, and C, each delaying the hydration process through distinct mechanisms. The retarder (N) delaying mechanism may result from forming a Zn-phase that, in a highly alkaline medium, transforms into $Zn(OH)_2$. This acts as an isolated barrier between the unreacted GGBS and the alkaline activator, thereby delaying the depolymerization reactions [197,198]. Retarder (M) acts as a chelating agent, binding with calcium ions and delaying calcium silicate hydrate (C-S-H) gel formation [199]. Retarder (B) introduces borate ions that form complexes with calcium ions, inhibiting early C-S-H gel formation [200,201]. Retarder (C) functions as a filler and nucleation site for C-S-H (as a filler, calcium carbonate occupies space in the matrix, reducing the contact area between slag particles and the alkaline activator, thereby slowing slag dissolution. As nucleation sites, it promotes more dispersed and controlled growth of C-S-H gel) [202]. Four levels were selected for each factor based on values in alkali-activated mixtures [59,155,167] and preliminary trial mixtures, as shown in **Table 5.2**.

Table 5.2: Factors and levels for mixture proportioning of AAS mixtures.

Factors	level 1	level 2	level 3	level 4
1: w/s	0.40	0.45	0.50	0.55
2: AD	4%	6%	8%	10%
3: RT	B	M	N	C
4: RD	0.0%	0.5%	1.0%	1.5%

An L16 orthogonal array was employed to optimize the combinations of these factors, accommodating four variables, each at four levels, resulting in sixteen trials (M1–M16) for analysis [194,203]. Due to the large number of variables influencing the AAS mixture performance

[196]. The mixture design combinations are presented in **Table 5.3**. In this study, the sixteen orthogonal arrays reflected various combinations of the control factors, using the "Larger the Better" S/N ratio criterion to maximize flowability and compressive strength and the "Smaller the Better" S/N ratio criterion to minimize yield stress and plastic viscosity. The experimental results were analyzed using MINITAB, a commercial statistical software, and the outcomes from all sixteen mixtures were treated as responses. The appropriate S/N ratio formula was selected for further analysis based on the nature of the reaction.

Table 5.3: Factors and levels in mixture design for L16 orthogonal array.

Trial	w/s	AD	RT	RD
M 1	0.40	4	B	0.0
M 2	0.40	6	M	0.5
M 3	0.40	8	N	1.0
M 4	0.40	10	C	1.5
M 5	0.45	4	M	1.0
M 6	0.45	6	B	1.5
M 7	0.45	8	C	0.0
M 8	0.45	10	N	0.5
M 9	0.5	4	N	1.5
M 10	0.5	6	C	1.0
M 11	0.5	8	B	0.5
M 12	0.5	10	M	0.0
M 13	0.55	4	C	0.5
M 14	0.55	6	N	0.0
M 15	0.55	8	M	1.5
M 16	0.55	10	B	1.0

5.3.5. Multi-optimization approaches

The Taguchi method optimizes the levels of variables by analyzing the S/N ratios for each property individually. This helps determine the optimal level and primary influence of each variable on the property being studied. For multiple response variables, the Taguchi-GRA technique is preferred [204,205]. Additionally, the TOPSIS approach optimizes mixture proportions for multiple qualities, predicting the best mixture based on targeted criteria such as flowability and compressive strength.

In this study, both approaches were used: the GRA approach targeted all measured criteria (flow diameter, time of second peak, yield stress, plastic viscosity, and compressive strength at 3, 7, and 28 days), while the TOPSIS approach focused on four equally important responses (flow diameter, yield stress, time of second peak, and compressive strength at 28 days).

5.3.5.1. Grey Relational Analysis

This optimization process includes three major steps as follows [195,206]:

1- **Normalization:** generating grey relational values by normalizing the S/N ratios of individual responses within a range of 0 to 1 using **Eq. 5.4**.

$$Y_{ij} = \frac{X_{ij} - \min(X_{ij})}{\max(X_{ij}) - \min(X_{ij})} \quad \text{Eq. 5.4}$$

2- **Computing Grey Relational Coefficients (GC_{ij}):** GC_{ij} are computed using normalized data to represent the interaction between anticipated and actual data, as **Eq. 5.5** indicates.

$$Y_{ij} = \frac{\Delta_{min} + \chi\Delta_{max}}{\Delta_{0ij} + \chi\Delta_{max}} \quad \text{Eq. 5.5}$$

Δ_{0ij} = absolute difference between Y_{0j} and Y_{ij} where Y_{0j}= maximum value of normalized S-N ratios. χ represents the identification coefficient, $\chi \in (0,1)$, generally taken as 0.5. Δ_{min}, Δ_{max} = minimum and maximum values of Δ_{0ij}.

3- **Determining Grey Relational Grades:** Grey relational grades (r) are determined by averaging the grey relational coefficients for each response parameter using **Eq. 5.6**. This is calculated as follows:

$$r = \frac{1}{k}\sum_{i=1}^{k} w_i \times GC_{ij} \quad \text{Eq. 5.6}$$

Where k represents the number of responses, and W_i is the weight of each output. In this case, weights are assumed to be equally distributed among the seven responses, with each weight being 0.14.

5.3.5.2. TOPSIS Analysis

This integrated approach ensures a more comprehensive and effective optimization process [207]. TOPSIS for optimization and decision-making involves five major steps [168]:

1- Normalization: This step enables efficient comparison between different criteria. The decision matrix is normalized using **Eq. 5.7**, allowing for the inter-criteria comparison.

$$\overline{X}_{ij} = \frac{X_{ij}}{\sqrt{\sum_{i=1}^{n} X_{ij}^2}} \qquad \text{Eq. 5.7}$$

Where X_{ij} is the S/N ratio for a performance criterion (response), and $\overline{X}_{ij}$ denotes the normalized vector of the X_{ij} vector.

2- Weight Assignment: Performance criteria weights were assigned based on their significance. The most important criteria to the user target received the highest weights, while equally relevant criteria were given equal weights. **Eq. 5.8** was used to calculate the weighted normalized matrix (V_{ij}) as follows:

$$V_{ij} = \bar{X}_{ij} \times W_j \qquad \text{Eq. 5.8}$$

3- Determining Ideal Solutions: The positive (V_j^+) and negative (V_j^-) ideal solutions were identified by assigning them to the maximum and minimum values in the weighted normalized matrix.

4- Calculating Separation Measures (Euclidean distance from the ideal best and worst): Eqs. 5.9 and 5.10 were used to calculate the separation measures, S_i^+ and S_i^-, from the ideal solutions.

$$S_i^+ = \left[\sum_{j=1}^{m} \left(V_{ij} - V_j^+\right)^2\right]^{0.5} \qquad \text{Eq. 5.9}$$

$$S_i^- = \left[\sum_{j=1}^{m} \left(V_{ij} - V_j^-\right)^2\right]^{0.5} \qquad \text{Eq.5.10}$$

5- Calculating Closeness Coefficient: The ranking score or closeness coefficient (P_i) was calculated using **Eq. 5.11** to determine the ideal combination. The P_i values were entered as Taguchi responses for each trial (M1 to M16). The Taguchi method then analyzed these responses, calculating the S/N ratios using both the "Larger-is-better" and "Smaller-is-better" characteristics. The ideal mixture was identified as the level with the highest S/N ratio.

$$P_i = \frac{S_i^-}{S_i^+ + S_i^-} \qquad \text{Eq. 5.11}$$

5.3.6. Mixtures preparation and testing procedure

All powder ingredients including GGBS, Na_2SiO_3, and the retarder were dry mixed for 1 minute, followed by gradual water addition over another minute while mixing continued at a speed of 139 rpm for an additional 3 minutes (**Fig. 5.4**) [42]. All mixtures were prepared, cured, and tested under ambient laboratory conditions (23 ± 2 °C, 55 ± 5% RH).

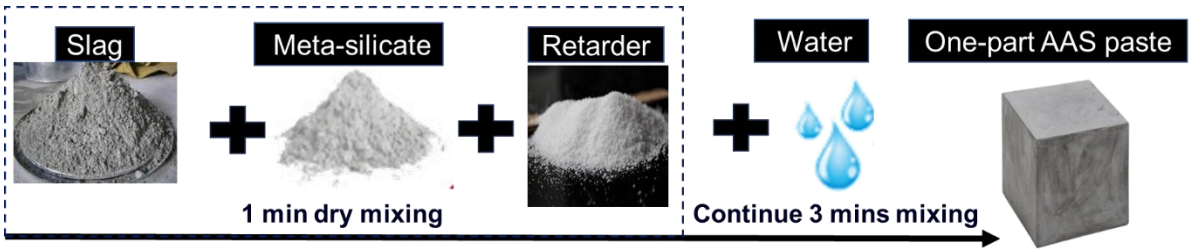

Fig. 5.4: Mixing procedure.

The mini-slump cone test evaluated flowability by measuring the average spread diameter in two perpendicular directions after removing the cone [96]. The relative flow diameter (RFD) value was calculated using the following equation **Eq. 5.12** [195].

$$RFD = \left(\frac{d}{d_0}\right)^2 - 1 \qquad \text{Eq. 5.12}$$

Where RFD represents the relative flow diameter, d is the average of the two measured diameters of the AAS mixtures, and d_0 is the bottom diameter of the conical cone (100 mm).

A Brookfield R.S.T. rheometer with a four-blade vane measured rheology evolution. Samples underwent high-speed pre-shear, followed by a 30-second relaxation before ascending and descending shear rate steps [208]. This pre-shear protocol is implemented to achieve a well-dispersed state and ensure that all samples are in a consistent reference state of stress and strain [209]. Dynamic yield stress and plastic viscosity were determined using Bingham fitting **Eq. 5.13** in the downward part of each flow curve [210].

$$\tau = \tau_0 + \mu \cdot \gamma \qquad \text{Eq. 5.13}$$

Where: τ is the shear stress; τ_0 is the dynamic yield stress in Pa; μ is the plastic viscosity in Pa ·s.; γ is the shear rate in 1/s.

Isothermal calorimetry determined the rate of early hydration for 120 hours at 25°C using approximately 80 g of paste for each mixture according to ASTM C1679 [156]. The compressive strength of 50 mm cubic specimens was tested at 3, 7, and 28 days following ASTM C109-20

[144], with specimens de-moulded after three days (**Fig. 5.5**) and stored in sealed plastic bags until testing [6].

Fig. 5.5: Demoulded cube specimens.

TGA was conducted on samples from 28-day specimens, heating approximately 16 mg of ground powder of optimized mixtures at 10 °C/min up to 850°C [155].

Microstructural studies were performed on optimized mixtures to analyze their morphologies, crystalline phases, and functional groups [211]. XRD and FTIR analyzed microstructure development and hydration products, with XRD following ASTM C1365-18 and FTIR scanning frequencies from 4000–500 cm^{-1}. Chemical analysis of the extracted AAS pore solution (**Fig. 5.6**) used Inductively Coupled Mass Spectrometry (ICP-MS) to measure Na, Si, Ca, K, and Mg concentrations (**Fig. 5.7**). All samples were first filtered through Nylon 0.45-micron syringe filter. Then, the solutions were stored at 5°C until testing and then diluted 1000 times using a mixture of 1.0% nitric acid (HNO_3) and 0.5% hydrochloric acid (HCl) before analysis. Solid-state ^{29}Si NMR spectroscopy on 28-day-old ground-selected samples was performed using a Bruker Advance III HD spectrometer, with analyses referenced to trimethyl silane (TMS) and performed using MestReNova software [212].

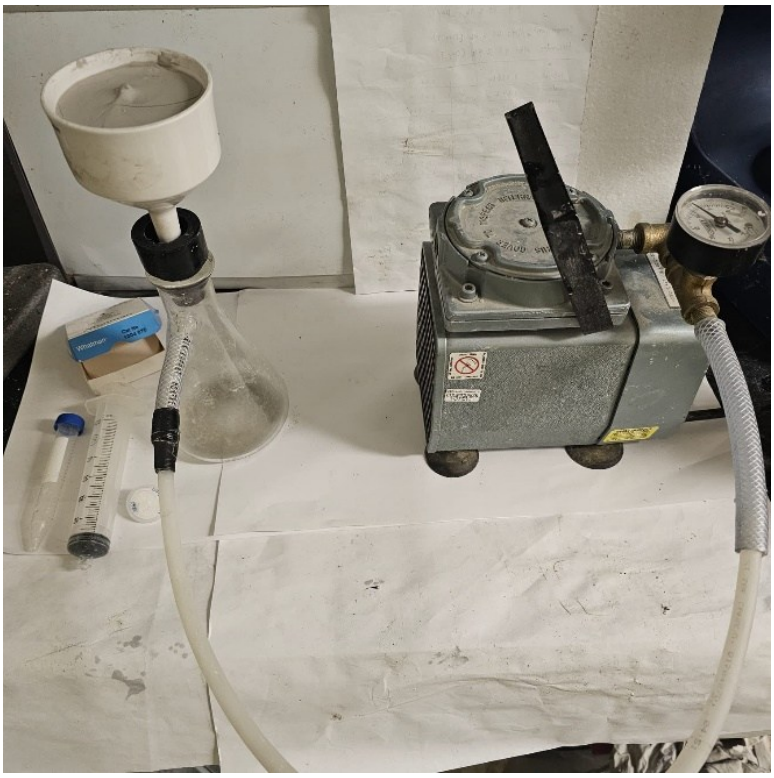

Fig. 5.6: Setup of solution extraction from AAS mixtures.

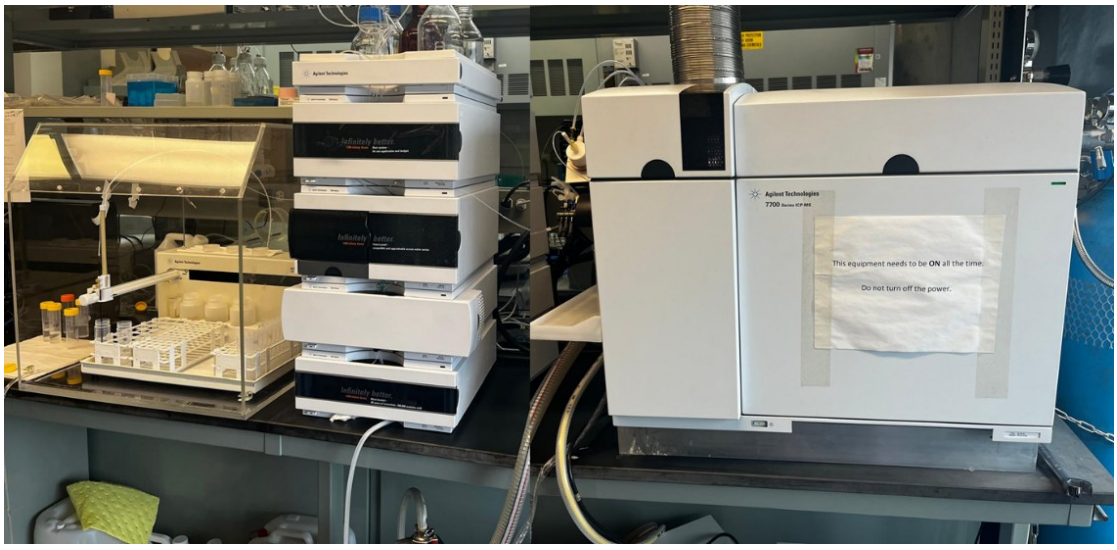

Fig. 5.7: Agilent ICP-MS 7700 series instrument.

pH and conductivity were measured immediately after extraction with a pH meter (**Fig. 5.8**) and a conductivity meter (**Fig. 5.9**), respectively. Electrical conductivity served as an indirect measure of alkalinity as hydroxide ions have higher conductivity than other ions in the solution [212].

Fig. 5.8: The pH meter setup.

Fig. 5.9: The conductivity meter measurement.

5.4. Results and Discussion

5.4.1. Mini-slump

To evaluate the influence of four design parameters on the flowability of AAS mixtures, a flow diameter test was conducted. The flow diameter and relative flow diameter results for the different

mixtures (M1 to M16) are presented in **Fig. 5.10**. Mixtures showed a thixotropic consistency (i.e. become less viscous and flowable while being agitated, but once the agitation stops, they slowly return to their high viscosity) [195]. The mixtures exhibited flow diameters ranging from 125 mm to 325 mm and relative flow diameters between 0.56 to 9.56.

The lowest and highest flow diameters and relative flow diameters were exhibited by M2 and M16, respectively. As expected, mixtures with a high w/s ratio (0.55) showed high flowability values exceeding 300 mm, while mixtures with a low w/s ratio (0.4) had low values, less than 130 mm. For instance, M14 exhibited approximately 58.3% higher flowability than M2. Additionally, for mixtures with the same w/s ratio, increasing the activator dosage resulted in a higher flowability, regardless of the used retarder type and its dosage [213]. For example, M1 (with a 4% activator dosage) exhibited around 32.55% lower flowability than M4 (with a 10% activator dosage). Increasing the activator dosage increases the release of Ca^{2+} and Mg^{2+} cations, which react with available silicate species, forming double-charged cations around precursor particles. This causes repulsion between these charged particles, enhancing flowability, as indicated by a zeta potential of approximately -36 mV [42,162]. Zeta potential is a key measure of the forces within the electrical double layer surrounding particles. These forces significantly influence whether suspended particles flocculate or disperse, which directly impacts the yield stress of the system [128]. Flowability, therefore, depends on both the binder's morphology and its zeta potential. The surface adsorption of silicate species enhances repulsive forces on the particle surfaces [15–17]. The high silica content further increases negative zeta potential values by promoting the adsorption or precipitation of silicate species onto slag particle surfaces. Upon the addition of water, the AAS system becomes shielded by a tightly bound shell of water molecules (HO–H) and adsorbed ions, stabilizing the system and enhancing its flowability [146].

Hence, it could be concluded that the w/s ratio has a dominant influence on flowability, followed by AD, while the RT and RD have a minor effect. This is consistent with previous studies on alkali-activated FA/Slag pastes activated by Na_2SiO_3, incorporating a high dosage of Borax up to 9% by weight of the precursor [71]. This study demonstrated that the AD and the water-to-binder ratio w/b significantly influenced flowability and compressive strength outcomes.

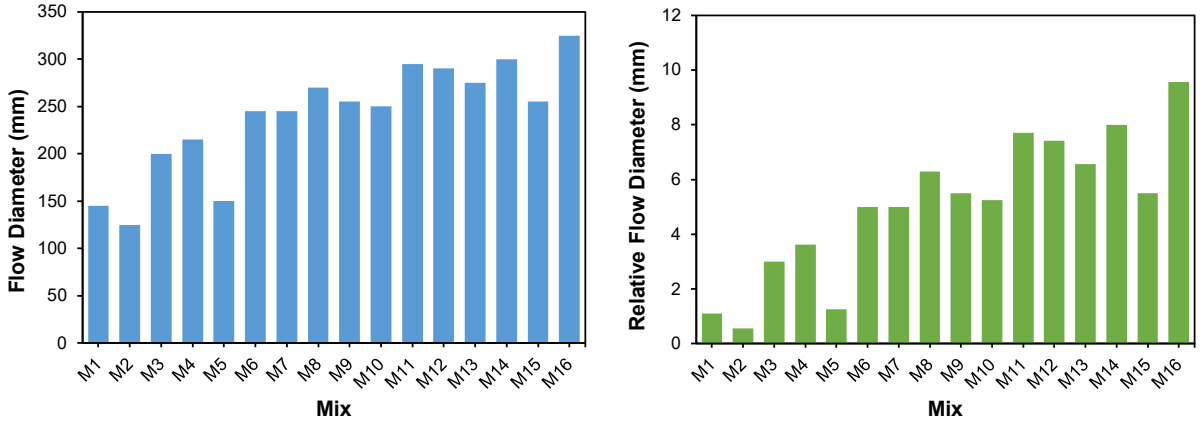

Fig. 5.10: Flow diameter results for AAS mixtures.

The mean S-N ratio plots of the flowability of the mixtures listed are illustrated in **Fig. 5.11**. The flowability of the mixtures was highly influenced by the w/s ratio (Rank1), followed by AD (Rank2), RT (Rank3), and RD (Rank4). Increasing the w/s ratio and AD enhances the mean S-N ratio, which can be attributed to the plasticizing effect of sodium meta-silicate, reducing the yield stress in the early stages [214]. A higher mean S-N ratio indicates the optimal level for each parameter, while a higher delta value highlights the most significant parameter. Therefore, the optimal parameters for flowability were w/s at Level 4, AD at Level 4, RT at Level 3, and RD at Level 4 (**Fig. 5.11**).

a)

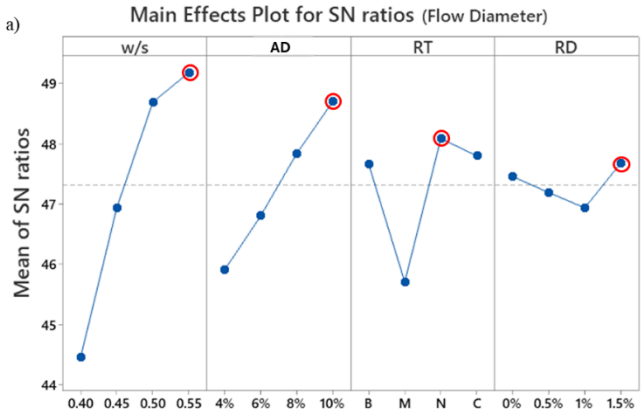

Signal-to-noise: Larger is better

b)

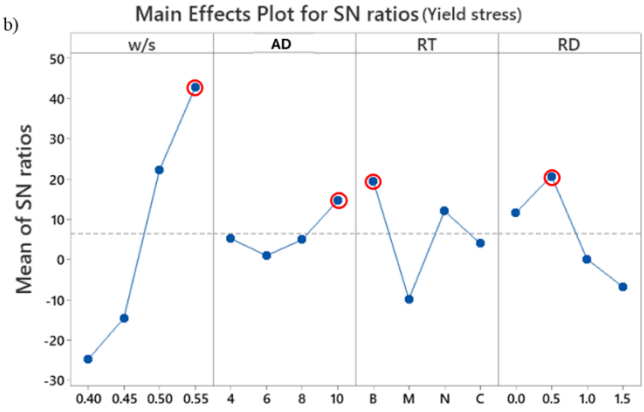

Signal-to-noise: Smaller is better

c)

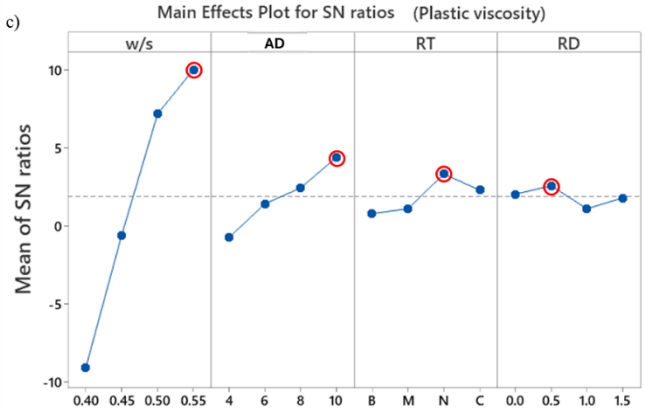

Signal-to-noise: Smaller is better

d)

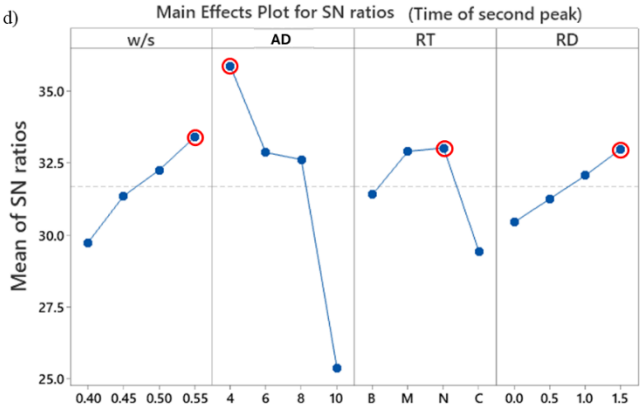

Signal-to-noise: Larger is better

e)

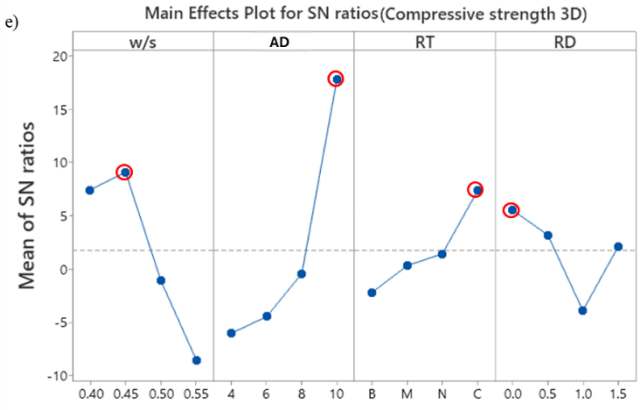

Signal-to-noise: Larger is better

f)

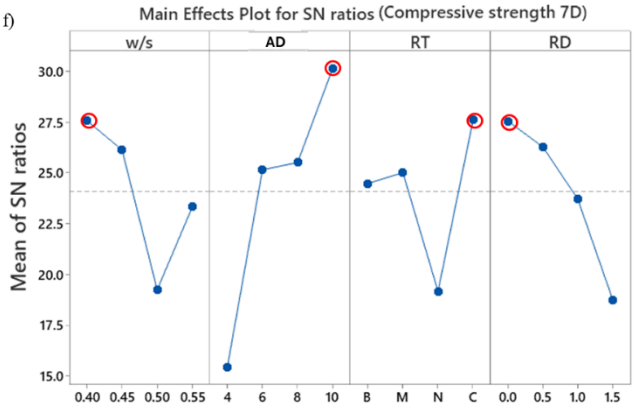

Signal-to-noise: Larger is better

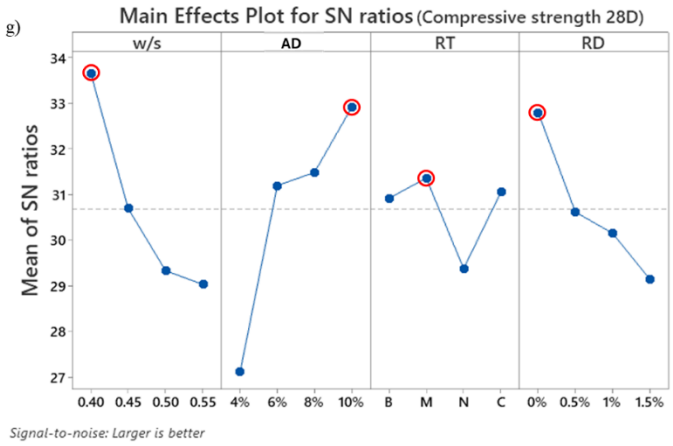

Fig. 5.11: Main effects plot for S-N ratios a) flow diameter, b) yield stress, c) plastic viscosity, d) time of the second peak, e) compressive strength-3 days, f) compressive strength-7 days, and g) compressive strength-28 days.

5.4.2. Rheological Properties (yield stress and plastic viscosity)

The rheological properties of mixtures are crucial for their field application potential. Confirming the flow diameter results, yield stress is the minimum stress required to initiate flow, while plastic viscosity measures resistance to flow after movement begins. To achieve high flowability, lower yield stress and plastic viscosity are preferred [215].

Fig. 5.12 illustrates the yield stress and plastic viscosity results for mixtures (M1 to M16). Mixtures with a low w/s ratio (0.4) exhibited high yield stress and plastic viscosity. For instance, M1 and M2 had the highest yield stress (27 Pa and 30 Pa) and plastic viscosity (4.99 Pa.s and 3 Pa.s). Higher activator dosages, such as in M4 and M8, resulted in a lower yield stress. Moreover, mixtures with high w/s ratios (0.5 and 0.55) such as M9, M11, M12, M13, M14, and M16 exhibited zero yield stress indicating high flowability. On the other hand, Mixtures with N or M at lower retarder dosages ($\leq 1\%$) showed higher yield stress and plastic viscosity. For example, yield stress for M3, M5, and M8 were 10.33, 20.5, and 2.33 Pa and plastic viscosity were 2.18, 1.69, and 0.73 Pa.s, respectively.

Generally, higher activator and higher retarder dosages resulted in a lower plastic viscosity, indicating a flowable mixture. There is a strong correlation between activator dosage and both yield stress and plastic viscosity. Higher activator dosages tend to lower these properties because of the repulsion between dissolved cations [42,162]. Retarder type and dosage also play significant roles, with certain combinations affecting yield stress and plastic viscosity. The mean S-N ratio confirms these results, with the optimal parameters for yield stress being w/s at Level 4, AD at

Level 4, RT at Level 1, and RD at Level 2 (**Fig. 5.11**). Also, B is the most effective retarder, achieving the lowest yield stress among all types of retarders. It reduces yield stress by forming a calcium-based borate layer in an alkaline solution, which delays hydration and inhibits crystal separation through the rapid formation of compounds [216].

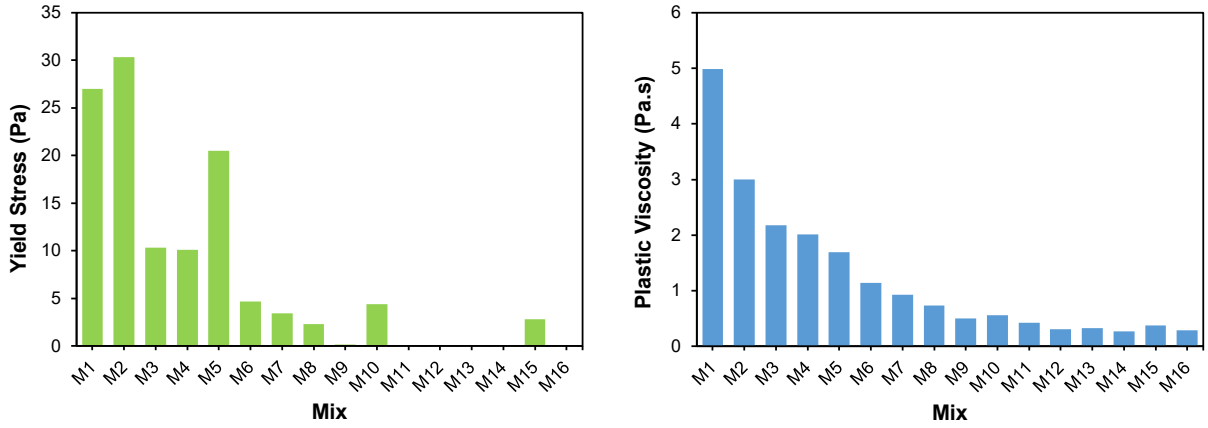

Fig. 5.12: Yield stress and plastic viscosity results for AAS mixtures.

5.4.3. Heat flow profile (Isothermal calorimetry)

Fig. 5.13 shows the time (in hours) of the second peak initiating for each mixture, marking the end of the dormant period and the start of the acceleration phase in the hydration process as clarified in (**cross-section 1**). All mixtures exhibited similar heat flow profiles with five distinguished stages: dissolution, induction, acceleration, deceleration, and the steady period [165,187].

The highest second peak time at around 98 hours for M9 indicates a strong retarding effect due to the combination of 1.5% N, a w/s ratio of 0.5, and an AD of 4%. This delay is agreed with the measured low yield stress and plastic viscosity results, suggesting a postponement in structural development. Retarder N is the most effective retarder as those AAS mixtures achieved high flowability. Adding small amounts of N significantly increased the induction period, delaying the nucleation and growth of the C–(N)–A–S–H gel, which is crucial for hardening [197]. This retardation occurs because N interacts chemically with other elements in the mixture, inhibiting the rapid formation of C–(N)–A–S–H gel by interfering with calcium (Ca^{2+}) and silicate ions (SiO_4^{4-}) [197].

Mixtures with lower second peak times (e.g. M4, M12) indicated quicker initiation of the acceleration phase, implying less effective retardation. High activator dosages (e.g. M4, M8, M12) with varying w/s ratios tend to have shorter second peak times. This could be attributed to the fast initial nucleation process and formation of hydration products [169]. Conversely, lower activator

dosages with higher retarder dosages generally result in higher second peak times, emphasizing the retarder dosage's importance in controlling the dormant period.

Overall, the type and dosage of the retarder besides activator dosage had a significant impact on the time of the second peak, which is crucial for controlling the hydration kinetics. The second peak time provided insights into the efficiency of retarders in delaying the hydration process, optimizing the flowability, and setting the time of AAS mixtures.

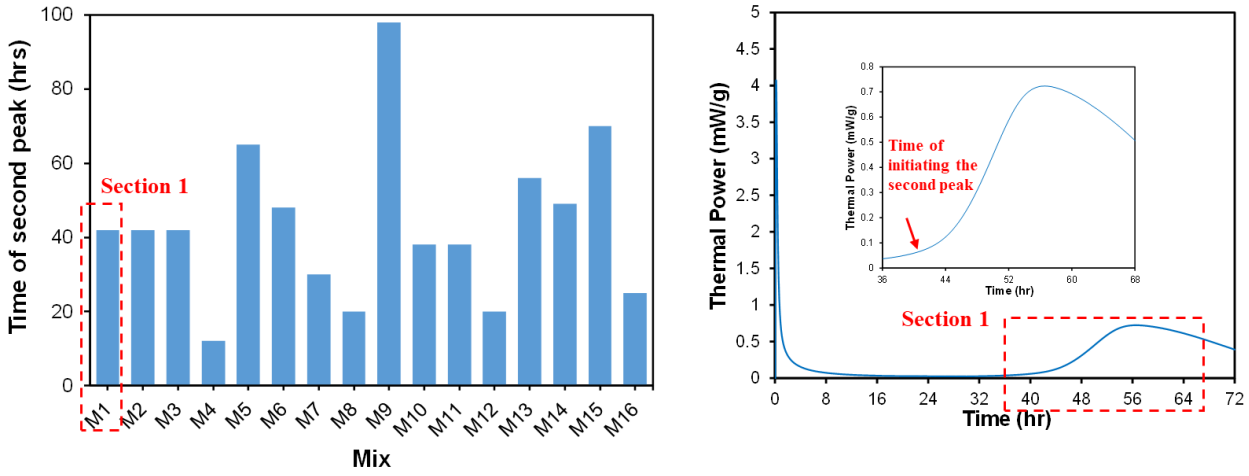

Fig. 5.13: Time of second peak of heat of hydration results for AAS mixtures.

5.4.4. Compressive strength

The compressive strength results of AAS mixtures (M1 to M16), tested after 3, 7, and 28 days are illustrated in **Fig. 5.14**. It was observed that M4 and M8 exhibited the highest early strength due to higher activator dosages and relatively low w/s ratios due to the high dissolution rate of slag, which accelerates the hydration product formation [96]. M1, M3, and M13 also showed significant strength development, indicating effective hydration and strength gain. At 28 days, M4 reached the highest strength, demonstrating superior long-term hydration. This mixture consistently showed high strength at all testing ages due to an optimal balance of w/s ratio, AD, and RT. Mixtures with high early strength often had shorter times to the second peak, indicating quicker setting times, and confirming the measured high-yield stress and viscosity results. The performance at 28 days often correlates with the type and dosage of retarders used, impacting long-term hydration and final compressive strength. M and N mixtures (e.g. M5, M9) showed moderate to high strengths, indicating effective retardation and subsequent strength gain, while C mixtures (e.g. M4, M13) showed higher strengths [217], enhancing long-term performance.

Generally, long-term compressive strength was significantly influenced by the RT and RD and the AD. Mixtures with higher activator dosages (e.g. M4, M12) and specific retarders (e.g. C, M) exhibited higher strengths at 28 days. Understanding the interaction between AD, RT, and RD is crucial for optimizing the compressive strength of AAS mixtures. The type and dosage of retarder, along with activator dosage and w/s ratio, were critical for strength development, requiring careful selection for desired properties at specific ages (**Fig. 5.11**).

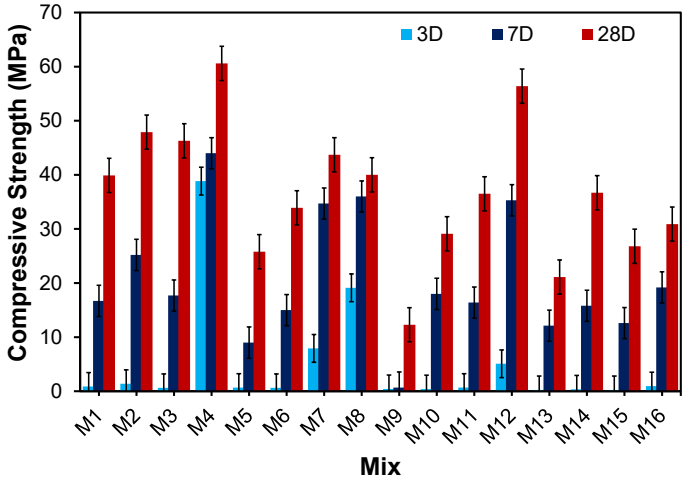

Fig. 5.14: Compressive strength results for AAS mixtures.

In the current study, linear regression equations were developed to predict individual responses such as flow diameter (FD), yield stress (YS), plastic viscosity (PV), and compressive strength (CS) at ages 3, 7, and 28 days. These dependent variables were expressed as linear functions of w/s ratio, AD, and RD for each RT. The developed predictive equations are presented in **Table 5.4**. The used slag's chemical composition is within the typical ranges of that produced worldwide [218]. Also, the basicity coefficient [K_b = (CaO + MgO)/(SiO_2 + Al_2O_3)] and the hydration modulus [CaO + MgO + Al_2O_3)/SiO_2] for the used GGBS were 1.06 and 1.63, respectively. This indicated that this is a highly reactive slag, satisfying the German and Japanese standards, even though its chemical composition is different.

Table 5.4: Linear regression equations for various retarder types.

Responses	B	M
FD (mm)	-201.2 - 3.50 RD + 11.25 AD + 795.0 w/s	-248.7 - 3.50 RD + 11.25 AD + 795.0 w/s
YS (Pa)	80.2 - 1.78 RD - 1.604 AD - 125.6 w/s	85.7 - 1.78 RD - 1.604 AD - 125.6 w/s
PV (Pa.s)	11.58 - 0.359 RD - 0.1696 AD - 17.71 w/s	11.22 - 0.359 RD - 0.1696 AD - 17.71 w/s
TSP (hrs)	24.4 + 13.75 RD - 6.86 AD + 108.5 w/s	35.4 + 13.75 RD - 6.86 AD + 108.5 w/s
CS- 3D (MPa)	15.4 + 2.95 RD + 2.400 AD - 70.8 w/s	16.5 + 2.95 RD + 2.400 AD - 70.8 w/s
CS-7D (MPa)	32.39 - 5.82 RD + 3.693 AD - 78.0 w/s	36.09 - 5.82 RD + 3.693 AD - 78.0 w/s
CS-28D (MPa)	75.4 - 6.94 RD + 3.251 AD - 121.3 w/s	79.3 - 6.94 RD + 3.251 AD - 121.3 w/s

Responses	N	C
FD (mm)	-197.5 - 3.50 RD + 11.25 AD + 795.0 w/s	-207.5 - 3.50 RD + 11.25 AD + 795.0 w/s
YS (Pa)	75.4 - 1.78 RD - 1.604 AD - 125.6 w/s	76.7 - 1.78 RD - 1.604 AD - 125.6 w/s
PV (Pa.s)	10.79 - 0.359 RD - 0.1696 AD - 17.71 w/s	10.83 - 0.359 RD - 0.1696 AD - 17.71 w/s
TSP (hrs)	38.4 + 13.75 RD - 6.86 AD + 108.5 w/s	20.2 + 13.75 RD - 6.86 AD + 108.5 w/s
CS- 3D (MPa)	19.8 + 2.95 RD + 2.400 AD - 70.8 w/s	26.5 + 2.95 RD + 2.400 AD - 70.8 w/s
CS-7D (MPa)	33.11 - 5.82 RD + 3.693 AD - 78.0 w/s	42.77 - 5.82 RD + 3.693 AD - 78.0 w/s
CS-28D (MPa)	72.9 - 6.94 RD + 3.251 AD - 121.3 w/s	78.7 - 6.94 RD + 3.251 AD - 121.3 w/s

5.4.5. Analysis of Variance (ANOVA)

ANOVA was used to determine each factor's contribution to specific responses based on experimental data. This statistical technique separates the variability in results into two sources: uncontrolled nuisance variables and independent variables. This separation reveals the variation caused by independent variables and estimates each factor's contribution to the desired response [168]. With 80% confidence, the contribution of each element to flowability, yield stress, plastic viscosity, the time of the second peak, and 28-day compressive strength was evaluated. **Fig. 5.15** depicted that the w/s ratio had the highest contribution to flowability (61%), yield stress (52%), and plastic viscosity (62%) [219]. The activator dosage followed, contributing 20%, 14%, and 9%, respectively.

Generally, a high w/s ratio and activator dosage increase the flowability of AAS mixtures due to the deflocculating and plasticizing effect of sodium meta-silicate [214], which reduces yield stress. Conversely, the retarder type and dosage had minimal contributions to all properties except compressive strength. These findings indicate that the w/s ratio and activator dosage predominantly control the fresh properties and compressive strength of AAS mixtures.

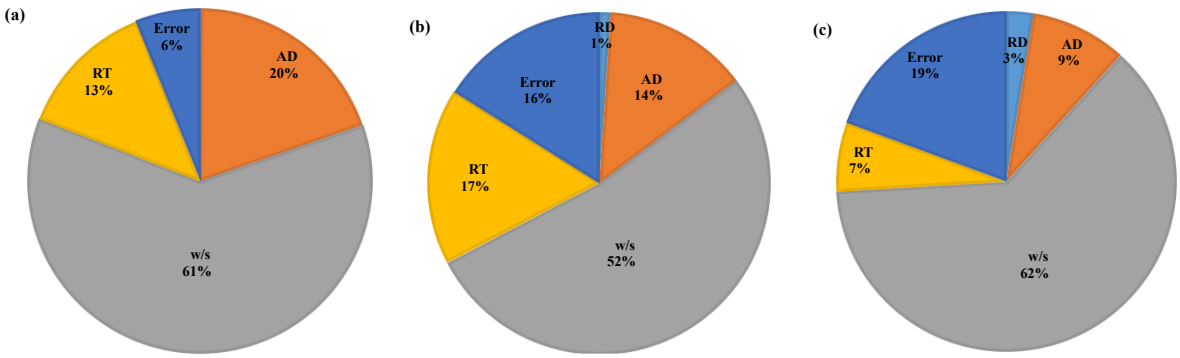

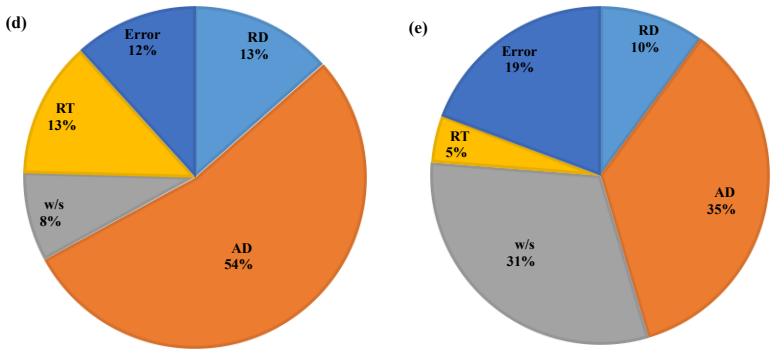

Fig. 5.15: Contribution of factors toward Taguchi optimization of the mixture for (a) flowability (b) yield stress, (c) plastic viscosity, (d) time of the second peak, (e) 28 days compressive strength.

5.4.6. Multi-objective optimization using GRA and TOPSIS

As outlined earlier, the Taguchi method was used to determine the optimal parameter levels for individual properties. This study combined the Taguchi method with GRA and TOPSIS for multi-objective optimization across all parameters. Details of these computations are outlined in the methodology section.

Table 5.5 to **Table 5.7** presented the calculated values of various variables at different stages of the Taguchi-GRA analysis for the tested AAS mixtures. After analyzing the results, M9 demonstrated the highest grey relational grade (r) of 0.792, indicating its potential as the optimal mixture combination for multiple responses. This mixture exhibited low yield stress, low plastic viscosity, the longest time to initiate the second peak, and a desirable flow diameter, all of which contribute to high flowability. However, it is important to note that despite these advantages, M9 exhibited the lowest compressive strength, raising concerns about its overall suitability for certain applications.

Table 5.5: S-N ratios for responses (X_{ij}).

Mixture	FD	YS	PV	TSP	CS- 3days	CS-7days	CS-28days
M-1	43.23	-28.63	-13.96	32.46	-1.11	24.45	32.02
M-2	41.94	-29.64	-9.54	32.46	2.92	28.03	33.61
M-3	46.02	-20.28	-6.77	32.46	-3.88	24.96	33.31
M-4	46.65	-20.10	-6.06	21.58	31.79	32.87	35.65
M-5	43.52	-26.24	-4.56	36.26	-3.35	19.08	28.23
M-6	47.78	-13.42	-1.14	33.62	-3.88	23.52	30.60
M-7	47.78	-10.76	0.63	29.54	17.97	30.81	32.81
M-8	48.63	-7.35	2.73	26.02	25.63	31.13	31.13
M-9	48.13	15.92	6.02	39.82	-7.13	-3.35	21.80
M-10	47.96	-12.87	5.04	31.60	-7.96	25.11	29.28
M-11	49.40	60.00	7.54	31.60	-3.35	24.30	31.25

M-12	49.25	26.02	10.17	26.02	14.12	30.96	35.03
M-13	48.79	60.00	9.63	34.96	-12.40	21.67	26.49
M-14	49.54	60.00	11.37	33.80	-8.87	23.97	31.29
M-15	48.13	-9.07	8.40	36.90	-12.40	22.01	28.56
M-16	50.24	60.00	10.75	27.96	-0.35	25.67	29.80

FD- flow diameter, YS- yield stress, PV- plastic viscosity, TSP- time of second peak from heat of hydration curve, CS- compressive strength

Table 5.6: Normalized S-N ratios (Y_{ij}).

Mixture	FD	YS	PV	TSP	CS- 3days	CS-7days	CS-28days
M-1	0.155	0.989	1.000	0.597	0.255	0.768	0.738
M-2	0.000	1.000	0.826	0.597	0.347	0.866	0.853
M-3	0.492	0.896	0.716	0.597	0.193	0.782	0.831
M-4	0.568	0.894	0.688	0.000	1.000	1.000	1.000
M-5	0.191	0.962	0.629	0.804	0.205	0.619	0.465
M-6	0.704	0.819	0.494	0.660	0.193	0.742	0.636
M-7	0.704	0.789	0.424	0.436	0.687	0.943	0.795
M-8	0.806	0.751	0.341	0.243	0.861	0.952	0.673
M-9	0.746	0.492	0.211	1.000	0.119	0.000	0.000
M-10	0.725	0.813	0.250	0.549	0.100	0.786	0.540
M-11	0.899	0.000	0.151	0.549	0.205	0.763	0.682
M-12	0.881	0.379	0.047	0.243	0.600	0.947	0.955
M-13	0.825	0.000	0.069	0.734	0.000	0.691	0.338
M-14	0.916	0.000	0.000	0.670	0.080	0.754	0.686
M-15	0.746	0.771	0.117	0.840	0.000	0.700	0.488
M-16	1.000	0.000	0.024	0.349	0.273	0.801	0.578

Table 5.7: Calculated values of terms in Taguchi-GRA analysis.

Mixture	Grey relational coefficient (**GCij**)							Grade (r)	Rank
	FD	YS	PV	TSP	CS- 3days	CS-7days	CS-28days		
M-1	0.763	0.336	0.333	0.456	0.662	0.394	0.404	0.558	9
M-2	1.000	0.333	0.377	0.456	0.591	0.366	0.370	0.582	7
M-3	0.504	0.358	0.411	0.456	0.722	0.390	0.376	0.536	12
M-4	0.468	0.359	0.421	1.000	0.333	0.333	0.333	0.541	11
M-5	0.724	0.342	0.443	0.383	0.709	0.447	0.518	0.594	6
M-6	0.415	0.379	0.503	0.431	0.722	0.403	0.440	0.549	13
M-7	0.415	0.388	0.541	0.534	0.421	0.346	0.386	0.505	16
M-8	0.383	0.400	0.595	0.673	0.367	0.344	0.426	0.531	15
M-9	0.401	0.504	0.703	0.333	0.808	1.000	1.000	0.792	1
M-10	0.408	0.381	0.667	0.477	0.833	0.389	0.481	0.606	10
M-11	0.357	1.000	0.767	0.477	0.709	0.396	0.423	0.688	5
M-12	0.362	0.569	0.913	0.673	0.455	0.346	0.344	0.610	14
M-13	0.377	1.000	0.879	0.405	1.000	0.420	0.596	0.780	2
M-14	0.353	1.000	1.000	0.427	0.862	0.399	0.422	0.744	3
M-15	0.401	0.394	0.810	0.373	1.000	0.417	0.506	0.650	8
M-16	0.333	1.000	0.953	0.589	0.647	0.384	0.464	0.728	4

To determine the overall optimal AAS mixtures, the mean grey relational grade (r) for all parameters was calculated. The parameter level with the highest mean r value is considered optimal, as it has the greatest impact on the responses. This optimal level indicated its significant

effect on achieving the desired mixture [195]. Notably, the highest mean grey relational grade corresponded to the following parameter levels: w/s = 0.55 at Level 4, AD = 4% at Level 1, RT = N at Level 3, and RD = 0.5% at Level 2, as shown in **Table 5.8**.

Table 5.8: Response table for the mean grey relational grade.

Parameter	Level 1	Level 2	Level 3	Level 4	Delta	Rank
w/s	0.5544	0.5450	0.6739	**0.7255**	0.1806	1
AD	**0.6809**	0.6201	0.5950	0.6028	0.0860	2
RT	0.6309	0.6092	**0.6507**	0.6080	0.0427	3
RD	0.6043	**0.6453**	0.6162	0.6329	0.0410	4

Equal weights (0.25) were assigned to the four selected responses in the Taguchi TOPSIS optimization method to calculate the closeness coefficient, as shown in **Table 5.9**. The average S-N ratios for each factor's corresponding values were then computed. **Fig. 5.16** demonstrated that increasing the w/s ratio positively impacted all targeted scenarios for both GRA and TOPSIS. Specifically, **Fig. 5.16 (a)** showed that the first optimal mixture for GRA requires a w/s ratio of 0.55, 4% AD, N RT, and 0.5% RD. In contrast, **Fig. 5.16 (b)** identified the second optimal mixture for TOPSIS as having a w/s ratio of 0.55, 10% AD, B RT, and 0.5% RD.

Table 5.9: Closeness coefficient of the optimum mixture.

Mix	**Normalized Weighted Decision Matrix**				S_i^+	S_i^-	P_i
	FD	YS	TSP	CS-28days			
M-1	0.0570	-0.0518	0.0634	0.0649	0.1610	0.0344	0.1762
M-2	0.0396	-0.0536	0.0634	0.0681	0.1638	0.0320	0.1634
M-3	0.0441	-0.0367	0.0634	0.0675	0.1466	0.0361	0.1974
M-4	0.0454	-0.0363	0.0421	0.0722	0.1497	0.0334	0.1825
M-5	0.0430	-0.0474	0.0708	0.0572	0.1575	0.0322	0.1699
M-6	0.0476	-0.0243	0.0657	0.0620	0.1341	0.0424	0.2400
M-7	0.0484	-0.0194	0.0577	0.0665	0.1300	0.0445	0.2551
M-8	0.0494	-0.0133	0.0508	0.0630	0.1253	0.0464	0.2701
M-9	0.0498	0.0288	0.0778	0.0442	0.0849	0.0903	0.5154
M-10	0.0506	-0.0233	0.0617	0.0593	0.1335	0.0406	0.2332
M-11	0.0526	0.1085	0.0617	0.0633	0.0193	0.1648	0.8953
M-12	0.0530	0.0470	0.0508	0.0709	0.0673	0.1053	0.6101
M-13	0.0537	0.1085	0.0683	0.0536	0.0214	0.1650	0.8853
M-14	0.0557	0.1085	0.0660	0.0634	0.0150	0.1657	0.9172
M-15	0.0553	-0.0164	0.0721	0.0579	0.1258	0.0521	0.2927
M-16	0.0584	0.1085	0.0546	0.0604	0.0260	0.1644	0.8633

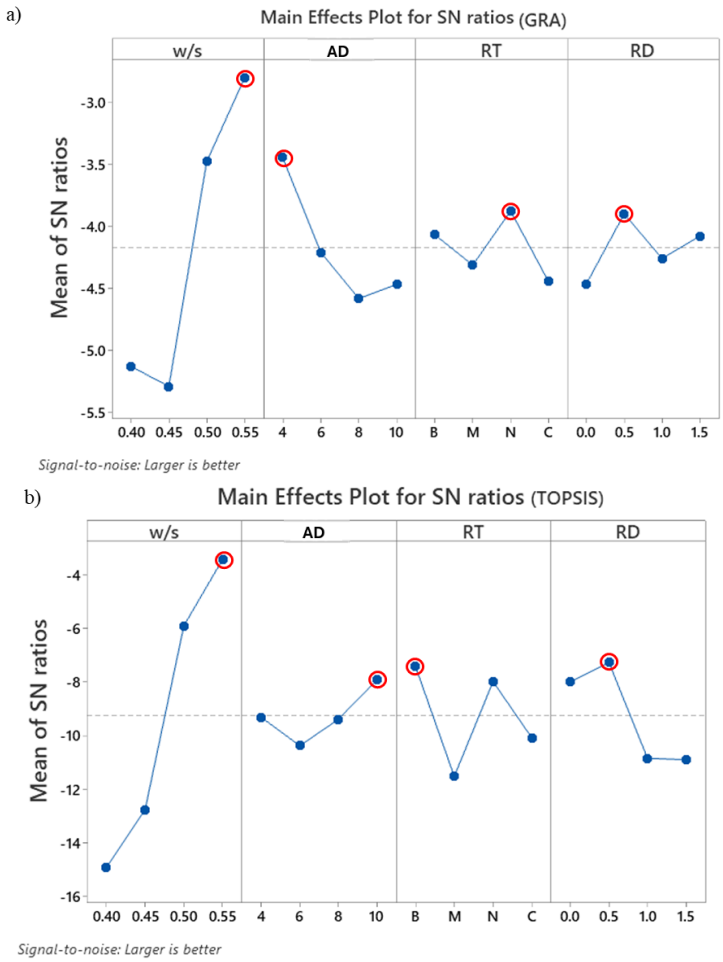

Fig. 5.16: S-N ratios of a) GRA scenario and b) TOPSIS scenario.

Based on the Taguchi approach, the optimized parameter levels for individual responses, combined responses using Taguchi GRA, and combined selected responses using Taguchi TOPSIS are listed in **Table 5.10**.

Table 5.10: Optimum parameter levels by Taguchi, Taguchi-GRA, and TOPSIS.

Response	Optimum levels of parameter		
	Taguchi analysis	Taguchi GRA	TOPSIS
FD	**w/s = 0.55, AD = 10%, RT= N, RD = 1.5%**	**w/s = 0.55, AD = 4%, RT= N, RD = 0.5%**	**w/s = 0.55, AD = 10%, RT= B, RD = 0.5%**
YS	**w/s = 0.55, AD = 10%, RT= B, RD = 0.5%**		
PV	**w/s = 0.55, AD = 10%, RT= N, RD = 0.5%**		
TSP	**w/s = 0.55, AD = 4%, RT= N, RD = 1.5%**		
CS-3days	**w/s = 0.45, AD = 10%, RT= C, RD = 0.0%**		
CS-7days	**w/s = 0.40, AD = 10%, RT= C, RD = 0.0%**		
CS-28days	**w/s = 0.40, AD = 10%, RT= M, RD = 0.0%**		

Through the validation phase, experiments were conducted using mixtures with optimal response levels determined by the Taguchi, Taguchi-GRA, and Taguchi TOPOSIS methods, as shown in

Table 5.10. The experimental results were then compared with the values predicted by the linear regression (**Table 5.4**). The findings in **Table 5.11** showed a strong correlation between the predicted outcomes and the actual experimental results within the specified input parameters. Given that reliable statistical analyses require error values to be less than 20% [220], the results from the confirmation tests confirm the success of the optimization achieved with the Taguchi method and linear regressions. The optimized mixtures, OM1 to OM6, represent the optimal mixture for each property according to the Taguchi single-criteria method. OM7 represents the optimized mixture for all seven measured properties based on the GRA. Additionally, OM2 is the optimal mixture for the TOPSIS approach, considering four selected properties.

Table 5.11: Validation results for optimum parameter levels.

		Taguchi method			
Mixture Code	Response	Optimum parameter levels	Predicted	Experimental	Error %
OM1	FD (mm)	**w/s = 0.55, AD = 10%, RT= N, RD = 1.5%**	347	330	-5.15
OM2	YS (Pa)	**w/s = 0.55, AD = 10%, RT= B, RD = 0.5%**	-5.81	0*	-----
OM3	PV (Pa.s)	**w/s = 0.55, AD = 10%, RT= N, RD = 0.5%**	-0.826	0*	-----
OM4	TSP (hrs)	**w/s = 0.55, AD = 4%, RT= N, RD = 1.5%**	91.26	80	-14.08
OM5	CS-3days (MPa)	**w/s = 0.45, AD = 10%, RT= C, RD = 0.0%**	18.64	22.3	+16.41
OM6	CS-7days (MPa)	**w/s = 0.40, AD = 10%, RT= C, RD = 0.0%**	48.5	47.3	-2.54
OM6	CS-28days (MPa)	**w/s = 0.40, AD = 10%, RT= M, RD = 0.0%**	63.29	55	-15.07
		Taguchi - GRA			
OM7	FD (mm)	**w/s = 0.55, AD = 4%, RT= N, RD = 0.5%**	283	278	-1.80
	YS (Pa)		-0.986	0*	-----
	PV (Pa.s)		0.191	0.238	19.74
	TSP (hrs)		77.51	70	-10.73
	CS-3days (MPa)		-8.06**	0	-----
	CS-7days (MPa)		2.07	2.1	1.3
	CS-28days (MPa)		15.72	16.6	5.30
		Taguchi - TOPSIS			
OM2	FD (mm)	**w/s = 0.55, AD = 10%, RT= B, RD = 0.5%**	346.8	330	-5.09
	YS (Pa)		-5.81	0*	-----
	TSP (hrs)		22.35	19	-17.63
	CS-28days (MPa)		37.73	31.8	-18.64

*The smallest value detectable by the rheometer is zero.
** This indicates a highly flowable mixture, as negative strength has no practical meaning.

5.4.7. Microstructural analysis

5.4.7.1. XRD and TGA Analysis

The XRD analysis of the optimized AAS mixtures revealed that the nature of the hydration products was largely consistent across the samples, as shown in **Fig. 5.17.** The primary hydration product was C-S-H at $2\theta = 30^{\circ}$ [195,221]. However, variations were observed in the crystalline content and the intensity of the C-S-H phase.

The crystalline content among the mixtures varied from 23.8% to 27.7%, with some samples exhibiting higher crystallinity, indicating a more ordered structure in the hydration products [222]. For instance, mixtures activated with a 10% activator dosage consistently showed a crystalline content of around 26%, regardless of the retarder type and dosage. Conversely, mixtures activated with a 4% activator dosage showed a lower crystalline content of around 24%. These findings confirm that the activator dosage is the predominant factor governing the formation of hydration products and supports the use of N and B as retarders. The intensity of the C-S-H phase, which reflects the amount and stability of C-S-H formed, also varied depending on the activator dosages used. Higher C-S-H intensity suggests more extensive hydration and a potentially denser microstructure. Additionally, there are traces of calcite, as indicated by small diffraction peaks around 25°, which could be attributed to the carbonation of C-A-S-H gels [195].

The TG and DTG curves of various AAS mixtures measured at 28 days are shown in **Fig. 5.18**. All AAS mixtures show weight loss as the temperature increases from room temperature to around 1000°C. The total weight loss ranges from 26 % to 14.8%, and the maximal value of weight loss occurs in OM3. Each DTG curve displays a prominent broad peak around 60°C, attributed to the decomposition of the C-S-H phase present in the samples [223].

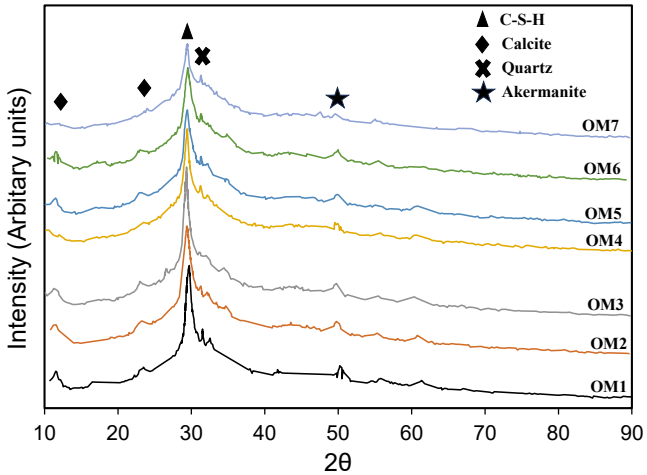

Fig. 5.17: X-ray diffractograms of 28-day-optimized AAS paste.

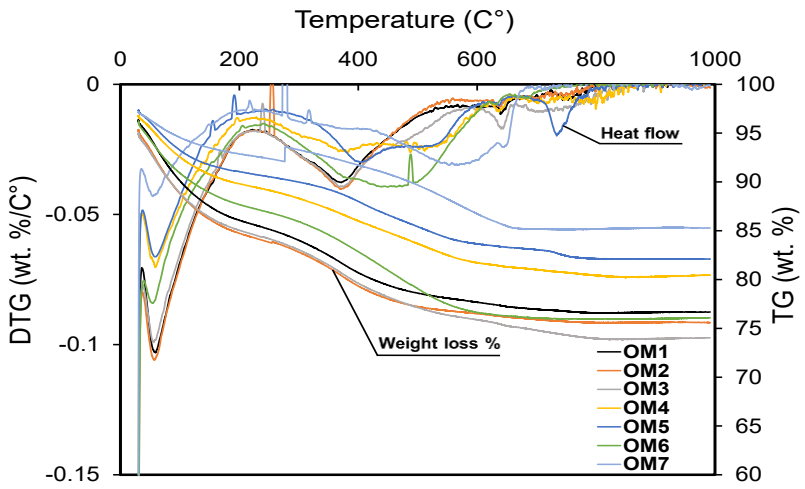

Fig. 5.18: TG-DTG curves of AAS mixtures at 28 days.

This observation supports the XRD analysis, which indicates that activator dosage is the primary factor influencing hydration products, independent of retarder type and dosage. The significant variations in weight loss across different mixtures correlate directly with the quantity of geopolymerization products formed [222].

5.4.7.2. FTIR Analysis

The FTIR spectra of the AAS mixtures were largely similar, with variations only in resonance intensity, indicating differences in the quantity of reaction products formed as shown in **Fig. 5.19**. This is consistent with the XRD results, which also showed similarities across mixtures. The primary binding phase's chemical structure appears to be consistent across different mixture proportions.

Key spectral bands were identified, including a band at 1630 cm^{-1} corresponding to H-O-H stretching, and a band at 3337 cm^{-1} attributed to O-H groups. These bands indicate the presence of water molecules within the C/N-A-S-H gel matrices. A peak at 951 cm^{-1}, characteristic of the Si-O bonds' asymmetrical stretching, suggests the formation of silicate networks, such as C-S-H and other silicate phases [168,195].

OM5 and OM6 exhibited higher hydration levels, as shown by the stronger O-H stretching bands, correlating with their higher compressive strength. In contrast, OM1, OM2, OM4, and OM7 showed slightly reduced hydration levels. All mixtures displayed strong Si-O-Si peaks, confirming the robust formation of silicate networks critical for the structural integrity and mechanical strength of the AAS pastes.

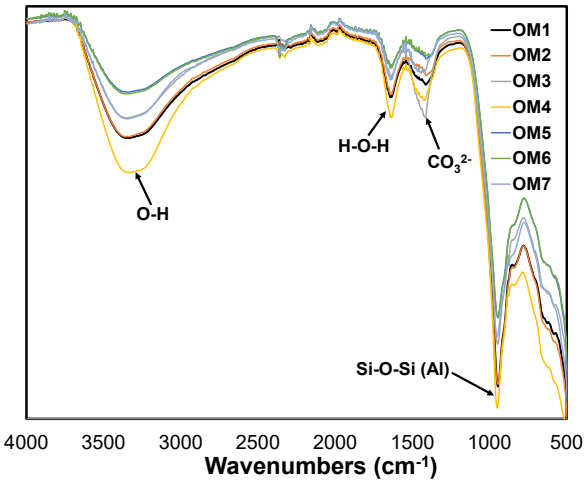

Fig. 5.19: FTIR spectra for optimized AAS mixtures at 28 days.

5.4.7.3. Conductivity and Ion Concentration Analysis

Chemical analysis was conducted on the extracted AAS pore solutions from optimized mixtures with different mixing factors (w/s ratios, AD, RT, and RD) to assess significant chemical changes. **Table 5.12** depicts the pH and electrical conductivity values for various optimized mixtures. The pH value plays a vital role in the slag's initial dissolution, releasing Ca^{2+} ion dissolution from the slag particle surface to the solution. The higher the activator dosage, the higher the electrical conductivity value and the faster the dissolution rate of slag (high Ca^{2+} and Al^{3+} ion concentrations dissolved from the slag) [37]. In the initial stage of activation, the high-pH activator breaks Ca–O, Al–O, and Si–O bonds on the slag surface, releasing species such as Ca^{2+}, $[H_2SiO_4]^{2-}$, $[H_3SiO_4]^{-}$, and $[H_4AlO_4]^{-}$ into the solution [37].

OM4 and OM7 exhibited the lowest alkalinity level and electrical conductivity due to the low activator dosage regardless of the retarder dosage. This confirms the long dormant period because of the longer time required for ionic species in the pore solution to reach the critical concentration and form the hydration products for OM4 and OM7 [224].

Table 5.12: pH and electrical conductivity values for extracted solutions after mixing.

Mixture Code	pH	Conductivity (S/cm)
OM1	12.97	139.5
OM2	12.85	130.6
OM3	12.85	135.2
OM4	12.21	87.6
OM5	13.12	150.4
OM6	13.12	144.0
OM7	12.59	88.7

Chemical analysis (ion concentration) findings confirmed the pH values of OM4 and OM7 had the lowest Al and Ca concentrations due to the slow dissolution of slag, as shown in **Table 5.13**. For N retarders, increasing the retarder dosage reduces the concentrations of Si and Ca ions, confirming the retardation effect. For example, the Si ion concentration in OM1 (323.58) was lower than in OM3 (369.07). At the same retarder dosage, a higher activator dosage leads to greater Ca and Al ion release, as seen when comparing OM1 and OM4. This indicates that OM1 achieves the highest flowability due to increased ion repulsion. Moreover, the highest concentration of Si and Ca for OM5 and OM6 confirmed the high dissolution rate of slag, resulting in high compressive strength at both early and late ages.

Table 5.13: Chemical analyses of pore solutions extracted from AAS mixtures (mmol/L).

Mixture Code	Na	Mg	Al	Si	K	Ca
OM1	551.61	5.75	14.29	323.58	5.41	0.35
OM2	609.00	8.92	14.37	390.96	5.57	0.40
OM3	570.07	8.31	12.41	369.07	4.76	0.36
OM4	258.08	0.64	2.51	166.79	3.69	0.11
OM5	668.16	10.33	19.28	391.20	7.32	0.56
OM6	805.39	19.57	23.97	493.19	6.89	0.66
OM7	256.59	0.64	2.56	165.47	3.36	0.05

5.4.7.4. Nuclear magnetic resonance spectroscopy (29Si NMR spectra) analysis

The deconvoluted ^{29}Si NMR spectra of OM2 and OM3 paste mixtures are presented in **Fig. 5.20** to evaluate the effects of two retarders, N and B while keeping all other ingredient proportions constant (i.e. w/s =0.55, AD = 10%, RD= 0.5%). Chemical shifts in the spectra are interpreted based on various silicon Q^n units, where Q represents a SiO_4 tetrahedral unit, and n indicates the number of bridging oxygen atoms connected to other silicon atoms. In AAS systems, the C-A-S-H gel primarily comprises Q^1, Q^2, and, $Q^2(1Al)$ units, the latter indicating the incorporation of aluminum into the silicate chains of the C-A-S-H structure [225,226]. The Q^1 unit corresponds to a peak observed between -73 and -78 ppm, while the Q^2 unit is associated with a peak between -83 and -85 ppm. The substitution of silicon (Si) by aluminum (Al) in the structure is identified as $Q^2(1Al)$, which causes a chemical shift of approximately 3 to 5 ppm towards more positive values. Consequently, the $Q^2(1Al)$ peak typically appears around -81 ppm [227]. These values indicate the primary reaction product (C-A-S-H) formation in AAS.

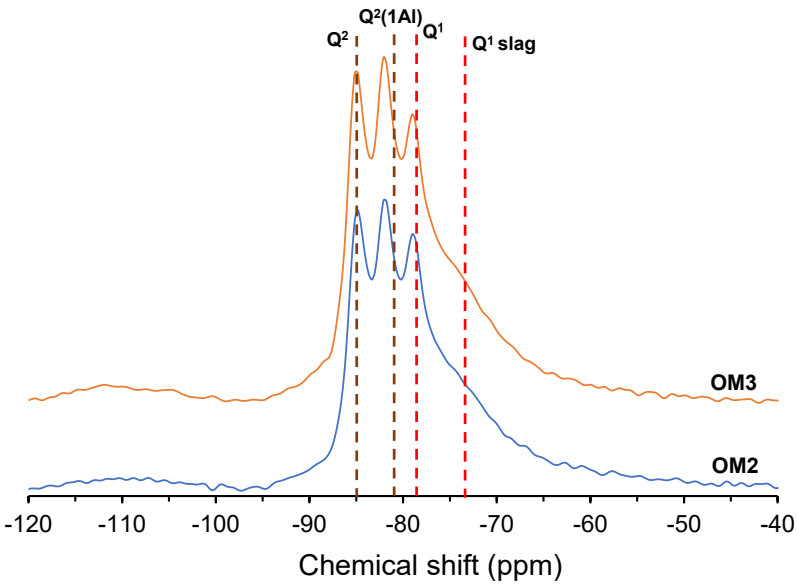

Fig. 5.20: ^{29}Si solid-state NMR patterns of AAS paste with 0.5% of retarder B and N.

The mean chain length (MCL), representing the degree of polymerization in C-S-H, and the Al/Si ratio in C-A-S-H, reflecting the substitution of Si by Al in tetrahedral positions [228–230], can be calculated using the following equations (**Eqs. 5.14** and **5.15**):

$$\mathrm{MCL} = \frac{2(Q^1 + Q^2 + 1.5Q^2(1\mathrm{Al}))}{Q^1} \qquad \text{Eq. 5.14}$$

$$\mathrm{Al/Si} = \frac{0.5\,Q^2(1\mathrm{Al})}{Q^1 + Q^2 + Q^2(1\mathrm{Al})} \qquad \text{Eq. 5.15}$$

Two types of retarders, B and N, exhibited the same layered structure in the C-A-S-H gel, as demonstrated in **Fig. 5.20** . This finding aligns with the results obtained from XRD, TGA, and FTIR, confirming that the nature of the hydration products remains unchanged regardless of the retarder used. **Table 5.14** highlights key values derived from the ^{29}Si MAS NMR analysis, revealing the formation of solid species with shorter tetrahedral silicate chains (MCL) in OM2. Notably, the C-A-S-H composition for the B mixture was less protonated and exhibited a shorter chain length compared to the N mixture. This result indicates a slight reduction in the degree of silicate polymerization in the presence of retarder B. The lower polymerization degree in the C-A-S-H gels of the B mixture suggests that the silicate chains undergo less intense C-A-S-H syneresis (i.e., contraction of the silicate gel structure) during the polymerization process.

Table 5.14: Parameters obtained with ^{29}Si MAS NMR (**Fig. 5.20**).

Mixture Code	RD	RT	MCL	Al/Si
OM2	0.5 %	B	7.25	0.166
OM3	0.5 %	N	7.27	0.166

5.4.8. Life Cycle Assessment analysis

The environmental performance of AAMs has increasingly attracted the attention of researchers. However, in many performance-oriented studies, their environmental benefits have often been assumed without thorough validation or comprehensive assessment [231]. However, the majority of studies on the environmental impact of alkali-activated mixtures only focus on CO_2 emissions or global warming potential, without conducting a proper life cycle assessment [232]. Thus, a comparative LCA study was conducted following ISO14040 standard framework (ISO, 2006a) and ISO14044 (ISO, 2006b) guidelines to compare the eco-efficiency of the various optimized AAS mixtures. The functional unit is 1kg of AAS mixture. The life cycle inventory data was retrieved from the Ecoinvent v3.10 database [233], and life cycle modeling was performed using openLCA. The system boundary includes material fabrication and transportation, similar to previous studies on alkali-activated pastes [234]. A significant debate exists on whether slag should be allocated to some of the environmental impacts of steel production [232]. Arguments for treating it as a useful by-product tested different allocation procedures [235,236]. Those against it argue that slag is a waste product that should not be allocated to the steel manufacturing process [237]. As such, only the environmental impacts stemming from generating the slag are considered (i.e., quenching of hot slag, grinding, etc.).

The raw data for the LCA was used to calculate normalized environmental impact values for various ingredients using the openLCA program as follows:

Silicate: Market for sodium silicate, without water, in a 37% solution state | Cutoff, U - RoW

GGBS: Market for ground granulated blast furnace slag | Cutoff, U - US

Borax: Market for borax, anhydrous, powder | Cutoff, U - GLO

ZnO: Market for zinc oxide | Cutoff, U - GLO

Direct calculations were performed using these raw data values to obtain the environmental impact values from the openLCA program for each ingredient (**Table 5.15**).

Table 5.15: Normalized impact extracted from openLCA program.

Ingredients	AP	CH	FT	MT	TT	NRE	EP	HT	RD	ODP	POF
Silicate	6.43E-03	1.15E+00	1.23E+00	2.57E+03	3.50E-02	1.07E+01	2.32E-03	5.17E+00	5.17E+00	7.47E-09	3.64E-04
Slag	5.79E-04	1.15E-01	7.08E-02	1.89E+02	2.16E-03	1.60E+00	1.68E-04	3.74E-01	3.74E-01	1.03E-09	3.49E-05
Borax	7.40E-03	2.04E+00	8.87E-01	2.65E+03	2.19E-02	2.64E+01	2.89E-03	4.02E+00	4.02E+00	2.01E-08	4.78E-04
ZnO	2.60E-03	7.79E-01	6.44E-01	1.45E+03	2.15E-02	1.04E+01	1.14E-03	2.71E+00	2.71E+00	1.07E-08	1.75E-04

Subsequently, these values were multiplied by the proportion of each ingredient in the mixture (**Table 5.16**) to determine the contribution of each ingredient to the overall environmental impact.

Table 5.16: Proportion for each ingredient in the mixture.

Mixture Code	Silicate	Slag	Borax	ZnO
OM1	0.057	0.582	0.000	0.008
OM2	0.058	0.585	0.003	0.000
OM3	0.058	0.585	0.000	0.003
OM4	0.026	0.612	0.000	0.009
OM5	0.062	0.628	0.000	0.000
OM6	0.064	0.651	0.000	0.000
OM7	0.026	0.615	0.000	0.003

To calculate the contribution of each ingredient, the proportion of the ingredient in the mixture was multiplied by its corresponding LCA-derived impact value. The result was then divided by the total environmental impact value for the entire mix (**Table 5.17**) to determine the relative contribution of each ingredient.

Table 5.17: Total environmental impact for each mixture.

Mixture code	AP	CH	FT	MT	TT	NRE	EP	HT	RD	ODP	POF
OM1	7.25E-04	1.39E-01	1.16E-01	2.68E+02	3.43E-03	1.63E+00	2.39E-04	5.35E-01	5.35E-01	1.11E-09	4.25E-05
OM2	7.36E-04	1.41E-01	1.15E-01	2.68E+02	3.36E-03	1.64E+00	2.42E-04	5.32E-01	5.32E-01	1.10E-09	4.31E-05
OM3	7.20E-04	1.37E-01	1.15E-01	2.64E+02	3.36E-03	1.59E+00	2.36E-04	5.28E-01	5.28E-01	1.07E-09	4.21E-05
OM4	5.44E-04	1.07E-01	8.08E-02	1.95E+02	2.42E-03	1.35E+00	1.73E-04	3.87E-01	3.87E-01	9.14E-10	3.23E-05
OM5	7.62E-04	1.44E-01	1.20E-01	2.78E+02	3.52E-03	1.67E+00	2.49E-04	5.55E-01	5.55E-01	1.11E-09	4.45E-05
OM6	7.88E-04	1.49E-01	1.25E-01	2.87E+02	3.64E-03	1.73E+00	2.58E-04	5.74E-01	5.74E-01	1.15E-09	4.60E-05
OM7	5.32E-04	1.03E-01	7.76E-02	1.88E+02	2.31E-03	1.30E+00	1.68E-04	3.74E-01	3.74E-01	8.63E-10	3.15E-05

Table 5.18 shows the percentage contribution of different ingredients (Silicate, Slag, ZnO, and B) to various environmental impact categories for each mixture (OM1 to OM7). The results indicated that silicate generally contributed a significant portion across most impact categories, except for OM4 and OM7, where its contribution was lower due to the low activator dosage (4%). On the other hand, slag had a greater impact than silicate in certain categories, particularly in non-renewable energy resources NRE, RD, and ODP. In mixtures such as OM4 and OM7, slag contributed more than 65% to climate change and other key categories. ZnO consistently had the smallest contribution across all impact categories in most mixtures. However, its highest contributions were observed in OD and E in OM4, where it accounted for 10.06% of ODP and 5.67% of EP. Retarder B made a minor contribution across all categories, with its highest impact in NRE (5.29%) and ODP (6.01%).

Table 5.18: Percentage of Contribution for each Ingredient (%).

Mixture Code	Ingredients	AP	CH	FT	MT	TT	NRE	EP	HT	RD	ODP	POF
OM1	Silicate	50.57	47.34	60.05	54.55	58.20	37.63	55.20	55.11	55.11	38.35	48.83
	Slag	46.49	48.07	35.41	41.01	36.65	57.13	40.90	40.73	40.73	53.77	47.78
	ZnO	2.94	4.59	4.54	4.44	5.15	5.24	3.90	4.16	4.16	7.88	3.39
OM2	Silicate	50.67	47.55	61.59	55.52	60.33	37.89	55.47	56.36	56.36	39.41	48.99
	Slag	46.01	47.69	35.87	41.23	37.53	56.82	40.60	41.15	41.15	54.58	47.36
	B	3.31	4.76	2.53	3.26	2.14	5.29	3.93	2.49	2.49	6.01	3.66
OM3	Silicate	51.79	48.99	62.02	56.35	60.35	39.14	56.82	56.82	56.82	40.55	50.15
	Slag	47.02	49.14	36.12	41.84	37.54	58.71	41.59	41.49	41.49	56.16	48.48
	ZnO	1.19	1.88	1.85	1.81	2.11	2.15	1.58	1.69	1.69	3.29	1.37
OM4	Silicate	30.74	28.06	39.47	34.24	37.65	20.74	34.83	34.75	34.75	21.25	29.27
	Slag	65.14	65.67	53.65	59.33	54.66	72.60	59.50	59.21	59.21	68.69	66.05
	ZnO	4.12	6.27	6.88	6.43	7.68	6.65	5.67	6.04	6.04	10.06	4.68
OM5	Silicate	52.31	49.82	63.10	57.28	61.55	39.90	57.64	57.69	57.69	41.82	50.74
	Slag	47.69	50.18	36.90	42.72	38.45	60.10	42.36	42.31	42.31	58.18	49.26
OM6	Silicate	52.20	49.71	63.00	57.18	61.45	39.80	57.53	57.59	57.59	41.72	50.63
	Slag	47.80	50.29	37.00	42.82	38.55	60.20	42.47	42.41	42.41	58.28	49.37
OM7	Silicate	31.41	29.05	41.05	35.50	39.36	21.52	35.95	35.94	35.94	22.53	30.02
	Slag	66.89	68.34	56.07	61.82	57.42	75.70	61.70	61.55	61.55	73.18	68.05
	ZnO	1.69	2.61	2.88	2.68	3.23	2.77	2.35	2.51	2.51	4.29	1.93

Fig. 5.21 provides a comparison of the normalized impacts across different mixtures (OM1 to OM7) for several environmental impact categories, with all results presented relative to OM1. Since OM1 represented the most flowable mixture. In general, OM5 and OM6 exhibit relatively higher impacts across most categories, setting the baseline for comparison. OM4 and OM7 show noticeably lower impacts in several areas, particularly in AP, CH, and FT due to their lower

activator dosages. On the other hand, OM6 stands out with a significantly higher impact in NRE compared to other mixtures. These results emphasized that high activator dosages significantly influence environmental impacts across multiple categories. These findings are consistent with previous study on the embodied carbon of meta-silicate activator [238].

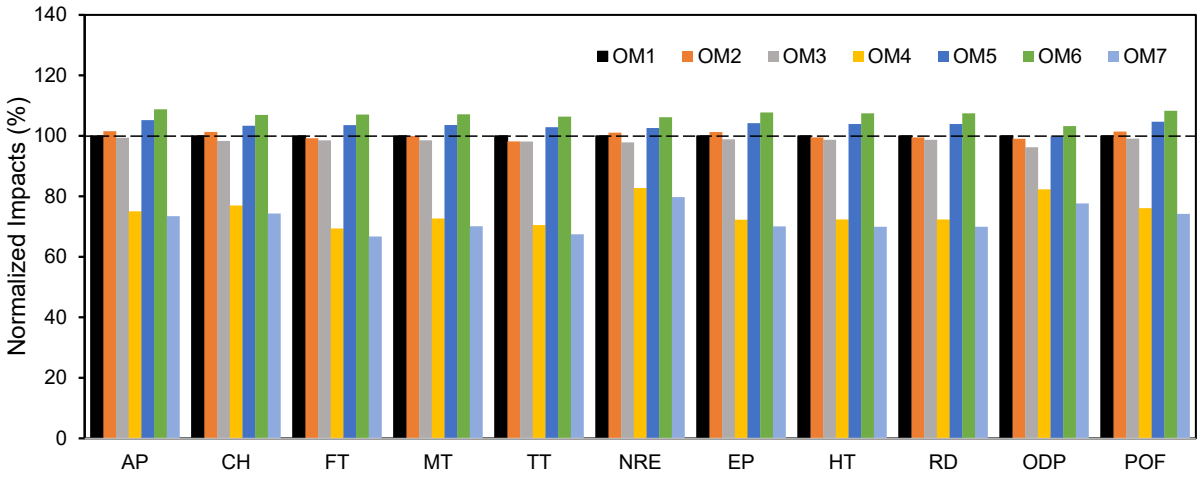

Fig. 5.21: Impact categories of the various optimized mixtures relative to the OM1.

5.5. Conclusions

This study offers a fundamental understanding of how different dosages and types of retarders, in combination with varying w/s ratios and AD, affect the rheological properties of AAS. The AD and w/s ratio play the most crucial role in controlling the dissolution rates of slag particles and the formation of various hydration products, which directly impact the rheological properties. Besides, providing comparative LCA for various optimized mixtures. Based on the results, the following conclusions can be drawn:

- Increasing the activator dosage resulted in higher flowability, regardless of w/s, retarder type, and dosage used within the tested range. This is evident as M4, M8, M12, and M16 achieved high flow diameters despite variations in retarder type, dosage, and w/s ratio.
- Borax is the most effective retarder, reducing yield stress by forming a calcium-based borate layer that delays hydration and crystal formation. However, nano zinc oxide is the most effective retarder for enhancing flowability in AAS mixtures, as small amounts significantly extend the induction period, delaying the formation of the C–(N)–A–S–H gel.
- ANOVA analysis revealed that w/s followed by activator dosage had the highest effect on all measured properties except time of second peak and compressive strength.

- Regression models with a reliable accuracy were developed, depicting good agreements between the measured and predicted values for all measured properties.
- The quantity and formation rate of hydration products were highly controlled by the optimizing parameters.
- The LCA results showed that silicate and slag are the main contributors to most environmental impacts, with slag having a higher impact in certain categories like non-renewable energy resources and ozone depletion.

Chapter 6: Influence of Viscosity Modifier Addition Methods on the Rheological Behavior of Alkali-Activated Slag Systems

VMAs, such as Sika Stabilizer, are commonly used in conventional concrete to enhance its rheological properties, particularly under challenging conditions or when specific performance requirements must be met. These admixtures primarily function by modifying the viscosity of the cement paste, thereby improving mix stability and workability, especially in cases of high water content. This functionality makes VMAs essential for applications like self-consolidating concrete (SCC), lightweight concrete, and mixes containing recycled aggregates. In AAMs, however, the reaction mechanism differs significantly from conventional concrete due to the polymerization process involved in their formation. This raises the question of whether VMAs would have a comparable effect on the rheological properties of AAMs, particularly in systems with high water content. Specifically, this study focuses on one-part AAS systems activated with meta-silicate.

Based on the investigation conducted in Chapter 3, which examined the addition sequences of the main ingredients, the optimal sequence was identified as the dry mixing of the activator and precursor before adding water. This sequence achieved reasonable flowability and setting time. Building on these findings, the current chapter adopts the optimal mixing sequence established in Chapter 3 to investigate the impact of VMA on the rheological behavior of one-part AAS. This study focuses on critical parameters, such as the timing and method of VMA addition. The VMA will be incorporated either dissolved in the mixing water or added separately. Understanding the influence of these variables is crucial for optimizing the performance of AAMs in applications that demand enhanced flowability and stability. The findings presented in this chapter will provide valuable insights into the role of VMAs in advancing the practical application of one-part AAS in sustainable construction.

6.1. Introduction

In the past century, research on AAMs within the construction industry has progressed considerably. Alkali-activated concrete, recognized as one of the most promising emerging technologies, has attracted considerable attention from both academic and industrial sectors [184]. AAS systems are gaining significant attention as sustainable alternatives to conventional OPC due

to their reduced environmental impact and promising mechanical properties [186,187,239]. Compared to OPC concrete of the same strength grade, the production of AASC consumes 2.4% less energy and produces 20.2% fewer CO_2 emissions [183]. However, challenges such as the high viscosity of fresh mixtures and susceptibility to segregation in highly fluid mixtures hinder their practical application [65,127,128]. To address these issues, VMAs have been used in cementitious composites to enhance the rheology, water retention, and stability of fresh mixtures [240,241]. While the interaction between VMAs and OPC systems is relatively well understood, the behavior of VMAs in AAS systems remains less explored [127].

VMAs are water-soluble polymers that increase the viscosity of mixing water, enhancing the ability of cement paste to suspend its components effectively [242]. VMAs are based on long-chain hydrophilic polymers, often derived from modified polysaccharides such as cellulose ethers, starches, and gums [67]. These admixtures work by adsorbing and retaining water molecules within their structure reducing the amount of free water available and limiting flowability. Additionally, VMAs further increase viscosity by forming a bridged network with binder particles and entangling with each other [67,68,243,244]. Furthermore, VMAs are widely incorporated into highly fluid cementitious mixtures to prevent solid-liquid separation and improve mixture stability [245]. Although their main role is to enhance cohesion, VMAs notably influence the material's rheological behavior, especially by modifying the properties of the aqueous phase [245].

Several studies have investigated the role of VMAs in modifying rheology and improving water retention in cementitious systems [67,68,240]. For instance, VMAs can significantly reduce the slump and spread diameter of fresh mixtures, particularly when added at higher dosages (0.12–0.36% of binder mass) [240]. Additionally, viscosity modifiers like super absorbent polymers (SAPs) have shown promise as rheology modifiers in 3D printable cementitious materials, offering advantages such as improved structural build-up and reduced shrinkage, with less impact on flowability compared to hydroxypropyl methylcellulose (HPMC)-based VMAs [243]. On the other hand, other studies had primarily focused on the effects of VMAs combined with high-range water reducers or superplasticizers on cement reactions [66–68], often in OPC and limestone calcined clay cement (LC_3) systems [246–248].

While the interaction between OPC and VMAs is well established, the behavior of VMAs appears to differ in AAS systems. Existing literature provides insights into how increasing VMA dosage affects the hydration kinetics of OPC. However, the influence of various mixing approaches and

VMA addition timings on the hydration kinetics of AAS mixtures remains unexplored. The investigated approaches include adding VMA separately (undissolved in water) or dissolved in water, as well as two addition timings: early addition (1 minute after dry mixing of the powder ingredients) and delayed addition (25 minutes after mixing and resting). This study aims to address this gap by investigating the impact of VMA on the fresh properties, rheological behavior, hydration kinetics, phase composition, microstructure, and compressive strength of AAS mixtures. By examining these properties, this study provides a comprehensive understanding of the impact of VMAs on the performance of AAS systems in both fresh and hardened states. The findings are expected to contribute to the development of more stable and workable AAS composites, enhancing their suitability for diverse applications such as 3D printing, ready-mix concrete, and construction in low-temperature environments.

6.2. Research Significance

Most research focuses on the combined use of VMAs with high-range water-reducing admixtures (HRWRAs) to evaluate their behavior and performance. The effect of using VMAs alone on the rheological properties of conventional cement paste has been explored in only a few studies. However, since HRWRAs are generally incompatible with AAS systems, this study aims to evaluate, for the first time, the compatibility and functionality of VMAs in AAS systems. The investigation examines different addition times (early and delayed addition) and methods (separate addition, undissolved in water, or dissolved in water) to provide a comprehensive understanding of their impact under varying water contents. The findings are expected to offer valuable insights into how VMA addition influences the mineral hydration process in one-part AAS systems, providing a detailed understanding of the rheological behavior of AAS after incorporating VMAs.

6.3. Experimental Work

6.3.1. Materials

GGBS was used as the precursor for all mixtures, with a specific gravity of 2920 kg/m^3, a Blaine fineness of 515 m^2/kg, an average particle diameter of 14.5 μm, and a basicity coefficient of 1.06. Anhydrous sodium meta-silicate (Na_2SiO_3) was used as a powder activator and added at a constant dosage of 10% by GGBS weight [42,151]. The granular texture and angular particle morphology of GGBS and Na_2SiO_3 are shown in **Fig. 6.1.** A constant dosage of a commercially available VMA meeting the specifications of ASTM C494 for Type S admixtures was used in all mixtures at 1%

of the slag weight, determined through laboratory trials. The chemical and physical properties of the VMA are detailed in **Table 6.1**. The used w/b were 0.45 and 0.50 [249].

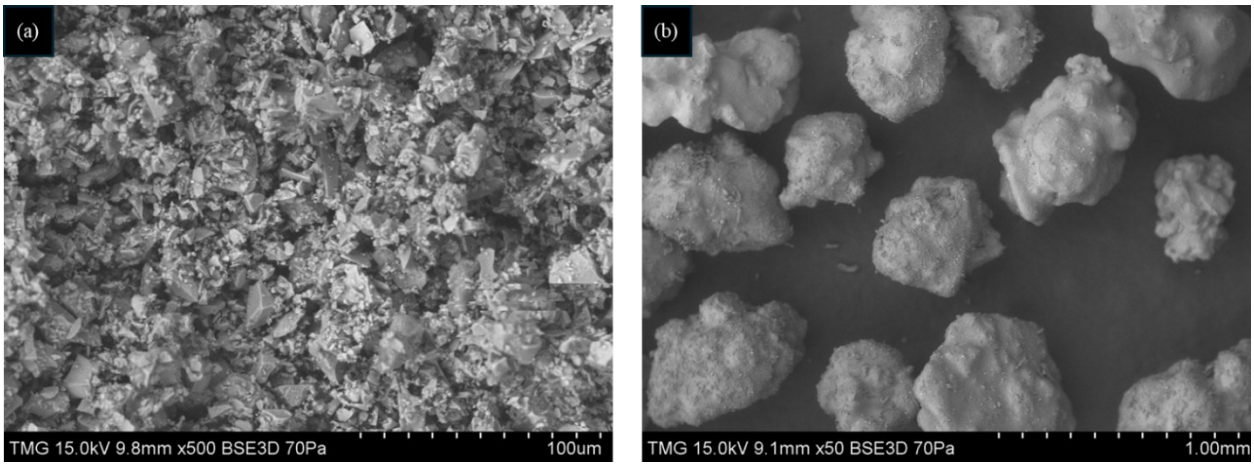

Fig. 6.1: Morphology of a) slag and b) sodium meta-silicate.

Table 6.1: Chemical and physical properties of VMA.

Total solids (%)	pH	Specific gravity
23	7.0	1.02

6.3.2. Mixing Methods

Fig. 6.2 illustrates different mixing procedures, which last for 30 minutes. Two key factors were investigated during mixing: the timing of VMA addition and the method used [250]. For the timing, VMA was either added after one minute of dry mixing of GGBS and Na_2SiO_3 or after a 25-minute, just before remixing following a 20-minute rest period. For the method of addition, VMA was either dissolved in 20% of the total mixing water or was incorporated directly into the mixture without being dissolved (separate addition). These variations were tested across different mixtures.

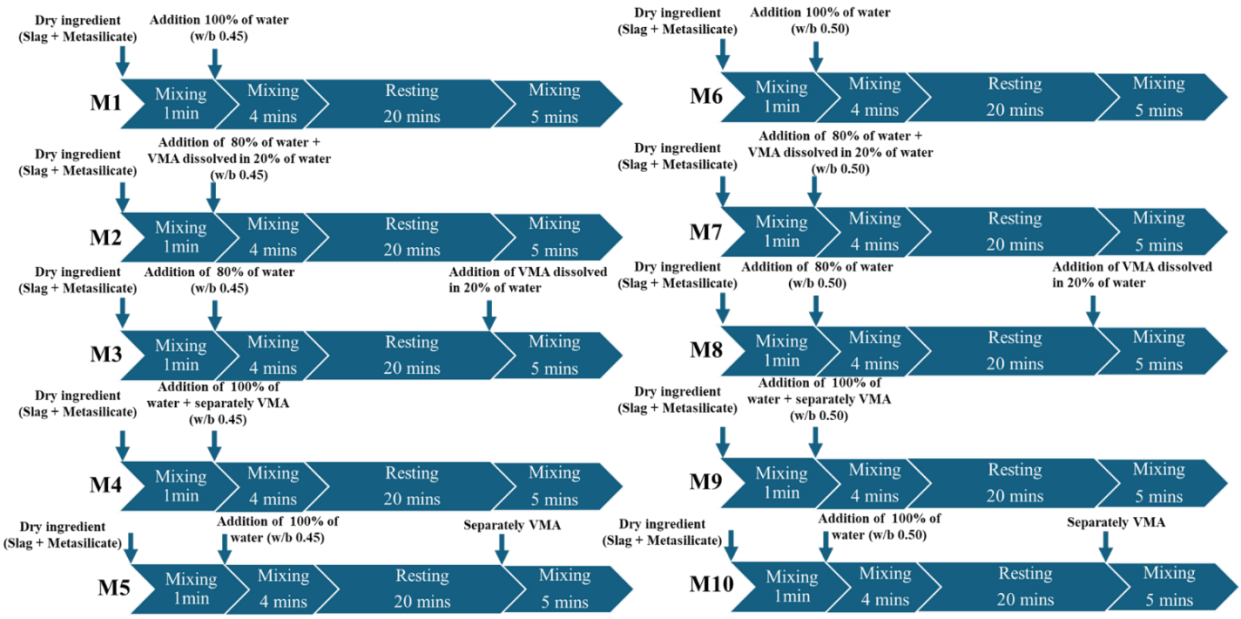

Fig. 6.2: Mixing procedures for all mixtures.

6.3.3. Mixtures preparation and testing procedure

All mixtures were prepared, cured, and tested under laboratory ambient conditions (T of 23 ± 2 °C and RH of 55 ± 5%). The flowability was assessed using the mini-slump cone test immediately after mixing [96]. Upon removing the filled mini cone, the D was recorded as the average of two measurements taken in perpendicular directions, representing the initial flow diameter. The mini-slump test was repeated every 2.5 minutes for the first 10 minutes, then at 5-minute intervals until there was no further spread (i.e. D_f = 100 mm), marked as the end of the flowability life [96]. The initial and final setting times were determined following ASTM C191-99 (Standard Test Method for the Time of Setting of Hydraulic Cement by Vicat Needle) [154]. These times were measured from the point of water addition to the dry ingredients (i.e. the wetting point) [155]. Samples were placed in a vicat cone, covered with a plastic sheet to avoid evaporation, and stored under ambient conditions.

Isothermal calorimetry was employed to assess the early hydration rate. For mixtures with a w/b ratio of 0.45, H1 represents the control mixture, H2 represents VMA added dissolved in 20% of the mixing water, and H3 represents VMA added separately. For mixtures with a w/b ratio of 0.50, H4 is the control mixture, H5 represents VMA added dissolved in 20% of the mixing water, and H6 represents VMA added separately. The test was conducted following ASTM C1679 (Standard Practice for Measuring Hydration Kinetics of Hydraulic Cementitious Mixtures Using Isothermal

Calorimetry) [156]. Approximately 70 grams of paste was prepared externally for each mixture and then loaded into the isothermal calorimeter. The heat evolution and cumulative heat release were recorded and normalized by the dry binder mass. The chamber temperature was maintained at 25°C for 68 hours.

Cubic specimens (50 mm) were used to evaluate compressive strengths at 3, 7, and 28 days, following ASTM C109-20 (Standard Test Method for Compressive Strength of Hydraulic Cement Mortars) [144]. Specimens were de-molded after three days and stored in sealed plastic bags under ambient laboratory conditions until the designated testing age.

Furthermore, unrestrained one-dimensional deformations (i.e. drying shrinkage) were measured using a comparator equipped with a dial gauge with an accuracy of 10 μm/m. Prismatic specimens (25 × 25 × 285 mm) were prepared according to ASTM C157/C127-17 (Standard Test Method for Length Change of Hardened Hydraulic-Cement Mortar and Concrete) [158]. Three days after casting, specimens from each mixture were exposed to ambient laboratory conditions for drying, with the first length measurement taken at 72 hours. Drying shrinkage and mass loss of the AAS paste were monitored for up to one month. To assess density variations and detect any internal defects or cracks, UPV tests were performed at 3, 7, and 28 days according to ASTM C597 (Standard Test Method for Pulse Velocity Through Concrete) [145].

A Brookfield R.S.T. rheometer, fitted with a four-blade vane (60 mm length, 30 mm diameter), was used to monitor the rheological evolution of the paste mixtures as shown in **Fig. 6.3**. Flow curve tests were recorded, with sample loading into the rheometer's measuring cup taking approximately 5 minutes. The shear protocol began with a high-speed pre-shear to break down any structure build-up, followed by a 30-second relaxation period to dissipate residual stresses [160]. The shear rate was then gradually increased and decreased. Dynamic yield stress and plastic viscosity were calculated using the Bingham model (Eq. 6.1) on the descending part of each flow curve [208,248]. The Bingham model is defined by yield stress needed for flow initiation and a constant slope representing plastic viscosity between shear stress and shear rate [210,251].

$$\tau = \tau_0 + \mu \cdot \gamma \qquad \textbf{Eq. 6.1}$$

Where: τ is the shear stress; τ_0 is the dynamic yield stress in Pa; μ is the plastic viscosity in Pa ·s.; γ is the shear rate in 1/s.

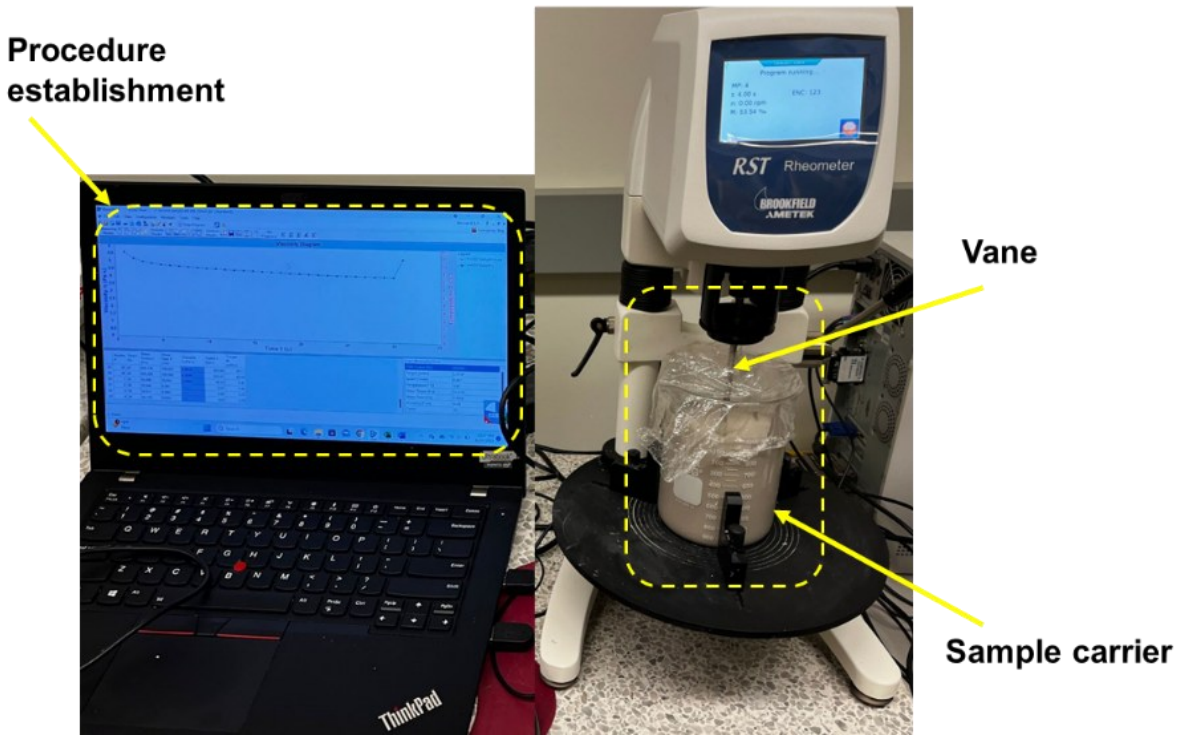

Fig. 6.3: Brookfield R.S.T. rheometer setup.

XRD was employed to examine microstructural development and the formation of hydration products. Small pieces from 3-day-old specimens of all mixtures were ground into powder for testing. XRD was conducted according to ASTM C1365-18 (Standard Test Method for Determination of the Proportion of Phases in Portland Cement and Portland-Cement Clinker Using X-Ray Powder Diffraction Analysis) using a Bruker D8 Advance diffractometer (Cu Kα radiation, 1.5406 Å) with an imaging plate detector, collecting data from $10^{o} < 2\theta \leq 90^{o}$ [161]. TGA was conducted to observe the development of hydration products. Small pieces from 3-day-old specimens were ground to a powder and sieved through a No. 200 sieve. A sample weighing approximately 10 mg was heated at a rate of 10 °C/min up to 1000°C. Data and curves were analyzed using TA Instruments thermal analysis software [96]. FTIR was employed to assess the change of functional groups of each mixture on 3-day-old powder samples. FTIR spectra were obtained using a Nicolet 6700 spectrometer (Thermo Scientific), with frequencies scanned in the range of 4000–500 cm^{-1}.

Additionally, SEM was performed on small chunks from selected specimens (**Fig. 6.4**) using a Hitachi S-3400N SEM at an accelerating voltage of 15.0 kV (**Fig. 6.5**). This was coupled with EDS using a JEOL 35-cf spectrophotometer for elemental mapping and spot analysis [161].

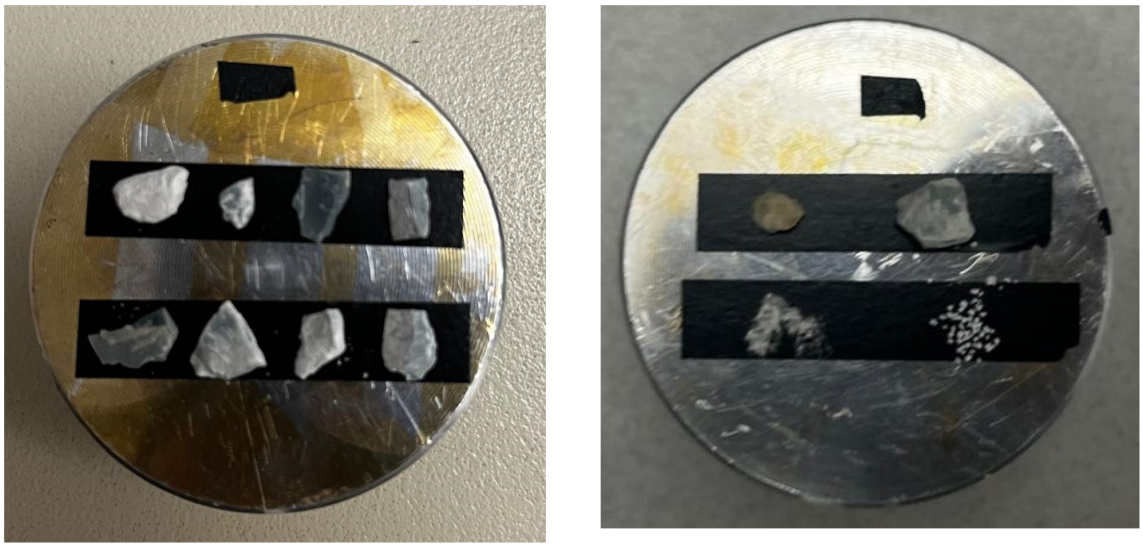

Fig. 6.4: SEM samples preparation.

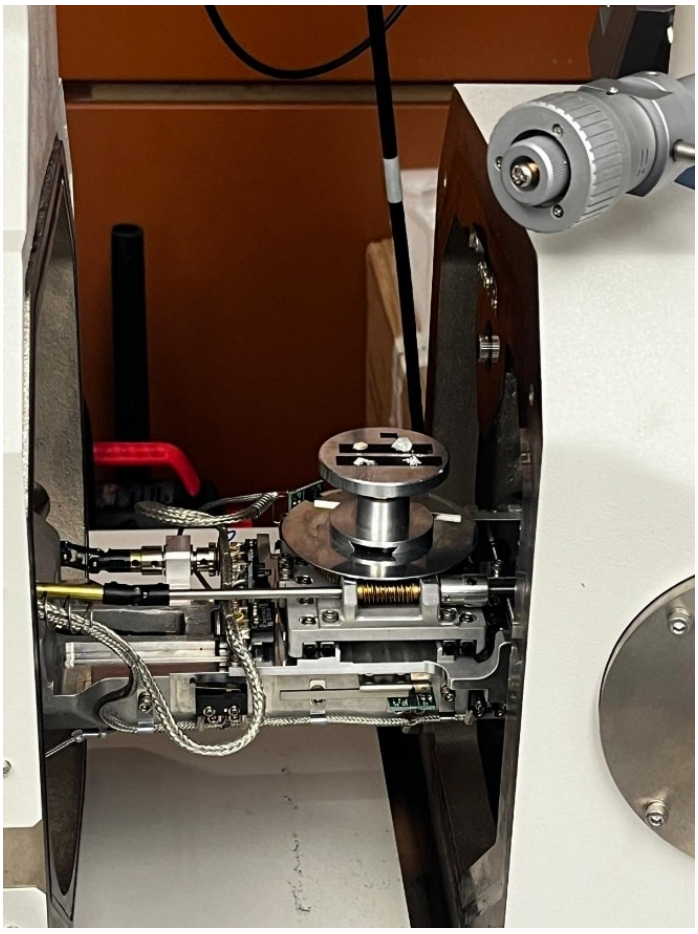

Fig. 6.5: SEM instrument setup.

The chemical analysis of the extracted AAS pore solution was performed using ICP-MS to measure the concentrations of Na, Si, Ca, K, and Mg. The solutions were stored at 5°C until testing,

then diluted 1000 times with a mixture of 1.0% nitric acid (HNO_3) and 0.5% hydrochloric acid (HCl) before analysis. pH and conductivity were measured immediately after extraction using a pH meter and a conductivity meter, with electrical conductivity serving as an indirect indicator of alkalinity due to the high conductivity of hydroxide ions [212].

6.4. Results and Discussion

6.4.1. Fresh properties

6.4.1.1. Mini-slump

Fig. 6.6 shows the mini-slump result for various mixtures considering the addition method, the timing of VMA addition, and the w/b ratios. At a high w/b ratio, the effects of the addition method and timing of VMA were marginal.

Results indicated the negative effect of VMA on the flowability of AAS. For a w/b ratio of 0.45, M1 has the highest initial flow diameter reaching around 170 mm. This is ascribed to the release of Ca^{2+} cations, which react with silicate species, forming double-charged cations around precursor particles. This causes repulsion between these charged particles (high zeta potential), enhancing flowability [42,162]. M2 and M3 showed the lowest flow diameters, under 110 mm, indicating increased stiffness. When VMAs dissolve in water, they create a network of long-chain polymers binding water molecules through hydrogen bonds, forming a gel-like structure [67,68,243,244]. This limited amount of available water for activator dissolution (i.e. 80%) decreases the silicate species needed for slag dissolution. Additionally, these polymers can adsorb onto slag particle surfaces, creating steric hindrance that prevents silicate species produced by the activator [59]. This was confirmed by the presence of unreacted slag particles, as observed by SEM, and will be shown later. In contrast, M4 and M5 exhibited higher initial flow diameters compared to M2 and M3, measuring 120 mm and 135 mm, respectively. This increase could be due to the redistribution of ions, such as calcium, sodium, and silicate, from the slag and activators, which occurs when the VMA is added separately. This observation is supported by the chemical ion concentration analysis, which will be presented later. By adsorbing onto slag particle surfaces, the VMA influences the hydration process by limiting water availability and slowing ion mobility, which enhances dispersion and initial flowability.

Conversely, there was minimal variation in the initial flow diameter across all mixtures, regardless of the timing or method of VMA addition for the w/b ratio of 0.50. This can be attributed to the

large amount of water, which was sufficient to dissolve the activator without being significantly impacted by the VMA's water-retaining and viscosity-modifying effects.

Generally, mixtures with a low w/b ratio of 0.45 had lower initial flow diameters across all addition times and methods compared to those with a w/b ratio of 0.50. This reduction is attributed to the decreased water content and the competition between silicate species and VMA polymers for water. Similar trends were observed regarding the effect of VMA addition timing and method, reinforcing the conclusion that adding VMA generally reduces flow due to increased viscosity in the paste as will be discussed later in plastic viscosity results.

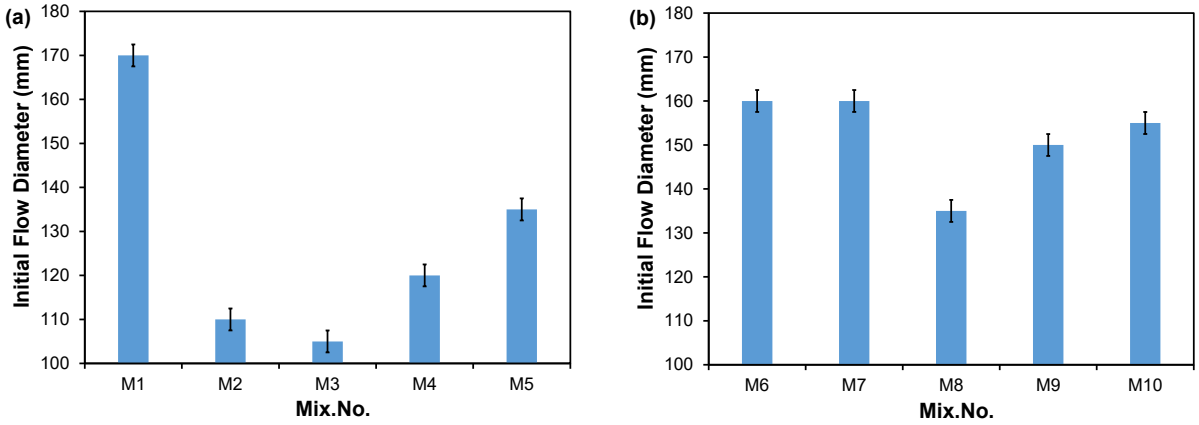

Fig. 6.6: Initial flow diameter results for various mixtures a) w/b =0.45 and b) w/b = 0.50.

The results of flow retention for different AAS mixtures with various w/b ratios were illustrated in **Fig. 6.7**. For the w/b ratio of 0.45, M1 demonstrated the longest flow retention, initially achieving a flow diameter of approximately 170 mm, which gradually decreased over about 65 minutes until it lost all flowability (i.e. D_f = 100 mm). In contrast, M2 and M3 experienced a rapid decline in flow, with flow diameter dropping sharply within the first 5 minutes. This quick loss in flowability can be attributed to the early addition of VMA, which accelerated the setting process [68,243]. M4 had a better flow retention compared to M2 and M3. The separate addition of VMA (i.e. M4 and M5) increased viscosity more gradually, resulting in better flow retention than mixtures where VMA was dissolved in water (i.e. M2 and M3).

On the other hand, for the w/b ratio of 0.50, M6 showed a gradual decrease in flow diameter over time, indicating better flow retention compared to other mixtures (i.e. M7, M8, M9, and M10). The high water content contributed to prolonged flow retention, as the increased initial flowability and long setting time reduced early stiffening. M8 had the shortest flow retention among all mixtures with a 0.50 w/b ratio. The delayed addition of VMA increased stiffening due to the

reduced water availability (80%) for early dissolution of the activator [163]. Among all mixtures, M10 exhibited the longest flow retention, highlighting the advantage of delayed, separate VMA addition in maintaining flowability.

It can be concluded that all mixtures with a w/b ratio of 0.50 exhibited better flow retention than the corresponding mixtures with a w/b ratio of 0.45. This is attributed to the higher water content in mixtures with a w/b ratio of 0.50 compared to those with a w/b ratio of 0.45. The early addition of VMA, particularly when dissolved in water, accelerates flow loss. However, the overall reduction in flow diameter is slower in mixtures with a w/b ratio of 0.50 compared to those with a w/b ratio of 0.45, as the high water content moderates the VMA's effect. Despite this, the timing and method of VMA addition significantly influence flow life, with delayed separate addition proving to be the most effective approach for maintaining flowability across both w/b ratios.

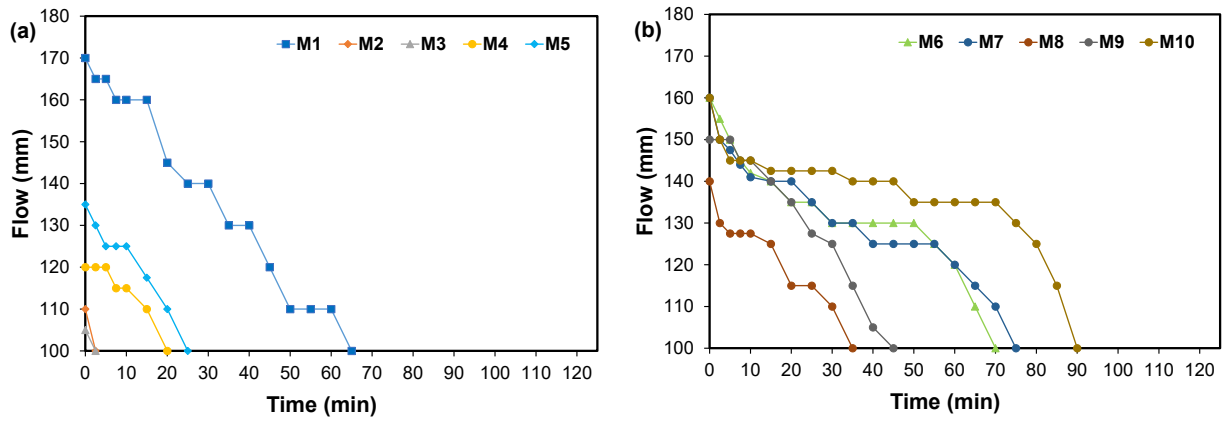

Fig. 6.7: Flow diameter results over time for various mixtures a) w/b =0.45 and b) w/b = 0.50.

6.4.1.2. Setting time

Fig. 6.8 shows the initial and final setting time of AAS mixtures. The VMA addition time and method had a great influence on the results. M1 exhibited the longest initial and final setting times (671 minutes and 1461 minutes, respectively) among all mixtures, aligning with the reported trends of initial flow diameter and flow retention. The early and delayed addition of VMA dissolved in water significantly shortened the setting time compared to the control mixture (M1). For instance, in M2, the initial and final setting times were reduced by 66.62% and 54.89% compared to M1, respectively. M3 recorded the shortest setting times, with 192 minutes for the initial and 353 minutes for the final. This can be attributed to the consumption of the available water during slag dissolution. Consequently, the delayed addition of VMA allowed the AAS paste to initiate hydration and form hydration products that wrapped around unreacted slag particles, leading to

agglomeration. Once the VMA was added, it rapidly accelerated the hydration reactions, significantly shortening the setting times [169]. The early separate addition of VMA extends the setting time more than the addition of VMA dissolved in water. For instance, M4 exhibited longer setting times compared to M2, with 53.52% and 18.13% increases in initial and final setting times, respectively. This can be attributed to the early separate addition of VMA in M4, which resulted in less efficient water retention compared to M2. Additionally, M5 exhibited a longer setting time compared to M3 by 193% and 122% for initial and final setting time, respectively.

For the w/b ratio of 0.50, The early and delayed addition of VMA dissolved in water slightly shortened the setting time compared to the control mixture (M6). For instance, M7 exhibited slightly shorter setting times by 7.03% and 3.93% for initial and final setting times compared to M6, respectively. M8 had the shortest setting times among all mixtures, with initial and final setting times of 495 minutes and 885 minutes, respectively. The early separate addition of VMA shortened the setting time more than the addition of VMA dissolved in water. For instance, M9 showed shorter setting times than M7 by 18.14% and 8.61% for initial and final setting times. Conversely, M10 had a longer setting time compared to M8 by 26.22% and 21.40% for initial and final setting times, respectively. The separate delay addition of VMA resulted in longer setting times due to the slower distribution of VMA in the paste, confirming the results of the mini-slump test.

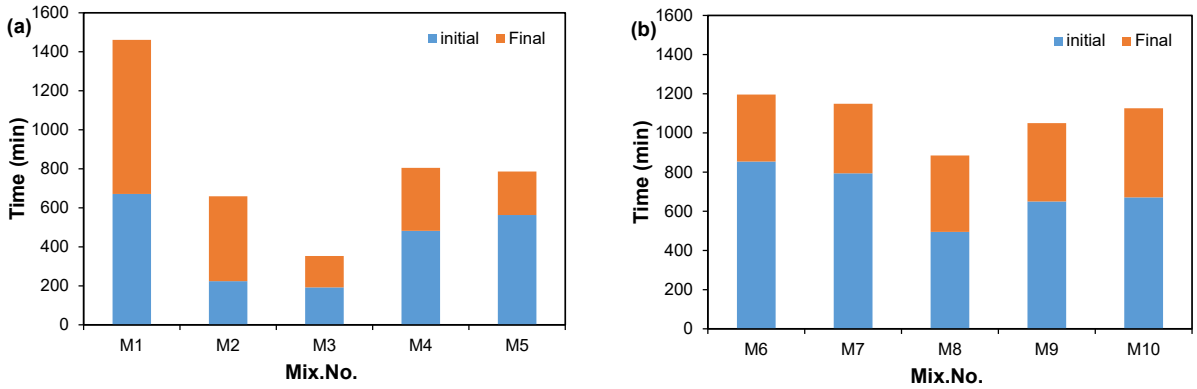

Fig. 6.8: Setting time results for various mixtures a) w/b =0.45 and b) w/b = 0.50.

6.4.1.3. Heat flow profile (Isothermal calorimetry)

All AAS mixtures demonstrated comparable heat flow profiles characterized by five distinct stages: dissolution, induction, acceleration, deceleration, and the steady period [149,165]. The impact of the VMA addition method on the hydration kinetics of AAS mixtures is predominantly influenced by the water content, as illustrated in **Fig. 6.9**. The rapid heat release observed in AAS

paste is a distinctive characteristic of its quick hydration reactions. This is attributed to the high activator dosage (i.e. 10%), which rapidly increases the pH, leading to a quick dissolution rate of slag. Results showed that the incorporation of VMA may have introduced steric hindrance or increased viscosity, thereby moderating the hydration rate and reducing the exothermic heat.

For a w/b ratio of 0.45, the dormant period was shorter for mixtures with VMA (H2 and H3) compared to H1, with reductions of 13.01% and 24.26% for H2 and H3, respectively. Additionally, the hydration peaks for H2 and H3 were lower by 60.38% and 53.85% compared to H1, respectively. This underscores the dominant effect of VMA addition time on reaction kinetics, regardless of the method of addition, due to the VMA's influence on reaction rate and paste stability, as demonstrated in the flow and setting time results. The total heat for H2 indicates a slow chemical reaction, attributed to the limited water available for activator dissolution (i.e. 80%), which reduces the silicate species required for slag dissolution as explained earlier. However, with separate additions, the low competition between the activator and VMA for water may explain the higher hydration peak of H3 compared to H2.

For a w/b ratio of 0.50, the dormant period remained constant across all mixtures. However, the separate addition of VMA in H6 had a more significant effect on slowing the hydration process compared to incorporating VMA dissolved in water (H5). For instance, H6 exhibited a lower hydration peak, reduced by 3.30% and 8.66% compared to H4 and H5, respectively. This reduction may be attributed to the separate addition of VMA, which redistributes ions (i.e. calcium, sodium, and silicate) from the slag and activators (**Table 6.4**). By adsorbing onto slag particle surfaces, the VMA limits water availability and slows ion mobility, creating a slight physical barrier to the hydration process. The cumulative heat release was similar for all mixtures with a w/b ratio of 0.50, highlighting the relatively minor effect of VMA on hydration kinetics in mixtures with higher water content. Generally, a high w/b ratio results in low thermal power peaks as the increased water content dilutes the paste, reducing the concentration of reactive ions, which in turn slows the hydration reactions and lowers the total heat release.

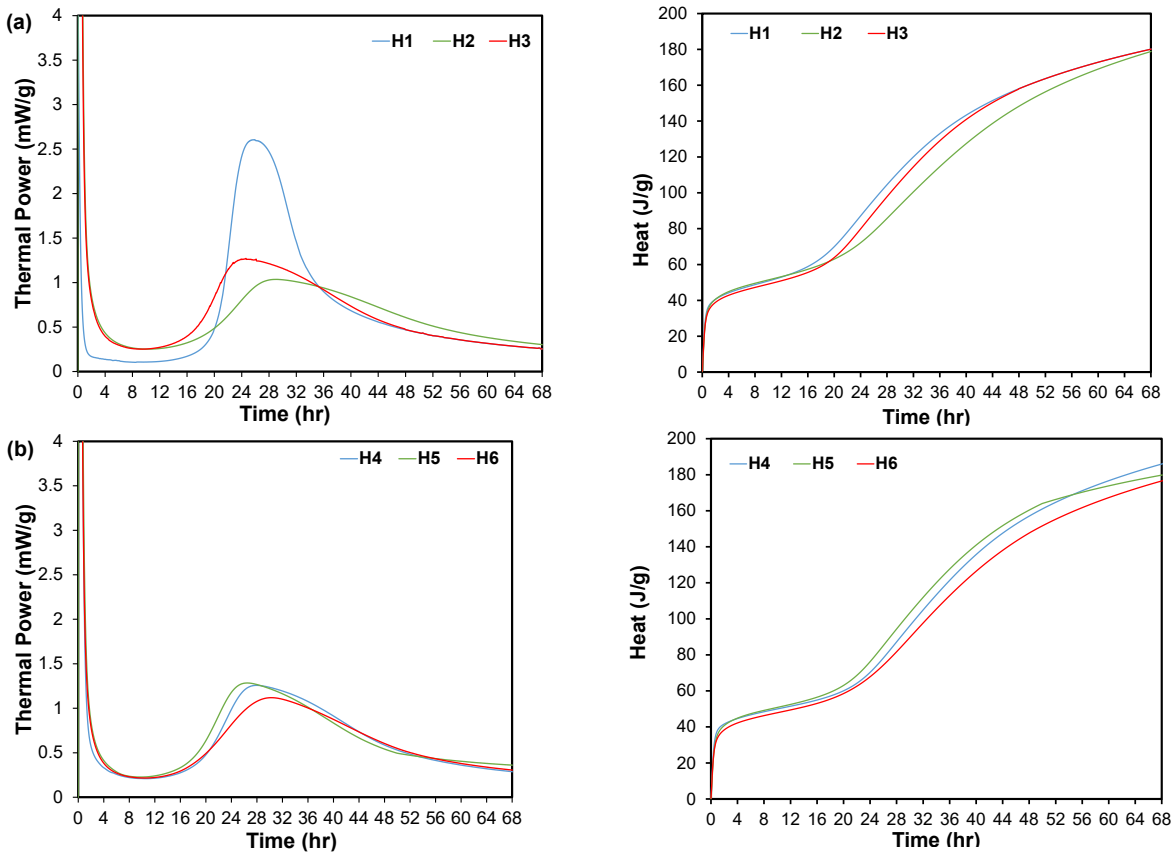

Fig. 6.9: Heat of hydration and cumulative heat for various mixtures a) w/b =0.45 and b) w/b = 0.50.

6.4.1.4. Flow curve tests

The shear stress and shear rate responses of all mixtures followed the Bingham fluid model, with correlation coefficients (R^2) exceeding 0.98, as shown in **Fig. 6.10**. For w/b ratio 0.45, M1 exhibited the lowest shear stress across all shear rates (132.6 Pa), indicating that the AAS paste had a low resistance to flow. Moreover, it had a dynamic yield stress of 18.35 Pa, and the least viscosity (1.16 Pa.s) as depicted in **Fig. 6.11**. In contrast, M2 and M3 demonstrated significantly higher shear stress, approximately three times that of M1. This can be attributed to the significant effect of the addition of VMA dissolved in water which reduced flowability and setting time as explained earlier. Interestingly, M3 showed a more notable increase in shear stress due to the delayed addition of VMA which allowed some structural buildup in the paste. Additionally, the degree of water retention and the availability of free water to lubricate the paste decreased with the dissolved VMA. The addition of VMA also enhanced pseudo-plasticity or shear thinning behavior [242]. This was confirmed by the higher dynamic yield stress in these mixtures due to the entanglement and interconnection of VMA polymer chains at low shear rates [242,245]. For

instance, the dynamic yield stress was 51.74 Pa for M2 and 44.63 Pa for M3. M4 and M5 exhibited lower shear stress, yield stress, and plastic viscosity compared to M2 and M3. Specifically, M4 had a shear stress of 417.83 Pa, a yield stress of 35.54 Pa, and a plastic viscosity of 3.82 Pa.s, while M5 had a shear stress of 307.44 Pa, a yield stress of 21.33 Pa, and a plastic viscosity of 2.95 Pa.s. M4 and M5 exhibited lower yield stress and plastic viscosity compared to M2 and M3, confirming their higher flowability and extended setting times as previously explained. This improvement in rheological properties for M4 and M5 compared to M2 and M3 can be attributed to the separate addition of VMA, which had a less significant impact on increasing the paste's viscosity, regardless of the timing of its addition.

For a w/b ratio of 0.50, minimal variation in shear stress and plastic viscosity was observed across all mixtures (**Fig. 6.10 and Fig. 6.11**), consistent with the results of the mini-slump tests, setting times, and hydration kinetics. The increased water content diminished the influence of VMA addition timing and method on rheological properties. These findings indicate that the rheological behavior of AAS pastes can be adjusted by controlling the VMA addition method and timing when using a low w/b ratio (i.e. 0.45). This provides a practical approach for optimizing flowability and stability in specific applications.

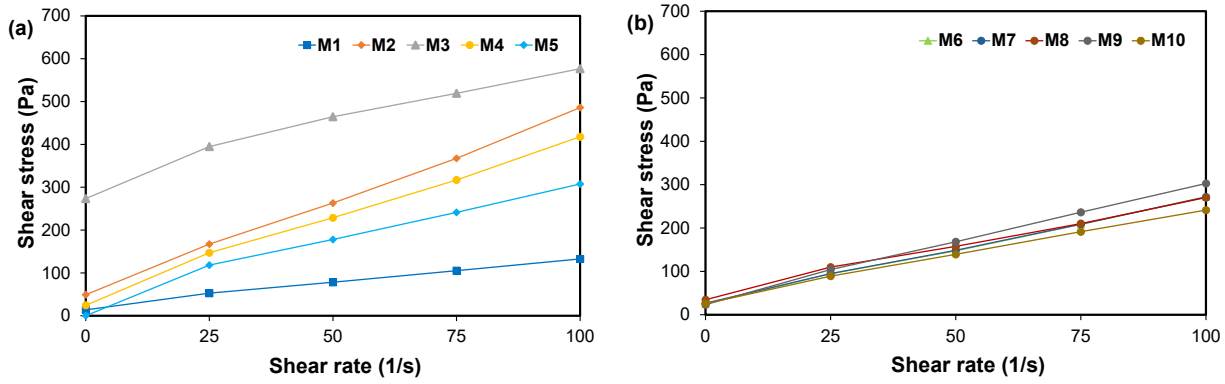

Fig. 6.10: Flow curves of various mixtures a) w/b =0.45 and b) w/b = 0.50.

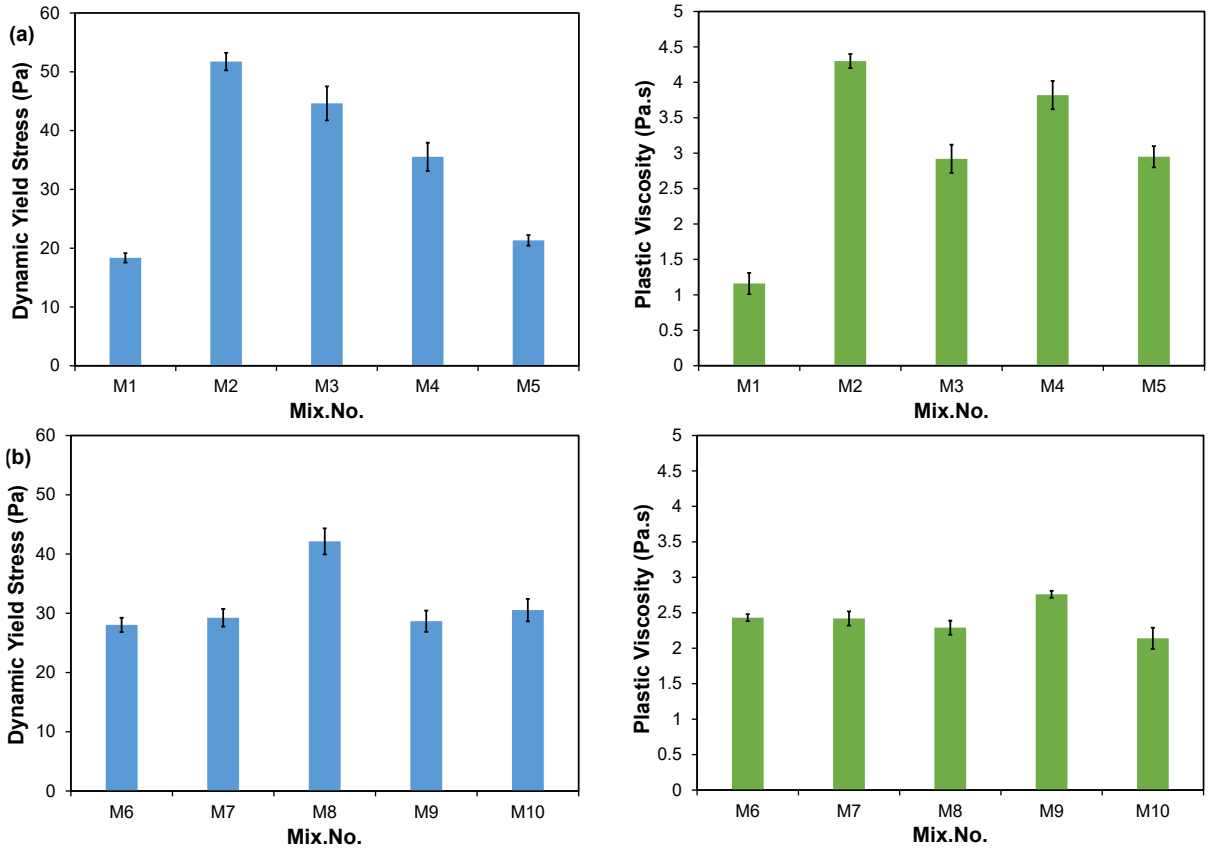

Fig. 6.11: Yield stress and plastic viscosity results for various mixtures a) w/b =0.45 and b) w/b = 0.50.

6.4.2. Harden properties

6.4.2.1. Compressive strength

Fig. 6.12 demonstrates the effect of different addition times and methods of VMA on compressive strength at 3, 7, and 28 days for various AAS mixtures. The strength of the mixture at 7 days increased with the addition of VMA regardless of the w/b ratio and the addition time and method. High compressive strength values were achieved at an early age due to the VMA binding effect, which could improve compaction, avoid segregation problems, and decrease the mixture porosity [68]. Conversely, the slight reduction in compressive strength for some mixtures could be due to either the occurrence of air entrapment or the weaker matrix due to the binding of VMA with C-(A)-S-H [246]. For a w/b ratio of 0.45, the early and late addition of VMA dissolved in water likely influenced the initial hydration process and microstructure formation, stabilizing the mixture and enhancing early strength development. This effect may result from water interacting with the VMA, which amplifies its impact on the hydration process. For example, M2 and M3 achieved higher compressive strengths at 3 days compared to M1, with values of 23.9 MPa and 25.45 MPa,

respectively. In contrast, separate VMA addition minimized its impact on the initial hydration reactions. This reduction is attributed to steric hindrance caused by VMA polymers adsorbing onto slag particle surfaces, which restricts the release of silicate species from the activator [59]. As a result, M4 and M5 exhibited lower compressive strengths at age 3 days of 14.9 MPa and 10.75 MPa compared to M2 and M3, respectively. The strength gain from 7 to 28 days was more pronounced in M2 and M3, with around 50.71% and 21.93% increase, respectively. Conversely, M4 and M5 showed strength gains of 12.32% and 36.90%, respectively.

For a w/b ratio of 0.50, the 28-day compressive strength for all mixtures was approximately 35 MPa, except for M7, which achieved a significantly higher strength of 42.1 MPa. This can be attributed to the limited impact of VMA on paste thickening at higher water content, which allows for improved hydration due to the increased availability of water necessary for the reaction. The variations in strength gain among the mixtures may be linked to the differences in their hydration rates, as previously discussed.

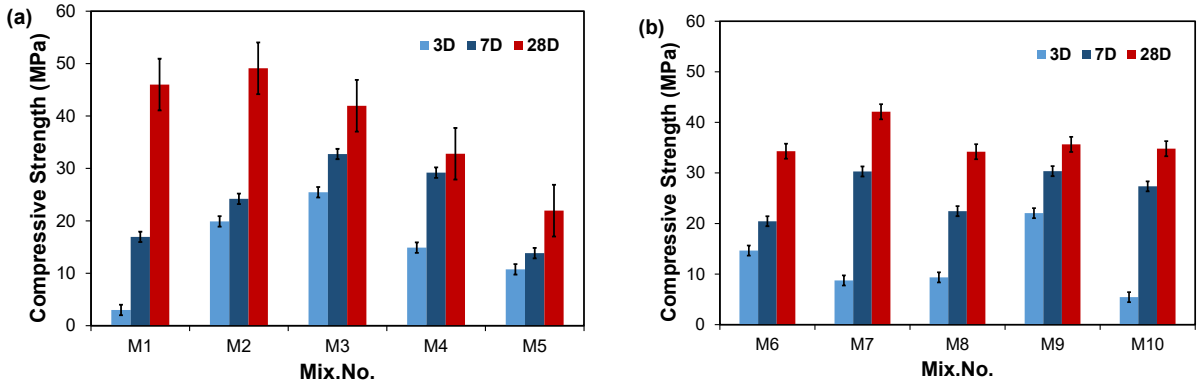

Fig. 6.12: Compressive strength results for various mixtures a) w/b =0.45 and b) w/b = 0.50.

6.4.2.2. Ultra Pulse Velocity

The UPV results for various AAS mixtures with different addition times and methods are presented in **Fig. 6.13**. UPV is a crucial indicator of microstructure quality, as it reflects the density and integrity of the material. The results showed that microstructure development improved over time for all mixtures. Between 3 and 7 days, the UPV values were nearly identical across the mixtures, with only slight variations, suggesting that the majority of the reaction occurred within the first 3 days. Importantly, these consistent UPV results indicate the absence of significant cracks or defects, underscoring the structural soundness of all mixtures.

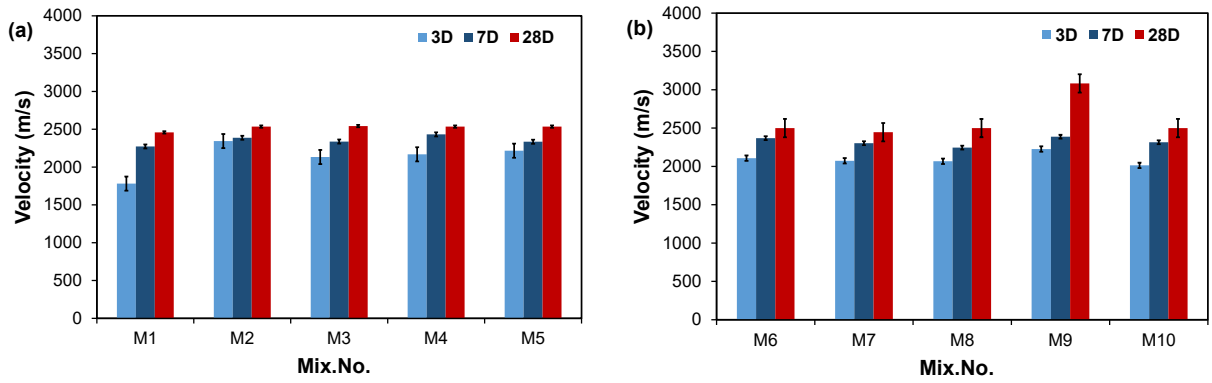

Fig. 6.13: Ultra Pulse velocity results for AAS mixes a) w/b =0.45 and b) w/b = 0.5.

6.4.2.3. Drying shrinkage

The drying shrinkage measurements for various AAS mixtures with different addition times and methods are presented in **Fig. 6.14**. Generally, for w/b of 0.45, dissolving the VMA in water (M2, M3) resulted in lower shrinkage compared to adding it separately (M4, M5). Among all mixtures, M3 exhibited the lowest drying shrinkage across all time intervals, making it the most effective in mitigating shrinkage. This performance is attributed to the higher percentage of activated slag particles in M3, leading to a denser paste with reduced porosity and, consequently, lower drying shrinkage, as reported in [178]. This observation was further supported by the SEM image of M3 (**Fig. 6.18**), showing a dense microstructure and confirming the findings of flowability and setting time. The delayed addition of VMA later significantly reduced shrinkage for both M3 and M5 compared to their counterparts added early (M2 and M4). For instance, M3 outperformed M1 with significantly reduced shrinkage at all time intervals (30.01% at 7 days, 32.78% at 14 days, and 25.06% at 28 days). On the other hand, M2 performed similarly to M1, with negligible differences in shrinkage (0.75% less shrinkage at 7 days, 4.91% more shrinkage at 14 days, and 1.17% less shrinkage at 28 days). The reduced shrinkage can be attributed to dissolving VMAs in water, which promotes the formation of a network of long-chain polymers as explained before. This gel effectively minimizes water evaporation, thereby reducing shrinkage [243]. In contrast, both M4 and M5 resulted in higher shrinkage compared to M1. For instance, M4 exhibited 45.36%, 37.42%, and 40.16% higher shrinkage at 7, 14, and 28 days, respectively. M5 showed 10.85%, 10.83%, and 19.06% higher shrinkage at 7, 14, and 28 days, respectively. This may be attributed to the excess free water, which was not consumed during the AAS reaction and subsequently evaporated, leading to increased shrinkage values. These findings align with the high flowability and setting time results.

For w/b of 0.50, M7 and M8 demonstrated reduced drying shrinkage compared to M6, with shrinkage reductions of 12.01% and 11.28% at 7 days, respectively. This trend continued at 14 and 28 days, indicating that dissolving the VMA in water effectively reduces shrinkage, regardless of the timing of its addition. At 28 days, M8 showed a slightly better shrinkage reduction than M7 (11.29% for M8 vs. 8.04% for M7) and achieved the highest overall shrinkage reduction across all time points. This can be attributed to the water retention by VMA which reduced the free water exposed to evaporation [67,68,243]. In contrast, M9 exhibited higher shrinkage than M6 (4.72%, 4.70%, and 3.24% at 7, 14, and 28 days, respectively), suggesting that the separate addition of VMA led to an increase in shrinkage. This may be attributed to the excess free water that was not consumed in the AAS reaction and was subsequently exposed to evaporation. M10 showed a modest reduction in shrinkage (3.73% to 2.46% across the time intervals), but it was less effective than M7 and M8. In general, mixtures incorporating the VMA demonstrated better performance in controlling shrinkage during the early stages (7 days). However, this trend became less pronounced by 28 days, particularly for M7 and M10.

In conclusion, the timing and method of VMA addition significantly influenced the drying shrinkage, particularly at w/b of 0.45. VMA was most effective in mitigating shrinkage when dissolved in water and added later in the mixing process. This aligns with previous findings, which demonstrated that VMA reduces shrinkage in LC3 paste [243].

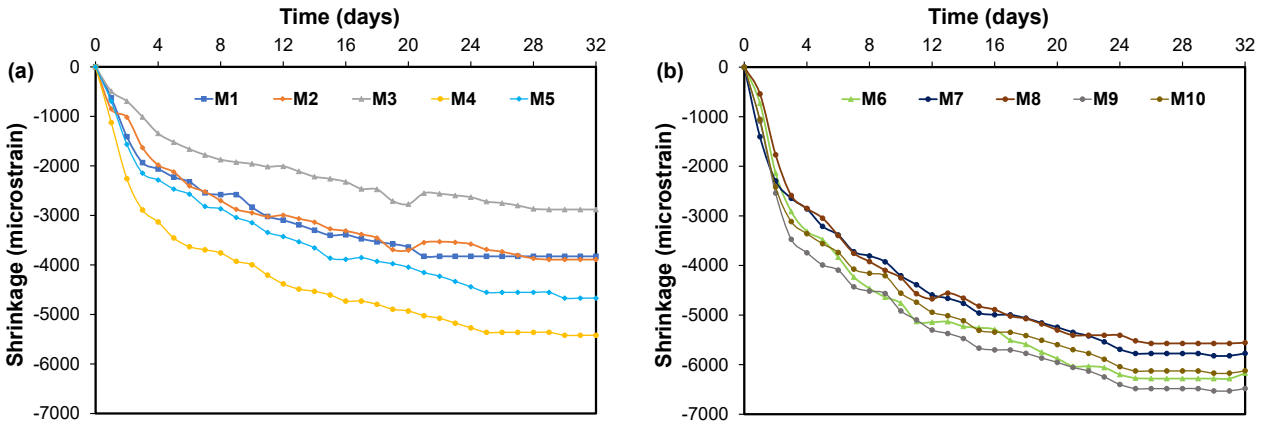

Fig. 6.14: Drying shrinkage results for various mixtures a) w/b =0.45 and b) w/b = 0.50.

6.4.3. Microstructural properties

6.4.3.1. XRD and TGA Analysis

The addition of VMA influences the microstructure of AAS mixtures and the formation of C-(A)-S-H and other hydration products. This effect potentially enhances the early-age mechanical properties of the binder by controlling the distribution of water and solids [243]. Qualitative phase composition analysis, conducted three days after casting, revealed variations in the crystalline composition and structure (indicated by differences in peak intensity) across all AAS mixtures as shown in **Fig. 6.15**. Notably, the addition of VMA did not alter the nature of the hydration products (e.g. formation of new minerals or loss of critical ones). The primary hydration products identified for all mixtures were C-(A)-S-H, with a prominent peak at $2\theta \approx 30°$, and calcite ($CaCO_3$), represented by a peak at $2\theta \approx 10°$ [195,221]. However, differences in the crystalline content and the intensity of the C-(A)-S-H phase were observed among the mixtures.

For w/b 0.45, the crystalline content among the mixtures varied from 38.4% to 48.3%, with some samples exhibiting higher crystallinity, indicating a more ordered structure in the hydration products [222]. The intensity of the C-(A)-S-H phase, which reflects the amount and stability of C-(A)-S-H formed, also varied depending on the addition time and method of VMA. A higher C-(A)-S-H peak intensity indicates more extensive hydration, often associated with a denser microstructure. For instance, M3 exhibited a more pronounced C-(A)-S-H peak, and this denser microstructure was further confirmed through SEM imaging (**Fig. 6.18**).

Additionally, there are traces of calcite, as indicated by diffraction peaks around 15° and 25°, which could be attributed to the carbonation of C-(A)-S-H gels [195]. This may result from the ability of VMAs to reduce ion mobility and slow hydration reactions, allowing more free calcium ions to carbonate and form calcite (**Table 6.4**). Additionally, some VMAs may introduce calcium-rich components, further promoting calcite precipitation. Furthermore, the internal curing effect of VMA enhances water retention by increasing mixture viscosity, reducing evaporation, and ensuring sufficient water for hydration, which supports the formation of calcium hydroxide and other hydration products [241,243]. These findings confirm the reduction in shrinkage achieved by using VMA, as discussed earlier.

For w/b 0.50, all mixtures exhibited similar C-(A)-S-H peak intensities, except for M9 and M10, which showed approximately 30% lower intensity. This reduction could be attributed to the separate addition of VMA, which retains more water and delays the formation of C-(A)-S-H

compared to other mixtures because of water retention as explained before. Despite this, M9 demonstrated the highest crystalline content at 44.5%, suggesting the formation of additional hydration products such as calcite and hydrotalcite. Overall, the crystalline content varied among the mixtures, ranging from 37.1% (lowest for M7) to 44.5% (highest for M9).

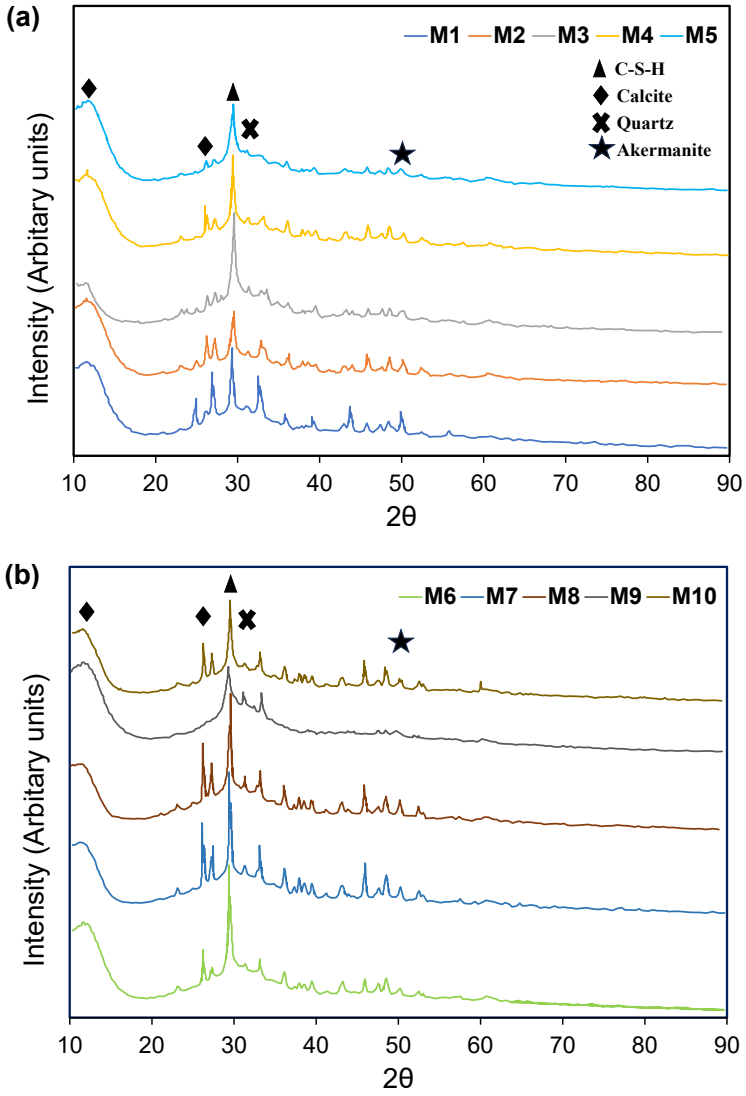

Fig. 6.15: X-ray diffractograms of 3-day-AAS mixtures a) w/b =0.45 and b) w/b = 0.50.

The TG and DTG results for the various AAS mixtures, measured at 3 days, are reported in **Fig. 6.16**. It can be found that a significant peak appeared at 60°C in DTG curves indicating water loss (decomposition) of C-(A)-S-H [223,252]. Additionally, a prominent peak at around 600°C corresponds to the decomposition of $CaCO_3$, attributed to carbonation. This carbonation could have occurred during the TGA test itself or due to the extended time required for sample preparation before freeze-drying [241]. Among the mixtures, the highest degree of C-(A)-S-H

decomposition was observed in M3 for w/b 0.45 and M10 for w/b 0.50, aligning with the findings of the XRD analysis. The total weight loss ranged from 14% to 18% across both w/b ratios, with the highest weight loss recorded for M2. For w/b 0.50, the differences in the decomposition of hydration products were minimal confirming the results of compressive strength and drying shrinkage.

Generally, the high pH reduces the effectiveness of the VMA in altering the viscosity of the solid suspension (changing the nature of hydration products). As a result, water molecules initially "trapped" by the VMA are gradually released, making them available for hydration. This process, often referred to as "internal curing," ensures that the water retained by the VMA contributes to the hydration reactions over time [241].

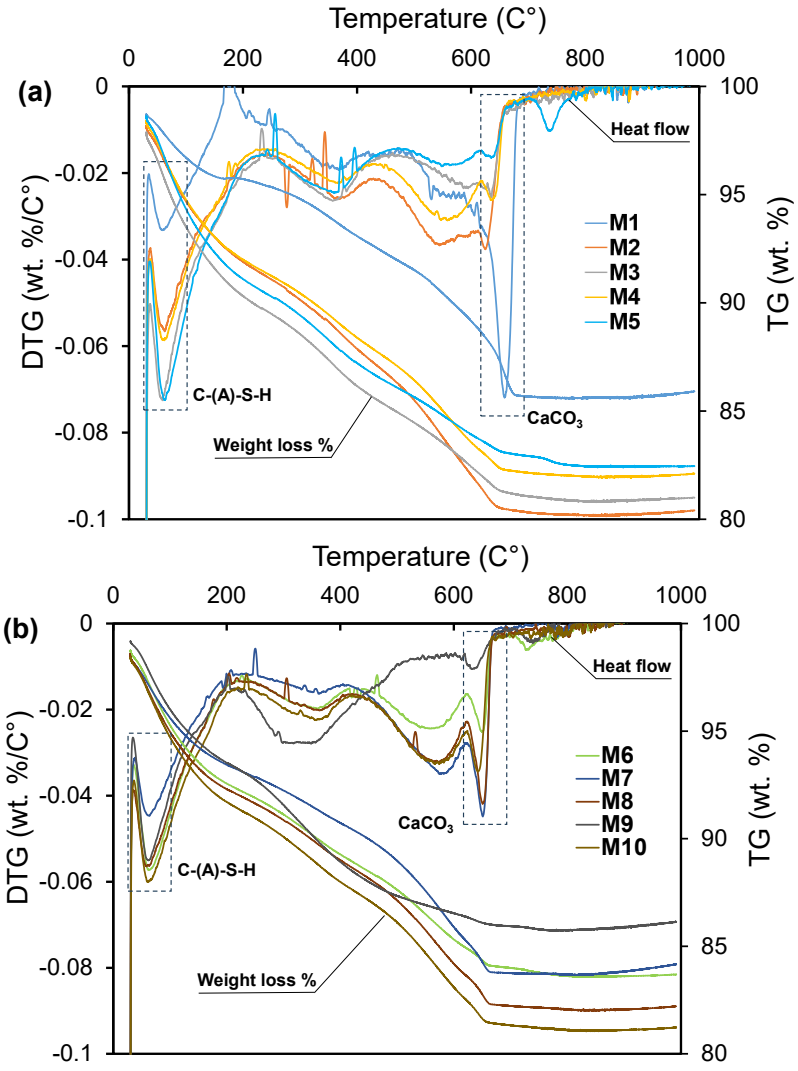

Fig. 6.16: TG-DTG curves 3-day-AAS mixtures a) w/b = 0.45 and b) w/b = 0.50.

6.4.3.2. FTIR Analysis

The FTIR spectra of the AAS mixtures were largely similar, with differences observed primarily in the resonance intensity, suggesting variations in the quantity of reaction products formed, as illustrated in **Fig. 6.17**. All mixtures exhibited prominent Si-O-Si peaks, confirming the formation of strong silicate networks essential for the structural integrity and mechanical strength of the AAS pastes [173,175].

Key spectral bands were identified, including a band at 1630 cm^{-1} corresponding to H-O-H stretching, and a band at 3337 cm^{-1} attributed to O-H groups [241]. These bands indicate the presence of water molecules within the C-(A)-S-H gel matrices. A peak at 951 cm^{-1}, characteristic of the Si-O bonds' asymmetrical stretching, suggests the formation of silicate networks, such as C-(A)-S-H and other silicate phases [168,195].

Upon analysis, the resonance intensity of the C-(A)-S-H (Si-O) peak showed a slight reduction for all VMA-containing mixtures compared to the control mixture. This suggests that the addition of the VMA caused a delay in the reaction kinetics. These findings align with the results of the calorimetry test, which demonstrated changes in the hydration behavior for mixtures.

The variations in O-H, H-O-H, and C-O peaks highlight the significant impact of the VMA's addition method and timing on hydration processes, water retention, and carbonation susceptibility. For instance, the H-O-H peak (around 1650 cm^{-1}) exhibited a slight reduction in intensity for VMA mixtures compared to the control, indicating changes in the structure of hydration products or reduced bound water content due to the early or delayed addition of the VMA. In contrast, the C-O peak (around 1450 cm^{-1}) increased in intensity for VMA mixtures, suggesting greater exposure to carbonation. This may be due to the VMA influencing the reaction kinetics, leading to incomplete hydration and prolonged vulnerability to atmospheric CO_2. These findings are corroborated by the TGA results, which revealed the formation of a larger amount of $CaCO_3$ in VMA mixtures, validating increased carbonation.

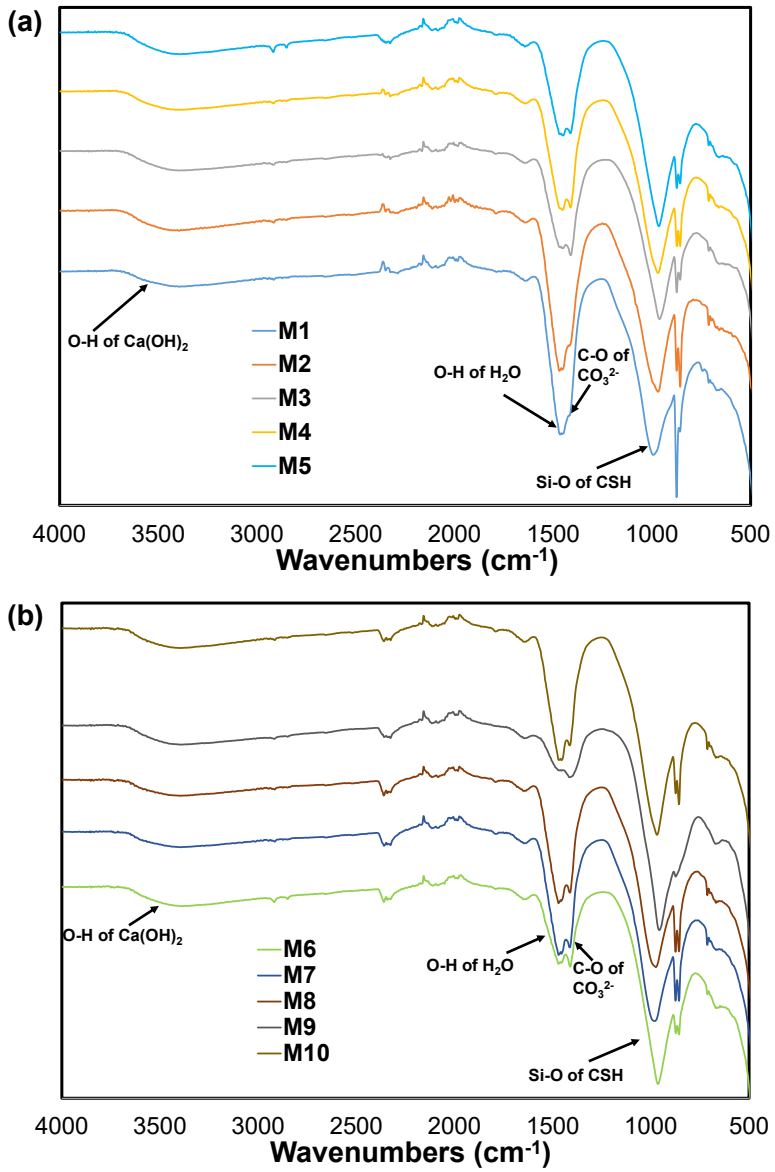

Fig. 6.17: FTIR curves of 3-day-AAS mixtures a) w/b = 0.45 and b) w/b = 0.50.

6.4.3.3. SEM analysis and EDS

The SEM images of AAS mixtures at 3 days are presented in **Fig. 6.18** and **Fig. 6.19**. For a w/b ratio of 0.45, the inclusion of VMA reduces the porosity of the paste compared to the control mixture as shown in **Fig. 6.18**. This aligns with the results of flowability and setting time tests and is consistent with the findings reported in [247]. Conversely, for a w/b ratio of 0.50 (**Fig. 6.19**), VMA showed only a slight impact on the microstructure compared to the control mixture M6. This supports the findings of the study, which indicate a minimal effect of the addition time and method of VMA on various fresh and hardened properties. M2 exhibited weak bonding in certain regions due to inadequate particle interlocking or incomplete hydration caused by the early addition of

VMA. The presence of microcracks suggests potential sites of weakness. M3 displayed a dense microstructure with some unreacted slag particles confirming flowability and setting time results. This observation was further supported by EDS results (**Table 6.2**), as the amount of unreacted slag particles correlates with detected Mg% [168]. A higher percentage of unreacted slag particles corresponds to higher Mg% detection. In contrast, M5 demonstrated a lower Mg% content, indicating greater slag particle dissolution and the formation of C-(A)-S-H, which indicates a reduced effect of VMA when added later and separately. Conversely, M8 and M10 exhibited almost similar Mg% values, confirming that the VMA had a minimal effect due to the availability of a high amount of water. These findings align with the results for fresh and hardened properties, confirming the slight influence of VMA on hydration and microstructure development.

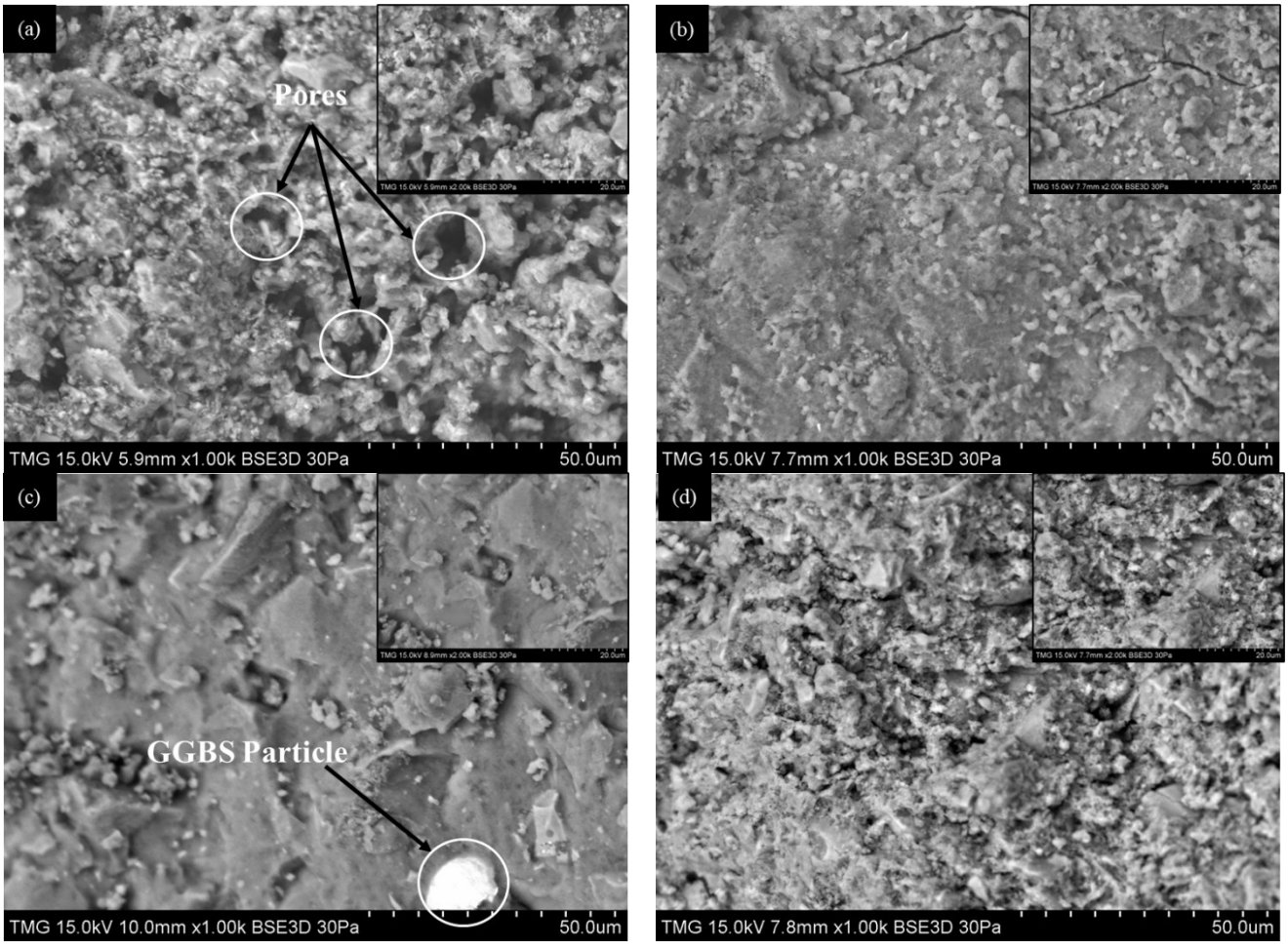

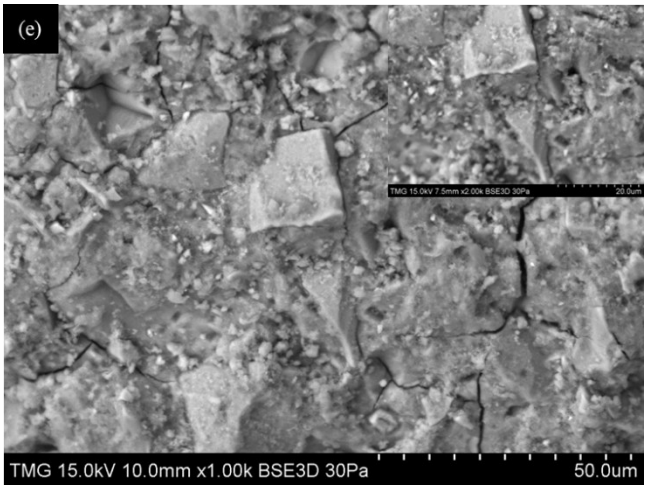

Fig. 6.18: SEM micrograph results of AAS mixtures activated by 0.45 w/b at 3 days age a) M1, b) M2, c) M3, d) M4, and d) M5.

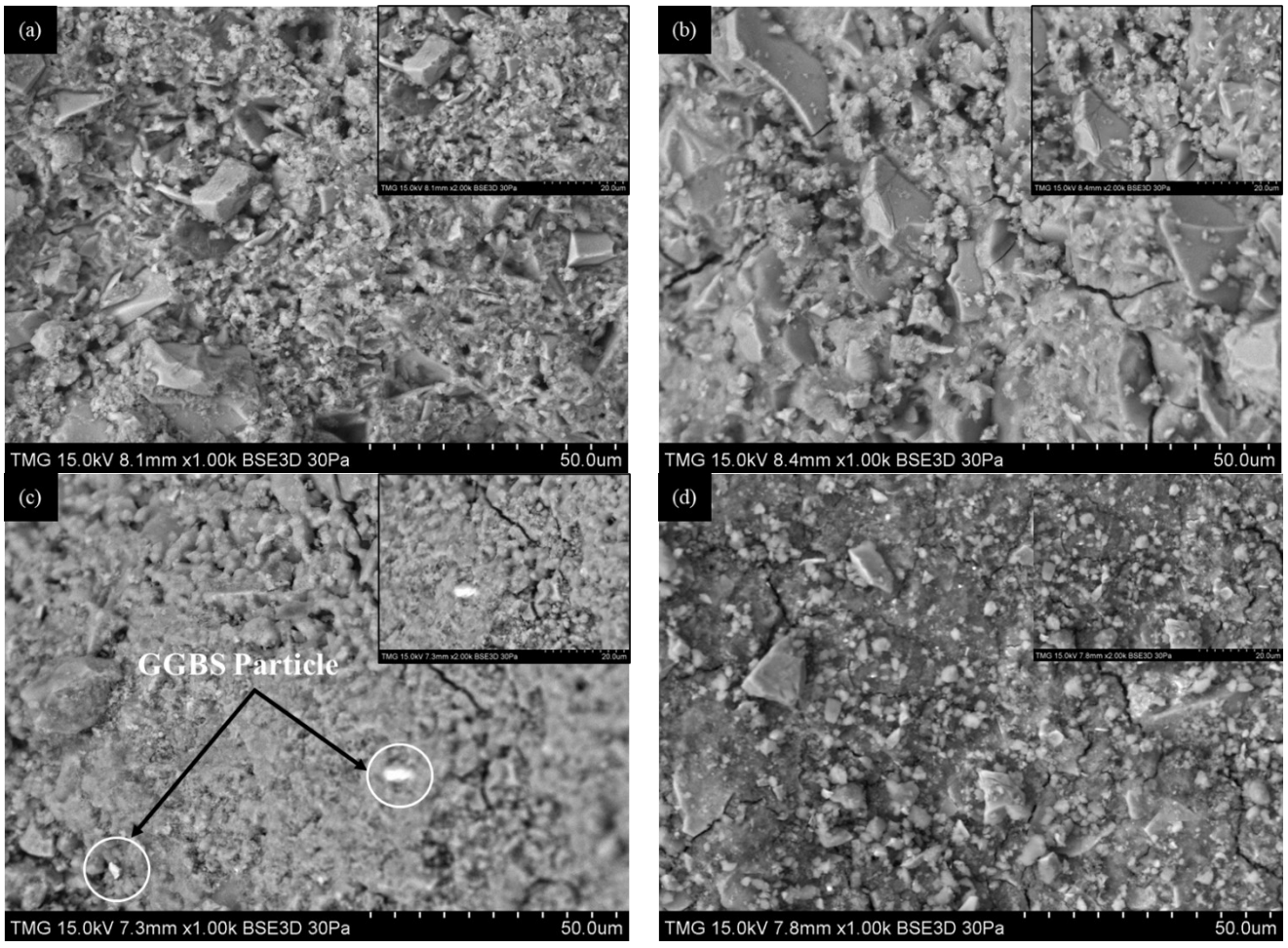

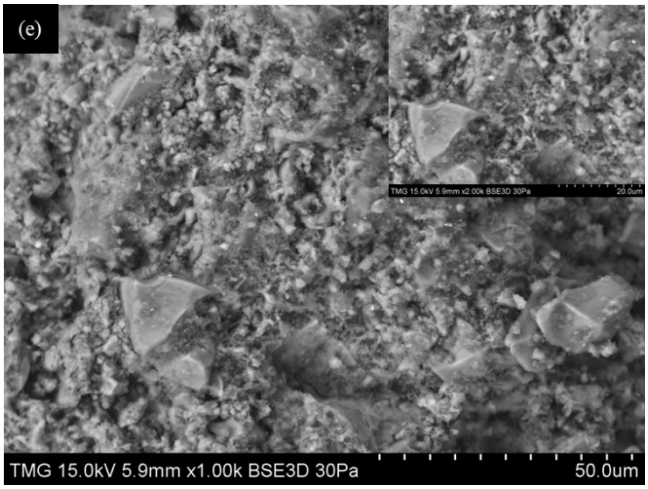

Fig. 6.19: SEM micrograph results of AAS mixtures activated by 0.50 w/b at 3 days age a) M6, b) M7, c) M8, d) M9, and d) M10.

To gain deeper insights into the extent and composition of the paste matrix, EDS analysis was conducted for selected mixtures alongside SEM imaging, as summarized in **Table 6.2**. This analysis focused on the elemental ratios, particularly aluminum (Al) and silica (Si), which indicate the formation of the C-(A)-S-H gel. The Si/Al ratio in M5 was higher than that in M3, suggesting a greater dissolution rate of slag particles in M5 [168]. During the activation process, variations in the Si/Ca ratio across the mixtures correspond to the formation of different phases of the C-(A)-S-H gel within the matrix highlighting the effect of the addition method of VMA.

Table 6.2: EDS point analysis of selected 3 days hydrated AAS mixtures (%wt.).

Mixture code	C	O	Na	Mg	Al	Si	S	Ca	K	Si/Ca	Si/Al
M3	5.25	50.15	3.45	5.34	3.34	12.97	0.74	18.74	-----	0.69	3.88
M5	3.66	30.89	1.98	1.57	1.91	11.59	-----	48.40	-----	0.24	6.07
M8	12.20	49.46	3.07	4.84	3.17	10.14	0.54	16.12	0.47	0.62	3.20
M10	3.94	45.38	3.40	5.40	3.96	15.13	1.22	21.57	-----	0.70	3.82

6.4.3.4. Conductivity and Ion Concentration Analysis

Chemical analysis was performed on the extracted pore solutions from all AAS mixtures to evaluate major chemical changes across these various mixing procedures. **Table 6.3** presents the pH, electrical conductivity, and measured temperature values for each mixture. The pH level plays a critical role in the initial dissolution of slag, where a higher pH promotes the release of Ca^{2+} ions from the slag particle surfaces into the solution. Electrical conductivity, on the other hand, serves as an indicator of the slag's dissolution rate, with higher conductivity values corresponding to an increased concentration of dissolved ions, such as Mg^{2+}, Ca^{2+}, and Al^{3+} [37]. Notably, mixtures

with a 0.45 w/b ratio showed significant changes in electrical conductivity, whereas mixtures with a 0.50 w/b ratio exhibited only minor changes. This difference may be attributed to a low competition between VMA and activator cations for water, which affects their interaction within the water-binder system.

VMAs contain hydrophilic polymers (e.g. cellulose ethers or polyacrylamides) that dissolve in water to increase the liquid phase's viscosity changing the conductivity values of mixtures. When VMAs are dissolved directly in water before mixing, they disperse evenly throughout the mixture. This dispersion allows the polymers to bind with water molecules, forming a network of hydrated polymer chains, which increases conductivity values (as observed in M2, M3, M7, and M8). In contrast, when VMAs are added separately to the slag paste, they may initially remain within the binder matrix, leading to delayed dispersion and localized areas of increased viscosity. This results in lower conductivity values compared to the dissolved addition of VMA. These findings are consistent with the flow diameter results.

Table 6.3: pH and electrical conductivity values for extracted solutions after mixing.

Mixture Code	pH	Conductivity (S/cm)	Temperature (˚C)
M1	13.54	159.2	21.1
M2	13.65	174.0	20.7
M3	13.72	194.8	21.4
M4	13.59	172.5	21.4
M5	13.59	175.5	20.9
M6	13.41	169.4	21.2
M7	13.39	168.6	21.0
M8	13.40	181.6	21.0
M9	13.67	167.6	21.0
M10	13.63	168.1	21.0

The ion concentration results confirmed the pH findings, showing that mixtures M7 and M8 had the lowest concentrations of Al and Ca ions due to the slower dissolution of slag (lower pH values), as shown in **Table 6.4**. For mixtures with a 0.45 w/b ratio, the early separate addition of VMA increased Si ion concentration compared to dissolving addition, indicating enhanced activator and slag dissolution. This resulted in the release of high Ca^{2+} cations, which react with silicate species. The reaction forms double-charged cations around precursor particles, leading to repulsion between these charged particles. This explains the higher initial flow diameter and flow retention of the mixtures. For instance, the Si ion concentration in M4 (341.19) was higher than in M2 (272.75). Additionally, with the separate addition method, a later VMA addition further increased Si ion release. For instance, the Si ion concentration in M4 (341.19) was higher than in M5

(375.39). The same trend was observed for mixtures of w/b of 0.50, validating all previous findings regarding various properties.

Table 6.4: Chemical analyses of pore solutions extracted from AAS mixtures (mmol/L).

Mixture Code	Na	Mg	Al	Si	K	Ca
M1	731.23	4.33	20.10	282.09	10.39	0.16
M2	815.93	4.39	22.94	272.75	10.92	0.13
M3	855.47	0.54	18.18	184.19	12.91	-0.04
M4	851.16	6.49	24.22	341.19	10.88	0.22
M5	876.03	5.96	25.37	375.39	11.45	0.14
M6	678.19	5.07	18.79	324.12	8.04	0.28
M7	527.14	2.25	11.15	223.91	7.52	0.09
M8	650.04	1.14	14.37	241.06	9.39	-0.01
M9	844.15	5.12	23.16	312.07	11.05	0.24
M10	680.58	4.52	18.92	285.66	8.37	0.20

6.5. Conclusions

This study provides a comprehensive understanding of the influence of the timing and method of VMA addition on the rheological properties of one-part AAS systems. The findings offer valuable insights into optimizing VMA usage to enhance the performance of AAS. The key contributions of this research are summarized as follows:

- Mixtures with a w/b ratio of 0.50 exhibited better initial flow diameter and flow retention compared to those with a 0.45 ratio due to the high water content.
- Early addition of VMA, particularly when dissolved in water, resulted in a faster flow loss and a low initial diameter.
- The method of VMA addition significantly influenced the hydration kinetics of AAS pastes, providing a strategic tool for controlling heat release and setting behavior.
- A high w/b ratio diluted the paste, reducing thermal power peaks by lowering reactive ion concentrations, slowing hydration reactions, and decreasing total heat release.
- The addition of VMA reduced the drying shrinkage of one-part AAS, regardless of the addition time, method, and w/b ratio used.
- At a high w/b ratio, the effects of the timing and method of VMA addition became less significant for all measured properties.

Chapter 7: Conclusion and future directions

This dissertation explored and tested various techniques (i.e. Mixing protocols, various retarders addition, VMA addition time, and method) to assess their influence on the rheological behavior of meta-silicate-activated AAS systems and comprehensive mineralogical analysis. Additionally, an optimization model was developed and validated to identify the most effective retarder, in combination with optimal ingredient proportions, for achieving highly flowable mixtures. These investigations provided a comprehensive and practical understanding of the role each strategy plays in the AAS system, with a particular focus on:

- The rheological behavior and mineralogical effects of each technique, along with their overall efficiency in AAS systems, and
- The resulting impact on the fresh and hardened properties of the AAS.

The findings offer valuable insights that contribute to advancing the development and optimization of AAS systems, paving the way for construction applications.

7.1. Contributions

The primary contributions of this thesis include:

1- **Addressing the gap in identifying the most effective sequence for adding ingredients** to achieve extended setting times and reduce competitive adsorption between the precursor and activator on water, without compromising compressive strength and other mechanical properties. This was achieved by investigating the impact of various addition sequences (precursor, activator, and water) on key properties such as flowability, setting time, heat of hydration, wetting point, and compressive strength, aiming to identify the optimal sequence that balances setting time and flowability with robust mechanical performance. The results showed that the shortest initial setting time occurred when meta-silicate dissolved in water was added to slag due to the relatively rapid dissolution rate of slag. Additionally, this sequence resulted in the highest reaction temperature. Changing the sequence of adding water or slag caused only a slight variation in flowability and compressive strength. The optimal mixture, prepared by dry mixing slag and meta-silicate, exhibited a balanced setting time and heat evolution profile. This approach effectively avoided a short setting

time and dormant period, making it suitable for various applications. Furthermore, it mitigates the corrosiveness of the activator, enhancing its practical usability in diverse construction practices.

2- **Tackling the unexplored effects of extended mixing time and modified mixing protocols** on one-part AAS systems by investigating the influence of extended mixing times, with and without interruptions (relaxation), on the rheological properties of AAS. The findings reveal that variations in mixing protocols have minimal impact on early and late strength due to the similarity in the hydration products formed. A detailed correlation matrix and ANOVA analysis highlight the dominant role of activator dosage in determining all evaluated properties. Additionally, identifying the potential maximum mixing time for ready-mix AAS (60 minutes) which is shorter than that for OPC, which is 90 minutes according to ASTM C94. Finally, the results demonstrate that mixing protocols significantly influence the properties of mixtures with low activator dosages, particularly in improving flow retention and setting time, though with marginal enhancements. Conversely, these protocols have little to no effect on mixtures with high activator dosages, underscoring that activator dosage is the primary factor governing the properties of AAS, rather than the mixing protocol.

3- **Developing for the first time, optimized models for the mixing proportions** of one-part AAS mixtures to achieve superior rheological properties while maintaining sufficient compressive strength when activated by anhydrous meta-silicate with various retarders. Also, offering valuable insights into the environmental impact of the optimized mixtures derived from the optimization model by a comparative LCA study. The findings revealed that increasing the activator dosage consistently improved flowability, regardless of the w/s ratio, retarder type, or dosage within the tested range. Among the retarders, borax proved most effective in reducing yield stress by forming a calcium-based borate layer, which delays hydration and crystal formation. However, nano zinc oxide emerged as the most effective retarder for enhancing flowability in AAS mixtures, as small amounts significantly extended the induction period, delaying the formation of the C–(N)–A–S–H gel. ANOVA analysis identified the w/s ratio, followed by the activator dosage, as the most influential factors affecting all measured properties, except for the time of the second peak and compressive strength. Regression models with reliable accuracy were developed,

showing strong agreement between the measured and predicted values for all properties. The LCA results highlighted silicate and slag as the primary contributors to most environmental impacts. Notably, slag had a higher impact in specific categories, such as non-renewable energy resources and ozone depletion.

4- **Conducting a comprehensive investigation into the timing (early versus delayed addition) and method (separate addition or dissolved in water) of VMA addition** on the rheological properties of one-part AAS. This contribution addresses a critical gap in understanding the role of VMA in AAS systems, as its impact has not been extensively explored. The findings offer valuable insights into how VMA addition influences the mineral hydration process in one-part AAS. Early addition of VMA, particularly when dissolved in water, resulted in faster flow loss and a reduced initial flow diameter. The method of VMA incorporation significantly affected the hydration kinetics of AAS pastes, serving as a strategic mechanism to regulate heat release and setting behavior. A high w/b ratio diluted the paste, reducing thermal power peaks by lowering the concentration of reactive ions, slowing hydration reactions, and decreasing the total heat release. At higher w/b ratios, the timing and method of VMA addition had a diminished impact on all measured properties, underscoring the interplay between mix design and admixture performance.

The findings of this research highlight the critical role of factors such as mixing method, mixing time, sequence of ingredient addition, and the integration of retarders and VMAs in the production of AAS. The techniques applied to AAS activated by meta-silicate demonstrate their ability to significantly influence the rheological and mineralogical properties, resulting in a more flowable AAS. The comprehensive understanding of the behavior and improved flowability expands the potential for practical applications, including ready-mix concrete and 3D printing, where enhanced rheological properties are essential.

7.2. Future directions

This thesis serves as a foundation for various techniques aimed at enhancing the flowability of AAS paste, offering a basis for adaptation. The proposed future directions are outlined as follows:

1- **Assess the synergistic effect of incorporating retarders**, particularly borax and nano zinc, alongside extended mixing times of up to 60 minutes using low activator dosages. This involves the dry mixing of slag, meta-silicate, and retarders for 1 minute, followed by the addition of water to produce one-part AAS mortar. Fresh and hardened properties will be evaluated according to EFNARC specifications to develop self-compacting concrete or other advanced concrete types with enhanced workability and performance.

2- **Investigate the extended use of borax and nano zinc retarders** by incorporating them at different addition times during mixing, based on the optimized mixture developed in this thesis to produce one-part AAS mortar. Evaluate the fresh and hardened properties to identify the optimal integration approach for enhanced performance of AAS.

3- **Evaluate the effects of increasing the dosage of borax and nano zinc retarders** on the fresh and hardened properties of one-part AAS mortar and concrete. This investigation will provide insights into optimizing retarder usage for improved structural performance of AAS concrete.

4- **Explore the synergistic effect of combining nano zinc and borax** as two distinct retarders within the same mixture on the fresh and hardened properties of one-part AAS systems. This investigation aims to assess how their interaction influences key performance properties (reaction kinetics) and contributes to optimizing mixture designs for enhanced functionality.

5- **Examine the combined effect of incorporating retarder and VMA admixture** within the same mixture on the fresh and hardened properties of one-part AAS systems. This evaluation aims to determine how the combined use of these admixtures influences fresh and hardened behavior.

6- **Validate the techniques developed in this thesis through on-site applications** by casting full-scale structural one-part AAS concrete elements. This approach will assess the practicality and scalability of the proposed methods, ensuring their suitability for real-world construction scenarios. By transitioning from laboratory-scale testing to full-scale

implementation, providing valuable insights into the performance, durability, and workability of the optimized AAS mixtures under actual field conditions.

7- **Assess the durability of structural one-part AAS concrete elements** after exposure to various environmental conditions on-site. This evaluation aims to provide critical insights into the long-term performance and resilience of AAS activated by meta-silicate under real-world conditions.

In conclusion, this thesis comprehensively evaluates the impacts of various techniques on the rheological and mineralogical properties of AAS activated by meta-silicate. The findings serve as a foundation for future advancements in utilizing these techniques to produce AAS-based mortar and concrete. By further refining and exploring the synergistic effects of these methods, the production of low-carbon AAS concrete can be significantly enhanced, paving the way toward greater decarbonization and sustainability in the construction industry. This research marks a vital step in advancing eco-friendly construction materials and contributing to a greener future.

References

[1] B.C. McLellan, R.P. Williams, J. Lay, A. Van Riessen, G.D. Corder, Costs and carbon emissions for geopolymer pastes in comparison to ordinary portland cement, J Clean Prod 19 (2011) 1080–1090. https://doi.org/10.1016/j.jclepro.2011.02.010.

[2] K.H. Yang, J.K. Song, K. Il Song, Assessment of CO 2 reduction of alkali-activated concrete, J Clean Prod 39 (2013) 265–272. https://doi.org/10.1016/j.jclepro.2012.08.001.

[3] I. Amer, M. Kohail, M.S. El-Feky, A. Rashad, M.A. Khalaf, A review on alkali-activated slag concrete, Ain Shams Engineering Journal (2021). https://doi.org/10.1016/j.asej.2020.12.003.

[4] C. Shi, A.F. Jiménez, A. Palomo, New cements for the 21st century: The pursuit of an alternative to Portland cement, Cem Concr Res 41 (2011) 750–763. https://doi.org/10.1016/j.cemconres.2011.03.016.

[5] J. Wei, Z. Jia, Y. Wang, Y. Jiang, Z. Miao, Y. Zhou, H. Zhang, Enhanced thermoelectric performance of low carbon cement-based composites by reduced graphene oxide, Energy Build 250 (2021). https://doi.org/10.1016/j.enbuild.2021.111279.

[6] C. Narattha, A. Chaipanich, Effect of curing time on the hydration and material properties of cold-bonded high-calcium fly ash–Portland cement lightweight aggregate, J Therm Anal Calorim 145 (2021) 2277–2286. https://doi.org/10.1007/s10973-020-09730-8.

[7] S.S. Reddy, M.A.K. Reddy, LIME CALCINED CLAY CEMENT (LC3): A Review, in: IOP Conf Ser Earth Environ Sci, IOP Publishing Ltd, 2021. https://doi.org/10.1088/1755-1315/796/1/012037.

[8] W. Hu, Q. Nie, B. Huang, X. Shu, Investigation of the strength development of cast-in-place geopolymer piles with heating systems, J Clean Prod 215 (2019) 1481–1489. https://doi.org/10.1016/j.jclepro.2019.01.155.

[9] C. Xu, Z. Zhang, X. Tang, Z. Gui, F. Liu, Synthesis and characterization of one-part alkali-activated grouting materials based on granulated blast furnace slag , uncalcined coal gangue and microscopic fly ash sinking beads, Constr Build Mater 345 (2022) 128254. https://doi.org/10.1016/j.conbuildmat.2022.128254.

[10] M. Criado, A. Fernández-Jiménez, A. Palomo, Alkali activation of fly ash. Part III: Effect of curing conditions on reaction and its graphical description, Fuel 89 (2010) 3185–3192. https://doi.org/10.1016/j.fuel.2010.03.051.

[11] M. Ozturk, M.B. Bankir, O.S. Bolukbasi, U.K. Sevim, Alkali activation of electric arc furnace slag: Mechanical properties and micro analyzes, Journal of Building Engineering 21 (2019) 97–105. https://doi.org/10.1016/j.jobe.2018.10.005.

[12] M.L. Granizo, S. Alonso, M.T. Blanco-Varela, A. Palomo, Alkaline activation of metakaolin: Effect of calcium hydroxide in the products of reaction, Journal of the American Ceramic Society 85 (2002) 225–231. https://doi.org/10.1111/j.1151-2916.2002.tb00070.x.

[13] A. Gruskovnjak, B. Lothenbach, L. Holzer, R. Figi, F. Winnefeld, Hydration of alkali-activated slag: Comparison with ordinary Portland cement, Advances in Cement Research 18 (2006) 119–128. https://doi.org/10.1680/adcr.2006.18.3.119.

[14] O. Burciaga-Díaz, I. Betancourt-Castillo, Characterization of novel blast-furnace slag cement pastes and mortars activated with a reactive mixture of MgO-NaOH, Cem Concr Res 105 (2018) 54–63. https://doi.org/10.1016/j.cemconres.2018.01.002.

[15] F. Puertas, T. Amat, A. Fernández-Jiménez, T. Vázquez, Mechanical and durable behaviour of alkaline cement mortars reinforced with polypropylene fibres, Cem Concr Res 33 (2003) 2031–2036. https://doi.org/10.1016/S0008-8846(03)00222-9.

[16] A. Fernández-Jiménez, J.G. Palomo, F. Puertas, Alkali-activated slag mortars Mechanical strength behaviour, 1999.

[17] S.M.S.M.K. Samarakoon, M. Kamali, K.F. Gebremariam, F. Tesfay, D.S. Mesfin, M.M. Baqala, S.Y. Oderji, Investigating the influence of precursor combinations on the development of one-part alkali-activated binders using SiMn, Case Studies in Construction Materials 21 (2024). https://doi.org/10.1016/j.cscm.2024.e03887.

[18] T. Omur, N. Miyan, N. Kabay, Utilization of eggshell powder in one-part alkali-activated metakaolin based binder, Constr Build Mater 445 (2024). https://doi.org/10.1016/j.conbuildmat.2024.137981.

[19] A. Kadhim, M. Sadique, R. Al-Mufti, K. Hashim, Developing one-part alkali-activated metakaolin/natural pozzolan binders using lime waste, Advances in Cement Research 33 (2021) 342–356. https://doi.org/10.1680/jadcr.19.00118.

[20] J. He, Y. Jie, J. Zhang, Y. Yu, G. Zhang, Synthesis and characterization of red mud and rice husk ash-based geopolymer composites, Cem Concr Compos 37 (2013) 108–118. https://doi.org/10.1016/j.cemconcomp.2012.11.010.

[21] S.A. Bernal, E.D. Rodríguez, R. Mejía De Gutiérrez, M. Gordillo, J.L. Provis, Mechanical and thermal characterisation of geopolymers based on silicate-activated metakaolin/slag blends, J Mater Sci 46 (2011) 5477–5486. https://doi.org/10.1007/s10853-011-5490-z.

[22] S.A. Bernal, E.D. Rodríguez, R. Mejia De Gutiérrez, J.L. Provis, S. Delvasto, Activation of metakaolin/slag blends using alkaline solutions based on chemically modified silica fume and rice husk ash, Waste Biomass Valorization 3 (2012) 99–108. https://doi.org/10.1007/s12649-011-9093-3.

[23] T. Luukkonen, Z. Abdollahnejad, J. Yliniemi, P. Kinnunen, M. Illikainen, One-part alkali-activated materials: A review, Cem Concr Res 103 (2018) 21–34. https://doi.org/10.1016/j.cemconres.2017.10.001.

[24] A. Fernández-Jiménez, A. Palomo, Composition and microstructure of alkali activated fly ash binder: Effect of the activator, Cem Concr Res 35 (2005) 1984–1992. https://doi.org/10.1016/j.cemconres.2005.03.003.

[25] A. Palomo, M.W. Grutzeck, M.T. Blanco, Alkali-activated fly ashes A cement for the future, 1999.

[26] H. Choo, S. Lim, W. Lee, C. Lee, Compressive strength of one-part alkali activated fly ash using red mud as alkali supplier, Constr Build Mater 125 (2016) 21–28. https://doi.org/10.1016/j.conbuildmat.2016.08.015.

[27] M. Askarian, Z. Tao, B. Samali, G. Adam, R. Shuaibu, Mix composition and characterisation of one-part geopolymers with different activators, Constr Build Mater 225 (2019) 526–537. https://doi.org/10.1016/j.conbuildmat.2019.07.083.

[28] S. Nazar, J. Yang, M. Ashraf, F. Aslam, M.F. Javed, S.M. Eldin, J. Xie, Formulation and characterization of cleaner one-part novel fly ash/lime-based alkali-activated material, Journal of Materials Research and Technology 23 (2023) 3821–3839. https://doi.org/10.1016/j.jmrt.2023.02.022.

[29] K. Yin, Y. Jiang, Y. Wang, W. Zhao, Z. Pan, Z. Li, Effect of rice straw powder on properties of one-part alkali-activated slag, Front Built Environ 8 (2022). https://doi.org/10.3389/fbuil.2022.999740.

[30] N. Marin, C. Orbeci, L. Bobirică, I. Rău, C. Deleanu, E.I. Bîru, P.O. Stănescu, A.C. Berbecaru, E. Matei, C. Bobirică, Alternative Solid Activators from Waste Glass for One-Part Alkali-Activated Fly Ash/Red Mud Cements, Materials 16 (2023). https://doi.org/10.3390/ma16206707.

[31] M. Turkoglu, O.Y. Bayraktar, A. Benli, G. Kaplan, Effect of cement clinker type, curing regime and activator dosage on the performance of one-part alkali-activated hybrid slag/clinker composites, Journal of Building Engineering 68 (2023). https://doi.org/10.1016/j.jobe.2023.106164.

[32] T. Yang, Z. Zhang, H. Zhu, W. Zhang, Y. Gao, X. Zhang, Q. Wu, Effects of calcined dolomite addition on reaction kinetics of one-part sodium carbonate-activated slag cements, Constr Build Mater 211 (2019) 329–336. https://doi.org/10.1016/j.conbuildmat.2019.03.245.

[33] S. Zhou, C. Tan, Y. Gao, Y. Li, S. Guo, One-part alkali activated slag using Ca(OH)2and Na2CO3instead of NaOH as activator: More excellent compressive strength and microstructure, Mater Res Express 8 (2021). https://doi.org/10.1088/2053-1591/ac16f4.

[34] Ö.C. Özen, D. Oktay, B. Aktürk, One-part sodium carbonate-activated slag/r-MgO based mixes: Influence of nano-silica incorporation on compressive strength and microstructural development, Constr Build Mater 422 (2024). https://doi.org/10.1016/j.conbuildmat.2024.135844.

[35] K. Yin, Y. Jiang, H. He, J. Ren, Z. Li, Characterization of one-part alkali-activated slag with rice straw ash, Constr Build Mater 345 (2022). https://doi.org/10.1016/j.conbuildmat.2022.128403.

[36] R.H. Geraldo, J.P. Gonçalves, G. Camarini, Production Process of an Eco-Friendly One-Part Alkali-Activated Binder, Materials Research 25 (2022). https://doi.org/10.1590/1980-5373-MR-2021-0433.

[37] F. Puertas, A. Fernández-Jiménez, M.T. Blanco-Varela, Pore solution in alkali-activated slag cement pastes. Relation to the composition and structure of calcium silicate hydrate, Cem Concr Res 34 (2004) 139–148. https://doi.org/10.1016/S0008-8846(03)00254-0.

[38] S.Y. Oderji, B. Chen, C. Shakya, M.R. Ahmad, S.F.A. Shah, Influence of superplasticizers and retarders on the workability and strength of one-part alkali-activated fly ash/slag binders cured at room temperature, Constr Build Mater 229 (2019) 116891. https://doi.org/https://doi.org/10.1016/j.conbuildmat.2019.116891.

[39] Y. Alrefaei, Y.S. Wang, J.G. Dai, The effectiveness of different superplasticizers in ambient cured one-part alkali activated pastes, Cem Concr Compos 97 (2019) 166–174. https://doi.org/10.1016/j.cemconcomp.2018.12.027.

[40] H.A. Abdel-Gawwad, E.E. Hekal, H. El-Didamony, F.S. Hashem, A.H. Mohammed, A new method to create one-part non-Portland cement powder, J Therm Anal Calorim 134 (2018) 1447–1456. https://doi.org/10.1007/s10973-018-7255-2.

[41] Y.S. Wang, J.L. Provis, J.G. Dai, Role of soluble aluminum species in the activating solution for synthesis of silico-aluminophosphate geopolymers, Cem Concr Compos 93 (2018) 186–195. https://doi.org/10.1016/j.cemconcomp.2018.07.011.

[42] Y. Alrefaei, Y.S. Wang, Y. Qian, J.G. Dai, Effects of Solid Activator and Fly Ash on Rheology and Thixotropy of One-Part Alkali-Activated Pastes, Journal of Advanced Concrete Technology 20 (2022) 139–151. https://doi.org/10.3151/jact.20.139.

[43] M. Refaat, A. Mohsen, E.S.A.R. Nasr, M. Kohail, Minimizing energy consumption to produce safe one-part alkali-activated materials, J Clean Prod 323 (2021). https://doi.org/10.1016/j.jclepro.2021.129137.

[44] J. Ren, H. Sun, Q. Li, Z. Li, L. Ling, X. Zhang, Y. Wang, F. Xing, Experimental comparisons between one-part and normal (two-part) alkali-activated slag binders, Constr Build Mater 309 (2021). https://doi.org/10.1016/j.conbuildmat.2021.125177.

[45] M.R. Ahmad, B. Chen, S.F.A. Shah, Influence of different admixtures on the mechanical and durability properties of one-part alkali-activated mortars, Constr Build Mater 265 (2020) 120320. https://doi.org/10.1016/j.conbuildmat.2020.120320.

[46] L. Coppola, D. Coffetti, E. Crotti, S. Candamano, F. Crea, G. Gazzaniga, T. Pastore, The combined use of admixtures for shrinkage reduction in one-part alkali activated slag-based mortars and pastes, Constr Build Mater 248 (2020). https://doi.org/10.1016/j.conbuildmat.2020.118682.

[47] Y. Sun, Y. Tao, A. V. Rahul, G. Ye, G. De Schutter, EFFECT OF SUPERPLASTICIZERS ON ALKALI-ACTIVATED SLAG CONCRETE, ACI Mater J 119 (2022). https://doi.org/10.14359/51737192.

[48] S. Aydin, B. Baradan, Effect of activator type and content on properties of alkali-activated slag mortars, Compos B Eng 57 (2014) 166–172. https://doi.org/10.1016/j.compositesb.2013.10.001.

[49] J.J. Chang, A study on the setting characteristics of sodium silicate-activated slag pastes, Cem Concr Res 33 (2003) 1005–1011. https://doi.org/10.1016/S0008-8846(02)01096-7.

[50] M. Palacios, E. Zurich, P.F.G. Banfill, Rheology and setting of alkali-activated slag pastes and mortars: Effect of organ admixture SEE PROFILE, 2008. https://www.researchgate.net/publication/283026701.

[51] F. Puertas, C. Varga, M.M. Alonso, Rheology of alkali-activated slag pastes. Effect of the nature and concentration of the activating solution, Cem Concr Compos 53 (2014) 279–288. https://doi.org/10.1016/j.cemconcomp.2014.07.012.

[52] J. Bickley, R.D. Hooton, K.C. Hover, Preparation of a performance-based specification for cast-in-place concrete, RMC Research Foundation (2006) 1–36.

[53] L. Li, J.X. Lu, B. Zhang, C.S. Poon, Rheology behavior of one-part alkali activated slag/glass powder (AASG) pastes, Constr Build Mater 258 (2020) 120381. https://doi.org/10.1016/j.conbuildmat.2020.120381.

[54] A.M. Rashad, A comprehensive overview about the influence of different admixtures and additives on the properties of alkali-activated fly ash, Mater Des 53 (2014) 1005–1025. https://doi.org/10.1016/j.matdes.2013.07.074.

[55] D. Marchon, F. Boscaro, R.J. Flatt, First steps to the molecular structure optimization of polycarboxylate ether superplasticizers: Mastering fluidity and retardation, Cem Concr Res 115 (2019) 116–123. https://doi.org/10.1016/j.cemconres.2018.10.009.

[56] T. Luukkonen, Z. Abdollahnejad, K. Ohenoja, P. Kinnunen, M. Illikainen, Suitability of commercial superplasticizers for one-part alkali-activated blast-furnace slag mortar, J Sustain Cem Based Mater 8 (2019) 244–257. https://doi.org/10.1080/21650373.2019.1625827.

[57] Y. Qin, C. Qu, C. Ma, L. Zhou, One-Part Alkali-Activated Materials : State of the Art and Perspectives, (2022).

[58] P. Zhang, K. Wang, Q. Li, J. Wang, Y. Ling, Fabrication and engineering properties of concretes based on geopolymers/alkali-activated binders - A review, J Clean Prod 258 (2020) 120896. https://doi.org/10.1016/j.jclepro.2020.120896.

[59] Y. Alrefaei, J.G. Dai, Effects of delayed addition of polycarboxylate ether on one-part alkali-activated fly ash/slag pastes: Adsorption, reaction kinetics, and rheology, Constr Build Mater 323 (2022) 126611. https://doi.org/10.1016/j.conbuildmat.2022.126611.

[60] D. Marchon, U. Sulser, A. Eberhardt, R.J. Flatt, Molecular design of comb-shaped polycarboxylate dispersants for environmentally friendly concrete, Soft Matter 9 (2013) 10719–10728. https://doi.org/10.1039/c3sm51030a.

[61] M. Palacios, F. Puertas, Effectiveness of mixing time on hardened properties of waterglass-activated slag pastes and mortars, ACI Mater J 108 (2011) 73–78. https://doi.org/10.14359/51664218.

[62] J. Sobhani, M. Najimi, A.R. Pourkhorshidi, Effects of retempering methods on the compressive strength and water permeability of concrete, Scientia Iranica 19 (2012) 211–217. https://doi.org/10.1016/j.scient.2011.12.012.

[63] M. Ghasemi, H. Rasekh, J. Berenjian, H. AzariJafari, Dealing with workability loss challenge in SCC mixtures incorporating natural pozzolans: A study of natural zeolite and pumice, Constr Build Mater 222 (2019) 424–436. https://doi.org/10.1016/j.conbuildmat.2019.06.174.

[64] Y. Qin, C. Qu, C. Ma, L. Zhou, One-Part Alkali-Activated Materials: State of the Art and Perspectives, Polymers (Basel) 14 (2022). https://doi.org/10.3390/polym14225046.

[65] A. Kiiashko, M. Chaouche, L. Frouin, Effect of phosphonate addition on sodium carbonate activated slag properties, Cem Concr Compos 119 (2021). https://doi.org/10.1016/j.cemconcomp.2021.103986.

[66] J.R. Tenório Filho, L.R.M. de Miranda, K.A. de M. Moraes, P.C.C. Gomes, S.B.B. Uchoa, Development of a Novel Viscosity Modifier Agent for Cementitious Materials: Preliminary Study, Journal of Materials in Civil Engineering 33 (2021). https://doi.org/10.1061/(asce)mt.1943-5533.0003625.

[67] B.A. Silva, A.P. Ferreira Pinto, A. Gomes, A. Candeias, Short- and long-term properties of lime mortars with water-reducers and a viscosity-modifier, Journal of Building Engineering 43 (2021). https://doi.org/10.1016/j.jobe.2021.103086.

[68] N. Ortiz-Álvarez, J. Lizarazo-Marriaga, P.F.B. Brandão, Y. Santos-Panqueva, J. Carrillo, Rheological properties of cement-based materials using a biopolymer viscosity modifying admixture (BVMA) under different dispersion conditions, Cem Concr Compos 124 (2021). https://doi.org/10.1016/j.cemconcomp.2021.104224.

[69] M. Jiang, X. Chen, F. Rajabipour, C.T. Hendrickson, Comparative Life Cycle Assessment of Conventional, Glass Powder, and Alkali-Activated Slag Concrete and Mortar, Journal of Infrastructure Systems 20 (2014). https://doi.org/10.1061/(asce)is.1943-555x.0000211.

[70] J. de Brito, R. Kurda, The past and future of sustainable concrete: A critical review and new strategies on cement-based materials, J Clean Prod 281 (2021). https://doi.org/10.1016/j.jclepro.2020.123558.

[71] S. Yousefi Oderji, B. Chen, E. Mohseni, The efficiency of borax as an additive on properties of one-part fly ash/slag-based alkali-activated materials, European Journal of Environmental and Civil Engineering 0 (2023) 1–13. https://doi.org/10.1080/19648189.2023.2182367.

[72] J.S.J. Van Deventer, J.L. Provis, P. Duxson, Technical and commercial progress in the adoption of geopolymer cement, Miner Eng 29 (2012) 89–104. https://doi.org/10.1016/j.mineng.2011.09.009.

[73] M. Di Mare, C.M. Ouellet-Plamondon, Greener, smarter, stronger: Self-sensing construction materials from one-part alkali-activated materials, Mater Lett 349 (2023). https://doi.org/10.1016/j.matlet.2023.134830.

[74] M. Di Mare, C.M. Ouellet-Plamondon, Highly piezoresistive, self-sensing, one-part potassium-activated inorganic polymers for structural health monitoring, Materials Today Sustainability 20 (2022). https://doi.org/10.1016/j.mtsust.2022.100261.

[75] Y. Alrefaei, Y.S. Wang, J.G. Dai, Q.F. Xu, Effect of superplasticizers on properties of one-part Ca(OH)2/Na2SO4 activated geopolymer pastes, Constr Build Mater 241 (2020). https://doi.org/10.1016/j.conbuildmat.2019.117990.

[76] J. Rasmus, K. Ohenoja, J. Oksanen, E. Adesanya, P. Kinnunen, M. Illikainen, Alternative alkali activator from pulp mill waste – One-part blast furnace slag mortar activated with recovery boiler fly ash, Journal of Building Engineering 76 (2023). https://doi.org/10.1016/j.jobe.2023.107113.

[77] Y. Wu, Z. Jia, X. Qi, W. Wang, S. Guo, Alkali-activated materials without commercial activators: a review, J Mater Sci 59 (2024) 3780–3808. https://doi.org/10.1007/s10853-024-09478-8.

[78] F.S. Lima, T.C.F. Gomes, J.C.B. Moraes, Effect of coffee husk ash as alkaline activator in one-part alkali-activated binder, Constr Build Mater 362 (2023). https://doi.org/10.1016/j.conbuildmat.2022.129799.

[79] E. Örklemez, S. İlkentapar, U. Durak, S. Gülçimen, N. Uzal, B. Uzal, O. Karahan, C.D. Atiş, Characterizing boron-enhanced one-part alkaline-activated mortars: Mechanical properties, microstructure and environmental impacts, Constr Build Mater 426 (2024). https://doi.org/10.1016/j.conbuildmat.2024.136078.

[80] A. Mobili, F. Tittarelli, H. Rahier, One-part alkali-activated pastes and mortars prepared with metakaolin and biomass ash, Applied Sciences (Switzerland) 10 (2020). https://doi.org/10.3390/app10165610.

[81] E. Adesanya, R. Dabbebi, C. Rößler, M. Pavlin, Z. Li, T. Luukkonen, J. Yliniemi, M. Illikainen, Analysis of alkali-activated mineral wool-slag binders: evaluating the differences between one-part and two-part variations, J Mater Cycles Waste Manag 26 (2024) 1001–1011. https://doi.org/10.1007/s10163-023-01878-3.

[82] J. Davidovits, PROPERTIES OF GEOPOLYMER CEMENTS, n.d. www.geopolymer.org.

[83] Y. Cao, Y. Mei, H. Yao, B. Hu, Mechanical and microstructural characterization of one-part binder incorporated with alkali-thermal activated red mud, Case Studies in Construction Materials 21 (2024). https://doi.org/10.1016/j.cscm.2024.e03634.

[84] Y. Chen, C. Zou, C.L. Yong, R.J.S. Jan, T.H. Tan, J. Lin, K.H. Mo, Utilization of waste glass as precursor material in one-part alkali-activated aggregates, Journal of Materials Research and Technology 33 (2024) 5551–5558. https://doi.org/10.1016/j.jmrt.2024.10.204.

[85] M.H. Samarakoon, P.G. Ranjith, W. Hui Duan, A. Haque, B.K. Chen, Extensive use of waste glass in one-part alkali-activated materials: Towards sustainable construction practices, Waste Management 130 (2021) 1–11. https://doi.org/10.1016/j.wasman.2021.04.060.

[86] Q. Fu, M. Bu, Z. Zhang, W. Xu, Q. Yuan, D. Niu, Hydration Characteristics and Microstructure of Alkali-Activated Slag Concrete: A Review, Engineering 20 (2023) 162–179. https://doi.org/10.1016/j.eng.2021.07.026.

[87] X. Li, H. Liu, J. Xing, M. Gan, Z. Ji, X. Fan, Z. Sun, Seawater Mixed with One Part Alkali Activated Material: An Environmental and Cost Evaluation, Materials 17 (2024). https://doi.org/10.3390/ma17164113.

[88] J.S.J. Van Deventer, J.L. Provis, P. Duxson, D.G. Brice, Chemical research and climate change as drivers in the commercial adoption of alkali activated materials, Waste Biomass Valorization 1 (2010) 145–155. https://doi.org/10.1007/s12649-010-9015-9.

[89] Q. Zhao, C. Ma, B. Huang, X. Lu, Development of alkali activated cementitious material from sewage sludge ash: Two-part and one-part geopolymer, J Clean Prod 384 (2023). https://doi.org/10.1016/j.jclepro.2022.135547.

[90] L. Qing, S. Shaokang, J. Zhen, W. Junxiang, L. Xianjun, Effect of CaO on hydration properties of one-part alkali-activated material prepared from tailings through alkaline hydrothermal activation, Constr Build Mater 308 (2021). https://doi.org/10.1016/j.conbuildmat.2021.124931.

[91] T. Luukkonen, Z. Abdollahnejad, J. Yliniemi, P. Kinnunen, M. Illikainen, Comparison of alkali and silica sources in one-part alkali-activated blast furnace slag mortar, J Clean Prod 187 (2018) 171–179. https://doi.org/10.1016/j.jclepro.2018.03.202.

[92] N.J. van Eck, L. Waltman, Software survey: VOSviewer, a computer program for bibliometric mapping, Scientometrics 84 (2010) 523–538. https://doi.org/10.1007/s11192-009-0146-3.

[93] A. Dacić, K. Kopecskó, O. Fenyvesi, I. Merta, The Obstacles to a Broader Application of Alkali-Activated Binders as a Sustainable Alternative—A Review, Materials 16 (2023). https://doi.org/10.3390/ma16083121.

[94] X. Yu, J. Shi, Z. He, Ç. Yalçınkaya, V. Revilla-Cuesta, O. Gencel, Review of the materials composition and performance evolution of green alkali-activated cementitious materials, Clean Technol Environ Policy 25 (2023) 1439–1459. https://doi.org/10.1007/s10098-023-02478-3.

[95] M.F. Alnahhal, T. Kim, A. Hajimohammadi, Waste-derived activators for alkali-activated materials: A review, Cem Concr Compos 118 (2021). https://doi.org/10.1016/j.cemconcomp.2021.103980.

[96] M. Almakhadmeh, A.M. Soliman, Effects of mixing water temperatures on properties of one-part alkali-activated slag paste, Constr Build Mater 266 (2021) 121030. https://doi.org/10.1016/j.conbuildmat.2020.121030.

[97] M. Dong, M. Elchalakani, A. Karrech, Development of high strength one-part geopolymer mortar using sodium metasilicate, Constr Build Mater 236 (2020) 117611. https://doi.org/10.1016/j.conbuildmat.2019.117611.

[98] R.L.D. C. Shi, Day A calorimetric study of early hydration of alkali.pdf, Cem Concr Res 25 (1995) 1333–1346.

[99] C. Ma, B. Zhao, S. Guo, G. Long, Y. Xie, Properties and characterization of green one-part geopolymer activated by composite activators, J Clean Prod 220 (2019) 188–199. https://doi.org/10.1016/j.jclepro.2019.02.159.

[100] D.M. Roy, Alkali-activated cements Opportunities and challenges, 1999.

[101] B. Yang, J.G. Jang, Environmentally benign production of one-part alkali-activated slag with calcined oyster shell as an activator, Constr Build Mater 257 (2020). https://doi.org/10.1016/j.conbuildmat.2020.119552.

[102] M. Najimi, N. Ghafoori, Engineering properties of natural pozzolan/slag based alkali-activated concrete, Constr Build Mater 208 (2019) 46–62. https://doi.org/10.1016/j.conbuildmat.2019.02.107.

[103] A. Galvão Souza Azevedo, K. Strecker, Kaolin, fly-ash and ceramic waste based alkali-activated materials production by the “one-part” method, Constr Build Mater 269 (2021). https://doi.org/10.1016/j.conbuildmat.2020.121306.

[104] L. Xie, K. Liu, Properties and Microstructure of Na2 CO3-Activated Binders Modified with Ca(OH)2 and Mg(OH)2, Materials 15 (2022). https://doi.org/10.3390/ma15051687.

[105] O.S.B. Al-Amoudi, Attack on plain and blended cements exposed to aggressive sulfate environments, Cem Concr Compos 24 (2002) 305–316.

[106] H. Chen, W. Guo, Z. Zhang, J. Li, Q. Zhao, Y. Qiu, R. Guo, Synthesis of a novel one-part alkali-activated material from solid wastes salt sludge and soda residue, Constr Build Mater 450 (2024). https://doi.org/10.1016/j.conbuildmat.2024.138734.

[107] G.S. Hasanain, T.A. Khallaf, K. Mahmood, Water evaporation from freshly placed concrete surfaces in hot weather, Cem Concr Res 19 (1989) 465–475. https://doi.org/10.1016/0008-8846(89)90035-5.

[108] A.A. Hoyos-Montilla, F. Puertas, J.I. Tobón, Microcalorimetric study of the effect of calcium hydroxide and temperature on the alkaline activation of coal fly ash, J Therm Anal Calorim 131 (2018) 2395–2410. https://doi.org/10.1007/s10973-017-6715-4.

[109] M. Criado, A. Palomo, A. Fernández-Jiménez, P.F.G. Banfill, Alkali activated fly ash: Effect of admixtures on paste rheology, Rheol Acta 48 (2009) 447–455. https://doi.org/10.1007/s00397-008-0345-5.

[110] K. Yamada, T. Takahashi, S. Hanehara, M. Matsuhisa, Effects of the chemical structure on the properties of polycarboxylate-type superplasticizer, Cem Concr Res 30 (2000) 197–207. https://doi.org/10.1016/S0008-8846(99)00230-6.

[111] M. Palacios, F. Puertas, Effect of superplasticizer and shrinkage-reducing admixtures on alkali-activated slag pastes and mortars, Cem Concr Res 35 (2005) 1358–1367. https://doi.org/10.1016/j.cemconres.2004.10.014.

[112] M. Palacios, Y.F. Houst, P. Bowen, F. Puertas, Adsorption of superplasticizer admixtures on alkali-activated slag pastes, Cem Concr Res 39 (2009) 670–677. https://doi.org/10.1016/j.cemconres.2009.05.005.

[113] D.L.Y. Kong, J.G. Sanjayan, Effect of elevated temperatures on geopolymer paste, mortar and concrete, Cem Concr Res 40 (2010) 334–339. https://doi.org/10.1016/j.cemconres.2009.10.017.

[114] B. Nematollahi, J. Sanjayan, Effect of different superplasticizers and activator combinations on workability and strength of fly ash based geopolymer, Mater Des 57 (2014) 667–672. https://doi.org/10.1016/j.matdes.2014.01.064.

[115] T. Bakharev, J.G. Sanjayan, Y.B. Cheng, Effect of admixtures on properties of alkali-activated slag concrete, Cem Concr Res 30 (2000) 1367–1374. https://doi.org/10.1016/S0008-8846(00)00349-5.

[116] M. Refaie, A. Mohsen, E.S.A.R. Nasr, M. Kohail, The Effect of Superplasticizers on Eco-friendly Low-Energy One-Part Alkali-Activated Slag, Int J Concr Struct Mater 17 (2023). https://doi.org/10.1186/s40069-023-00615-2.

[117] S.F.A. Shah, B. Chen, S.Y. Oderji, M.A. Haque, M.R. Ahmad, Improvement of early strength of fly ash-slag based one-part alkali activated mortar, Constr Build Mater 246 (2020). https://doi.org/10.1016/j.conbuildmat.2020.118533.

[118] Y. Cheng, P. Cong, H. Hao, Q. Zhao, L. Mei, A. Zhang, Z. Han, M. Hu, Improving workability and mechanical properties of one-part waste brick power based-binders with superplasticizers, Constr Build Mater 335 (2022). https://doi.org/10.1016/j.conbuildmat.2022.127535.

[119] K.H. Yang, J.K. Song, J.S. Lee, Properties of alkali-activated mortar and concrete using lightweight aggregates, Materials and Structures/Materiaux et Constructions 43 (2010) 403–416. https://doi.org/10.1617/s11527-009-9499-6.

[120] M.C.G. Juenger, F. Winnefeld, J.L. Provis, J.H. Ideker, Advances in alternative cementitious binders, Cem Concr Res 41 (2011) 1232–1243. https://doi.org/10.1016/j.cemconres.2010.11.012.

[121] K.H. Yang, A.R. Cho, J.K. Song, S.H. Nam, Hydration products and strength development of calcium hydroxide-based alkali-activated slag mortars, Constr Build Mater 29 (2012) 410–419. https://doi.org/10.1016/j.conbuildmat.2011.10.063.

[122] X. Shi, N. Xie, K. Fortune, J. Gong, Durability of steel reinforced concrete in chloride environments : An overview, Constr Build Mater 30 (2012) 125–138. https://doi.org/10.1016/j.conbuildmat.2011.12.038.

[123] A.F. Abdalqader, F. Jin, A. Al-Tabbaa, Development of greener alkali-activated cement: Utilisation of sodium carbonate for activating slag and fly ash mixtures, J Clean Prod 113 (2016) 66–75. https://doi.org/10.1016/j.jclepro.2015.12.010.

[124] B.S. Gebregziabiher, R. Thomas, S. Peethamparan, Very early-age reaction kinetics and microstructural development in alkali-activated slag, Cem Concr Compos 55 (2015) 91–102. https://doi.org/10.1016/j.cemconcomp.2014.09.001.

[125] A.G. Gaddam, G. Amulya, S.K. Yamsani, V.R. Gondu, Efficacy of Coal Gangue as a Precursor in Synthesis of Geopolymer, Indian Geotechnical Journal 54 (2024) 1043–1055. https://doi.org/10.1007/s40098-023-00804-6.

[126] T. Dong, T. Sun, F. Xu, G. Ouyang, H. Wang, F. Yang, Z. Wang, Effect of Solid Sodium Silicate on Workability, Hydration and Strength of Alkali-Activated GGBS/Fly Ash Paste, Coatings 13 (2023). https://doi.org/10.3390/coatings13040696.

[127] X. Zeng, C. Ma, G. Long, H. Dang, Y. Xie, Hydration kinetics of cement composites with different admixtures at low temperatures, Constr Build Mater 225 (2019) 223–233. https://doi.org/10.1016/j.conbuildmat.2019.07.153.

[128] J. Wei, W.J. Long, J. Liu, B. Zhou, Effect of organic phosphonate on fresh properties of alkali-activated slag composites under different systems: Na2SO4, Na2SiO3, Na2CO3, Constr Build Mater 443 (2024). https://doi.org/10.1016/j.conbuildmat.2024.137698.

[129] M. Palacios, P.F.G. Banfill, F. Puertas, Rheology and setting of alkali-activated slag pastes and mortars: Effect if organic admixture, ACI Mater J 105 (2008) 140–148. https://doi.org/10.14359/19754.

[130] K.H. Yang, J.K. Song, A.F. Ashour, E.T. Lee, Properties of cementless mortars activated by sodium silicate, Constr Build Mater 22 (2008) 1981–1989. https://doi.org/10.1016/j.conbuildmat.2007.07.003.

[131] C. Lu, Z. Zhang, J. Hu, QijunYu, C. Shi, Effects of anionic species of activators on the rheological properties and early gel characteristics of alkali-activated slag paste, Cem Concr Res 162 (2022) 106968. https://doi.org/10.1016/j.cemconres.2022.106968.

[132] Y. Liu, Z. Zhang, C. Shi, D. Zhu, N. Li, Y. Deng, Development of ultra-high performance geopolymer concrete (UHPGC): Influence of steel fiber on mechanical properties, Cem Concr Compos 112 (2020). https://doi.org/10.1016/j.cemconcomp.2020.103670.

[133] Y. Alrefaei, Y.S. Wang, J.G. Dai, Effect of mixing method on the performance of alkali-activated fly ash/slag pastes along with polycarboxylate admixture, Cem Concr Compos 117 (2021) 103917. https://doi.org/10.1016/j.cemconcomp.2020.103917.

[134] G. Masi, A. Filipponi, M.C. Bignozzi, Fly ash-based one-part alkali activated mortars cured at room temperature: Effect of precursor pre-treatments, Open Ceramics 8 (2021). https://doi.org/10.1016/j.oceram.2021.100178.

[135] H.A. Abdel-Gawwad, A.M. El-Khayatt, A. Alkaoud, A.M. Rashad, P. Smarzewski, M.A. Elrahman, K. Al-Jabri, T.A. Tawfik, The potential application of partial activation for

synthesizing one-part alkali-activated slag/fly ash precursor: A way for commercializing alkali-activated materials, Case Studies in Construction Materials 21 (2024). https://doi.org/10.1016/j.cscm.2024.e03461.

[136] M.I. Rasuli, Y. Tajunnisa, A. Yamamura, M. Shigeishi, A consideration on the one-part mixing method of alkali-activated material: problems of sodium silicate solubility and quick setting, Heliyon 8 (2022). https://doi.org/10.1016/j.heliyon.2022.e08783.

[137] M.H. Samarakoon, P.G. Ranjith, W.H. Duan, V.R.S. De Silva, Properties of one-part fly ash/slag-based binders activated by thermally-treated waste glass/NaOH blends: A comparative study, Cem Concr Compos 112 (2020). https://doi.org/10.1016/j.cemconcomp.2020.103679.

[138] M. Refaat, A. Mohsen, E.S.A.R. Nasr, M. Kohail, Utilization of optimized microwave sintering to produce safe and sustainable one-part alkali-activated materials, Sci Rep 13 (2023). https://doi.org/10.1038/s41598-023-31581-0.

[139] H. Chen, Y. Zhang, J. Chen, Z. Qin, P. Wu, Effect of fly ash and gypsum on drying shrinkage and mechanical properties of one-part alkali-activated slag mortar, Structural Concrete (2024). https://doi.org/10.1002/suco.202400006.

[140] R. Rakesh Kumar Reddy, S.C. Yaragal, A. sagar Srinivasa, One-part eco-friendly alkali-activated concrete – An innovative sustainable alternative, Constr Build Mater 408 (2023). https://doi.org/10.1016/j.conbuildmat.2023.133741.

[141] W. Teo, K. Shirai, J.H. Lim, L.B. Jack, E. Nikbakht, Experimental Investigation on Ambient-Cured One-Part Alkali-Activated Binders Using Combined High-Calcium Fly Ash (HCFA) and Ground Granulated Blast Furnace Slag (GGBS), Materials 15 (2022). https://doi.org/10.3390/ma15041612.

[142] K. Yin, Y. Jiang, Y. Pan, Z. Li, N. Xie, J. Meng, Properties comparison of one-part and two-part alkali-activated slag pastes, Case Studies in Construction Materials 21 (2024). https://doi.org/10.1016/j.cscm.2024.e03884.

[143] M. Elzeadani, D. V. Bompa, A.Y. Elghazouli, One part alkali activated materials: A state-of-the-art review, Journal of Building Engineering 57 (2022). https://doi.org/10.1016/j.jobe.2022.104871.

[144] ASTM International, ASTM C109 / C109M - 2002. Standard Test Method for Compressive Strength of Hydraulic Cement Mortars (Using 2-in. or [50 mm] Cube Specimens), Annual Book of ASTM Standards 04 (2002) 9.

[145] ASTM C 597-02, Pulse Velocity Through Concrete, United States: American Society for Testing and Material. 04 (2003) 3–6.

[146] S. Tanada, M. Kabayama, N. Kawasaki, T. Sakiyama, T. Nakamura, M. Araki, T. Tamura, Removal of phosphate by aluminum oxide hydroxide, 2003. www.elsevier.com/locate/jcis.

[147] Y. Sun, S. Zhang, A. V Rahul, Y. Tao, F. Van Bockstaele, K. Dewettinck, G. Ye, G. De Schutter, Cement and Concrete Research Rheology of alkali-activated slag pastes : New insight from

microstructural investigations by cryo-SEM, Cem Concr Res 157 (2022) 106806. https://doi.org/10.1016/j.cemconres.2022.106806.

[148] C. Li, H. Sun, L. Li, A review: The comparison between alkali-activated slag (Si + Ca) and metakaolin (Si + Al) cements, Cem Concr Res 40 (2010) 1341–1349. https://doi.org/10.1016/j.cemconres.2010.03.020.

[149] I.P. Segura, T. Luukkonen, J. Yliniemi, H. Sreenivasan, A.J. Damø, L.S. Jensen, M. Canut, A.M. Kantola, V.V. Telkki, P.A. Jensen, Comparison of One-Part and Two-Part Alkali-Activated Metakaolin and Blast Furnace Slag, Journal of Sustainable Metallurgy 8 (2022) 1816–1830. https://doi.org/10.1007/s40831-022-00606-9.

[150] D.M. Kanaan, A.M. Soliman, Performance of One-Part Alkali-Activated Self- Consolidated Mortar, ACI Mater J 119 (2022) 181–195. https://doi.org/10.14359/51734201.

[151] M. Gonçalves, I.S. Vilarinho, M. Capela, A. Caetano, R.M. Novais, J.A. Labrincha, M.P. Seabra, Waste-based one-part alkali activated materials, Materials 14 (2021) 1–17. https://doi.org/10.3390/ma14112911.

[152] M. Almakhadmeh, ALKALI ACTIVATED MATERIALS: INTERACTIONS BETWEEN INGREDIENTS TO ACHIEVE SUSTAINABILITY, 2020.

[153] R. Concrete, Ready-Mixed Concrete 1, 04 (2003) 1–10.

[154] ASTM, U.S. Int'l, Standard Test Method for Time of Setting of Concrete Mixtures by Penetration Resistance C 403/C 403M, (1999).

[155] N. Ali, A. Soliman, Effect of ingredients adding sequences on rheological properties of alkali-activated slag paste, Innovative Infrastructure Solutions 9 (2024) 145. https://doi.org/10.1007/s41062-024-01462-0.

[156] A.V. V Usherov-Marshak, M.J. Ciak, Isothermal calorimetry in the standard ASTM C1679-08, Cement Wapno Beton 15 (2010) 108-+.

[157] Z. Abdollahnejad, T. Luukkonen, M. Mastali, C. Giosue, O. Favoni, M.L. Ruello, P. Kinnunen, M. Illikainen, Microstructural Analysis and Strength Development of One-Part Alkali-Activated Slag/Ceramic Binders Under Different Curing Regimes, Waste Biomass Valorization 11 (2020) 3081–3096. https://doi.org/10.1007/s12649-019-00626-9.

[158] ASTM international, Standard Test Method for Length Change Of Hardened Cement Mortar And Concrete (ASTM C157), 04 (2017) 1–7.

[159] Y. Sun, S. Ghorbani, X. Dai, G. Ye, G. De Schutter, Evaluation of rheology and strength development of alkali-activated slag with different silicates sources, Cem Concr Compos 128 (2022) 104415. https://doi.org/10.1016/j.cemconcomp.2022.104415.

[160] A. Kashani, J.L. Provis, G.G. Qiao, J.S.J. Van Deventer, The interrelationship between surface chemistry and rheology in alkali activated slag paste, Constr Build Mater 65 (2014) 583–591. https://doi.org/10.1016/j.conbuildmat.2014.04.127.

[161] D. Kanaan, A. el M. Safhi, A.R. Suleiman, A.M. Soliman, Fresh, Hardened, and Microstructural Properties of Ambient Cured One-Part Alkali-Activated Self-Consolidating Concrete, Sustainability (Switzerland) 15 (2023). https://doi.org/10.3390/su15032451.

[162] V. Živica, Effects of type and dosage of alkaline activator and temperature on the properties of alkali-activated slag mixtures, Constr Build Mater 21 (2007) 1463–1469. https://doi.org/10.1016/j.conbuildmat.2006.07.002.

[163] D. Jiang, C. Shi, Z. Zhang, Recent progress in understanding setting and hardening of alkali-activated slag (AAS) materials, Cem Concr Compos 134 (2022). https://doi.org/10.1016/j.cemconcomp.2022.104795.

[164] I. Sereewatthanawut, C. Panwisawas, C. Ngamkhanong, L. Prasittisopin, Effects of extended mixing processes on fresh, hardened and durable properties of cement systems incorporating fly ash, Sci Rep 13 (2023). https://doi.org/10.1038/s41598-023-33312-x.

[165] K.L. Scrivener, A. Nonat, Hydration of cementitious materials, present and future, Cem Concr Res 41 (2011) 651–665. https://doi.org/10.1016/j.cemconres.2011.03.026.

[166] S.K. Nath, S. Mukherjee, S. Maitra, S. Kumar, Kinetics study of geopolymerization of fly ash using isothermal conduction calorimetry, J Therm Anal Calorim 127 (2017) 1953–1961. https://doi.org/10.1007/s10973-016-5823-x.

[167] M. Palacios, S. Gismera, M.M. Alonso, J.B. d'Espinose de Lacaillerie, B. Lothenbach, A. Favier, C. Brumaud, F. Puertas, Early reactivity of sodium silicate-activated slag pastes and its impact on rheological properties, Cem Concr Res 140 (2021) 106302. https://doi.org/10.1016/j.cemconres.2020.106302.

[168] O. Najm, H. El-Hassan, A. El-Dieb, Optimization of alkali-activated ladle slag composites mix design using taguchi-based TOPSIS method, Constr Build Mater 327 (2022). https://doi.org/10.1016/j.conbuildmat.2022.126946.

[169] L. Struble, G.-K. Sun, Viscosity of Portland Cement Paste as a Function of Concentration, 1995.

[170] N. Roussel, A. Lemaître, R.J. Flatt, P. Coussot, Steady state flow of cement suspensions: A micromechanical state of the art, Cem Concr Res 40 (2010) 77–84. https://doi.org/10.1016/j.cemconres.2009.08.026.

[171] X. Luo, L. Huang, L. Wei, M. Chen, Z. Zhou, T. Zhang, A technique for preparing one-part geopolymers by activating alkali-fused lithium slag with solid sodium silicate, Constr Build Mater 435 (2024). https://doi.org/10.1016/j.conbuildmat.2024.136817.

[172] Y. Zuo, M. Nedeljković, G. Ye, Coupled thermodynamic modelling and experimental study of sodium hydroxide activated slag, Constr Build Mater 188 (2018) 262–279. https://doi.org/10.1016/j.conbuildmat.2018.08.087.

[173] R. Rumman, M.R. Kamal, A. Bediwy, M.S. Alam, Partially burnt wood fly ash characterization and its application in low-carbon mortar and concrete, Constr Build Mater 402 (2023) 132946. https://doi.org/10.1016/j.conbuildmat.2023.132946.

[174] P. Li, J. Tang, X. Chen, Y. Bai, Q. Li, Effect of temperature and pH on early hydration rate and apparent activation energy of alkali-activated slag, Advances in Materials Science and Engineering 2019 (2019). https://doi.org/10.1155/2019/3531543.

[175] A. Fauzi, M.F. Nuruddin, A.B. Malkawi, M.M.A.B. Abdullah, Study of Fly Ash Characterization as a Cementitious Material, in: Procedia Eng, Elsevier Ltd, 2016: pp. 487–493. https://doi.org/10.1016/j.proeng.2016.06.535.

[176] T. Bakharev, J.G. Sanjayan, Y.-B. Cheng, Effect of elevated temperature curing on properties of alkali-activated slag concrete, 1999.

[177] R.J. Thomas, D. Lezama, S. Peethamparan, On drying shrinkage in alkali-activated concrete: Improving dimensional stability by aging or heat-curing, Cem Concr Res 91 (2017) 13–23. https://doi.org/10.1016/j.cemconres.2016.10.003.

[178] S. Narimani Zamanabadi, S.A. Zareei, P. Shoaei, F. Ameri, Ambient-cured alkali-activated slag paste incorporating micro-silica as repair material: Effects of alkali activator solution on physical and mechanical properties, Constr Build Mater 229 (2019). https://doi.org/10.1016/j.conbuildmat.2019.116911.

[179] W. Chen, B. Li, J. Wang, N. Thom, Effects of alkali dosage and silicate modulus on autogenous shrinkage of alkali-activated slag cement paste, Cem Concr Res 141 (2021). https://doi.org/10.1016/j.cemconres.2020.106322.

[180] G. Sadeghian, K. Behfarnia, M. Teymouri, Drying shrinkage of one-part alkali-activated slag concrete, Journal of Building Engineering 51 (2022). https://doi.org/10.1016/j.jobe.2022.104263.

[181] F. Collins, J.G. Sanjayan, Effect of pore size distribution on drying shrinking of alkali-activated slag concrete, Cem Concr Res 30 (2000) 1401–1406.

[182] Douglas C. Montgomery, Douglas C. Montgomery - Design and analysis of experiments-Wiley (2020), John Wiley & Sons (n.d.).

[183] W.J. Long, J.J. Wei, Y.C. Gu, F. Xing, Research on dynamic mechanical properties of alkali activated slag concrete under temperature-loads coupling effects, Constr Build Mater 154 (2017) 687–696. https://doi.org/10.1016/j.conbuildmat.2017.08.015.

[184] M. Wu, Y. Zhang, Z. Liu, C. Liu, W. She, Z. Wu, Experimental study on eco-friendly one-part alkali-activated slag-fly ash-lime composites under CO2 environment: Reaction mechanism and carbon capture capacity, Constr Build Mater 421 (2024). https://doi.org/10.1016/j.conbuildmat.2024.135779.

[185] A.S.S.S. Nedunuri, S. Muhammad, The role of zinc sulphate as a retarder for alkali activated binders and its influence on the rheological, setting and mechanical behaviour, Constr Build Mater 344 (2022) 128128. https://doi.org/10.1016/j.conbuildmat.2022.128128.

[186] J. Xiang, Y. He, X. Cui, L. Liu, Enhancement of setting times and hardening of alkali-activated slag binder using CO2-modified slag, Cem Concr Compos 134 (2022). https://doi.org/10.1016/j.cemconcomp.2022.104797.

[187] L. Li, J. Xie, B. Zhang, Y. Feng, J. Yang, A state-of-the-art review on the setting behaviours of ground granulated blast furnace slag- and metakaolin-based alkali-activated materials, Constr Build Mater 368 (2023). https://doi.org/10.1016/j.conbuildmat.2023.130389.

[188] J. Wei, C. Fang, B. Zhou, Z. Wu, Effect of organic phosphonate types on performance of alkali-activated slag-based materials and its mechanism, Cem Concr Compos 151 (2024). https://doi.org/10.1016/j.cemconcomp.2024.105597.

[189] X. Wang, W. Wu, L. Zhang, L. Fu, X. Li, Preparation of one-part alkali-activated nickel slag binder using an optimal ball milling process, Constr Build Mater 322 (2022). https://doi.org/10.1016/j.conbuildmat.2021.125902.

[190] H. Zheng, Y. He, Y. Zhu, L. Liu, X. Cui, Novel procedure of CO2capture of the CaO sorbent activator on the reaction of one-part alkali-activated slag, RSC Adv 11 (2021) 12476–12483. https://doi.org/10.1039/d1ra01353j.

[191] K. tuo Wang, L. qiu Du, X. sen Lv, Y. He, X. min Cui, Preparation of drying powder inorganic polymer cement based on alkali-activated slag technology, Powder Technol 312 (2017) 204–209. https://doi.org/10.1016/j.powtec.2017.02.036.

[192] K.N. Ballantyne, R.A. van Oorschot, R.J. Mitchell, Reduce optimisation time and effort: Taguchi experimental design methods, Forensic Sci Int Genet Suppl Ser 1 (2008) 7–8. https://doi.org/10.1016/j.fsigss.2007.10.050.

[193] G.D. Bowden, B.J. Pichler, A. Maurer, A Design of Experiments (DoE) Approach Accelerates the Optimization of Copper-Mediated 18F-Fluorination Reactions of Arylstannanes, Sci Rep 9 (2019). https://doi.org/10.1038/s41598-019-47846-6.

[194] B.W. Chong, R. Othman, R.P. Jaya, M.R.M. Hasan, A.V. Sandu, M. Nabiałek, B. Jeż, P. Pietrusiewicz, D. Kwiatkowski, P. Postawa, M.M.A.B. Abdullah, Design of experiment on concrete mechanical properties prediction: A critical review, Materials 14 (2021). https://doi.org/10.3390/ma14081866.

[195] K. Mahendra, M.C. Narasimhan, G. Bhanu Prakash, A.K. Das, Multi-objective optimization of one-part alkali-activated mortar mixes using Taguchi-Grey relational analysis, Constr Build Mater 412 (2024). https://doi.org/10.1016/j.conbuildmat.2023.134761.

[196] S. V. Dave, A. Bhogayata, The strength oriented mix design for geopolymer concrete using Taguchi method and Indian concrete mix design code, Constr Build Mater 262 (2020). https://doi.org/10.1016/j.conbuildmat.2020.120853.

[197] N. Garg, C.E. White, Mechanism of zinc oxide retardation in alkali-activated materials: An: in situ X-ray pair distribution function investigation, J Mater Chem A Mater 5 (2017) 11794–11804. https://doi.org/10.1039/c7ta00412e.

[198] A. Mohsen, M.S. Amin, F.A. Selim, M. Ramadan, The impact of wurtzite and mesoporous Zn-Al-CO3 LDH on the performance of alkali-activated-slag: Setting times, compressive strength, and radiation attenuation, Constr Build Mater 438 (2024). https://doi.org/10.1016/j.conbuildmat.2024.137218.

[199] A.R. Brough, M. Holloway, J. Sykes, A. Atkinson, Sodium silicate-based alkali-activated slag mortars: Part II. The retarding effect of additions of sodium chloride or malic acid, Cem Concr Res 30 (2000) 1375–1379.

[200] Y. Shen, W. Zhang, H. Zhu, J. Li, S. Shi, Effect of borax on calcium sulfoaluminate cement properties, Ceramics - Silikaty 67 (2023) 10–19. https://doi.org/10.13168/cs.2022.0055.

[201] M. Zajac, J. Skocek, F. Bullerjahn, M. Ben Haha, Effect of retarders on the early hydration of calcium-sulpho-aluminate (CSA) type cements, Cem Concr Res 84 (2016) 62–75. https://doi.org/10.1016/j.cemconres.2016.02.014.

[202] T. Matschei, B. Lothenbach, F.P. Glasser, The role of calcium carbonate in cement hydration, Cem Concr Res 37 (2007) 551–558. https://doi.org/10.1016/j.cemconres.2006.10.013.

[203] M.F. Maherian, S.N. Bicakci, S. Baran, H.N. Atahan, Determining Mechanical and Permeability Properties of Fly Ash and Nano-silica Containing Mixtures Using Taguchi Design Method, in: Lecture Notes in Civil Engineering, Springer Science and Business Media Deutschland GmbH, 2023: pp. 699–709. https://doi.org/10.1007/978-3-031-32519-9_68.

[204] B.E. Yuce, P.V. Nielsen, P. Wargocki, The use of Taguchi, ANOVA, and GRA methods to optimize CFD analyses of ventilation performance in buildings, Build Environ 225 (2022). https://doi.org/10.1016/j.buildenv.2022.109587.

[205] K. Mahendra, M.C. Narasimhan, G.B. Prakash, A.K. Das, Experimental investigation and optimization of one-part alkali-activated self-compacting concrete mixes, Case Studies in Construction Materials 21 (2024). https://doi.org/10.1016/j.cscm.2024.e04062.

[206] Y. Kuo, T. Yang, G.W. Huang, The use of a grey-based Taguchi method for optimizing multi-response simulation problems, Engineering Optimization 40 (2008) 517–528. https://doi.org/10.1080/03052150701857645.

[207] B. Dutta, T. Singha, M. Goh, M.T. Lamata, J.L. Verdegay, Post factum analysis in TOPSIS based decision making method, Expert Syst Appl 138 (2019). https://doi.org/10.1016/j.eswa.2019.07.023.

[208] N. Ali, A.M. Soliman, Influence of mixing protocols on flow retention of one-part alkali activated slag systems, Constr Build Mater 450 (2024). https://doi.org/10.1016/j.conbuildmat.2024.138467.

[209] M.F. Alnahhal, T. Kim, A. Hajimohammadi, Distinctive rheological and temporal viscoelastic behaviour of alkali-activated fly ash/slag pastes: A comparative study with cement paste, Cem Concr Res 144 (2021). https://doi.org/10.1016/j.cemconres.2021.106441.

[210] N. ELsayed, A. Soliman, Alkali-Activated Concrete Workability and Effect of Various Admixtures: A Review, in: 2024: pp. 729–738. https://doi.org/10.1007/978-3-031-35471-7_52.

[211] N.R. Rakhimova, V.P. Morozov, A.A. Eskin, B.M. Galiullin, Feasibility of Design One-Part Sodium Silicate Activated Metamontmorillonite-Limestone Cements, Iranian Journal of Materials Science and Engineering 20 (2023) 1–7. https://doi.org/10.22068/ijmse.3272.

[212] W. Al Makhadmeh, A. Soliman, On the mechanisms of shrinkage reducing admixture in alkali activated slag binders, Journal of Building Engineering 56 (2022). https://doi.org/10.1016/j.jobe.2022.104812.

[213] E.K. Fayed, F.I. El-Hosiny, I.M. El-Kattan, H. Al-Kroom, M.A. Elrahman, H.A. Abdel-Gawwad, An innovative method for sustainable utilization of blast-furnace slag in the cleaner production of one-part hybrid cement mortar, Materials 14 (2021). https://doi.org/10.3390/ma14195669.

[214] C. Lu, Z. Zhang, C. Shi, N. Li, D. Jiao, Q. Yuan, Rheology of alkali-activated materials: A review, Cem Concr Compos 121 (2021) 104061. https://doi.org/10.1016/j.cemconcomp.2021.104061.

[215] N. Ajay, S. Girish, A.M. Joshi, N. Bharadwaj, Studies on Rheological Properties of High-Flowable Concrete, in: 2024. https://doi.org/10.1007/978-3-031-38841-5_4.

[216] L. Zhang, Y. Ji, J. Li, F. Gao, G. Huang, Effect of retarders on the early hydration and mechanical properties of reactivated cementitious material, Constr Build Mater 212 (2019) 192–201. https://doi.org/10.1016/j.conbuildmat.2019.03.323.

[217] R.B. Kogbara, A. Al-Zubi, Y. Mortada, A. Hammoud, E.A. Masad, M.K. Khraisheh, Lime-activated one-part geopolymer mortars from construction, demolition and industrial wastes, Results in Engineering 21 (2024). https://doi.org/10.1016/j.rineng.2023.101739.

[218] W. Matthes, A. Vollpracht, Y. Villagrán, S. Kamali-Bernard, D. Hooton, E. Gruyaert, M. Soutsos, N. De Belie, Ground granulated blast-furnace slag, Properties of Fresh and Hardened Concrete Containing Supplementary Cementitious Materials: State-of-the-Art Report of the RILEM Technical Committee 238-SCM, Working Group 4 (2018) 1–53.

[219] B. Ma, Z. Zhu, W. Huo, L. Yang, Y. Zhang, H. Sun, X. Zhang, Assessing the viability of a high performance one-part geopolymer made from fly ash and GGBS at ambient temperature, Journal of Building Engineering 75 (2023). https://doi.org/10.1016/j.jobe.2023.106978.

[220] M.H. Cetin, B. Ozcelik, E. Kuram, E. Demirbas, Evaluation of vegetable based cutting fluids with extreme pressure and cutting parameters in turning of AISI 304L by Taguchi method, J Clean Prod 19 (2011) 2049–2056. https://doi.org/10.1016/j.jclepro.2011.07.013.

[221] N. Mobasher, S.A. Bernal, J.L. Provis, Structural evolution of an alkali sulfate activated slag cement, Journal of Nuclear Materials 468 (2016) 97–104. https://doi.org/10.1016/j.jnucmat.2015.11.016.

[222] C. Ma, G. Long, Y. Shi, Y. Xie, Preparation of cleaner one-part geopolymer by investigating different types of commercial sodium metasilicate in China, J Clean Prod 201 (2018) 636–647. https://doi.org/10.1016/j.jclepro.2018.08.060.

[223] R.J. Myers, E. L'Hôpital, J.L. Provis, B. Lothenbach, Effect of temperature and aluminium on calcium (alumino)silicate hydrate chemistry under equilibrium conditions, Cem Concr Res 68 (2015) 83–93. https://doi.org/10.1016/j.cemconres.2014.10.015.

[224] W. Al Makhadmeh, A. Soliman, Understanding the shrinkage behaviour of alkali-activated slag binders modified by the superabsorbent polymer, Constr Build Mater 365 (2023). https://doi.org/10.1016/j.conbuildmat.2022.130053.

[225] G. Renaudin, J. Russias, F. Leroux, C. Cau-dit-Coumes, F. Frizon, Structural characterization of C-S-H and C-A-S-H samples-Part II: Local environment investigated by spectroscopic analyses, J Solid State Chem 182 (2009) 3320–3329. https://doi.org/10.1016/j.jssc.2009.09.024.

[226] I.G. Richardson, A.R. Brough, R. Brydson, G.W. Groves, C.M. Dobson, Location of Aluminum in Substituted Calcium Silicate Hydrate (C-S-H) Gels as Determined by 29Si and 27Al NMR and EELS, Journal of the American Ceramic Society 76 (1993) 2285–2288. https://doi.org/10.1111/j.1151-2916.1993.tb07765.x.

[227] I. Ismail, S.A. Bernal, J.L. Provis, S. Hamdan, J.S.J. Van Deventer, Drying-induced changes in the structure of alkali-activated pastes, J Mater Sci 48 (2013) 3566–3577. https://doi.org/10.1007/s10853-013-7152-9.

[228] I.G. Richardson, G.W. Groves, The structure of the calcium silicate hydrate phases present in hardened pastes of white Portland cement/blast-furnace slag blends, 1997.

[229] J. Skibsted, M.D. Andersen, The effect of alkali ions on the incorporation of aluminum in the calcium silicate hydrate (C-S-H) phase resulting from portland cement hydration studied by 29Si MAS NMR, Journal of the American Ceramic Society 96 (2013) 651–656. https://doi.org/10.1111/jace.12024.

[230] H. Ye, A. Radlińska, Shrinkage mechanisms of alkali-activated slag, Cem Concr Res 88 (2016) 126–135. https://doi.org/10.1016/j.cemconres.2016.07.001.

[231] A. Talaat, A. Emad, M. Kohail, Environmental Impact Assessment for Performance-Oriented Geopolymer Concrete Research, Journal of Materials in Civil Engineering 35 (2023). https://doi.org/10.1061/(asce)mt.1943-5533.0004526.

[232] M. Nikravan, R. Firdous, D. Stephan, Life cycle assessment of alkali-activated materials: a systematic literature review, Low-Carbon Materials and Green Construction 1 (2023). https://doi.org/10.1007/s44242-023-00014-6.

[233] G. Wernet, C. Bauer, B. Steubing, J. Reinhard, E. Moreno-Ruiz, B. Weidema, The ecoinvent database version 3 (part I): overview and methodology, International Journal of Life Cycle Assessment 21 (2016) 1218–1230. https://doi.org/10.1007/s11367-016-1087-8.

[234] A. Zhou, K. Li, T. Liu, D. Zou, X. Peng, H. Lyu, J. Xiao, C. Luan, Recycling and optimum utilization of engineering sediment waste into low-carbon geopolymer paste for sustainable infrastructure, J Clean Prod 383 (2023). https://doi.org/10.1016/j.jclepro.2022.135549.

[235] C. Chen, G. Habert, Y. Bouzidi, A. Jullien, A. Ventura, LCA allocation procedure used as an incitative method for waste recycling: An application to mineral additions in concrete, Resour Conserv Recycl 54 (2010) 1231–1240. https://doi.org/10.1016/j.resconrec.2010.04.001.

[236] G. Habert, J.B. D'Espinose De Lacaillerie, N. Roussel, An environmental evaluation of geopolymer based concrete production: Reviewing current research trends, J Clean Prod 19 (2011) 1229–1238. https://doi.org/10.1016/j.jclepro.2011.03.012.

[237] M. Salman, M. Dubois, A. Di Maria, K. Van Acker, K. Van Balen, Construction Materials from Stainless Steel Slags: Technical Aspects, Environmental Benefits, and Economic Opportunities, J Ind Ecol 20 (2016) 854–866. https://doi.org/10.1111/jiec.12314.

[238] D. V. Bompa, B. Xu, O. Corbu, Evaluation of One-Part Slag–Fly-Ash Alkali-Activated Mortars Incorporating Waste Glass Powder, Journal of Materials in Civil Engineering 34 (2022). https://doi.org/10.1061/(asce)mt.1943-5533.0004532.

[239] A. Alzaza, K. Ohenoja, M. Illikainen, One-part alkali-activated blast furnace slag for sustainable construction at subzero temperatures, Constr Build Mater 276 (2021). https://doi.org/10.1016/j.conbuildmat.2020.122026.

[240] Y. Chen, S. He, Y. Zhang, Z. Wan, O. Çopuroğlu, E. Schlangen, 3D printing of calcined clay-limestone-based cementitious materials, Cem Concr Res 149 (2021). https://doi.org/10.1016/j.cemconres.2021.106553.

[241] S. Chaves Figueiredo, O. Çopuroğlu, E. Schlangen, Effect of viscosity modifier admixture on Portland cement paste hydration and microstructure, Constr Build Mater 212 (2019) 818–840. https://doi.org/10.1016/j.conbuildmat.2019.04.020.

[242] M. Lachemi, K.M.A. Hossain, V. Lambros, P.C. Nkinamubanzi, N. Bouzoubaâ, Performance of new viscosity modifying admixtures in enhancing the rheological properties of cement paste, Cem Concr Res 34 (2004) 185–193. https://doi.org/10.1016/S0008-8846(03)00233-3.

[243] Y. Chen, M. Liang, Y. Zhang, Z. Li, B. Šavija, E. Schlangen, O. Çopuroğlu, Can superabsorbent polymers be used as rheology modifiers for cementitious materials in the context of 3D concrete printing?, Constr Build Mater 371 (2023). https://doi.org/10.1016/j.conbuildmat.2023.130777.

[244] R. Srinivasan, D. DeFord, S.P. Shah, The use of extrusion rheometry in the development of extruded fiber-reinforced cement composites, Concrete Science and Engineering 1 (1999) 26–36.

[245] R. Bouras, A. Kaci, M. Chaouche, Influence of viscosity modifying admixtures on the rheological behavior of cement and mortar pastes, Korea Australia Rheology Journal 24 (2012) 35–44. https://doi.org/10.1007/s13367-012-0004-3.

[246] S. Bhattacherjee, S. Jain, M. Santhanam, Investigating the Interaction of Limestone Calcined Clay and OPC-Based Systems with a Methyl Hydroxyethyl Cellulose-Based Viscosity

Modifier Used for 3D Printable Concrete, Journal of Materials in Civil Engineering 36 (2024). https://doi.org/10.1061/jmcee7.mteng-17728.

[247] M. Saric-Coric, K.H. Khayat, A. Tagnit-Hamou, Performance characteristics of cement grouts made with various combinations of high-range water reducer and cellulose-based viscosity modifier, Cem Concr Res 33 (2003) 1999–2008. https://doi.org/10.1016/S0008-8846(03)00214-X.

[248] A. Mechaymech, J.J. Assaad, Stability of Self-Consolidating Concrete Containing Different Viscosity Modifiers, Civil Engineering Infrastructures Journal 52 (2019) 245–263. https://doi.org/10.22059/ceij.2019.262859.1502.

[249] N. Ali, A.M. Soliman, Single and multi-response optimization of retarded admixture on alkali activated slag rheological behavior by the taguchi method, Constr Build Mater 459 (2025) 139812. https://doi.org/10.1016/j.conbuildmat.2024.139812.

[250] K.A. Snyder, D.P. Bentz, J.M. Davis, Using Viscosity Modifiers to Reduce Effective Diffusivity in Mortars, Journal of Materials in Civil Engineering 24 (2012) 1017–1024. https://doi.org/10.1061/(asce)mt.1943-5533.0000524.

[251] M. Benaicha, O. Jalbaud, A. Hafidi Alaoui, Y. Burtschell, Porosity effects on rheological and mechanical behavior of self-compacting concrete, Journal of Building Engineering 48 (2022). https://doi.org/10.1016/j.jobe.2021.103964.

[252] D. Coffetti, S. Candamano, F. Crea, L. Coppola, On the role of alkali content on one-part alkali activated slag pastes produced with tri- blend solid activators, Constr Build Mater 409 (2023). https://doi.org/10.1016/j.conbuildmat.2023.133868.